Highly Resolved Paleoclimatic Aerosol Records:

Continuous Flow Analysis and the Potential of Flow Cytometry for the Characterisation of Aeolian Dust in Polar Ice Cores

Author: Ernesto Kettner

Supervisors:

Anders Svensson
Centre for Ice and Climate
Niels Bohr Institute
University of Copenhagen

Matthias Bigler
Oeschger Centre for Climate Change Research
Climate and Environmental Physics
University of Bern

Compiled: December 7, 2013

THIS THESIS HAS BEEN SUBMITTED TO THE
PHD SCHOOL OF THE FACULTY OF SCIENCE,
UNIVERSITY OF COPENHAGEN
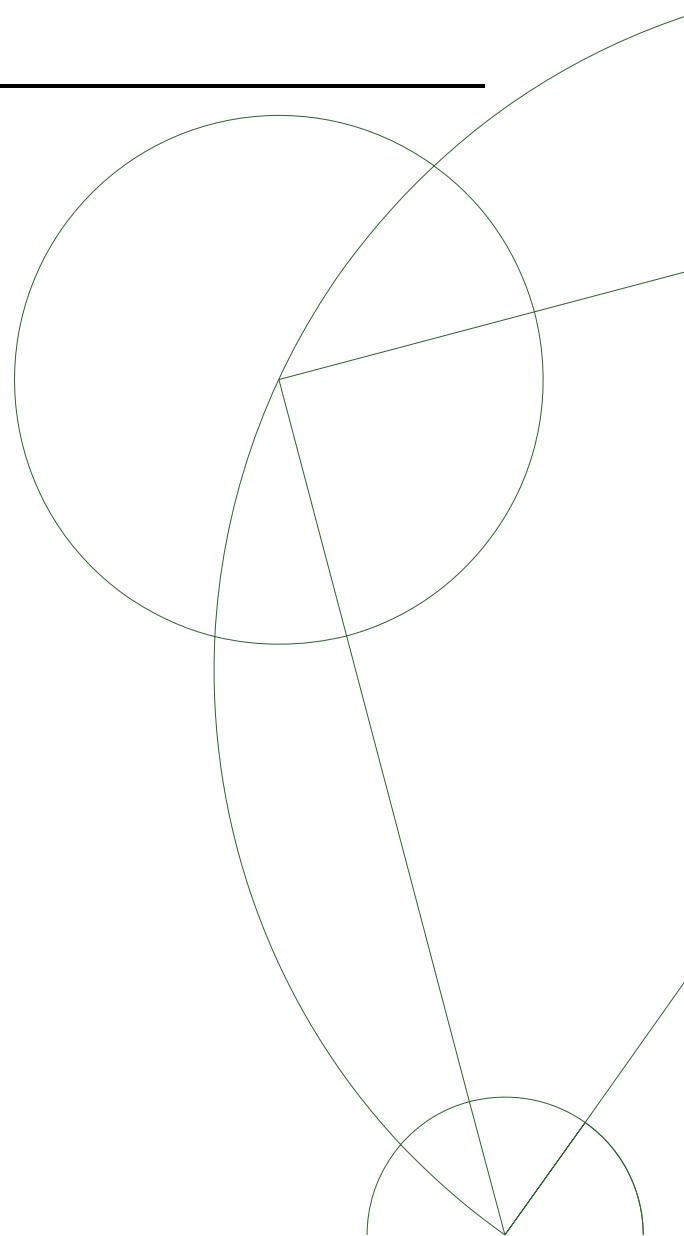
'Pourquoi', se demandait un jour le petit prince, 'pourquoi ne pas connecter une tronçonneuse et en conclure sur le climat passé?'

Après de Saint-Exupéry (Le Petit Robert, 2006, p. 2692)

Abstract

In ice cores a plethora of proxies for paleoclimatic conditions is archived. Air trapped in the ice during firnification allows for direct measurements of the concentrations and isotope ratios of paleoatmospheric gases while, the isotopic composition of the ice matrix itself is related to paleotemperatures. Impurities in the matrix are comprised of particulate and soluble aerosols, each carrying information on its source's activitiy and|or proximity.

Opposed to gases and water isotopes, the seasonality of many aerosols is not smoothed out in the firn column so that large concentration gradients with frequently changing signs are preserved. Therefore, these aerosol records can be used for dating by annual layer counting. However, with increasing depth the annual layer thicknesses decreases due to pressure and ice flow and accurate dating is possible only as long as the rapid variations can be resolved experimentally.

Over the last decades Continuous Flow Analysis (CFA) has become a well-established technique for aerosol quantification. In CFA, a piece of core is melted continuously and the melt water is analysed for an array of chemical impurities. When designing a CFA system, a trilemma between high sample throughput, high resolution and a large number of detected species is encountered.

In this experimental work, subsequent to contributing to the construction of a CFA system optimised for high resolution, possibilities for the improvement of the insoluble aerosol records' quality were investigated. Whereas soluble aerosols can be analysed for concentration changes only, insoluble aeolian dust can reveal additional information on its atmospheric residence time via changes in the mean grain sizes.

Volumes of particulate matter in ice cores are most reliably determined with Coulter counters, but since a Coulter counter performs measurements on discrete samples, it cannot be connected to a CFA system. Attenuation sensors, on the other hand, can be integrated into a CFA set-up, but are known to yield poor dust size records.

The dilemma between high quality sizing and high depth resolution was found impossible to circumvent by employing a third detection technique - laser scattering. Reliable information on size changes, even relative ones, cannot be obtained using optical methods. It is therefore proposed to focus further efforts on electrical measurements, making use of the advancements made over the past decade in impedance cytometry.

Resumé

Et væld af proxydata for paleoklimatiske forhold bliver arkiveret i iskerner. Luftbobler fanget i isen under firnifikationsprocessen giver mulighed for direkte at måle koncentrationen og isotopsammensætningen af paleoatmosfæriske gasser, mens den isotopiske sammensætning af selve isen er relateret til paleotemperaturer. Urenheder i ismatricen består af både partikulære og opløselige aerosoler, som alle indeholder oplysninger om aktiviteten og|eller nærheden af hver sin kilde.

I modsætning til gasser og vandisotoperne bliver sæsonudsving i mange aerosoler ikke udglattet i firnen, hvilket bevirker at store koncentrationsgradienter med skiftende fortegn bevares. Derfor kan disse aerosoldata benyttes til datering af iskernen ved optælling af årlag. Med dybden mindskes årlagstykkelserne dog på grund af øget tryk og isens flydning, og en præcis datering er kun mulig så længe de hurtige variationer kan opløses eksperimentelt.

Gennem de seneste årtier er Continuous Flow Analysis (CFA) blevet en veletableret teknik til at kvantificere de varierende aerosolkoncentrationer. I CFA bliver et stykke iskerne smeltet kontinuerligt, og smeltevandet analyseres for en række kemiske urenheder. Når man designer et CFA system støder man på et trilemma mellem at balancere høj produktivitet, høj opløsning og detektion af et stort antal forskellige slags urenheder.

I dette eksperimentelle arbejde, efter at bidrage til opbygningen af et CFA system optimeret til høj dataopløsning, blev mulighederne undersøgt for at forbedre kvaliteten af målingerne af uopløselige aerosoler.

Den mest pålidelige måde at bestemme en iskernes partikelindhold er ved hjælp af Coulter counterer, men eftersom en Coulter counter udfører målinger på diskrete prøver, kan dette instrument ikke tilsluttes et CFA system. Dæmpningssensorer kan derimod integreres i et CFA system, men disse er kendt for at give dårlige data for støvkornsstørrelser.

Dilemmaet mellem høj kvalitet af støvkornsstørrelse data og høj dybdeopløsning blev fundet umuligt at omgå ved at benytte en tredje detektionsteknik – laserspredning. Pålidelig information om ændringerne i støvkornsstørrelse, selv relative, kan ikke opnås ved hjælp af optiske metoder. Det foreslås derfor at fokusere en yderligere indsats på elektriske målinger, der gør brug af de fremskridt, der er gjort i løbet af det seneste årti indenfor impedanscytometri.

Contents

Introduction

Ice Cores as Paleoclimatic Archives Polar ice caps constitute archives of the paleoatmospheric composition. Aerosols and precipitation deposited on the ice sheets can reveal information on their respective sources at lower latitudes and on processes undergone during transport (e.g. Legrand and Mayewski, 1997; Fischer et al., 2007). If the stratigraphy at the sampling site is unperturbed, establishment of the age-depth relationship is straight forward.

Therefore, a wealth of information on paleoclimate and paleoclimatic changes can be extracted from ice cores drilled in Greenland and Antarctica reaching back 130ka (NEEM members, 2013) and 800ka (Jouzel et al., 2007), respectively. Relative to other archives, ice cores preserve their information at a remarkably high temporal resolution (e.g. Legrand and Mayewski, 1997) and are the only archive giving direct access to the gaseous composition of the paleoatmosphere.

Gases frequently extracted from ice cores for subsequent measurements are N_2 and O_2 (e.g. Sowers et al., 1989; Kawamura et al., 2007), CO_2 (e.g. Stauffer and Berner, 1978; Stauffer et al., 1998), CH_4 (e.g. Blunier et al., 1995; Brook et al., 2000) and N_2O (e.g. Sowers et al., 2003; Flückiger et al., 2004). Recently, gas measurements have been extended to also incorporate noble gases (Severinghaus et al., 2010). Since the atmospheric residence time of the gases measured is long compared to the time scale on which interhemispheric mixing takes place (Chappellaz et al., 1993), the air bubbles entrapped in the ice during firnification primarily carry global climate signals.

However, the gases' respective and isotopic ratios have also been used as proxies for local summer time insulation and surface temperature (e.g. Severinghaus et al., 1998; Landais et al., 2004) or to model processes taking place in the firn prior to entrapment (Schwander et al., 1997; Buizert et al., 2012). Further, as CO_2, N_2O and CH_4 are greenhouse gases, their increasing mixing ratios during the last 1^{1}/$_{2}$ centuries have attracted considerable attention (e.g. Blunier et al., 1995; Etheridge et al., 1996)

When linking gas records to information obtained from an analysis of the ice matrix, it has to be taken into account that, because of the diffusion taking place in the porous firn, the entrapped gases are not of the same age as the enclosing ice (Schwander and Stauffer, 1984; Schwander et al., 1997). From the isotopic composition of the latter, conclusions with

respect to paleotemperatures can be drawn.

As the precipitation is transported poleward from its evaporation site, it is depleted in heavy isotopes during every phase change (Johnsen et al., 1989; Masson-Delmotte et al., 2005), such that the isotopic composition of the precipitation is a function of the temperature gradient between the sites of evaporation and condensation, respectively (Dansgaard, 1964). To a first order approximation, the ice matrix' isotopic composition can therefore be interpreted as a function of cloud condensation temperature at the deposition site (Jouzel and Merlivat, 1984).

Impurities in the ice matrix are present in the form of dissolved and particulate aerosols that have been dry or wet deposited contemporaneously with the precipitation. Many aerosols are, opposed to the gases and the isotopic composition of the firn, not subjected to post-depositional diffusion. Of those irreversibly deposited aerosols, species with seasonal variations mark annual layers, allowing for accurate dating of the entire core by layer counting (Meese et al., 1997; Andersen et al., 2006; Svensson et al., 2006).

However, accurate dating by layer counting is only possible as long as the detection systems succeed in resolving the annual layers. This justifies any effort to improve the depth resolution in an attempt to capture sub-seasonal variations in aerosol concentrations at ever greater depths. Classically, soluble aerosol concentrations are detected by ion chromatography (IC) on discrete and carefully decontaminated samples (see e.g. Hammer, 1977; Petit et al., 1981; Legrand and Delmas, 1987). However, decontamination procedures and measurement times have been prohibitive to the full exploitation of the high temporal resolution preserved by many aerosol records.

Continuous Flow Analysis   This has encouraged Sigg et al. (1994) in Bern to develop a measurement technique capable of continuously measuring the concentrations of multiple species. In their Continuous Flow Analysis (CFA) system a rod of ice is vertically placed on top of a temperature-controlled metal plate and the melt water is analysed for an array of impurities (see section 1.3). The CFA system in Bern (B CFA) was subsequently improved by redesigning its components and developing additional detection lines for further aerosols (Röthlisberger et al., 2000; Kaufmann et al., 2008). The Bern group's work, laying the basics for an improved resolution of not only aerosol records, but also gas and water isotope time series, is described in chapter 1.

Having the demonstrated ability to significantly improve the depth resolution, the drawback of a CFA system is the limited amount of species for which CFA detection methods exist. Consequently, as Littot et al. (2002) point out, CFA is presently only complemen-

tary to IC, not replacing it. In chapter 2 an overview of existing CFA detection lines for soluble aerosols that show an annual cycle, and potentially also do so at depth intervals not resolvable with the B CFA system, is given.

To increase the range of layer thicknesses that can be resolved - in other words, to expand the time interval in which annual layer counting can be used for accurate dating - a CFA system was built in Copenhagen (C CFA) optimising every aspect with respect to the obtainable depth resolution (Bigler et al., 2011). Its components and the first results it yielded are presented in chapter 3, together with the development of new detection lines (Kjær et al., 2011, 2013) and the complete redesign of existing ones (Gkinis et al., 2011; Stowasser et al., 2012).
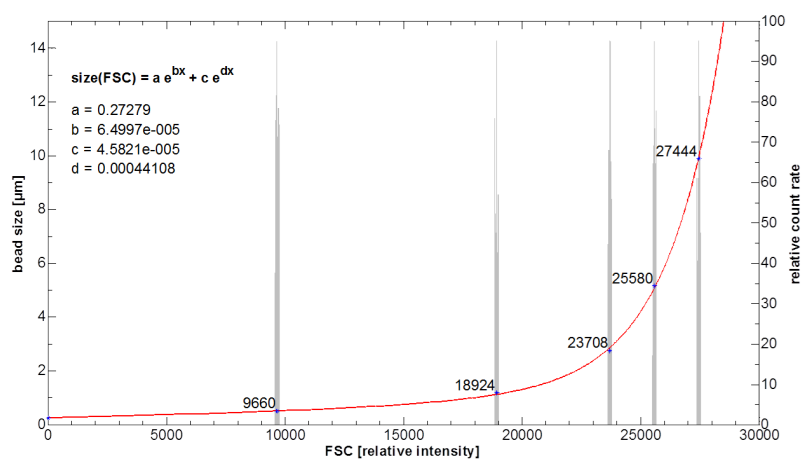
Figure 1: Very first calibration of the CyFlow SL

Insoluble Aerosols   Part II zooms in on insoluble aerosols deposited on the ice. As Pye (1987) points out, particulate aerosols can be of cosmogenic, biogenic, volcanic, anthropogenic or terrestrial origin. All of source also contribute to the particulate matter in ice cores: Cosmogenic insolubles as mini-meteoroids (Winckler and Fischer, 2006), biogenic particles are found in the form of microbial cells (Miteva et al., 2009) or pollen (Bourgeois, 2000; Rousseau et al., 2003), volcanic ones in the form of tephras (De Angelis et al., 1985; Abbott and Davies, 2012), evidence of anthropogenic insolubles is, for example, visible in an increase in soot particle concentration since the industrialisation (McConnell et al., 2007) and terrestrial matter is present in the form of long-range transported dust particles.

Hereafter both, insolubles and dust will be used to refer to long-range transported mineral dust with grain sizes smaller than $20\mu m$, if not explicitly stated otherwise. An

overview over mineral aerosols as 'key player in the earth system', to paraphrase a book currently written in a concerted effort by the mineral aerosol community, and the knowledge on - and obtained through - dust in ice cores is given in chapter 4.

Knowledge on dust grain size and number has traditionally been acquired via Coulter counter measurements (Petit et al., 1981; Steffensen, 1997) and, marking the first expansion of CFA beyond the realm glaciochemistry, with sensors detecting the attenuation caused by particles flowing through a laser beam (Ruth et al., 2002). Both direct measurement techniques, however, have drawbacks. This, and methods for indirect dust quantification in ice core science are elaborated upon in more detail in chapter 5.

Addressing the respective shortfalls of Coulter counters (discrete measurements) and attenuation sensors (inaccurate sizing) was attempted by integrating a flow cytometer into the C CFA. Flow cytometers make use of a third detection technique - light scattering. Figure 1 shows the first promising calibration attempt of a flow cytometer with latex beads in the size range of dust grains found in ice cores. In chapter 6 the potential of light scattering for particle sizing is evaluated in more detail and first results of flow cytometric analysis of dust in ice cores are presented.

Yet another approach to avoid light attenuation sensors is possible, taking advantage of the technological progress in soft lithography over the last decade (Rogers and Nuzzo, 2005). This has facilitated the fabrication of micro Coulter counters and impedance-based flow cytometers, which combine the advantages of Coulter counters (volume determination by electrical impedance measurements) and attenuation sensors (on-line detection). In cooperation with the University of Southampton, a self-made impedance cytometer was connected to the C CFA. The results presented in chapter 7 can be seen as a proof-of-concept and indicate that sticking to the established volumetric technique is superior to abandoning it.

Eventually, in the last chapter, it is demonstrated what additional information can be obtained from highly resolved dust size records. The data was obtained with the University of Bern's attenuation sensor, connected to the B CFA system during the NEEM 2009 and 2010 field seasons, and indicates intraannually changing transport patterns to Greenland and a likely input of a proximate secondary source during the Holocene.

Part I
Continuous Flow Analysis

Chapter 1

The Advent of Continuous Flow Analysis

Summary *Continous Flow Analysis (*CFA*) has become a standard detection technique for aerosols in ice cores. It is superior to ion chromatography (IC) in that allows for the exploitation of the high resolution with which the composition of the paleoatmosphere is preserved, but inferior in that the array of detectable aerosols is not as wide.*

In CFA *a slab of ice is placed vertically on a melthead and melt water from the inner and outer parts are removed through different drainage systems. This allows for effective decontamination while keeping sample handling efforts at a minimum. Uncontaminated sample from the inner part is subsequently pumped through different analysis lines.*

Detection of ionic species is achieved by mixing the sample in-flow with reagents to form absorbing or fluorescent complexes. The reaction kinetics are often enhanced by temperature manipulation and pH modification of the sample-reagent mix.

CFA *has long left its niche as a method for glociochemical analysis only, although methods for the detection of soluble aerosols are still being developed and improved. Next to detection lines aiming at quantifying insoluble aerosols, the ease of decontamination and potentially high number of data points per depth interval have also encouraged the development of analysis lines for the isotopic composition of the ice and the air trapped within.*

1.1 Key Components of a CFA system

The first CFA system was designed at the University of Bern and presented by Sigg et al. (1994). Until then, the sample preparation for the analysis of impurities was time-consuming as the outer part of each sample had to be scraped off with a microtome knife. Ultimately, the high resolution with which transient climate signals are preserved in polar ice cores could not be exploited due to the loss of sample material during decontamination and the subsequent analysis, carried out using ion chromatography on discrete samples.

CFA systems consist of three principle components, a melthead, a debubbler and a

series of analysis lines. Generally speaking the design of a CFA setup has to make choices within the trilemma of a high resolution, a high sample throughput and a large number of components measured. After a short introduction on the general characteristics on the systems components, several CFA setups will be discussed and their peculiarities will be pointed out.

A melthead consists of a heated plate on which the vertically centred sample is continuously melted at a constant rate. As contamination of the sample is confined to the surfaces, effective decontamination can be achieved dividing the melthead's surface into multiple concentric sections, separated by sharp ridges. The melt water from each section is removed by distinct drainage systems and measurements are generally conducted on the sample stream stemming from the inner section only. By removing less water from the inner section than melted by means of peristaltic pumping, an outward flow on the melthead is produced ruling out the possibility of contaminated melt entering the inner drainage systems.

Debubbling of the produced sample stream is necessary since the flow from the melthead is still segmented, containing roughly 10% air (Stauffer and Berner, 1978). Air in the system can alter the sample flow and will further cause false signals in several detection cells, often over extended periods of time. The debubbled sample is then led to a manifold and split into several lines of detection.

Classical CFA detection lines are continuous flow systems adopting fluorescence and absorption methods from Flow Injection Analysis (FIA) (Röthlisberger et al., 2000). A reagent is mixed with the sample in flow, given time to form fluorescent or absorbent complexes in mixing coils and eventually led into the detector. Several measures can be taken to enhance the reaction kinetics, such as the manipulation of the sample's pH and the buffer's composition (e.g. Genfa and Dasgupta, 1989). Endothermic reactions are often accelerated by leading the sample-reagent mix through a heat bath, after which the sample solution needs to be cooled down and debubbled once again to remove microbubbles that might have formed (Kaufmann et al., 2008).

A valve is placed between the melthead and the debubbler ensuring that, in case no sample is melted, a stream of demineralised water (mQ) is injected into the system and air is prevented from entering the analysis lines. Calibrations are then performed by injecting standard solutions into the analysis lines instead of mQ water. Most methods are linear in response and a one standard calibration is sufficient (Sigg et al., 1994; Röthlisberger et al., 2000).

In their study comparing different aerosol analysis techniques, Littot et al. (2002) conclude that 'that the determination of the full range of [soluble] species still requires a combination of analytical methods'. However, apart from its limited applicability to the wide range of ionic species, CFA is acknowledged for its superior depth resolution and for its efficient decontamination technique, making CFA the method of choice for contamination-prone analytes.

1.2 Depth resolution

As the ice thins due to compression and glacial flow it is desirable to keep the depth resolution of the CFA system as high as possible. Indeed, annual layer thicknesses in basal ice at NorthGRIP were predicted (Johnsen et al., 2001; Andersen et al., 2006) and found to be (Svensson et al., 2011) in the order of 10mm. Due to lower accumulation rates in Antarctica, layer thicknesses in that range are not uncommon in Antarctic ice cores, even in the upper part of a core (e.g. Bazin et al., 2013). The depth resolution is limited by dispersion in the CFA system, where mixing is taking place in small volumes within the setup at the melthead, in the debubbler detection cells and the tubings.

1.2.1 Enhancement by Restitution

Sigg et al. (1994) applied partial restitution to the obtained signal where the mixing length of the entire system is replaced by a shorter one, using an following Robinson and Treitel (1980, cited by Sigg et al., 1994) . The system is approximated as a single mixing volume, which can mathematically expressed by a low-pass filter:

$$g(x) = \int_0^\infty f(x-t)\lambda^{-1}e^{-t/\lambda}dt \tag{1.1}$$

where $g(x)$ is the detected, convoluted signal, $f(x)$ the original function and λ the mixing length of the system, defined by

$$\lambda = \frac{vV}{F} \tag{1.2}$$

with v the melt rate, V the volume of the system and F the flow rate. The subsystems' mixing lengths were determined experimentally and Sigg et al. found that reducing the mixing length to 25% of its original value yielded optimal restitution without amplifying noise, see figure 2a for their restituted signal.

Rasmussen et al. (2005) proposed a spectral approach adapted from Johnsen et al. (2000, cited by Rasmussen et al., 2005) who designed a filter to correct for the diffusion of stable water isotopes in firn. Via spectral analysis Rasmussen et al. separated the signal from the noise in the recorded data and constructed an optimum filter. The restauration filter, obtained by combining the inverse of the mixing filter with the optimal filter, has no singularity but a maximum amplitude after which it steadily decays until amplification stops at a wavelength well below the original data's minimal detectable frequency.

(a) Restitution, taken from Sigg et al. (1994)

(b) after Rasmussen et al. (2005)
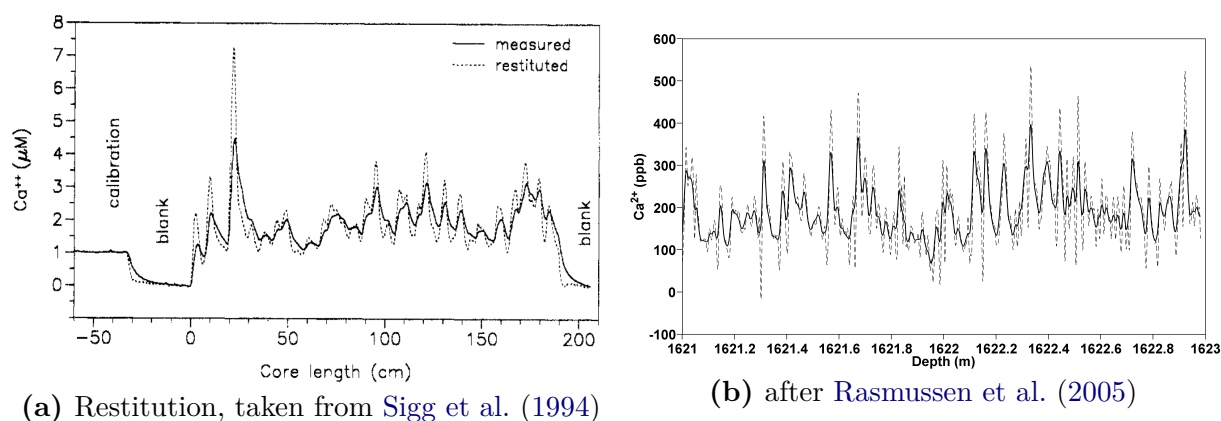
Figure 2: Restituted data for a sections of the GRIP (a) and NGRIP (b) core

Both, the mixing length in the approach presented by Sigg et al. (1994) and the mixing filter in the method favoured by Rasmussen et al. (2005) were obtained from the response of the stepfunction during calibration, when the valves are switched from blank to standard and back. This means, however, that restitution can only be done for the volume the standard as well as the sample flow through, which in the cases presented by Sigg et al. and Rasmussen et al. means that the mixing volumes at both the melthead and the debubbler are excluded.

1.2.2 Minimising the Mixing Lengths

Even though Sigg et al. (1994) and Rasmussen et al. (2005) show that restitution can reduce the detectable layer thickness up to about 30%, the former notes that 'a reduction of the dispersion in the system is still favorable'.

The resolution can, as a look at equation (1.2) reveals, be improved by taking measures to either decrease the volume, to decrease the melt rate or to increase the flow rate. However, these measures are limited by practicalities and often have to be traded off against one another.

Even though the chemical reactions forming absorbing or fluorescent complexes need not to reach their chemical equilibrium (as this is not the case during calibration either), the closer to the equilibrium the reaction gets the higher the methods sensitivity will be. Consequently, flow and volume need to ensure sufficient reaction time.

Mixing volumes are located at the melthead, in the debubbler, the detection cells and the tubings. The volume at the melthead can be neglected compared to the dispersion taking place in the debubbler (commonly the largest volume in the setup) and the individual detection cells (Sigg et al., 1994). Minimising the mixing volumes is limited by not compromising the efficiency of the debubbler and the sensitivity of the detection method. Especially absorption methods are compromised easily be decreasing the detection cell's volume.

Decreasing the melt rate reduces not only sample throughput and comes at the expense of extended measuring times. Without simultaneously increasing the melted core section's cross section, also the amount of sample available for subsequent analysis is reduced such that only a smaller set of impurities can be measured.

Increasing the flow rates through selected detection lines further comes at the expense of reducing the amount of sample available for other analyses while it is also practically limited by the increased back pressure. Thus, when designing a CFA system, fundamental choices have to be made with respect to the desired resolution, the number of measured components and sample throughput.

1.3 The GRIP system designed by Sigg et al. (1994)

The University of Bern's first CFA system was successfully deployed in the field during the GRIP campaign and presented by Sigg et al. (1994). Its melt head featured a circular inner section with a diameter of 11mm on top of which a sample with a cross section of 1.8×1.8cm was placed and melted with a rate of 5cm/min. Contamination of the inner section by melt from the outer one was ensured by removing only 75% of the melted sample.

Debubbling was done by leading the melt water stream from the melthead into a pipette tip open to atmosphere. Undissolved gases would be released and an overflow control located above the individual analysis line's inlet would ensure the removal of superfluous sample (see figure 3). The volume of this 'mechanical' debubbler was $200\mu l$.

Sigg et al. measured four components in parallel. The dissolved gases formaldehyde (HCHO) and hydrous peroxide (H_2O_2) and the soluble aerosols ammonium (NH_4^+) and calcium (Ca^{2+}). For HCHO, H_2O_2 and NH_4^+ fluorometric techniques were adapted from
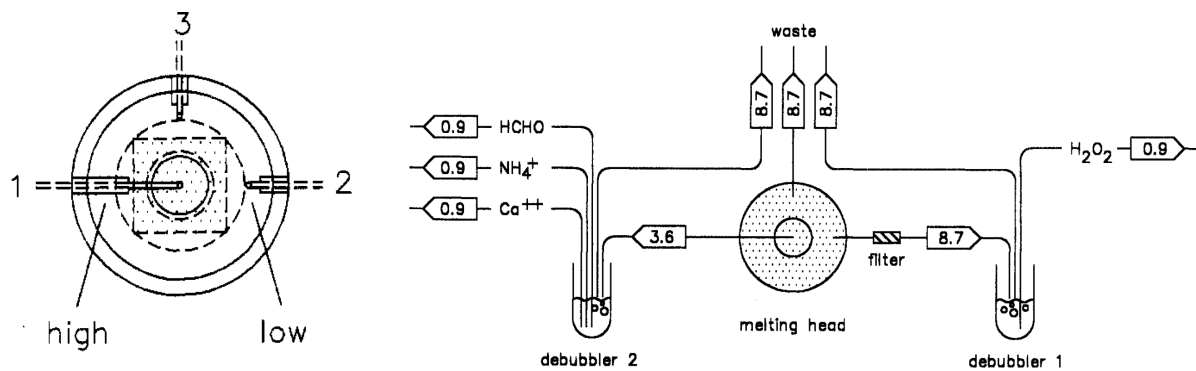
Figure 3: Melt head used by Sigg et al. during the GRIP campaign

Lazarus et al. (1985), Dong and Dasgupta (1987) and Genfa and Dasgupta (1989; see section 2.2.1), respectively. Calcium on the other hand was measured using an absorption technique described in Kagenow and Jensen (1983), which required a large ($300\mu l$) detection cell.

Consequently, the depth resolution for Ca^{2+} was poor compared to NH_4^+ and HCHO. As H_2O_2 is not sensitive to contamination, Sigg et al. decided to use sample from the outer section for this analysis. This, however, increased the mixing volume of the H_2O_2 detection line at the melthead relative to the other components and also resulted in sub-optimal depth resolution.

As subsequent steps Sigg et al. suggested tackling these two resolution problems by finding a fluorometric method for Ca^{2+} and refraining from taking sample from the outer section, also for species robust against contamination. Expansion of the system with 'any species for which a sensitive continuous flow analysis method exists' is also encouraged.

1.4 The EPICA system presented in Röthlisberger et al. (2000)

Röthlisberger et al. (2000) modified the system for employment in Antarctica in the framework of the EPICA project. The lower aerosol concentrations and the generally lower accumulation rates in Antarctica called for an improvement of the existing setup.

Sigg et al. (1994) point out themselves that their setup cannot be used for the measurement of firn cores. Capillary forces in the porous firn create an upward force soaking up the melt water and thereby compromise the depth resolution. Röthlisberger et al. solve this by engraving narrow, radial slits into the melthead creating capillary forces downward greater than the upward forces created by the firn's texture, see figure 4.

Depth resolution was enhanced for the existing species by following the suggestions

in Sigg et al. (1994). H_2O_2 was now measured on sample melted in the melthead's inner section and the absorbance-based method for Ca^{2+} was replaced with a fluorometric one (Tsien et al., 1982; section 2.3.1). The detection cells for all fluorometric detection methods were replaced with low-volume cells (18μl) featuring mirrored inside surfaces to increase excitation.

A series of new absorbance methods for sodium (adopted from Quiles et al., 1993; section 2.2.2), nitrate (McCormack et al., 1994; section 2.3.3) and sulphate (Madsen and Murphy, 1981; section 2.3.2) were tested and implemented into the improved CFA system, as was a conductometer measuring the melt water conductivity as a bulk signal of all solubles.
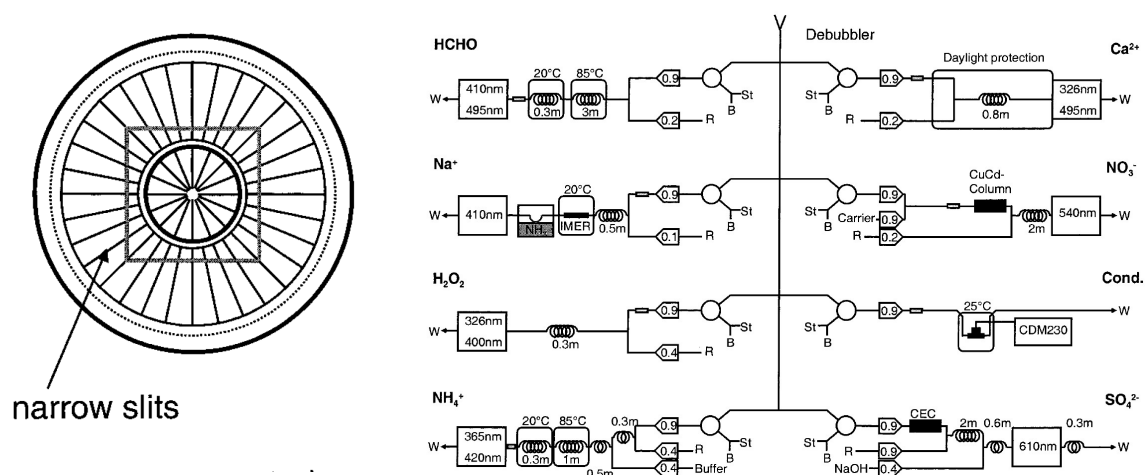
Figure 4: Firn Melt head and CFA system described by Röthlisberger et al. (2000)

To further increase the depth resolution, the melt rate was decreased to 4cm/min, which, together with the expansion from 4 to 8 components rendered an increased sample amount necessary. Slabs of ice melted at EPICA therefore had a cross section of 3×3cm and the inner section of the melthead was 20mm in diameter.

1.5 The system employed at NEEM (Kaufmann et al., 2008)

The EPICA system was lost during shipment and opened the opportunity for a redesign of the entire system. Kaufmann et al. (2008) opted for a modular sign facilitating transport in future field campaigns and reducing the time needed for installation at the site of employment.

Kaufmann et al. redesigned the melthead to accommodate the need for an ever growing amount of sample. Its inner part was enlarged to a diameter of 24mm and the inner part

was shaped slightly conical as it was found that the lateral outward flow was increasing disproportionally (Bigler, 2008). To further address this and to limit the dispersion taking place on the melthead due to the increased range of distances for the melt water to the drainage hole the inner section was drained through six circularly arranged holes, see figure 5.

This re-designed system also marked the beginning of a still lasting trend to incorporate measurements that are not confined to the detection of (soluble) aerosols any more. Kaufmann et al. closed off the debubbler to the atmosphere and thereby enabled sample delivery to systems measuring the concentration of gases that can be wet extracted (e.g. Schüpbach et al., 2009; Stowasser et al., 2012; Chappellaz et al., 2013).
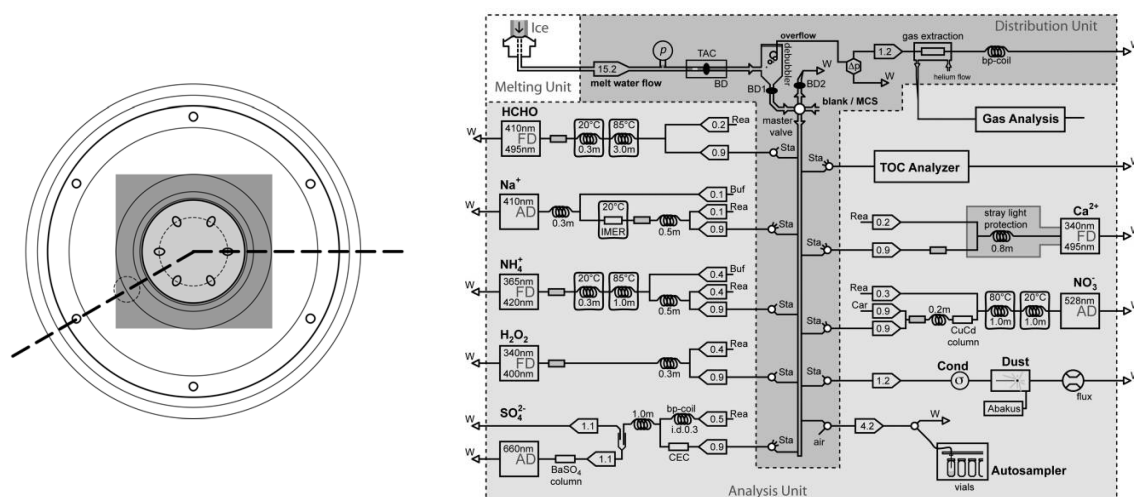
Figure 5: Modular design of the system presented by Kaufmann et al. (2008)

Further innovations were the introduction of a device monitoring the total air content on-line (Kaufmann et al., 2008), the total organic carbon (Federer et al., 2008) and the concentration of insoluble particles and their size distribution (Ruth et al., 2003). The previously troublesome sodium method has been optimised by - following the advice of Quiles et al. (1993) - increasing the pH of the sample reagent mix. Detection of sulphate (SO_4^{2-}) as envisioned by Röthlisberger et al. (2000) had never worked and therefore another absorbance-based method was developed and implemented (Bigler et al., 2007; see section 2.3.2).

The system as described was employed during extensive laboratory campaigns measuring ice obtained during the TalDICE project, and - with the melthead changed to a slightly larger version of the one developed for the Copenhagen High Resolution CFA (see section 3.1, figure 11) - also at NEEM.

1.6 The Proliferation of Meltheads

For the sake of their reliable and - in terms of discarded sample amount - efficient decontamination, meltheads have often been used to other ends than initially intended by Sigg et al. (1994). Autosamplers have been developed by Osterberg et al. (2006) and Kaufmann et al. (2008) to perform collection tasks of discrete samples for a subsequent analysis with traditional discrete techniques. Others directly integrated instruments performing discrete measurements into CFA systems.

Traversi et al. (2002) and Cole-Dai et al. (2006) collected the continuous stream of melt water in a loop and periodically injected it into ion chromatographs (IC). By engenieering the measurement time of their instruments down, they were able to obtain time series of ionic species in a depth resolution previously impossible with IC, profiting from the minimised sample loss during decontamination. Similarly, the resolution of trace element records acquired with inductively coupled plasma mass spectrometry (ICPMS) could be improved (McConnell et al., 2002; Knüsel et al., 2003; Osterberg et al., 2006).

Leaving the field of glaciochemistry behind, McConnell et al. (2007) nebulised the melt water stream and flushed it into a single particle soot photometer. Particles in the now gaseous sample stream were lined up in a single file and lead through the focal point of a laser, causing soot particles to glow. The laser-induced incandescence, detected by a photometer, is a function of particle size. This single particle interrogation is very similar to the basic principles of particle detection in flow cytometry, which will be elaborated upon in chapter 6.

The potentially high resolution and time-saving sample preparation have encouraged the Bern group to develop interfaces connecting isotope ratio mass spectrometers (IRMS) to the B CFA. With a continuous-flow IRMS Huber and Leuenberger (2003) were able to obtain truly continuous δD time series, while the the sample stream for subsequent analysis of $\delta^{18}O$ (Leuenberger and Huber, 2002) and paleoatmospheric gases (Huber et al., 2003; Schüpbach et al., 2009) were integrated over one measurement period.

Many of the above can be combined, as the setup presented by McConnell et al. (2002) demonstrates. The evolved trend to not only take advantage of a CFA system's optimal resolution exploitation, but also its cost-efficiency by integrating multiple measurements, from a variety of experimental fields into one system was also picked up in Copenhagen and described in more detail in section 3.4.

Chapter 2

CFA and Stratigraphic Dating

Summary   *Various methods can be used to establish a chronology of climatic changes detected in paleoclimatic archives at different locations. Perturbations - e.g. rapidly increasing methane concentrations or volcanic eruptions - present in multiple archives enable the construction of relative time scales. Volcanic events may even allow for absolute dating.*

Since the sources of many aerosols have a distinct annual productivity cycles, absolute dating is also possible by counting annual layers marked by irreversibly deposited aerosols. Some impurities stem from multiple sources, but this can be corrected for by assuming constant abundance ratios of different species stemming from the same source.

Irreversibly deposited aerosol species that do exhibit seasonal cycles and for which a CFA detection channel exists are discussed in this chapter. CFA lines are usually modified 'flow injection analysis' (FIA) lines, that need to be tuned to the very low concentrations found in polar ice cores.

Most of the analysis lines have undergone a maturing process in parallel with the CFA system as such. Still, however, not all of them reliably yield satisfactory data. Several methods still rely on absorption techniques, where fluorescence based methods are preferable due to their superior signal-to-noise ratios.

2.1 Ice Core Dating

Accurate dating of individual records is fundamental in palaeoclimatology to know the chronology and phasing of climatic events at different sites. Multiple methods can be used to assign an age to a given sample interval of a given archive. Reference horizons common to multiple archives, e.g. volcanic signals (Hammer et al., 1978; Zielinski et al., 1997; Davies et al., 2010) can sometimes even attribute an absolute age to the layer in question (e.g. Hammer, 1980; Abbott and Davies, 2012) while the identification of climatic changes in different archives still allow for relative dating.

A peculiarity of ice cores is, that the paleoatmospheric gaseous composition is archived, so that rapid changes therein - e.g. of the methane mixing ratios - have been used for

synchronising cores from various sites (e.g. Chappellaz et al.,1997; Blunier et al.,1998; Schüpbach et al.,2011; also section 3.4.2). The most accurate dating method is, however, the identification and subsequent counting of annual layers (e.g. Meese et al., 1997). This dating method with - in the NGRIP core - an error of less than 5% at an age of $60\,ka\ b2k$ (Svensson et al., 2006) is not only independent of other archives, but also absolute.

Stratigraphic information is stored in the ice matrix' physical properties (Alley et al., 1990) and its composition. With the isotopic composition of the precipitation being a function of the temperature at the time of condensation to first order (e.g. Jouzel and Merlivat, 1984; see also section 3.4.1), peaks in its heavy isotope fraction can be used to identify summer precipitation (Dansgaard, 1964). Unfortunately, the isotopic ratios are altered by diffusion, the seasonal signal is rapidly smoothed out and the interval in which water stable isotopes can be used for stratigraphic dating is confined to the top part of a core (Meese et al., 1997; Anklin et al., 1998; Vinther et al., 2006).

However, as Sigg et al. (1994) point out to emphasize the importance of CFA systems, not only the precipitation's stable isotopes exhibit a seasonal cycle, but also many of the impurities. Since with a sufficiently high depth resolution, aeolian deposits can be resolved down to sub-annual time scales (e.g. Röthlisberger et al., 2000; Bigler et al., 2011) and multiple proxies will improve dating accuracy (Alley et al., 1997; Meese et al., 1997; Rasmussen et al., 2006), CFA is an excellent dating tool with its potential to yield a multitude of layer-indicating impurity time series simultaneously.

A multi-proxy approach makes identification of annual layers more robust for several reasons. First, because different impurities often differ in seasonality during interglacials, the annual maximum be missing in one record due to low or absent accumulation during any given season and still be preserved in another (Anklin et al., 1998). Second, detected signals are frequently the result of various processes and non-seasonal inputs might mask the source generating the seasonal pattern (Meese et al., 1997). Finally, data gaps in any record can be compensated for by continuous records of other impurities in the interval in question (Rasmussen et al., 2006).

Still, the observation of Littot et al. (2002) that CFA is only complementary to existing techniques holds. While the respective impurity records are mutually independent, their acquisition is not - and coinciding data gaps in CFA records do occur. As mentioned above, for annual layer identification it is 'the more, the merrier', meaning that independently obtained time series such as discrete impurity or isotope measurements (e.g. Johnsen et al., 1992) or the core's visual stratigraphy (e.g. Svensson et al., 2005) are valuable additions.

2.2 Modules in the Copenhagen System

The system set up in Copenhagen was optimised with the aim of obtaining aerosol records of unprecedented high resolution (Bigler et al., 2011; also chapter 3). This entails fundamental choices, that would eventually reduce the amount of sample needed (section 1.2.2).

Therefore, lesser components than in the system presented by McConnell et al. (2002) or Kaufmann et al. (2008) could be measured. It was opted to install a laser light attenuation sensor for insoluble aerosols Ruth et al. (2002; see section 5.2) and two classical CFA detection lines for ammonium and sodium. These species are well suited for the robust identification of annual layers as they stem from different sources and exhibit different seasonal patterns.

2.2.1 Ammonium (NH_4^+)

A proxy for biomass burning Ammonium deposited on the polar ice sheets is a product of either ammonia (NH_3) emissions of terrestrial and marine ecosystems (Fuhrer et al., 1996; Legrand et al., 1998) or biomass burning (Legrand et al., 1992). NH_4^+ emissions of the latter can be identified by contemporaneous peaks in other species such as NO_3^-or potassium, so that the maxima-showing impurities resemble the chemical composition of aerosols from aged biomass (Whitlow et al., 1994). Inputs from the combustion of biomass are up to one order of magnitude larger than ecosystem emissions and can obliterate the biological activity (Anklin et al., 1998).

While no seasonal pattern can be observed in the NH_4^+ levels in Antarctic ice (Legrand and Mayewski, 1997), records from Greenland show a peak during summertime (Whitlow et al., 1994) and drop back to almost zero during winter (Fuhrer et al., 1993). This has been explained by the lack of biological decomposition of plant material and excreta, which increases with temperature and is almost absent during winter (Legrand et al., 1998). This is also reflected in the fact that the NH_4^+ concentrations found in recent ice are about twice as high as they have been during the last glacial (Fuhrer et al., 1996).

Assuming that the present day conditions - consisting of a general westerly circulation of storm tracks across Greenland and a dominant NH_4^+ source region in North America as suggested by Taylor et al. (1996) - have not changed, Fuhrer et al. (1996) show that the background levels of ammonium can be linked to the retreat of the Laurentide ice sheet and the subsequent temperature changes in the dominant source region.
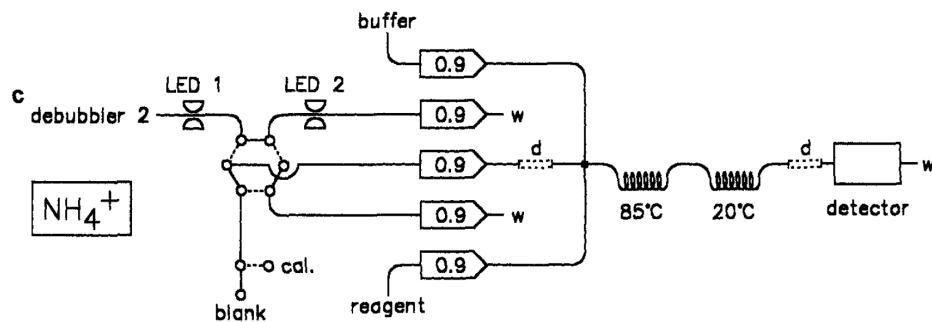
Figure 6: Detection line for ammonium as presented by Sigg et al. (1994)

Detection Technique Ammonium has been measured already in the CFA system presented by Sigg et al. (1994; see section 1.3) and the method has remained fundamentally unchanged ever since. The analysis is based on a fluorimetric method discovered by Roth (1971). Roth reported that 'o-Phthaldialdehyde [OPA] reacts with amino acids in alkaline medium in the presence of a reducing agent such as 2-mercaptoethanol [ME]' form highly fluorescent products, he had not identified.

Genfa and Dasgupta (1989) found that sensitivity can be increased by replacing ME with sulphite and presented a flow-injection system based on the modofied reaction. Figure 6 shows the detection line for NH_4^+ as implemented by Sigg et al. (1994). The reaction takes place at elevated temperatures to accelerate the endothermic reaction, as suggested by Genfa and Dasgupta.

However, increasing the temperature decreases the amount of gas that can be dissolved in the sample, consequently, microbubbles will form and have to be removed. Sigg et al. address this by first cooling the sample and subsequenty debubbling it again by leading it through a hydrophobic Accurrel capillary membrane (Membrana, Germany) before injection into the detection cell where fluorescence is excited at 365nm and detected at 425nm.

2.2.2 Sodium (Na^+)

A sea salt proxy Sodium levels are tracers of sea salt (Legrand et al., 1988; Wolff et al., 2003) and Legrand and Mayewski (1997) point out the usefulness of Na^+ for stratigraphic dating as it stems from a single source and smoothing of the initial signal is a function of thinning only. Indeed, Röthlisberger et al. (2002) find the amount of Na^+ deriving not from sea salt ($nssNa^+$) contributing only 2% to the total sodium levels detected during

the Holocene. Their calculations are based on

$$ssNa^+ = \left[Na^+\right] - \frac{nssCa^{2+}}{R_t} \tag{2.1}$$

$$nssCa^{2+} = \left[Ca^{2+}\right] - R_m \times ssNa^+ \tag{2.2}$$

where $nssCa^{2+}$ is the sea-salt and non-sea-salt contribution to the simultaneously detected calcium levels ($[Ca^{2+}]$) and $R_m = .038$ and $R_t = 1.78$ (Bowen, 1979) are the $\frac{Ca^{2+}}{Na^+}$ elemental ratios in marine aerosols and continental crust respectively. It has to be pointed out, however, that depending on the ratios used $nssNa^+$ could contribute up to 25% to glacial sodium levels and that these ratos are not uncontested. Bigler et al. (2006) have, for example, empirically found $R_m = .043$ and $R_t = 1.06$ for Dome C, Antarctica.

Concentrations show maxima in both Greenland (Legrand and Mayewski, 1997) and Antarctica (Legrand and Delmas, 1984) during winter. Wolff et al. (2003) explain this by invoking the findings of Wagenbach et al. (1998) to contest that 'the sea ice surface, not the open water, is the source' of the sodium found in ice cores. They further point out that their postulated correlation between sea ice extend and detected sodium levels is supported by independently reconstructed sea ice extend from diatom records in marine cores.

On glacial-interglacial time scales Na^+ fluxes - i.e. the concentration times the mean accumulation rate (Dansgaard et al., 1993) - increase by a factor of roughly 3 for both, Greenland and Antarctica (Fischer et al., 2007). Fischer et al. follow Wolff et al. (2003) and explain these observed changes with changes in source strengths, suggesting that 'the formation of sea-salt aerosol from sea ice may play a pivotal role'.
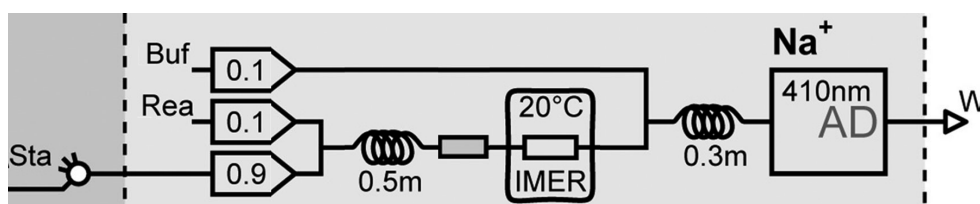
Figure 7: Detection line for sodium adopted from Kaufmann et al. (2008)

Detection Technique Röthlisberger et al. (2000) were the first to demonstrate the ability to continuously monitor the Na^+ concentration in a stream of melt water by adopting the enzymatic absorption method developed by Quiles et al. (1993). Absorption methods are generally less favourable than fluorimetric ones, because the signal to noise ratio is usually smaller and via the length of the detection cell, the methods sensitivity and its resolution have to be traded off against each other.

Enzymatic methods are typically indirect, in that the reaction is catalysed by an enzyme, whose activity depends on the presence of the solvent to be quantified. The method proposed by Quiles et al. is based on the absorbance of o-nitrophenol, a product of the hydrolysis of o-nitrophenylgalactoside (ONPG), which is catalysed by the enzyme β-galactosidase.

$$\text{OPNG} \xrightarrow[\beta-galactosidase]{Na^+} \text{o}-\text{nitrophenol} + \text{galactose}$$
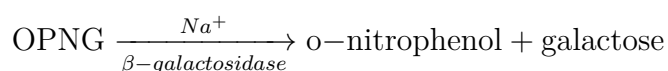
The enzyme, immobilised on controlled pore glass beads (Masoom and Townshend, 1985) and filled into a immobalised enzyme reactor (IMER), are found to disintegrate at temperatures above 40° and are therefore kept at room temperature. Optimal reaction kinetics are found at a pH of 7.2, while the maximum absorption of o-nitrophenol takes place at a pH at 10-11 (Quiles et al., 1993).

Figure 7 shows the Na^+ detection line as used in most CFA systems today (Kaufmann et al., 2008; Bigler et al., 2011), which differs from the original detection line only in the direct addition of the buffer into the sample stream; Röthlisberger et al. altered the pH by having ammonium vapour diffuse through a membrane into the sample-reagent mix.

2.3 Developed CFA Detection Lines

Since the inception of CFA, various channels have been designed for the detection of further aerosols that are not integrated into the Copenhagen system presented in chapter 3 (e.g. Ruth et al., 2002; McConnell et al., 2007; Federer et al., 2008). Amongst the first 'classical' CFA lines (i.e. complex forming chemistry coupled with spectrophotometric detection) presented by Sigg et al. (1994) were those for H_2O_2 (adopted from Dong and Dasgupta, 1987) and HCHO (Lazarus et al., 1985).

Their levels are of climatic relevance, as they allow conclusions on the atmospheric OH radical abundance (Sigg and Neftel, 1991; Fuhrer et al., 1993). The atmosphere's oxidising capacity in turn influences the life times of greenhouse gases such as CH_4 and CO (Thompson, 1992). These aerosols are gaseous, however, and thus not deposited irreversibly. The resulting damping of their annual cycle with maxima in summer (Legrand and Mayewski, 1997) limit their value for annual layer recognition (e.g. Anklin et al., 1998). In the following section, the overview commenced above, only reviews systems used to quantify impurity levels using 'classical' methodology on irreversibly deposited aerosols.

2.3.1 Calcium (Ca^{2+})

An aeolian dust load proxy As is the case for sodium, calcium found in polar ice cores has two sources, crustal and marine aerosols (Whitlow et al., 1992). In Antarctica, the contributions of the marine and terrestrial sources to the total Ca^{2+} level are of the same order of magnitude, resulting in very little variation as the former peaks in winter and the latter in summer (Legrand and Mayewski, 1997). Due to Greenland's proximity to the calcium's continental sources - being identical to the source of dust - the Ca^{2+} deposited together with continental dust dominates (Whitlow et al., 1992).

Consequently, records from Greenlandic cores show peaks during spring (Whitlow et al., 1992; Anklin et al., 1998) and can be used for the identification of annual layers. Quantification of the marine source's contribution is possible if simultaneously another impurity with the same sources is monitored. Röthlisberger et al. (2002), for example, have used the sodium levels (see supra) to identify the respective calcium sources' relevance; the value of Ca^{2+} as dust proxy is discussed in section 5.4.

During the LGM, calcium fluxes are about 15-20 times the present day value in Greenland and 10-15 times in Antarctica (Fischer et al., 2007). In terms of concentration, these changes are, of course, more pronounced. Fuhrer et al. (1999) report, the Ca^{2+} concentrations in Greenland were more than two orders of magnitude higher than during the Holocene and explain this with changes in both, the source's strength and extend and in the transport process.
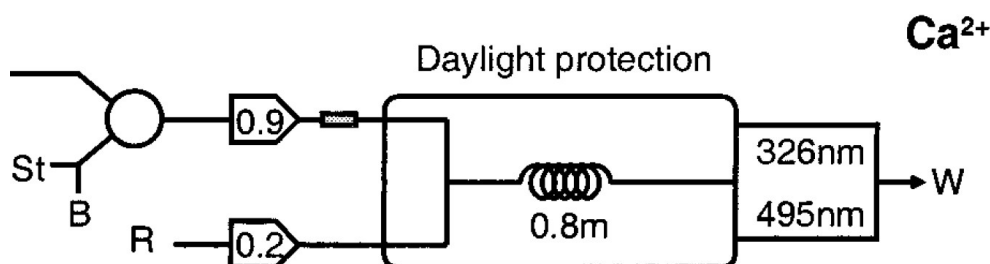
Figure 8: Detection line for calcium as modified by Röthlisberger et al. (2000)

Detection Technique Sigg et al. (1994) employed a Ca^{2+} detection line, utilising an absorption method sensitive to magnesium (Mg^{+}) and Ca^{2+} from Kagenow and Jensen (1983). Kagenow and Jensen let all alkaline earth metals form complexes with a polyether diamine-type ligands, and subsequently added potassium to scavenge the Mg^{+} complexes rapidly and the Ca^{2+} complexes slowly. A further added metal indicator (o-cresolphthalein complexone) would then instantly form coloured complexes with the liberated metal ions.

From two sequential absorption measurements the concentrations of Mg^+ and Ca^{2+} could then be calculated, assuming all Mg^+ ions had formed absorbing complexes and the increase between the two measurements was solely due to the Ca^{2+} present. However, the sensitivity of the method was found to be too low and the need for a large absorption cell compromised the depth resolution (Sigg et al., 1994).

Therefore Sigg et al. (1994) suggested to find a fluorescence-based method to increase the sensitivity with which Ca^{2+} could be detected - a advice followed by Anklin et al. (1998), who adopted a Ca^{2+} method used in cell biology (Tsien et al., 1982; Clarke et al., 1988). The tetracarboxylate ligand quin2 can penetrate cell membranes and is used to stain free calcium intracellularly (Tsien et al., 1982).

Quin2 shows a fluorescence maximum at about 490nm (excitation at ca. 435nm), but that fluorescence is increased about five-fold after the formation of a 1:1 complex with free Ca^{2+}. However, Clarke et al. (1988) report that a similar effect is observed for complexes formed by quin2 and trivalent lanthanides such as Pr^{3+}, Tb^{3+}, Dy^{3+}, and Yb^{3+}. Clarke et al. also point out that ethylenedinitrilotetraacetate (EDTA) replaces the lanthanide ions much faster from its quin2 complexes than it replaces Ca^{2+}, so that the addition of EDTA renders a more selective calcium detection line.

In the version of the B CFA described in Röthlisberger et al. (2000), the absorption method based on Kagenow and Jensen (1983) was then also replaced by a fluorescence method based on quin2. The presently used Ca^{2+} detection line is depicted in figure 8 and it is worth to point out the peculiarity described by Röthlisberger et al., that the sample reagent mix are shielded from daylight in order to prevent the photolytic decomposition of the fluorescent complexes.

2.3.2 Sulphate (SO_4^{2-})

A proxy for past volcanism Sources for SO_4^{2-} detected in ice cores are sea salt aerosols (Na_2SO_4), the marine and terrestrial biosphere (Herron, 1982; Neftel et al., 1985) as well as volcanic eruptions (e.g. Hammer, 1977; Delmas et al., 1985). Both biogenic and volcanic activity emit precursors of the SO_4^{2-} preserved in ice cores - such as dimethyl sulphate (($CH_3)_2S$, DMS), SO_2 and H_2S - into the atmosphere (Legrand et al., 1998), the latter ones being reduced to H_2SO_4 (e.g. Hammer et al., 1980). Since the 1950s, anthropogenic emissions of SO_4^{2-} precursors have surpassed the natural fluxes (Neftel et al., 1985; Mayewski et al., 1986), so that non-sea salt sulphate ($nssS$) can serve as an indicator for industrial pollution (McConnell et al., 2007).

Due to its biological sources, SO_4^{2-} exhibits a natural annual cycle with maxima during spring and summer (Legrand and Mayewski, 1997), its real value for dating, however, lies in its volcanic source. Volcanic eruptions eject insoluble, particulate matter (e.g. tephra) and gases into the atmosphere (Delmas et al., 1985), but depending on the volcanic plume, the spreading thereof and the deposition pattern, one of the two fractions of volcanic deposits may be absent in polar ice cores (Abbott and Davies, 2012). However, volcanic ejecta that entered the stratosphere will be deposited in the same hemisphere during the years following the eruption (Hammer, 1977; Delmas and Boutron, 1980).

Insoluble volcanic debris can be found in ice cores as such (De Angelis et al., 1985), whereas as the gases can be found in the form of ions stemming from volcanic acids, mainly H^+ and SO_4^{2-} (Zielinski et al., 1997). As the soluble volcanic aerosols can be monitored continuously over the length of the ice core, they are valuable in establishing a global chronology of volcanic eruptions, while the insoluble fraction can, after a geochemical analysis, pinpoint the exact source and identify synchronous stratigraphic layers in multiple archives (Zielinski et al., 1997; Davies et al., 2010).

In a pioneering study, Hammer (1977) analysed the melt water conductivity and identified several 'acid layers' caused by soluble volcanic input in the course of the preceding century. Succeeding studies by, e.g. Herron (1982), Legrand and Delmas (1987) or Zielinski et al. (1994), used different techniques to identify volcanic layers. Possible methods were summarised by Delmas et al. (1985) and consisted - next to Hammer's original approach - of (1) the electroconductrimetry directly of the ice, which is dominated by protons due to their high specific conductivity, (2) the determination of the ice's acidity or (3) the detection of SO_4^{2-} in the melt water.

Measurements directly on the ice are non-destructive and can be performed by either elctroconductivity measurements (ECM, Hammer, 1980) or dielectric profiling (DEP, Moore et al., 1992; Wilhelms et al., 1998), but both methods are sensitive to the sample's dust content, potentially obliterating the signal (Bigler et al., 2007). Until the recent development of pH analysis lines by Pasteris et al. (2012) and Kjær (2013), acidity measurements could not be conducted continuously and the development of a SO_4^{2-} line has proven troublesome (see infra), such that highly resolved records of volcanic input are still sparse.

Detection Technique The first revision of the B CFA as published by Röthlisberger et al. (2000), however, envisioned the incorporation of a sulphate detection line, based on methylthymol blue colorimetry, a method adopted from Madsen and Murphy (1981). It
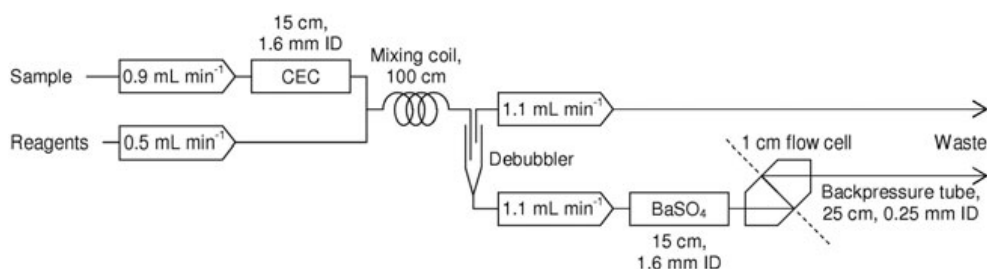
Figure 9: Detection line for sulphate as developed by Bigler et al. (2007)

is based on the competitive reaction of SO_4^{2-} and Methylthymol blue (MTB) with barium (Ba^{2+}). MTB itself has an absorption maximum at 460nm and reacts with Ba^{2+} to form a coloured complex absorbing at 608nm (Colovos et al., 1976).

$$Ba^{2+} + MTB^{6+} \rightleftharpoons BaMTB^{4-} \tag{2.3}$$

$$BaMTB^{4-} + SO_4^{2-} \rightleftharpoons BaSO_4 + MTB^{6-} \tag{2.4}$$
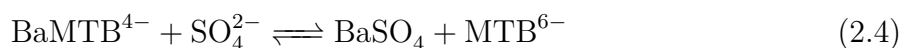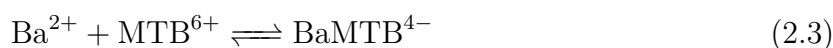
As is evident from reaction 2.4 it becomes clear that the concentrations of both $BaMTB^{4-}$ and MTB^{6-} are related to the SO_4^{2-} content if the barium level is constant and all barium has been either complexed by MTB or precipitated as $BaSO_4$. Technically, the SO_4^{2-} level could thus be derived by monitoring the increasing absorption at 460nm (due to uncomplexed MTB) or a decrease at 608nm. Madsen and Murphy (1981) find the decrease to be three times larger than the increase, so that Röthlisberger et al. (2000) opted for the latter.

In the detection line presented by Röthlisberger et al. the interference of bivalent cations is addressed by leading the sample through a cation exchange column (CEC) before mixing it in-flow with a reagent containing dissolved Ba^{2+} and MTB. To enhance dissolution in the reagent, ethanol is added (Madsen and Murphy, 1981) which complicates the sample handling in that special pump tubes have to be used. Further will the heat produced when merging alcohol with water lead to degassing of the sample, if not countered by increasing the backpressure in the system. The barium-MTB reaction's (equation (2.3)) kinetics are enhanced by a high pH (Madsen and Murphy, 1981), and as the absence of free Ba^{2+} ions is essential, NaOH is added to the reagent-sample mix.

The method proved to have a rather high detection limit of 40ppbw (ng g^{-1}), about four times the lowest SO_4^{2-} levels that can be expected in Greenland ic (Bigler et al., 2002) and to be further unsuitable 'showing occasional baseline instabilities, a non-linear calibration curve, a too high limit of detection and strong interferences from bivalent cations' (Bigler et al., 2007).

Kaufmann et al. (2008) consequently abandoned the SO_4^{2-} detection line based on MTB. Following a suggestion by Bigler et al. (2007), an improved analysis line similar to the previous method, was implemented. Kondo et al. (1982) showed that the barium cations could also be complexed with dimethylsulphonazo-III (DMS-3)instead of MTB before scavenging the complexes with SO_4^{2-}. Again, by monitoring the decoloration of the barium complex, now at 662nm, the SO_4^{2-} concentration could be determined.

The advantage of the DMS-3 method is that the reaction kinetics can be enhanced by leading the sample-reagent mix through a reaction column filled with $BaSO_4$ immobilised on beads (Yang et al., 1997) or as powder (Burakham et al., 2004). Therefore, as can be seen from figure 9, Bigler et al. (2007) and Kaufmann et al. (2008) insert a $BaSO_4$ column in the flow line before the absorption cell. Baseline fluctuations could be lmited by replacing the previously used H^+-type cation exchange resins by Na^+-type resins (as proposed by Burakham et al., 2004) and the removal of the backpressure regulator (Bigler, 2008). Instead, the bubbles that were formed were removed by a second 'pipette-tip' debubbler.

While this method was significantly facilitated handling and operation, it did not improve the detection limit (Bigler et al., 2007). Eventually, Kaufmann et al. (2008) were able to decrease the detection limit to 10ppbw by creating different backpressure regimes for sample and reagent.

2.3.3 Nitrate (NO_3^-)

A proxy for nitrate The sources of nitrate are, as Legrand and Mayewski (1997) put it, 'most difficult to assess'. In Antarctica Wolff et al. (1998) find the NO_3^- background source to be an 'enigma'. Herron (1982) report, however, that the unidentified NO_3^- source is more active in northern hemisphere. They further preclude the NO_3^- to be the result of extraterrestrial influence or to be of oceanic origin. Most likely, NO_3^- caries information on atmospheric processes with lightnings (Legrand and Kirchner, 1990) and oxidation of ammonia or N_2O (Herron, 1982) producing nitrogen oxides.

Nitrate is, just as SO_4^{2-}, not emitted directly into the atmosphere but derives from its precursors NO_x as a product of chemical processes in the atmosphere (Legrand and Kirchner, 1990). It is known to have an annual cycle with peaks during spring|summer (Legrand and Mayewski, 1997), generally succeeding the peak in SO_4^{2-} (Beer et al., 1991). Anklin et al. (1998) report that while NO_3^- has been a reliable seasonal indicator at greater depths, the natural NO_3^- variability has been obscured by anthropogenic interferences (see also Neftel et al., 1985; Mayewski et al., 1986).

Legrand and Mayewski (1997) point out that the paleoenvironmental significance of nitrate is not yet clear, but similar to H_2O_2 and HCHO (see supra) nitrogen oxides have an influence on the atmospheric hydroxyl radical's (OH) abundance (Legrand and Kirchner, 1990), thereby indirectly affecting the atmospheric residence time of several greenhouse gases.
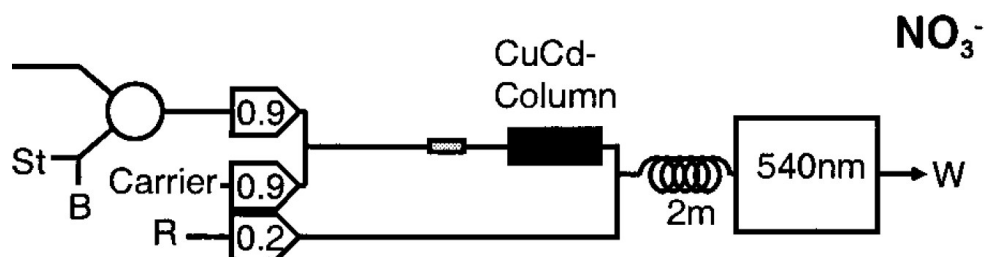
Figure 10: Detection line for nitrate as implemented by Röthlisberger et al. (2000)

Detection Technique   For their study on the 'annual accumulation at two sites in north-west Greenland', Anklin et al. (1998) had augmented the number of analysis lines relative to the B CFA system as described by Sigg et al. (1994). Amongst others, they adopted a colorimetric standard method listed in APHA (2005) for NO_3^- and nitrite (NO_2^-) detection.

This absorption line, originally proposed by Wood et al. (1967), was also included in the B CFA as presented by Röthlisberger et al. (2000) It relies on the reduction of nitrate to nitrite and the nitrite's subsequent diazotisation. As a reducing agent, Wood et al. suggested to use copperised cadmium, packed in a column, through which the sample was lead. To prolong the columns life time, the freed cadmium ions were complexed with the tetrasodium salt of ethylenediaminetetraacetic acid (EDTA).

$$NO_3^- + Cd + EDTA^{4-} + H_2O \longrightarrow NO_2^- + Cd(EDTA)^{2-} + 2\,OH^- \tag{2.5}$$
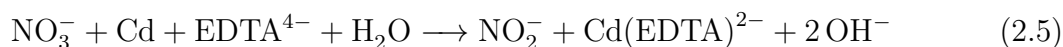
Bendschneider and Robinson (1952) have shown that NO_2^-, if diazotized with sulphanilamide

$$HNO_2 + NH_2SO_2C_6H_4NH \cdot 2\,HCl \longrightarrow NH_2S_{02}C_6H_4N\equiv NCl + 2\,H_2O \tag{2.6}$$

and coupled with N-(1-naphthyl)-ethylenediamine (NED)

$$NH_2SO_2C_6H_4N\equiv NCl + NED \longrightarrow$$

$$NH_2SO_2C_6H_4N=NNHCH_2CH_2NH(C_{10}H_7) \cdot 2\,HCl + HCl \tag{2.6a}$$

$$NH_2SO_2C_6H_4N=NC_{10}H_6NHCH_2CH_2NH_2 \cdot 2\,HCl + HCl \tag{2.6b}$$

forms a red-coloured complex absorbing at 540nm. The exact nature of the complex is not known, but Bendschneider and Robinson propose reactions 2.6a and 2.6b as the most likely ones.

Giné et al. (1980) then developed a flow injection analysis (FIA) method based on this reaction, mixing the sample first with a carrier catalysing the reduction and complexing the freed cadmium with EDTA, before merging the sample with the complex-forming reagent as proposed by Bendschneider and Robinson (1952).

As is evident from reaction 2.5, the detected absorption is a signal of both, nitrate and nitrite since all NO_3^- is reduced to NO_2^-. In the FIA method Giné et al. solved this by alternately bypassing the column - which yields the NO_2^- concentration only - and reducing the NO_3^- in the sample. The nitrate concentration can then be deduced from the difference between the two signals. This is impossible in a single CFA line, but Röthlisberger et al. (2000), invoking Legrand and Mayewski (1997), point out that NO_2^- levels in polar ice cores are too low to be influencing the measurement and that the $NO_2^- + NO_3^-$ signal is representative for the nitrate concentration.

Chapter 3

The Copenhagen CFA (C CFA) system

Summary   *The wide-spread use of meltheads has opened up the possibility for building highly specialised CFA systems. Indeed, systems have been set up maximising the number of measured proxies (in Reno) or been designed in a modular fashion to facilitate transport and field employment (in Bern).*

Whereas the latter has opted for a middle path between a high resolution and a large number of components measured, the Copenhagen CFA (C CFA) has found its raison d'être *in producing highly resolved data sets. Long analysis times and a small number of detected species were accepted and the system's hardware adjusted. These adjustments included melthead modifications to compensate for the mixing due to differing residence times of melt water on the melthead as much as possible and a complete redesign of the debubbler to minimise its volume.*

Efforts were rewarded with the ability to resolve layers of 11mm thickness allowing for experimental dating at depth were previously model results had to be invoked. Nevertheless, the development of a phosphate line showed that tendency to expand the CFA's scope was not halted and the integration of cavity ring-down spectrometers stands in line with the trend to employ CFA for more than merely aerosol detection.

3.1 High Resolution CFA optimised by Bigler et al. (2011)

The Copenhagen system was designed to yield the highest possible resolution. This is highly desirable when studying climatic changes in order 'to better constrain the triggering, mediating and evolving processes' (Ruth et al., 2007), but also to allow for more accurate dating of a core by annual layer counting (e.g. Svensson et al., 2008), see section 2.1.

All possible measures for resolution enhancement, i.e. decreasing the volume and the melt rate and increasing the flow rate (see equation (1.2)), were taken. Mixing volumes at the melthead and in the debubbler were minimised, flow rates through selected detectors were increased and the melt rate was decreased by 66% to 1.5cm/min. A consequence of a lower melt- and a higher flow rate is a decreased amount of available sample. Thus,

fundamental choices had to be made concerning the species that are to be measured since their number had to be limited.

As the purpose of the newly designed system is to improve the dating accuracy for selected sections of the core, species with prominent annual maxima had to be chosen. In order to identify annual layers as accurately as possible, the measured species should peak preferably in different seasons in case a single season is not recorded at the site of drilling. It was therefore opted to install detection lines for dust, ammonium (NH_4^+) and sodium (Na^+) with peaks in spring, summer and winter (see chapter 2), respectively. These species are to first order proxies of terrestrial, biogenic and marine environments (Legrand and Mayewski, 1997; Bigler et al., 2011), such that obtained CFA profiles - despite the limited number of components measured - still yielding good picture of the climate at the time of precipitation.

Dispersion at the melthead occurs when simultaneously melted sample is removed at different times due to different distances to the drainage hole. This was remedied by engraving starring channels into the melthead's inner section's surface. These channels facilitate drainage of freshly melted sample also at points far from the drainage hole, see figure 11. The new square design (as opposed to the C CFA's Swiss predecessors) was adopted from McConnell et al. (2002) for more efficient use of the sample available. An edge of 26mm for the inner section was chosen, together with an outer section of 35×35mm² allowing save decontamination of slabs with a cross section of $(32mm)^2$ to $(37mm)^2$, which are typical dimensions of core sections allocated for CFA measurements when the ice is cut in the field.
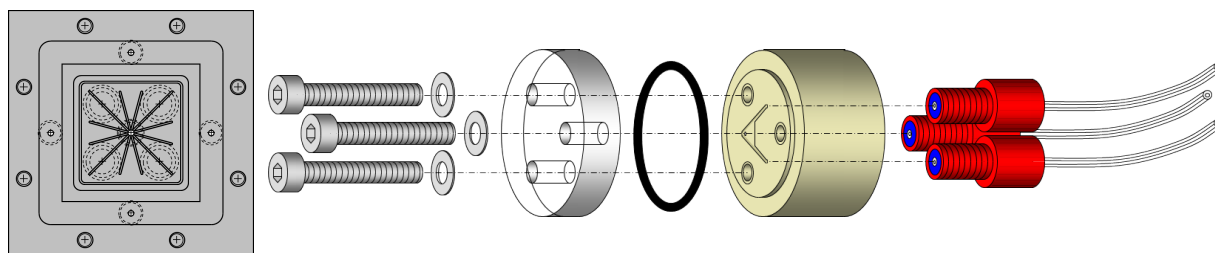
Figure 11: Redesigned melthead and debubbler, taken from Bigler et al. (2011)

Figure 11 further shows a completely redesigned debubbler. The reduced throughput means that less air has to be removed in a given time interval, which allows for dramatically decreased debubbler volume: 90μl as opposed to 300μl in the system presented by (Kaufmann et al., 2008). In addition to the decrease in volume also the design of the debubbler was changed to an equilateral triangular cell with in the corners the sample inlet,

an outlet for the debubbled sample and an outlet for the excess sample including all the air. This way a constant flow in the debubbler is assured and a dead volume, which has been the core of the debubbler used by Sigg et al. (1994), is avoided.
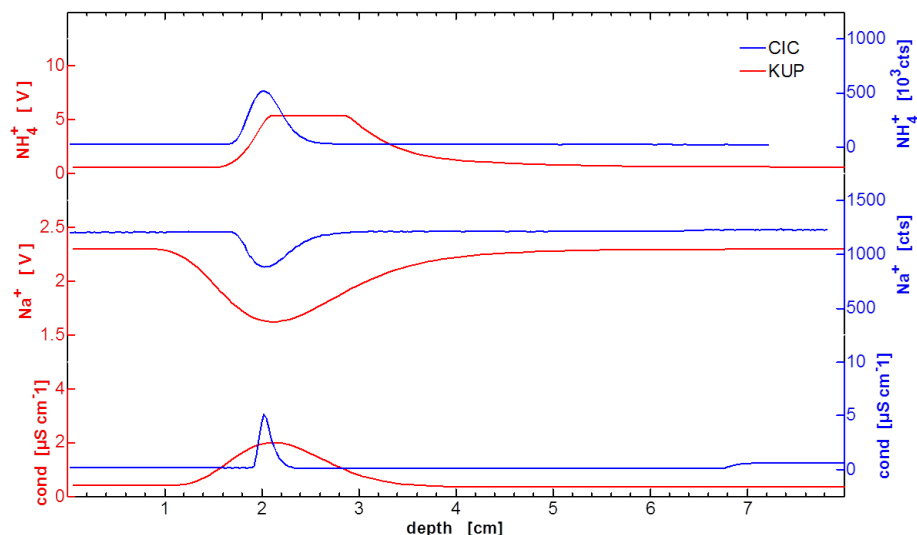
Figure 12: Response of the B CFA and the C CFA to a δ-function

The flow scheme of the C CFA is shown in figure 15, and it can be seen that here, as opposed to the B CFA in figure 5, the standard solutions are injected before the mixing volume constituted by debubbler. Hereby the flow path common to the standard and the sample - and in its slipstream the volume that can be restituted for (section 1.2.1) - is increased.

Even without restitution, figure 12 witnesses the resolution enhancement accomplished by comparing the responses of the B CFA and the C CFA to a 'δ-function', i.e. a drop of multi-component standard between to blank-ice cubes. Figure 4 in appendix A goes one step further and compares the responses to δ-functions entering the systems via the melthead or as a solution via the injection valve. The conclusion there is that the newly designed debubbler introduces almost no mixing (Bigler et al., 2011), whereas that is the case for the most recent B CFA (Kaufmann et al., 2008).

3.2 Annual Layers in NGRIP Basal Ice

The accuracy with which an ice core can be dated crucially depends, as Legrand and Mayewski (1997) and Anklin et al. (1998) point out, on the accumulation rate. Or, more

precisely, on the annual layer thickness, which is a function of accumulation rate and thinning with depth (Dansgaard and Johnsen, 1969). The reason for this is that the most accurate dating method, the counting of annual layers in the visual stratigraphy (Svensson et al., 2008) or impurity records (e.g. Rasmussen et al., 2006) is precluded by the detection techniques' inability to resolve layers below a certain limit. Therefore, the GICC05 time scale, a composite time scale based on stratigraphic layer counting of multiple Greenlandic cores, only reaches back to 60ka b2k (Svensson et al., 2008), whereafter dating relies on the modelled GICC05modelext (Wolff et al., 2010).

The NGRIP core covering the last 120ka (NGRIP members, 2004), however, has the potential to allow stratigraphic dating throughout the entire last glacial. Basal melt at the NGRIP site has reduced the thinning and the modelled NGRIP time scale 'ss09sea' (Johnsen et al., 2001; Andersen et al., 2006) predicts annual layer thicknesses to be larger than 1cm even in basal ice. The increased heat flux gives further rise to rapid crystal growth destroying the visual stratigraphy as obtained from line-scan images (Svensson et al., 2005; see page 40) and it is hypothesised that annual layers are also disturbed in the ionic (Barnes et al., 2003) and insoluble (Faria et al., 2010) impurities as they are being moved by the growing crystal grains' boundaries.

These predictions concerning the layer thicknesses and the nature of the insolubles' record, together with the capabilities of the C CFA, were tested on three sections of NGRIP ice (at depth of about 3070m, 3040m and 2995m). The results are presented on page 40 and in appendix B. It is found that (1) the insoluble record preserves the annual cycle, (2) the ss09sea model can be confirmed to first order but tends to overestimate layer thicknesses in the basal ice, and (3) that the C CFA is able to resolve these layers of about 11mm (Svensson et al., 2011). This means that the C CFA can be used to identify annual layers in both Greenland (NGRIP) and Antarctica (EDC, Bazin et al., 2013).

3.3 Development of a Phosphate Detection Line

A proxy for biological activity Air-born phosphorus can be of marine, terrestrial, biological as well as volcanic origin (Filippelli, 2008; Mahowald et al., 2008). Being one of the limiting nutritions to the terrestrial biosphere (Falkowski et al., 1998), phosphate constrains the possible extend of it. Consequently, the atmospheric phosphate abundance - reflected in phosphate levels in ice cores - can be used as a tracer for biological activity.

Previous measurements of phosphate in ice cores have shown that it is far from abundant (.25ppb), and that biomass burning can indeed be responsible for increased phosphate levels

Annual layering in the NGRIP ice core during the Eemian

Anders Svensson (1), Matthias Bigler (1, 2), Ernesto Kettner (1), Maibritt Nielsen (1), Sigfus Johnsen (1), Dorthe Dahl-Jensen (1), and Jørgen Peder Steffensen (1)

(1) Centre for Ice and Climate, Niels Bohr Institute, University of Copenhagen, Denmark (as@gfy.ku.dk), (2) Climate and Environmental Physics, Physics Institute, University of Bern, Switzerland

CENTRE FOR
ICE AND CLIMATE

ABSTRACT

The Greenland NGRIP ice core continuously covers the period from present day back to 123 ka before present, which includes several thousand years of ice from the previous interglacial period, MIS 5e or the Eemian. In the glacial part of the core annual layers can be identified from impurity records and visual stratigraphy, and stratigraphic layer counting has been performed back to 60 ka. In the deepest part of the core, however, the ice is close to the pressure melting point, the visual stratigraphy is dominated by ice crystal boundaries, and annual layering is not visible to the naked eye.

In this study, we apply a newly developed setup for high-resolution ice core impurity analysis to produce continuous records of dust, sodium and ammonium concentrations as well as conductivity of melt water. We analyzed three 2.2 m sections of ice from the Eemian and the glacial inception. In all of the analyzed ice, annual layers can clearly be recognized, most prominently in the dust and conductivity profiles. Part of the samples is, however, contaminated in dust, most likely from drill liquid that entered the core through grain boundaries. It is interesting that the annual layering is preserved despite a very active crystal growth and grain boundary migration in the deep and warm NGRIP ice.

Based on annual layer counting of the new records, we determine a mean annual layer thickness close to 10 mm for all three sections, which, to first order, confirms the modeled NGRIP time scale (ss09sea). The counting does, however, suggest a longer duration of the climatically warmest part of the NGRIP record (MIS5e) of up to 1 ka as compared to the model estimate.

Our results suggest that stratigraphic layer counting is possible basically throughout the entire NGRIP ice core provided highly-resolved profiles become available. A 120 ka independent Greenland time scale would provide an important tool for climate reconstructions and we hope to make such a chronology available in the coming years.
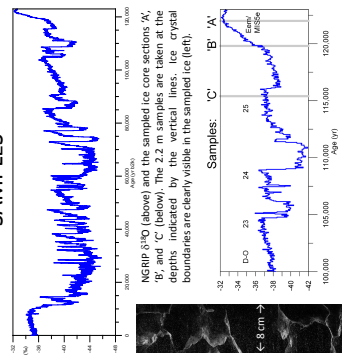
ANALYTICAL METHODS
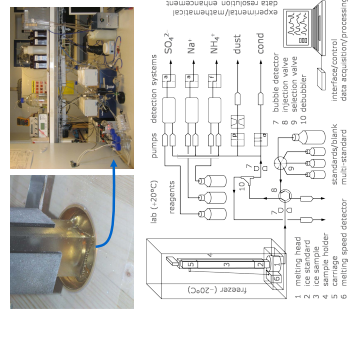
The ice core impurities are measured by a Continuous Flow Analysis (CFA) system that melts and analyses ice at a speed of 1.5 cm ice per minute.

RESULTS

Records of dust, ammonium, sodium, and conductivity from sample 'A' shown together with the ice core visual stratigraphy. The uppermost curve shows the dust contamination problem that is related to grain boundaries.

SAMPLES

NGRIP δ18O (above) and the sampled ice core sections 'A', 'B', and 'C' (below). The 2.2 m samples are taken at the depths indicated by the vertical lines. Ice crystal boundaries are clearly visible in the sampled ice (left).

ANNUAL LAYER COUNTING

Examples of annual layer counting in samples 'C', 'B', and 'A', respectively (above). Annual layers are resolved in dust (black) and conductivity (green) and occasionally in sodium (red), whereas the ammonium signal (blue) is smoothed by post-depositional processes. 'Certain' and 'uncertain' annual layers are indicated with full and dotted grey vertical lines, respectively. The induced annual layer thicknesses are compared to model estimates (below).

MEASUREMENT RESOLUTION

Power spectra of CFA records of 9.9 m early Holocene ice and early Holocene ice demonstrating the resolution of the measurements. The annual layer thickness of about 75 mm is clearly seen as a peak in most series. Furthermore, power corresponding to a layer thickness of 10 mm is well above the noise level for most parameters suggesting that annual layers of that thickness can be resolved.

Power spectra comparing early Holocene and Eemian sample 'A' records for 2.0 m of ice. Assuming similar deposition patterns for the two climatic periods, the difference between the curves reflects the ice deformation and the diffusion in the ice over about 110 ka. In the Holocene spectra an annual layer peak is visible at around 75 mm, whereas the Eemian spectra show no clear indication of an annual peak.

CONCLUSIONS

Surprisingly, it is possible to identify annual layers in the deepest part of the NGRIP ice core from high-resolution measurements of dust and conductivity. The analysis of three deep ice core sections shows that:

• The annual signal is likely to be preserved throughout the entire NGRIP ice core despite a very active crystal dynamics in the deepest ice.

• The modeled NGRIP time scale (ss09sea) is confirmed to first order although the MIS5e section of the ice core may be longer than suggested.

• The NGRIP ice core has the potential for providing a continuous stratigraphic time scale throughout the entire last glacial cycle provided continuous high-resolution profiles are obtained.

(Edwards et al., 2007, cited by Kjær et al., 2013) . Phosphate is, however, believed to vary significantly on glacial-interglacial time scales (e.g. Mahowald et al., 2008), as a result of the exposure of ocean shelves on which phosphate was previously deposited, making the phosphate available for subsequent entrainment (Filippelli, 2008);

Since phosphorus lacks a gaseous phase (Filippelli, 2008), it can be transported to the interior of the Greenlandic ice sheet only as particulate matter or as PO_4^{3-}, the reactive fraction of the total phosphate concentration; i.e. the fraction available for biological uptake (Paytan and McLaughlin, 2007). By comparing the dissolved reactive phosphate (DRP) concentrations with those of further aërosols indicating the strength of the multiple potential phosphate sources, Kjær et al. (2013) resolve those source's relative contributions.

They conclude that, although the dust concentration could potentially explain all the DRP present in the ice, the low degree of correlation between the dust and DRP concentrations indicates multiple sources. These could be biogenic particles as well as biomass burning events, while sea salt and volcanic contributions are found to be unlikely and the strength of a possible anthropogenic contribution to be in the data's uncertainty band.

(a) Employed at NEEM

(b) Improved PO_4^{3-} detection line, presented in Kjær et al. (2013)
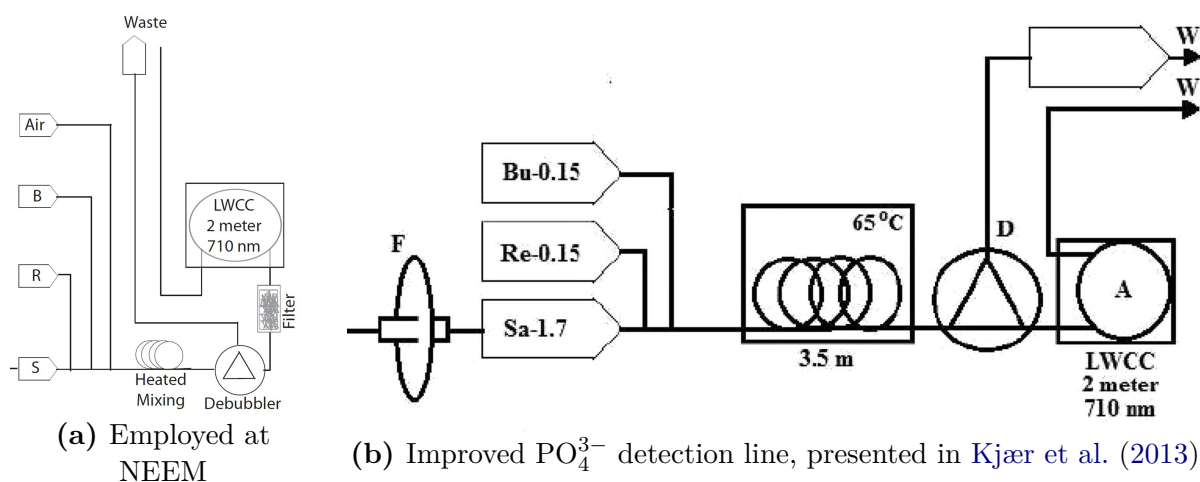
Figure 13: CFA detection lines for Phosphate (Kjær et al., 2011, 2013)

Detection Technique The detection method developed here is an adaptation of Zhang and Chi's (2002) absorption method for an 'Automated analysis of nanomolar concentrations of phosphate in natural waters with liquid waveguide'. A liquid wave guide capillary cell (LWCC) is an absorption cell - in this case of 2m length with a volume of $1/2$ cm^3 - within which repeated total reflection increases the effective absorption length. This is the key to lowering the detection limit well into the nano-molar range.

Continuous analysis of phosphate in a Greenland shallow ice core

Helle A. Kjær (1), Anders Svensson (1), Matthias Bigler (2), Ernesto Kettner (1), Paul Vallelonga (1), and Dorte Dahl-Jensen (1)
(1) Centre for Ice and Climate, Niels Bohr Institute, University of Copenhagen, Denmark (2) Climate and Environmental Physics, Physics Institute, University of Bern, Switzerland

ICE AND CLIMATE CENTRE FOR

Vienna EGU May 2010
XY239

Introduction

Phosphate is an important and sometimes limiting nutrient for primary production in the oceans. Global atmospheric phosphate mainly comes in the form of mineral aerosols, however approximately 15 % is from anthropogenic sources and a small fraction is primary biogenic particles (Mahowald et al. 2008).

Due to deforestation and the use of phosphate as a fertilizer changes in the phosphate cycle have occurred over the last centuries (Paytan and McLaughlin, 2007). On longer time scales, sea level changes are thought to have also caused changes in the phosphate cycle (Filippelli, 2008). Analyzing phosphate concentrations in ice cores may help to gain important knowledge about the processes.

The concentration of phosphate in ice cores is not known. However the concentration of phosphorus has been measured with ICP-MS showing ppb levels (Edwards et al. 2007). Hence the expected amount of phosphate in ice cores is of the same order.

In the present study we attach a phosphate detection line to an existing continuous flow analysis (CFA) setup for ice core analysis at the University of Copenhagen. The CFA system is optimized for high-resolution measurements of insoluble dust particles, electrolytic melt water conductivity, and the concentrations of ammonium and sodium.

For the phosphate analysis we apply a continuous and highly sensitive absorption method that has been successfully applied to determine phosphate concentrations of sea water (Zhang and Chi, 2002). The method has a detection limit of 0.1 ppb.

Preliminary studies of parts of the central Greenland NEEM S1 shallow ice core shows that the method is useful and that most the phosphate arrive as mineral dust. However some phosphate seems to arrive independent of dust.

Ice sample and CFA

Ice cores present archives of climates past and provide information on various parameters such as temperature, ocean volume, precipitation, chemical and gas composition of the lower atmosphere, volcanic eruptions and solar variability

Ice core impurities are measured by a Continuous Flow Analysis (CFA) system. The set up consists of a melt head that melts a section of ice separated for avoiding contamination into an inner part (sample) and an outer part (waste).

The ice core is analyzed for its content of soluble sodium (mainly deriving from sea salt), soluble ammonium (related to biological processes and biomass burning events), insoluble dust particles (basically transported from Asian deserts to Greenland), and the electrolytic melt water conductivity (which is a bulk signal for all ionic constituents) and now phosphate too.

With a melt speed of 3.0 cm ice per minute our method allows to resolve seasonal variability of phosphate in the firn.

Figure 1 (right):
Schematic of the CFA set up from Copenhagen illustrating how the ice is melted and transported through the system. The sample used for phosphate measurements is the one used for dust detection.

Figure 2 (below):
A picture of the melt head.

1. melting head
2. ice standard
3. ice sample
4. sample holder
5. carriage
6. melting speed detector

lab (+20ºC)   pumps detection systems

reagents

Dust

Sample to PO₄³⁻

freezer (-20ºC)

Na⁺   NH₄⁺   cond

standards/blank
multi-standard

7. bubble detector
8. injection valve
9. selection valve
10 debubbler

interface/control
data acquisition/processing
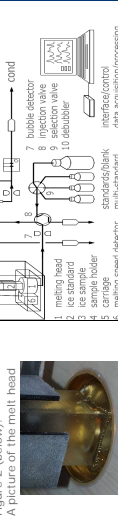
Phosphate setup
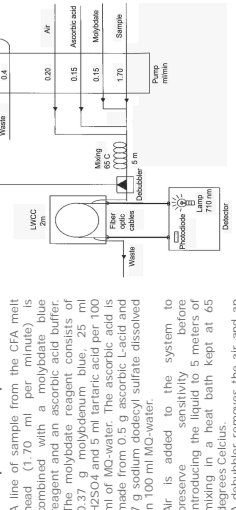
A line of sample from the CFA melt head (1.70 ml per minute) is combined with a molybdate blue reagent and an ascorbic acid buffer. The molybdate reagent consists of 0.37 g molybdenum blue, 25 ml H_2SO_4 and 5 ml tartaric acid per 100 ml of MQ-water. The ascorbic acid is made from 0.5 g ascorbic L-acid and 7 g sodium dodecyl sulfate dissolved in 100 ml MQ-water.

Air is added to the system to preserve sensitivity before introducing the liquid to 5 meters of mixing in a heat bath kept at 65 degrees Celcius.

A debubbler removes the air and an absorption measurement takes place in a 2 meter liquid waveguide capillary cell (LWCC) with an inner volume of 0.5 ml at wavelength 710 nanometer. The method has a detection limit of around 0.1 ppb and good linearity.

Waste   0.4   Air
0.20   Ascorbic acid
0.15   Molybdate
1.70   Sample
Pump ml/min

Mixing 65 C
Debubbler   5 m

LWCC 2m
Fiber optic cables
PhotoDiode
Lamp 710 nm
Detector
Waste

Figure 3 (above):
Configuration and flow diagram of phosphate analysis. Flow rates are in ml per minute and detection wavelength is 710 nm (Zhang et Chi, 2002).

Optimizing
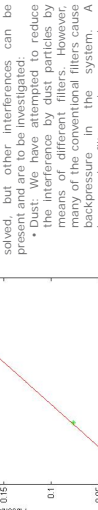
The optimization of several parameters has been investigated:
- Mixing length
- Temperature
- Concentrations of molybdate, L-ascorbic acid and H2SO4
- Flow rates of reagent, buffer and sample
- Air flow and debubbler

Interferences

Interference from dust has almost been solved, but other interferences can be present and are to be investigated:

- Dust: We have attempted to reduce the interference by dust particles by means of different filters. However, many of the conventional filters cause backpressure in the system. A homemade filter using a column stuffed with glass wool seems to give the best results.
- Silicate: The molybdate does react with silicate. Tartaric acid is added to avoid this, but how much silicate interferes has yet to be determined.
- Arsenate: The molybdate reacts with arsenate to an extent that reamins to be determined.

$$Abs = 0.024 * PO_4^{2-}(ppb) + 0.005$$
$$R=0.9994$$
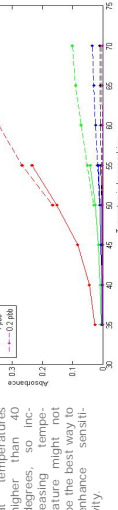
Figure 4 (above):
Figure 5 (right):
The relationship between concentration and absorbance is linear.

The reaction is highly temperature dependent But a reaction between molybdate and silicate is expected to occur at temperatures higher than 40 degrees, so increasing temperature might not be the best way to enhance sensitivity.

Temperature dependence
- 20 ppb
- 5 ppb
- 2 ppb
- 1 ppb
- 0.2 ppb

Results on the ice core "NEEM S1 2007"
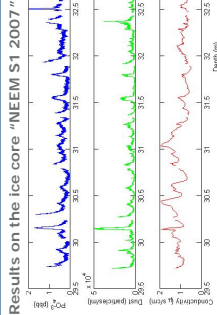
Figure 6 (above): Raw phosphate (blue), dust (green) and conductivity (red) measurements from the NEEM S1 core plottet on a function of depth.

Figure 7 (below): Smoothed data for phosphate (blue) and dust (green) from the NEEM S1 core plottet on a function of depth. Arrows indicate differences.

2 cm smoothed NEEM S1
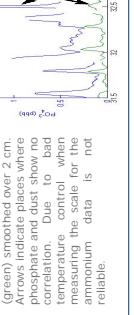
Figure 8 (right): Phosphate (blue) and ammonium (green) smoothed over 2 cm. Arrows indicate places where phosphate and dust show no correlation. Due to bad temperature control when measuring the scale for the ammonium data is not reliable.

Conclusion

A method similar to that used by Zhang and Chi (2002) has been tested and optimized for continuous flow analysis of ice cores in Copenhagen.

Interference problems with dust is almost avoided using a column stuffed with glass wool as filter. The sensitivity has been increased to 0.1 ppb by introducing air bubbles to separate the flow, and by increasing temperature to 65 degrees celcius. The latter however introduces the risk of interference from silicates. Interference from arsenate is also to be investigated.

Phosphate has been measured in the Greenland ice core NEEM S1 from northern Greenland (75.74 N, 43.20 W) and show a level during a period of approximately 19 years in the first half of the 20th century between 0 and 2 ppb with a mean of pbb 0.37 pbb (fig 6). It is clear that large parts of the phosphate arrives with mineral aerosols (fig 7). A correlation coefficient of 0.61 shows the significance, however some spikes occuring at the same time as spikes in NH_4^+ has been detected (fig. 8), yet no correlation between phosphate and ammonium is present (correlation=0.03) when applying data from the whole period. The spikes however do suggest that the same processes are sometimes responsible for both NH4+ and phosphate.

We expect learn more on the behavior and variation of phosphate in ice cores during the coming field season on the NEEM ice core drilling project positioned 77°27'N 51°3.6'W, Greenland.

References
Edwards et al (2007), abstract for AGU
Filippelli (2008). Elements, 4, 89-95.
Mahowald (2008), Global Chemical Cycles, 22, GB 4026.
Paytan and McLaughlin (2007). Chem. Rev. 1 563-576
Zhang and Chi (2002). Environmental science and technology, 36, 1048-1053

Contact
Helle Astrid Kjær
Centre for Ice and Climate, Juliane Maries Vej 30,
DK-2100 Copenhagen Ø, Denmark
phone (+45) 50 52 80 04, e-mail: hellek@fys.ku.dk

Eventually, the absorption at 710nm of a blue coloured molydophospheric complex is spectrometrically detected. The choice of complex forming reaction as well as the reaction kinetics enhancement measures (heating the reaction coil and reducing the pH) were adapted from Murphy and Riley (1962), subsequently modified following suggestions of Zhang et al. (1999). To minimize the loss of depth resolution in the system employed at NEEM and described by Kjær et al. (2011), the sample stream was intentionally gas-segmented and prior to analysis debubbled, see figure 13a.

During subsequent refinement of the method in Copenhagen, the gas-segmentation became redundant as the distance between melthead and detection cell was reduced. Further improvement was achieved by moving the dust filter upstream, now to be located before the junction of the reagent flow with the sample stream (Kjær et al., 2013; see figure 13b). Due to the slightly acidic nature of the chemicals added to the sample stream (Murphy and Riley, 1962), insolubles need to be removed prior to the reagent's addition. Else phosphorus adhering to insoluble aerosols can be detached and labelled, ultimately leading to a systematic overestimation of the DRP when using the method described by Kjær et al. (2011) and discussed on page 42.

After improvement, the response of the PO_4^{3-} detection line is linear up to a PO_4^{3-} concentration of $10ppb$ and the uncertainty of the data has been reported to be about 1% of that (Kjær et al., 2013). Due to the length of the detection cell and - more importantly - the mixing coil, the response time (5-95% signal) is with $20sec$ rather long. This corresponds to smoothing over a depth of $.5cm$ in the C CFA and roughly $1.2cm$ in the Bern CFA (described by Kaufmann et al., 2008).

3.4 Cavity Ring Down Spectrometers

As mentioned in section 1.6, CFA has moved beyond being an analysis technique for aerosol studies only and ventured into the 'classical' fields of measurements on water isotopes and gases. A trend established a decade ago, when the ease of sample handling and the potential for unprecedented high resolution have encouraged Huber and Leuenberger at the University of Bern to connect isotope ratio mass spectrometers (IRMS) to the predecessors of the B CFA system (Leuenberger and Huber, 2002).

Making use of CFA standard measures taken in classical soluble aerosol detection, such as in-flow mixing of the reagents and temperature manipulation to enhance the reaction kinetics, they succeeded in, for example, rapidly bringing CO_2 and the sample water stream into isotopic equilibrium (Leuenberger and Huber, 2002). In a similar manner Huber and

Leuenberger (2003) developed a method to equilibrate H_2 and the melt water stream and both gases, H_2 and CO_2, could subsequently be injected into IRMSs for an analysis of δD and $\delta^{18}O$, respectively.

Utilising the same gas extraction used for separating the CO_2 and the melt water in their $\delta^{18}O$ detection line, Huber and Leuenberger (2004) also constructed a system to measure the abundance ratios of $\delta^{15}N$, $\delta^{17}O$, and $\delta^{18}O$ in the air enclosed in the ice. Thus, by 2005, Huber and Leuenberger had presented semi-continuous detection techniques that could yield isotopic time series on both water and gases in high temporal resolution when connected to a melthead.

Detection System   The step towards even higher resolution and field-deployability was made possible by the commercial availability of laser spectrometers. As the molecules of interest (CH_4 and the different isotopologues of water) have distinct absorption spectra in the infrared region due to individual rovibrational transitions (Kerstel et al., 1999), their abundance can be deducted from the absorption of laser light in that frequency range.

Rather than for instruments detecting directly the absorption of the molecules inside the cavity, it was opted to purchase Picarro's cavity ring-down spectrometers (CRDS) CFADS36 CO_2|CH_4|H_2O and L1102-i for measurements of atmospheric CH_4 mixing ratios and the melt water's isotopic composition, respectively.

In CRDS, light is injected into the cavity through one of the (partially transmissive) mirrors and the intensity building up is monitored by a detector located behind a second mirror; on page 51 the instrument's cavity is schematically shown. When a certain threshold is reached, the laser is switched off and the 'ring-down' time, i.e. the time it takes for the exponentially decaying intensity to fall below a second threshold is measured (Crosson, 2008).

Losses of light intensity are a function of (a) cavity imperfections, i.e. the not perfectly reflective mirrors, which are constant over time, and (b) scattering and absorption of the sample gas. Typical empty-cavity ring-down times are around 40 μsec (Crosson, 2008), a period within which the laser light has travelled a distance on the order of tens of kilometres through the cavity. Path lengths of this magnitude result in high sensitivity to changes in the abundance of the interrogated molecules.

Interfaces   In order to connect the CRDSs to the C CFA the basics from the work of Huber and Leuenberger were adopted by Gkinis et al. (2010) and Stowasser et al. (2012) for measurements on melt water and air, respectively.

Continuous online measurement of water isotopic content and methane concentration in ice cores with near-IR absorption spectroscopy coupled to Continuous Flow Analysis systems

Trevor J. Popp, Vasileios Gkinis, Christopher Stowasser, Thomas Blunier, Sigfus Johnsen, and Ernesto Kettner
Centre for Ice and Climate, Niels Bohr Institute, University of Copenhagen, Denmark

The 2nd International Symposium on the Dome Fuji ice core and related topics, 2009

Introduction

One of the most important features of ice cores as climate and atmospheric paleoarchives is their potential for high temporal resolution. The measurement of chemical impurities in ice cores that fully exploits this high resolution has become standard with the advent of Continuous Flow Analysis (CFA) often performed in the field. Meanwhile, the measurement of water stable isotopic composition (deuterium and oxygen-18) and atmospheric trace gas composition continues, for the most part, to be performed offline via discrete sampling with traditional mass spectroscopy and gas chromatography. These offline procedures are time consuming, expensive, and often come at the expense of fully exploiting the temporal resolution available in the ice core. Here we describe a new method and the first results for water isotopic content and methane concentrations measured continuously via laser based absorption spectrometers (Picarro, http://www.picarro.com/) coupled to a CFA system. The details of these systems have been tested with a deployment to the North Greenland Eemian Ice Drilling (NEEM) camp coupled to the University of Bern CFA system and in the laboratory with NGRIP ice coupled to the University of Copenhagen CFA system. For water isotope s results show that the system already produces the highest resolution interpretable records available that are comparable to the precision from than traditional spectroscopic methods. The methane measurements also offer unprecedented temporal resolution and with precision comparable to discrete methods.

Copenhagen Continuous Flow System overview

1 melt head 6 bubble detector
2 clean ice 7 injection valve
3 ice sample 8 selection valve
4 carriage 9 de-bubbler
5 melt speed detector
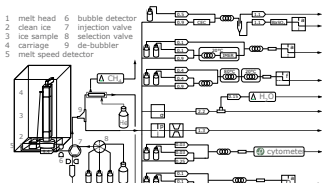
After melting the trapped bubbles are separated from the melt water stream. A dedicated fraction of the bubble-free water stream is delivered to the water isotope instrument. A water-bubble mixture is delivered to the methane instrument where a second water-air separation step occurs before measurement.

Water isotopes

A) System design

A carefully controlled fraction of the CFA melt stream is de-bubbled and subsequently evaporated directly into the laser cavity for simultaneous analysis of both deuterium and oxygen-18 content.
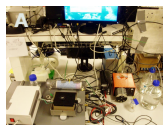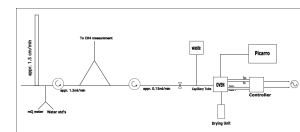
The system in the laboratory in Copenhagen (A), is essentially identical to its configuration when deployed to the field and can easily be adapted to different melter systems. The flash evaporator (B) is heated and supplied with a dry air carrier. The water vapor has a direct connection to the Picarro inlet from the evaporator. Dry air flow rate is controlled by the Picarro itself. Water flow rate is set by setting a pressure gradient to force a very small amount of the melt water through a capillary into the flash evaporator with the remaining fraction going to waste.
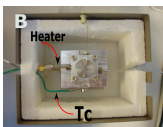
Water isotopes

B) Calibration

Humidity dependence. Upper 3 panels show raw data series as it is measured in real time from the Picarro instrument. The instrument monitors humidity level in the measurement cavity, $\delta^{18}O$, and δD. There is a strong dependence on isotopic ratios with humidity that can be characterized and corrected for in the case of fluctuations in water delivery (Lower 2 panels). The values are subsequently calibrated relative to V-SMOW with known standards.
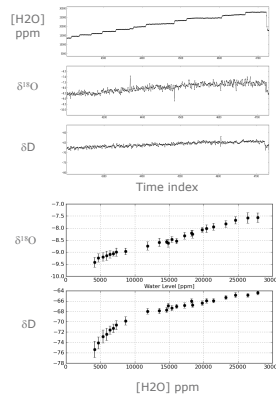
C) NGRIP Holocene data

2.2 meters of NGRIP ice calibrated plotted together with dual inlet mass spectrometer data over the same interval. The dD series is measured with a precision of 0.4 ‰ and d18O series with a precision of 0.15 ‰. The source of obvious outliers in the d18O series is not known and have not been filtered from the data.
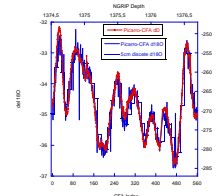
D) NEEM Holocene data

Uncalibrated data acquired in the field at NEEM in 2009 using the University of Bern CFA melter system.
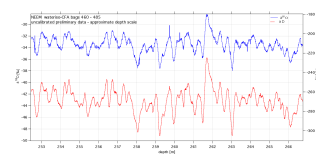
Outlook

The enormous potential of these systems is being realized, both in the density and resolution of the produced records in connection with other highly resolved series, and in the efficiency by which the records can be produced. Among other things, time series from the isotopic and gas analysis will benefit ice core dating via both layer counting and relative dating via gas correlations across abrupt shifts. The high resolution series will also benefit paleo reconstructions via isotopic diffusion studies in firn and ice.

Atmospheric CH₄ concentration

Gases are separated from the CFA melt water stream via a hydrophobic membrane, dried and introduced into the laser cavity of the CH$_4$ analyzer via a carrier stream of Helium or Nitrogen. Partial pressure of CH$_4$ (Picarro) and O$_2$ (OceanOptics) are measured and used to calculate the CH$_4$ concentration of the air that has been trapped in the ice.

A) Setup

*Schematic of the setup for continuous CH$_4$ measurements coupled to the Continuous Flow Analysis (CFA) at the University of Copenhagen.
The overflow of the debubbler, a mixture of water and gas, is directed to the hydrophobic degassing unit where the gases are flushed with helium or nitrogen towards the analyzer. The gas stream is kept at underpressure to optimize the degassing process.
On the way the sample stream passes a drying unit, consisting of a Nafion membrane and a purge flow of dried ambient air. For calibration of the setup degassed MilliQ water is mixed with a CH4 standard in the ratio 10:1, forwarded through the whole setup and measured by the analyzer.*
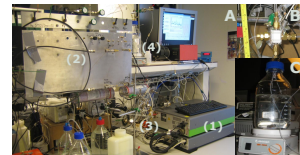
Setup for continuous CH$_4$ measurements coupled to the Continuous Flow Analysis (CFA) at the University of Copenhagen. A: An overview of the setup showing CH$_4$ Analyzer (1), drying unit (2), degassing unit (3) and calibration standard (4). B: The degassing unit in detail, which is kept at ca. 500 mbar. C: The calibration standard in detail. MilliQ water is degassed and mixed with CH4 standards (NOAA) in 10:1 water to gas ratio as seen in ice cores.

B) Calibration
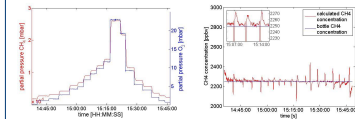
Dry air is diluted with helium. The dilution is changed stepwise. Left panel: Partial pressure of CH$_4$ and O$_2$ is measured by the Picarro CH$_4$ analyzer and the oxygen probe, respectively. Right panel: From the partial pressure of CH$_4$ and O$_2$ the concentration of CH$_4$ in the air extracted from the ice core can be calculated. Spikes are due to steep sudden concentration changes.

The CH$_4$ analyzer measures the number of CH$_4$ molecules in its cavity. Normally, with pressure and volume of the cavity known the concentration of CH$_4$ can be calculated. Here, however, the sample is diluted with an unknown amount of carrier gas. In order to obtain the true CH$_4$ concentration, measurement of another component is mandatory as a proxy for the undiluted sample. An oxygen sensor was implemented for this correction close to the cavity of the CH$_4$ analyzer in a temperature and pressure stable compartment.

C) First Preliminary Results
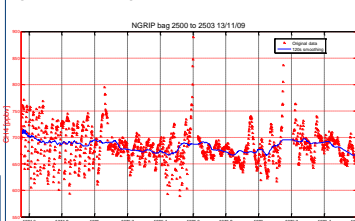
First results from measurements of ca. 2m of early Holocene ice from the NGRIP ice core are shown above.
Fluctuations in the data are caused by variations in the amount of sample with time. These variations are a result of changing bubble concentration in the melt water stream.
Even with the smoothed signal the temporal resolution is one measurement every three centimeters of ice core.

Centre for Ice and Climate
Juliane Maries Vej 30
DK-2100 Copenhagen Ø, Denmark

trevor@nbi.ku.dk (isotopes)
v.gkinis@nbi.ku.dk (isotopes)
stowasser@fys.ku.dk (methane)
blunier@nbi.ku.dk (methane)
e.kettner@nbi.ku.dk (CFA)

Just as Huber et al. (2003), Stowasser et al. (2012) implemented a hydrophobic membrane of the same type used in classical CFA detection lines to remove micro-bubbles after the chemical reactions, downstream of the debubbler. However, Stowasser et al. did not use a custom-built unit but rather implemented a commercially available degassing device (MicroModule G591, Membrana), on page 51 the different degassing unites are described.

For their analysis of the melt water Gkinis et al. (2010) were able to reduce the mixing volume of their analysis line with respect to Huber and Leuenberger (2003). The detection line presented by Huber and Leuenberger contained mixing volumes in the form of (a) an evaporation chamber filled with a catalyst-coated hydrophobic polymer in which the water vapour and additionally injected H_2 were to reach isotopic equilibrium and (b) a water trap further downstream to prevent any water vapour from entering the IRMS.

Gkinis et al. (2010) were able to avoid these mixing volumes and consequently increase their detection line's depth resolution. As the CRDS performs analysis directly on the water vapour, a water trap was redundant. By further placing the open split regulating the amount of sample injected into the spectrometer upstream of the evaporation chamber, only a stream of the order of nanolitres per minute had to be evaporated. Therefore a heated T-split, flushed with a stream of previously dried air could serve as completely re-engineered 'continuous stream flash evaporator'.

3.4.1 Water Isotopic Composition

A temperature proxy From the isotopic composition of the ice matrix the temperature difference between the precipitation's source area and its condensation site can be inferred (Dansgaard, 1964). Therefore, the isotopic signature has been interpreted as a proxy for cloud temperature at the time of condensation (Jouzel and Merlivat, 1984; Masson-Delmotte et al., 2005) and has been used as the standard record to represent past temperature variations in Greenland and Antarctica (e.g. Johnsen et al., 1995; Jouzel et al., 1997; Petit et al., 1997).

The isotopic composition of water is commonly described using the δ-notation, a measure of the relative deviation of a sample's isotope abundance ratio (in this case $\frac{^{18}O}{^{16}O}$ and $\frac{^{2}H}{^{1}H}$) with respect to that of a common standard (for water this is commonly Vienna Standard Mean Ocean Water, VSMOW).

With an increasing temperature gradient, lower δ-values are observed. This results in identifiable seasonal cycles also in the isotope records. However, the isotopic composition of the precipitated snow is subject to post-depositional diffusion and reliable dating based

on the isotope record is confined to the top part of a core (Vinther et al., 2006).

When data on both isotopic ratios is available, the deuterium excess (D_{XS}) can be calculated following (Craig et al., 1963) via

$$D_{XS} = \delta D - 8 \times \delta^{18}O$$

D_{XS} records have been interpreted as a signal of the relative humidity and the temperature at the site of evaporation, and rapid changes in source conditions (e.g. Dansgaard et al., 1989; Johnsen et al., 1989) or changes in source region could be identified in Greenlandic cores, with deuterium excess changing within a few years at the Bølling-Allerød transition (Steffensen et al., 2008).
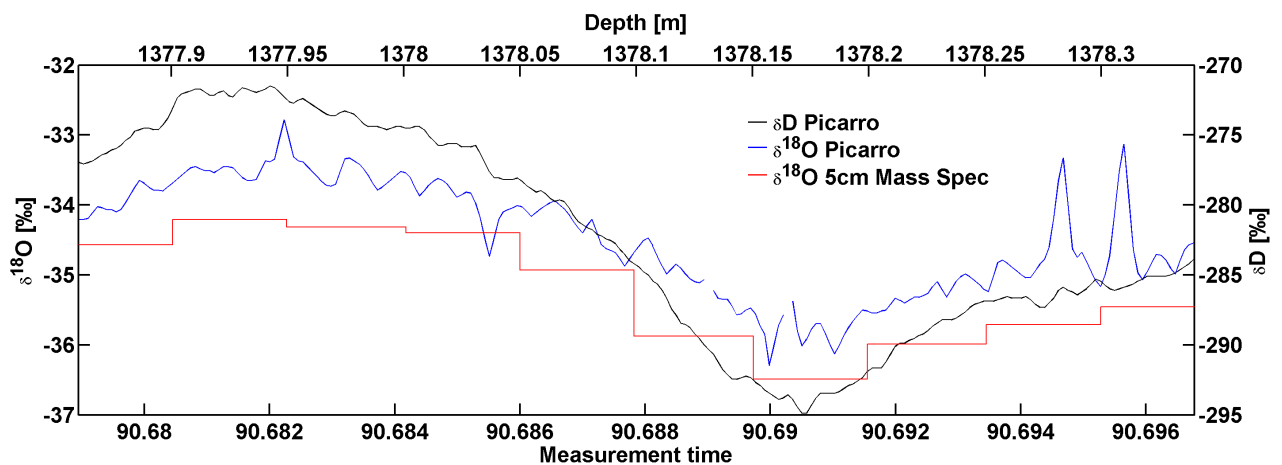
Figure 14: Raw data of the very first continuous water isotope record of a polar ice core

Detection Technique   Information on the ice matrix' isotopic composition is commonly obtained using isotope ratio mass spectrometry (IRMS). Traditionally, mass spectrometers cannot analyse a sample for both isotopic abundance ratios, due to differing sample preparation for the subsequent analysis of $\delta^{18}O$ (Epstein and Mayeda, 1953; Leuenberger and Huber, 2002) and δD (e.g. Vaughn et al., 1998; Huber and Leuenberger, 2003).

Even though Begley and Scrimgeour (1996) developed a method allowing for simultaneously measurements of $\delta^{18}O$ and δD, analysing a complete core in high resolution (i.e. discrete measurements in 2.5cm or 5cm intervals) remained time consuming.

Kerstel et al. (1999) were the first to show the functionality of laser spectroscopy to determine the abundance ratios directly on water vapour, making the time consuming and potentially error introducing sample handling redundant.

Continuous online field deployable high precision and high resolution water isotope analysis from ice cores

Vasileios Gkinis[1], Trevor J. Popp[1], Sigfus J. Johnsen[1], Thomas Blunier[1], Christopher Stowasser[1], Ernesto Kettner[1]

[1]Centre for Ice and Climate, Niels Bohr Institute, University of Copenhagen, Denmark

CENTRE FOR ICE AND CLIMATE

The high temporal resolution of ice cores is currently not fully exploited with the existing water isotope analysis methods.
The sampling of the core is done in a discrete mode resulting in loss of resolution and a very time consuming procedure for the analysis of the full ice core

Goals of this study
- ✓ Perform continuous water isotope analysis on an ice core
- ✓ Exploit the resolution of the core
- ✓ Field deployable system.
- ✓ Precision comperable or better to IRMS

We build an interface between a commercial CW-CRDS Infra Red Spectrometer and an ice core continuous melting system for Continuous Flow Analysis (CFA) of chemical impurities.

Boundaries
- ✓ Ability to adjust to the flow rates of the CFA system
- ✓ Deliver a continuous water vapour stream to the CRDS spectrometer at the nominal mixing ratio for optimum spectrometer performance
- ✓ 3 phase changes ice → liquid water → water vapour with zero fractionation in a continuous mode
- ✓ Semi - autonomous operation
- ✓ Minimize dead volume - Sample dispersion - Estimate Resolution

Technical Goal

From an initial liquid water stream of ≈ 0.1 ml/min we want to split off a fraction of ≈ 1 μl/min. The micro flow should then be vaporized with 100% efficiency and the produced water vapour mixed with dry air in a controlled manner so the final product is moist air with a stable humidity level of 20.000 ppm. The system has to be adjustable to different main flows and dry air flows.

Solution

We use a fused silica 40 μm capillary on a PEEK tee (T1 in fig. 1) to split off a micro flow from the main flow of ≈0.1ml/min. Flow through the capillary is kept stable via controlling the back pressure imposed by a restriction on the waste line downstream of T1. The microflow is injected in the evaporation chamber (T2) where temperature is finely controlled at 170 °C. Upon evaporation, the water vapour stream is mixed with dry air in the evaporation chamber and transferred to the optical cavity. The flow of the moist air is finely controlled by the spectrometer's proportional valves in a feedback loop.
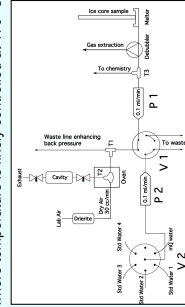
Figure 1

Allan variance test

We test the stability of the system by continuously injecting mQ Copenhagen water for a period of ≈16h. Injection takes place via the 6 port selection valve (V2 in figure 1). A 6 port injection valve (V1 in figure 1) switches the system between ice core sample line and standards - mQ water. This allows for periodic calibrations with local standard waters. System shows an optimum integration time at ≈ 5000 sec after which long term instrumental drifts are observed.
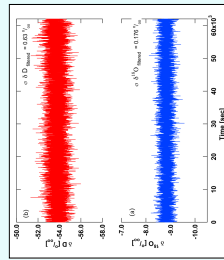
Figure 2

Figure 3

Water concentration:

We vary the flow rates on the peristaltic pump P2 and inject mQ water. The test reveals a dependency of the system on the water mixing ratio of the sample. We choose to perform all measurements around the linear response area of the 20 kppm.
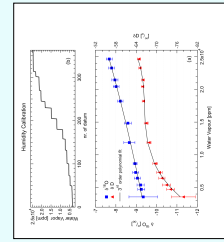
Figure 4

VSMOW calibration:

Local water standards are injected via the V2 valve. In that way we can periodically calibrate the system with respect to VSMOW. The calibration procedure takes ≈10 min per standard and consumes ≈2 ml of standard water. It can be automized via the use of electrically actuated valves and control software.
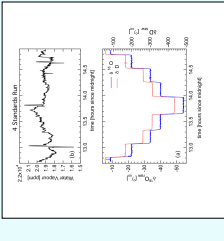
Figure 5

Sample dispersion - Memory Effects

Sample dispersion and memory effects can be characterized via the introduction of a an isotopic step. The measured signal is a smoothed sigmoid curve that we assume to be the convolution of a step function with a Gaussian smoothing filter. Use of spectral methods can give an estimate of the damping of signals with different frequencies. In this case δD periodic signals with $f \leq 0.02$ Hz are damped by ≈90% and are critically close to the noise level of the measurement (figure 7).
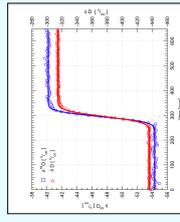
Figure 6
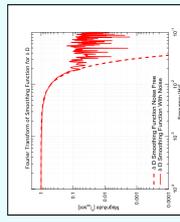
Figure 7

NGRIP melt runs:

Measurements of Holocene ice are presented in figure 8. Depth registration is done via the use of an optical encoder during the melting process. Results for $\delta^{18}O$ are compared to 5cm resolution IRMS measurements. In figure 9 we plot $\delta^{18}O$ vs δD. Results lie on the meteoric water line, an indication of an efficient evaporation step with zero fractionation.
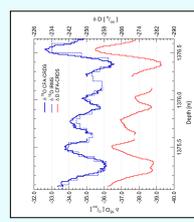
Figure 8
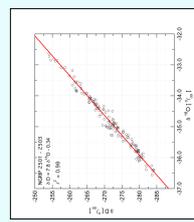
Figure 9

Figure 14 shows the very first simultaneously obtained δ^{18}O and δD records of an ice core section in hitherto unprecedented resolution using laser spectroscopy techniques, demonstrating the interface's functionality. Accuracy and precision were subsequently improved by developing a calibration procedure (Gkinis et al., 2010) and by deconvolution of the obtained time series during data evaluation Gkinis et al. (2011). Results from measurements of NGRIP and NEEM ice are presented on page 45.

After careful characterisation of the entire system, Gkinis et al. (2011; see also page 48) eventually report that the system's uncertainties lie below .1‰ for δ^{18}O and .5‰ for δD. These are values comparable to off-line IRMS and are a slight improvement with respect to Huber and Leuenberger (2005), who used a melthead for IRMS sample preparation and report accuracies of .1‰ and 1‰ for δ^{18}O and δD, respectively.

3.4.2 Methane Mixing Ratios

A proxy for the activity of terrestrial ecosystems   Atmospheric methane (CH_4) mixing ratios are sensitive to climatic changes as wetlands - the most prominent sources of atmospheric CH_4 - become more extensive and productive (Chappellaz et al., 1990, 1993). Over the last $800 ka$ CH_4 mixing ratios have varied between $350 ppbv$ during glacial periods and up to $800 ppbv$ during interglacials (Spahni et al., 2005; Loulergue et al., 2008).

Chappellaz et al. (1993) have shown the temperature over Greenland to by and large vary in phase with the atmospheric CH_4 concentration. However, Brook et al. (2000) find that the increase in atmospheric CH_4 is outpaced by the accompanying changes in the precipitation's isotopic composition - a result interpreted to 'reflect the time scale of terrestrial ecosystem response to rapid climate change'. In Antarctic ice cores, Delmotte et al. (2004) identified a systematic lag of CH_4 concentrations relative to atmospheric temperature changes, see also Severinghaus et al. (1998)

Due to its short atmospheric lifetime of 9 years (e.g. Brook et al., 2000), CH_4 records can show large concentration gradients not only interhemispherically, but also over short core sections. Although the interhemispheric gradient reveals information on the geographical distribution of CH_4 sources (Chappellaz et al., 1993; Brook et al., 2000), interhemispheric mixing still happens on time scales shorter than the atmospheric life time of CH_4 (Blunier and Brook, 2001; Fischer et al., 2008).

Even though seasonal signals of CH_4 are never preserved due to diffusion in the firn, the methane record is valuable for dating. Steep increases are used for synchronising different ice cores at depths when thinning prohibits accurate dating by layer counting. Indeed, in

the absence of resolvable annual layers CH_4 mixing ratios have frequently been used to establish relative time scales (e.g. Chappellaz et al., 1997; Blunier et al., 1998).

Schüpbach et al. (2011) point out that constraints on the accuracy of the relative time scales obtained are introduced by firnification processes differing from site to site (Fabre et al., 2000), especially when the accumulation rate is low (Landais et al., 2006). However, synchronisation via atmospheric composition down to the accuracy possible given these natural constraints, has not yet been achieved (Stowasser et al., 2012). The coarse resolution of the CH_4 records obtained from ice cores prohibits more accurate synchronisation, legitimising any effort to develop detection techniques that aim at fully exploiting the resolution with which the CH_4 concentration changes of the paleoatmosphere are preserved.
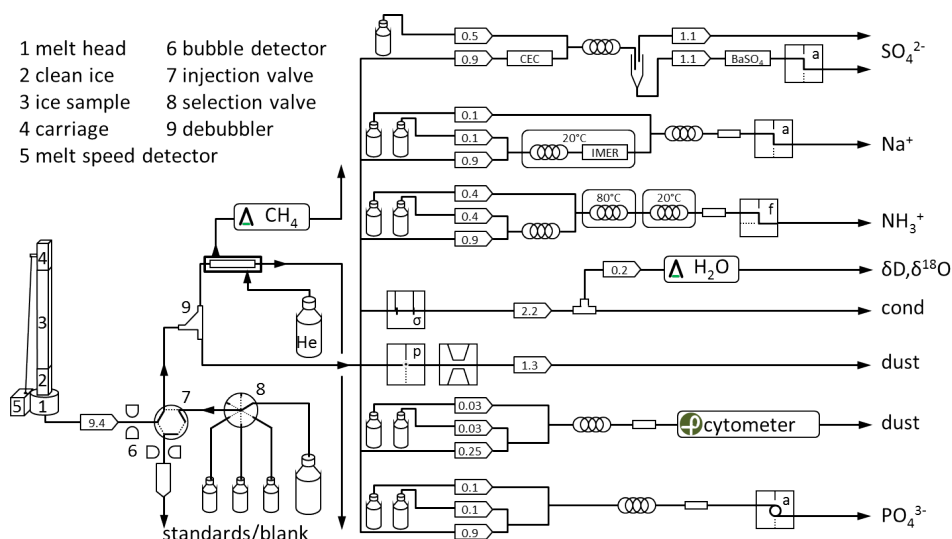
Figure 15: Flow scheme of the C CFA system as of September 2011

Detection Technique In order to obtain information on paleoclimatic mixing ratios, air has been extracted from discrete ice core samples and subsequently been injected into gas chromatograph (GC) over decades and in the vast majority of laboratories (e.g Chappellaz et al., 1990; Sowers et al., 1997; Flückiger et al., 2004). The preparation of discrete samples is time-consuming, especially, as Stowasser points out, when aiming for highly resolved records. Consequently, records spanning a complete core commonly have depth resolutions of one sample per 2m interval; only in exceptional cases were these intervals reduced to the order of centimetres (Stowasser, 2013).

The first attempt to improve the resolution of paleoclimatic CH_4 mixing ratios with continuous sample preparation using a melthead was undertaken by Schüpbach et al. (2009).

Continuous field-deployable methane concentration measurements from ice cores with near-infrared cavity ring-down spectroscopy

Christopher Stowasser, Thomas Blunier, Vasileios Gkinis, Trevor J. Popp, Ernesto Kettner, Paul Vallelonga, and David M. Balslev-Clausen

Centre for Ice and Climate, Niels Bohr Institute, University of Copenhagen, Denmark

European Geosciences Union
General Assembly 2010
Vienna, Austria, 02 -07 May 2010

ICE AND CLIMATE — CENTRE FOR

Introduction

One of the most important features of ice cores as climate and atmospheric paleoarchives is their potential for high temporal resolution. The measurement of chemical impurities in ice cores that fully exploits this high resolution has become standard with the advent of Continuous Flow Analysis (CFA) often performed in the field.

Meanwhile, the measurement of atmospheric trace gas composition continues, for the most part, to be performed offline via discrete sampling by means of traditional mass spectroscopy and gas chromatography. These offline procedures are time consuming, expensive, and often come at the expense of fully exploiting the temporal resolution available in the ice core.

Here we describe a new method and the first results for methane (CH_4) concentrations measured continuously via a near-infrared cavity ring-down spectrometer (Picarro Inc., http://www.picarro.com/) coupled to a CFA system. The system has been tested with a deployment to the North Greenland Eemian Ice Drilling (NEEM) camp coupled to the University of Bern CFA system and in the laboratory with the NGRIP ice coupled to the University of Copenhagen CFA system.

The system yields CH_4 concentration measurements of unprecedented temporal resolution and a precision comparable to discrete methods.

Theory of measurement

The near-infrared cavity ring-down spectrometer (NIR-CRD spectrometer) determines concentrations of CH_4 in its sample cavity by measurements of cavity ring-down time (CRD time).

Cavity ring down time:
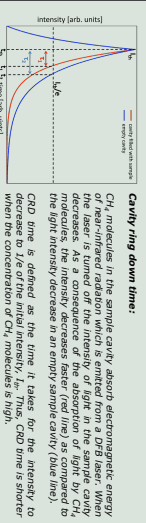
CH_4 molecules in the sample cavity absorb electromagnetic energy of near-infrared radiation which is emitted from a DFB laser. When the laser is turned off the intensity of light in the sample cavity decreases. As a consequence of the absorption of light by CH_4 molecules, the intensity decreases faster (red line) as compared to the light intensity decrease in an empty sample cavity (blue line).

CRD time is defined as the time it takes for the intensity to decrease to $1/e$ of the initial intensity, I_{in}. Thus, CRD time is shorter when the concentration of CH_4 molecules is high.

The spectrometer:

Near-infrared radiation (wavenumber of ca. 6057 cm^{-1}) is injected in a 3-mirror high-finesse ring cavity. A photo detector measures the intensity which is transmitted through one of the mirrors. To measure CRD time the laser is turned off and the intensity decays exponentially. A typical empty-cavity CRD time is 40 μs.

The sample gas is filtered and injected into the cavity where CH_4 molecules interact with the near-infrared radiation. Pressure and temperature in the cavity are kept constant.

Specifications:

Precision: < 0.5 ppbv (1σ)
Drift over 24 hours: < 1 ppbv
Frequency of measurement: 0.8 Hz
Sensitivity : $1.6 \cdot 10^{-11} cm^{-1}/Hz^{1/2}$
(noise absorption equivalent)
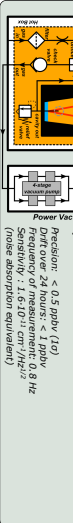
The 2009 NEEM field season

In order to test the performance of the system for continuous measurements of CH_4 concentrations under field conditions, it was deployed to the NEEM camp for the first time in spring 2009.

Here, the system was connected to the University of Bern CFA system and ice cores were melted continuously at a rate of 3.5 cm/min. Gases, trapped in bubbles in the ice, are continuously extracted and measured by the NIR-CRD spectrometer.

University of Bern Continuous Flow Analysis System

The main dome of the NEEM camp.
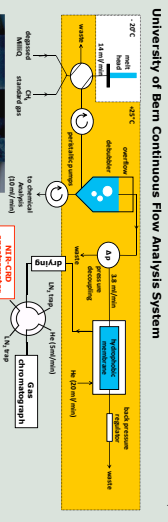
Air bubbles are separated from the melt water stream by means of a debubbler and a hydrophobic membrane. Helium is used as a purge gas and flushes the extracted gases away from the membrane.

The dried mixture of helium and past atmospheric air is sent into the near-infrared cavity ring-down spectrometer (NIR-CRD spectrometer) for measurements of CH_4 concentration.

Ice on the melt head.

Supportive measurements of total air content via an oxygen sensor

The dilution of sample gas with helium during the extraction process makes measurements of total air content necessary. For this purpose an oxygen sensor (Ocean Optics Inc., http://www.oceanoptics.com) is installed in the gas stream of the NIR-CRD spectrometer. The atmospheric concentration of oxygen is assumed to be constant over time and total air content of the sample/helium mixture can be determined.

The oxygen sensor:

A fluorophore at the tip of the probe of the oxygen sensor (150 mm length, 1.6 mm OD) is excited by a LED light source. The degree of fluorescence quenching by oxygen molecules is related to the partial pressure of oxygen in the gas stream and measured by a spectrometer.

Specifications:

Accuracy: 5% of reading
Precision: 0.05 mbar
Frequency of measurement: 1 Hz

Results from the 2009 NEEM field season

Past atmospheric concentrations of CH_4 were measured along 12.1 m of ice from the early Holocene period.

Temporal resolution: 2 cm
Precision: ±25 ppbv (dry measurements)
Accuracy: Problems with the calibration of the oxygen sensor caused the results to be inaccurate.

Precision and accuracy of the method have been improved for the coming field season based on experiences from the measurements during the 2009 NEEM field season.

interruptions of the sample stream

humid sample
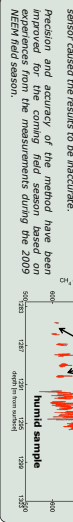
The 2010 NEEM field season

During the 2010 NEEM field season the system for continuous measurements of CH_4 concentration is scheduled to measure hundreds of meters of ice from the last glacial period.

An improved version of the 2009 system has been tested by measuring glacial ice from the NGRIP core in the laboratory. Both precision and accuracy of the method could be improved and compared to the results from the 2009 field season.

The new gas extraction system

The underground science trench of the NEEM camp.

Hydrophobic membrane module:

Residual water is removed from the sample stream by sending the air/water mixture through a bundle of hydrophobic membrane tubes which is sealed to the ambient atmosphere. Air which diffuses through the membrane is immediately sucked away by the vacuum pump of the NIR-CRD spectrometer.

This extraction technique makes dilution of the sample with helium obsolete. Thus, the supportive measurement of total air content for the determination of CH_4 concentration can be omitted.

The underground science trench of the NEEM camp.

Spectroscopic measurements of gases, stable water isotopes and dust during the 2010 NEEM field season

The field lab:

Six laser-based spectrometers are utilized during the 2010 field season (5 x Centre for Ice and Climate, 1 x LGGE)

They are installed in a laboratory cell in the underground science trench of the NEEM camp.

1) Discrete measurements of stable water isotopes (CRDS, CIC)
2) Continuous measurements of CH_4 concentration (CRDS, CIC)
3) Continuous measurements of CH_4 and N_2O concentration (CEAS*, LGGE)
4) Continuous measurements of dust (single particle counter, CIC)
5) Continuous measurements of stable water isotopes (CRDS, CIC)
6) Discrete measurements of N_2O concentration and stable isotopes (CRDS, CIC)

*CEAS: Cavity-enhanced absorption spectroscopy.

The system for trace gas concentration measurements:
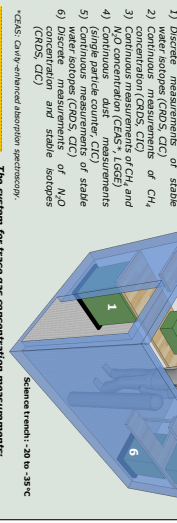
Both CEA and CRD spectrometer measure a continuous stream of 1.5 ml/min of pure atmospheric air. Pressure is controlled by electronically controlled PID valves.

A 6-port valve distributes sample between the CRD spectrometer for discrete measurements of N_2O isotopes (incl. a pre-concentration system) and a gas chromatograph from the University of Bern.

A two meter long nafion membrane dryer in combination with a dry purge gas dries the humid sample after the gas extraction system.

Continuous debubbler overflow & melt water stream from the CFA laboratory

Science trench: -20 to -35°C

Warm lab: +20°C

CRDS cavity CH4/N2O
CRDS cavity CH4
CRDS N2O isotopes
Gas chromatograph CH4

Centre for Ice and Climate
Juliane Maries Vej 30
DK-2100 Copenhagen Ø., Denmark

stowasser@nbi.ku.dk
blunier@nbi.ku.dk
v.gkinis@nbi.ku.dk

trevor@nbi.ku.dk
e.kettner@nbi.ku.dk
pravis@nbi.ku.dk

dbc@nbi.ku.dk

Connecting a GC to the B CFA system, they were able to obtain a semi-continuous record with at least one measurement per 15cm. However, the precision could correspond to an uncertainty of as much as 20ppbv during interglacials, inferior to state-of-the-art reproducibility of 3ppbv (Mitchell et al., 2011).

Apart from being semi-continuous only - GC measurements are performed on a sample stream integrated over a certain period of time - the method developed by (Schüpbach et al., 2009) is also destructive, precluding subsequent analysis for other trace gases. Güllük et al. (1997) developed 'a high-frequency modulated tunable diode laser absorption spectrometer for measurements of CO_2 , CH_4 ,N_2O, and CO in air samples of a few cm^3', that potentially solved both these issues, allowing for non-destructive, continuous measurements.

Combining the advantages of laser spectroscopy and employing a melthead for sample preparation, Stowasser et al. (2012) have demonstrated that truly continuous CH_4 records can be obtained. To integrate the CRDS into the C CFA, the initial flow scheme, shown on page 40, had to be altered. The new flow scheme depicted in figure 15 featured an extra pump tube between the melthead and the debubbler to ensure reliable extraction. This was found to compromise resolution of the aerosol records as a result of the increased mixing volume only slightly.

As Picarro's CO_2|CH_4|H_2O analyser was designed for measuring atmospheric samples, its volume was not optimised for the small amounts of air extractable from a CFA system. In order to flush the cavity in a reasonable amount of time (i.e. to improve the depth resolution of the detection line), this was remedied for the initial proof-of-concept by flushing the degassing unit with helium (He) and correcting the detected mixing ratios based on the oxygen content of the gas mixture injected into the analyser (see page 51). Eventually, (Stowasser et al., 2012) further improved the system by reducing the cavity's volume, thereby rendering the He flow redundant.

Using the 'Center for Ice and Climate firn air model' (Buizert et al., 2012), Stowasser et al. show that a their depth resolution is sufficient to take full advantage of the record's preserved temporal resolution down to about $70ka\ b2k$. First results of the re-designed system are shown on page 45. This led to a temporal resolution of $100sec$, corresponding to a depth resolution of $2.5cm$ at the C CFA's standard melt rate, and $5.3cm$ when connected to the B CFA system with a melt rate of $3.2^{cm}/_{min}$. The instruments reproducibility at $\pm$ $8ppb$ is close to what is currently possible using GCs (Mitchell et al., 2011; Baumgartner et al., 2012).

Part II
Aeolian Dust

Chapter 4

Insoluble Aerosols

Introduction   *Aeolian dust can alter the planet's radiative balance directly via absorption and scattering of incoming or outgoing radiation and indirectly by being the locus for cloud condensation or ice formation. Additionally can the nutrients mineral dust bears or consists of interact the global biogeochemical cycles, most prominently via iron fertilisation of marine or phosphate fertilisation of terrestrial ecosystems.*

Particles that are available for long-range transport ouside the planetary boundary layer rarely show modes smaller than 5μm. Coarser particle's are usually dry deposited within 30km from their source areas. Depending on their size and source area, the grains' physical and chemical characteristics will vary, rendering the dust-climate interaction difficult to quantify, but allowing for source identification. Sources at present are Asian deserts and possibly the Sahara for Greenland, and arid areas in South America and Australia for Antarctica. During the last glacial maximum (LGM) only Asian and South American inputs could be identified in ice cores. Concentrations in melted samples of glacial ice reflect the increased atmospheric dust load and vary in anti-phase with the $\delta^{18}O$ record.

4.1 The mineral Aerosol

Technically, as Prospero et al. (1983) points out, the term 'aerosol' applies to both, the suspension of liquids and the solid particles in a gas. However, in the scientific literature on aeolian dust, 'aerosol' is generally used to refer to solid particles alone. Pye (1987) lists the various sources of solids suspended in the atmospherere, being cosmogenic, volcanic, marine, terrestial or biogenic in nature. All of which contribute to the aerosol load deposited at high latitudes, see e.g. Winckler and Fischer (2006), Abbott and Davies (2012), Wolff et al. (2006) or Miteva et al. (2009).

Terrestrial, mineral aerosols are commonly classified according to their size and classified in a three-fold typology. The exact limits vary to some extend (see e.g. Pye, 1987). Table 1 shows the classification referred to hereafter is as used in the review by Muhs (2013) and will be used hereafter.

class	size		
clay		d <	$2.5\mu m$
silt	$2.5\mu m$	< d <	$50\mu m$
sand	$50\mu m$	< d <	$2mm$

Table 1: Classification of mineral aerosols (Muhs, 2013)

4.1.1 Climatic Impact

Air-born mineral dust interacts with climate in various ways. It can alter the planet's radiative balance directly and indirectly and affect the global biogeochemical cycles. The direct radiative effect refers to the dust's ability interact with the incoming solar radiation or the outgoing terrestrial long-wave radiation Tegen (e.g. 2003). Dust grains can also indirectly affect the radiative properties of the atmosphere by acting as cloud condensation nuclei (CNN, e.g. Kumar et al., 2011) or ice nuclei (IN) (IN, e.g. Toon, 2003) and alter the planet's albedo. Geochemical cycles are indirectly affected by the external supply of potentially limiting nutrients to marine (e.g. Boyd and Ellwood, 2010) and terrestrial (e.g. Okin et al., 2008) ecosystems, thereby enhancing primary productivity.

Radiative effects Air-borne minerals can affect the atmospheric directly by absorbing or scattering of incoming or outgoing electromagnetic radiation (e.g. Claquin et al., 1998). Absorption of solar energy will lead to a warming of the atmosphere and a cooling of the underlying surface (Haywood and Boucher, 2000), while scattering of incoming radiation will lead to a cooling due to a decreased downward radiance (Shine and de Forster, 1999)

However, in its last report, the International Panel on Climate Change (IPCC, 2007) pointed to the high uncertainty in the net radiative effect of the dust's absorption and scattering on the atmosphere's energy balance, both in sign and magnitude. The uncertainty in the models stems from the unsatisfactory parametrisation of dust in models regarding its physical properties (Claquin et al., 2003; Balkanski et al., 2007; see also section 4.1.3) and its morphology (Maher et al., 2010).

There are various indirect effects on the radiative balance due to interaction with hydrological cycle. Most prominent among the dust-cloud interactions is the 'Twomey effect' (Twomey, 1977). By acting as CCN, the mineral dust effectively increases the planetary albedo (e.g. Kumar et al., 2011).

Gibson et al. (2006) have shown that water condensates particularly well on air-borne calcite, suggesting that the Twomey effect is a function of the dust's carbonate fraction. However, as Scheuvens and Kandler (2014) point out, mineral dust is quickly coated with

soluble aerosols (e.g. sulphate or nitrate), which changes their hygroscopicity, i.e. their potential as CNN. This coating, on the other hand, restricts particulate matter from acting as IN (Niedermeier et al., 2011; Tobo et al., 2012), which uncoated mineral dust particles do readily (Sassen et al., 2003; Zimmermann et al., 2008).

Overall, the Twomey effect has a cooling effect due to a global albedo enhancement with the amount of energy of reflected short-wave radiation exceeds that of trapped thermal radiance (Lohmann and Feichter, 2005).

Biogeochemical cycles In large parts of the ocean the primary productivity (i.e. the photosynthetic activity) is limited by the nutrients nitrate and phosphate (Mahowald et al., 2005). However, at least 25% of the ocean are so-called *high nutrient low chlorophyll* (HNLC) regions, where despite the sufficient supply of nitrate and phosphate little photosynthesis takes place (Boyd and Ellwood, 2010).

The 'iron hypothesis' (Martin, 1990) claims, that in HNLC regions the primary productivity was iron-limited. Indeed, Boyd et al. (2007) conducted field experiments and have shown that iron fertilisation can stimulate phytoplankton growth.

Since iron supply to the oceans by fluvial systems is limited to coastal areas unless rivers discharge beyond the shelf, iron provided by aeolian dust deposition (Jickells et al., 2005). Thus, by supplying iron to HNLC regions in non-coastal areas, mineral dust can affect the carbon cycle (i.e. atmospheric CO_2) and thus climate. It is argued that during the LGM (and previous glacial maxima) the oceanic iron content was responsible for up to 25% of the CO_2 decrease (Sigman and Boyle, 2000).

As Mahowald et al. (2008) points out, are humans preferentially supply ecosystems with nitrogen, ecosystems may shift from being nitrogen-limited to trace elements or phosphorus. The latter is believed to limit marine ecosystems on geological time scale (Falkowski et al., 1998), but Okin et al. (2004) points out that also 'very old landscapes', with the Amazon as prominent example, are limited in their productivity by the phosphate abundance in their soils (see also section 3.3).

Phosphate, however lacks a solid phase (Filippelli, 2008), and atmospheric transport is possible only when adhering to dust. Cinsequently, as it is the case for the provision of HNLC with iron, dust deposition can increase the ecosystem's productivity by supplying it with the limiting nutrient.

4.1.2 Entrainment and Transport

For a particle to be ejected from the bed, the drag and lift caused by the air flow around the particle must - at the moment of entrainment - be larger than the combined forces of that particle's weight, the bed friction and interparticle cohesion (see Pye, 1987, p.30). This means that any conditions decreasing the former by increasing the surface's roughness - such as snow or vegetarian cover, or decreasing the latter - such as moisture or particle surface charge will decrease source productivity (e.g. Mahowald et al., 2005; Washington et al., 2006).

Once entrained, particles are moved by either 'surface creep', 'saltation' or in suspension (Pye, 1987, p.43). The former refers to rolling and sliding across the surface, whereas saltation is a 'bouncing' movement (see figure 16). In which mode of transportation a particle engages, is a function of its settling velocity $U_f = \frac{\rho_p g}{18\mu}D^2$ (Pye, 1987, p.45), with μ the air's viscosity, ρ_p the particle's density and D its diameter.
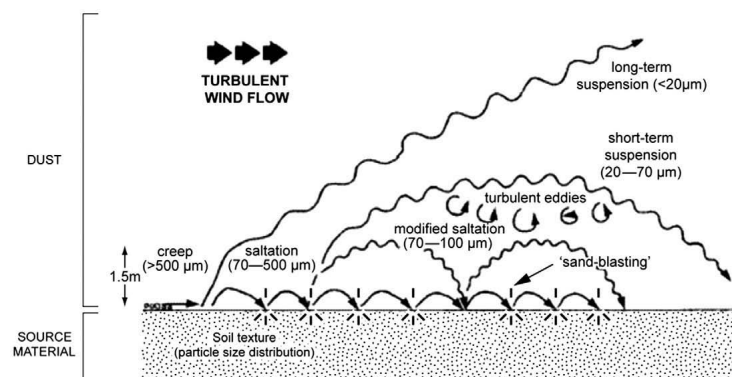
Figure 16: Dust deflation and entrainment processes
(after Pye (1987), taken from Maher et al. (2010))

The air flow needed around a particle for it to be directly entrained (i.e. by the wind alone) is a function of particle size (e.g. Mahowald et al., 2005). Bagnold (1960) found that, in order to entrain fine powders, very high threshold velocities were needed to overcome the interparticle cohesion. However, if impacted by saltating particles (i.e. subjected to 'sandblasting') the fine powder was easily injected into the air flow. Bagnold (1941, cited by Mahowald et al., 2005) , had reported earlier that the threshold velocity also increases with grain size, leaving particles of 60-80μm the easiest to lift off (Mahowald et al., 2005). The horizontal saltation flux is proportional to the wind speed's third power (Gillette, 1974).

Due to their relatively large settling velocity, particles with diameters greater than $20 \mu m$ can only be in short-term suspension (Maher et al., 2010; Muhs, 2013; Pye, 1987, p.125) and are rarely transported further than $30 km$ from their source. Particles smaller than $10 \mu m$ can stay in long-term suspension (Gillette, 1978) and can, once lifted above the planetary boundary layer into the free troposphere, be transported thousands of kilometers (see e.g. Prospero, 1999; Mahowald et al., 2005). The occurrence of meteorological events entraining significant amounts of dust is strongly episodic (Knippertz, 2014) and a few events are responsible for entire annual flux (Rea, 1994).

4.1.3 Physical and Chemical Characteristics

Aeolian dust consist primarily of silicates and carbonates. While the former are dominated by quartz (SiO_2) and feldspar, the majority of latter are calcite ($CaCO_3$) and dolomite ($CaMg(CO)_3$) (Muhs, 2013; Scheuvens and Kandler, 2014). It should be noted, however, that dust detected in ice cores is of the aeolian load's clay-sized fraction (Steffensen, 1997; Lambert et al., 2008). The minerals in this size range are mainly illite, kaolinite and chlorite.

Depending on its mineralogical composition (i.e. its source), a dust plume will have varying optical properties (Tegen, 2003). The inaccurate approximation of especially the refractive index' imaginary part (accounting for the particles' absorption) has been found to yield large uncertainties when estimating the direct radiative effect (Claquin et al., 1998). This has lead to extensive compilation of the optical properties of fine silt and clay-sized minerals (Sokolik and Toon, 1999; Balkanski et al., 2007).

Next to the particulate matter's optical properties will its size (and shape) influence its radiative forcing (Maher et al., 2010). Most of the long-term suspended material is smaller than about $20 \mu m$ (e.g. Mahowald et al., 2006; Pye, 1987, p.125). Whereas in the first days of transport size fractionation can be observed downwind, this is not the case any more after about $1000 km$ of transport (Scheuvens and Kandler, 2014). Particles are now log-normally distributed around a modal diameter of 2-3.5μm (e.g Mahowald et al., 2006; Maher et al., 2010) and only marginal further decrease can be detected.

Opposed to the real and imaginary part of the refractive index, where differentiation has been strived for since the turn of the century (e.g. Sokolik and Toon, 1999), when attributing a mass to an observed volume distribution, homogeneity is still assumed between the average density of crustal material reported by Sugimae (1984) of 2.6 $g\ cm^{-3}$ and 2.5 $g\ cm^{-3}$ (Ruth et al., 2008).

4.2 Dust in Ice Cores

The paleoatmospheric dustload is archived in a varity of different archives. These include (1) loess deposits; (2) lake sediments; (3) soils; (4) deep-ocean basins and (5) ice sheets and smaller glaciers (Muhs, 2013). In ice core science mineral dust particles are particularly intriguing impurities. Insoluble aerosols are a non-reactive and non-volatile species which does not undergo post-depositional processes, but in addition to mere concentration changes indicating annual layers (e.g. Andersen et al., 2006; Svensson et al., 2008) caused by deposition maxima during spring|summer time (Steffensen, 1988; Whitlow et al., 1992), they can also reveal information about paleoatmospheric transport patterns (Muhs, 2013).

4.2.1 Variations with Climate

As can be seen from figures 17 and 18 paleodust records show very distinct features on glacial-interglacial time scales. Petit et al. (1981) and Steffensen (1997) have reported an increased mineral dust load over the polar ice caps and Kohfeld and Harrison (2001) estimated global dust fluxes during glacials to have been two to five times larger than at present day. The proposed mechanisms behind this, summarised in Muhs (2013), are based on data from (Kohfeld and Harrison, 2001) and modelling results by Mahowald et al. (1999; 2011; see also figure 17).

(a) Contemporary global dust fluxes   **(b)** Global dust fluxes during the LGM

	<1	1-2	2-5	5-10	10-20	20-50	50-100	100-200
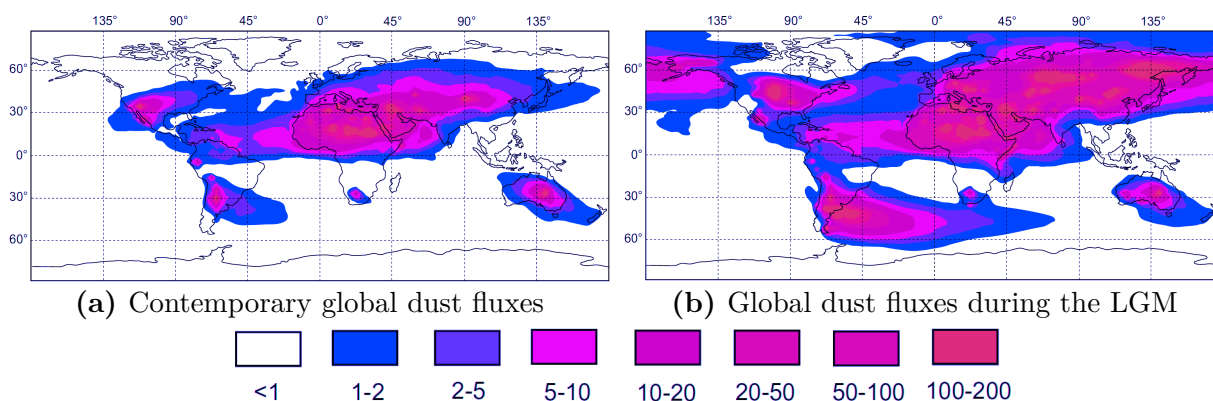
Figure 17: Global dust fluxes during the LGM and at present $[g/m^2/yr]$ (modelled by Mahowald et al. (2006), modified from Muhs (2013))

Generally speaking, conditions changed such that entrainment was facilitated (see section 4.1.2) by (1) increased wind speeds, (2) decreased soil moisture, (3) decreased vegetation cover and (4) additional source areas due to exposed continental shelves. Further was (5) the particles' atmospheric lifetime prolonged by a decreased intensity in the hydrolog-

ical cycle, leading to less wet deposition (see infra), during which air-born dust could be transported further due to (1).

Muhs (2013) stresses that the increase in aeolian dust load is thus a combination of climatic (i.e. altered wind speed and hydrological cycle), and geologic (i.e. increase in source regions) factors. Models prior to Mahowald et al. (2006), whose results are presented in figure 17 have not sufficiently accounted for the latter, the glaciogenic sources due to advancing ice sheets and glaciers, and consequently not been able to capture the increase of the aeolian dust load over the polar ice sheets (see figure 18).

(a) Concentration and isotope record from Vallelonga and Svensson (2014)

(b) Dust size distributions taken from (Ruth et al., 2003)
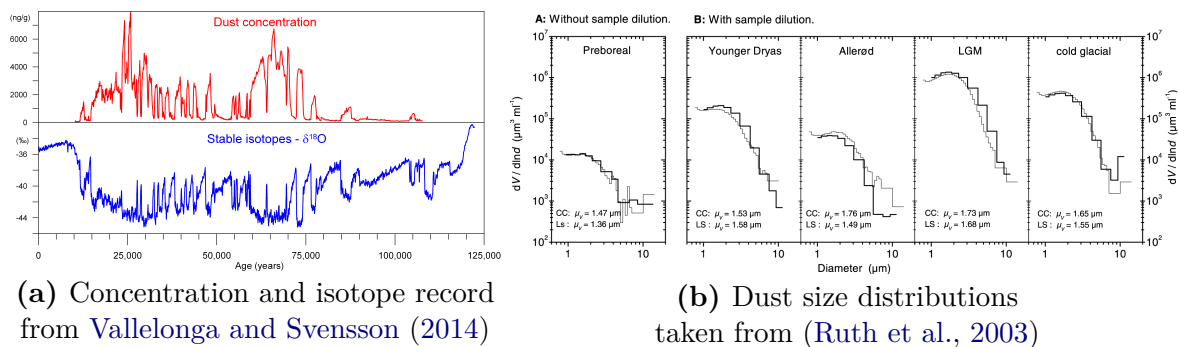
Figure 18: NGRIP dust (Ruth et al., 2003) and δ^{18}O records (NGRIP members, 2004)

Figure 18 shows the dust's variations with climate as recorded in Greenlandic ice cores. In figure 18a the anticorrelation of 'dustiness' (Ruth et al., 2003) and δ^{18}O (NGRIP members, 2004) of the precipitation isotopes - a measure of paleotemperature, see section 3.4.1 - is illustrated by the example of the NGRIP core.

Glacial dust concentrations in Greenlandic cores are by two orders of magnitude larger than Holocene (e.g. Steffensen, 1997), and differ by a factor of 5 to 18 across Dansgaard-Oeschger events (Ruth et al., 2003). However, it has to be noted that, depending on the proxy invoked for dust load approximation (see chapter 5), the detected concentrations cab vary by a factor of two (Ruth et al., 2008). Indeed, the Ca^{2+} content has been reported to only decrease by a factor of 80 across the last termination (Fuhrer et al., 1999; Fischer et al., 2007)

Comparing the grain size frequency histograms of samples from different climatic periods (figure 18b) it becomes apparent that the mode of a lognormal distribution fitted to represent the observed distribution is larger during colder climates while the sigma of that distribution decreases (e.g. Steffensen, 1997; Ruth et al., 2003).

4.2.2 Provenance Studies

To fully exploit the information contained by paleodust deposition sites, i.e. to constrain the possible past atmospheric circulation patterns (Rea, 1994; Muhs, 2013), the source areas of the archived minerals needs to be identified. Dust provenance studies are carried on bulk samples or individual grains to determine their mineralogical and isotopical (Biscaye et al.; 1997; Bory et al.; 2002)or elemental (Banta et al., 2008) composition. By comparing these findings with results on dust collected in potential source areas (PSA), likely sources of the dust deposits can be appointed.

(a) Kaolinite to chlorite ratios for PSAs of dust deposited on Greenland taken from Bory et al. (2002)

(b) Isotopical characterisation of PSAs and snow pit samples taken from Bory et al. (2003)
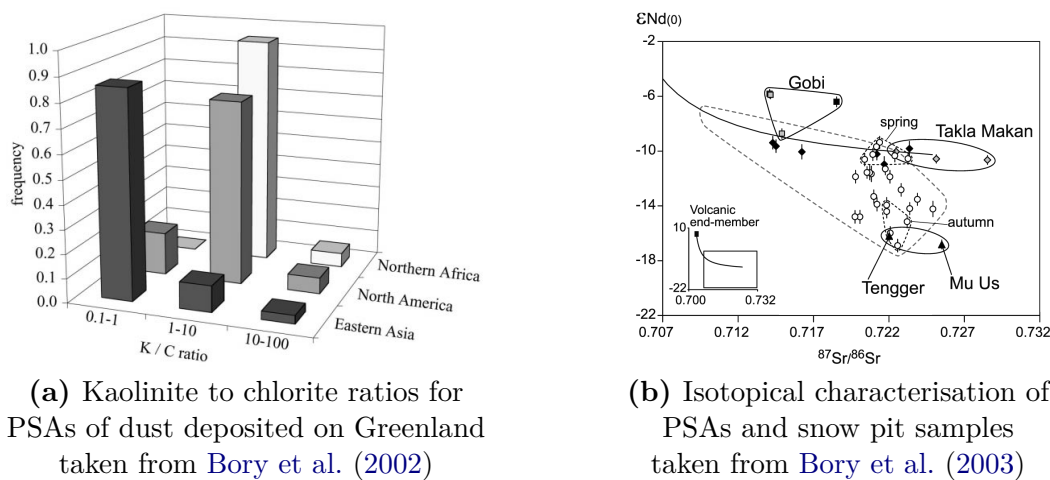
Figure 19: Minerology and isotopic fingerprint of PSAs for Greenland dust

As clay-sized particles are - by definition - of the same size range, little segregation of the major minerals illite, kaolinite and chlorite can be expected (Formenti et al., 2011). Their ratios remain correlated to the parent's material composition during entrainment and removal processes and are thus characteristic the source area (Schütz and Sebert, 1987). In figure 19a a compilation of kaolinite to chlorite ratios of PSAs for dust deposited on the Greenlandic ice sheet are presented. Generally speaking, Asian samples are characterised by low kaolinite abundance, but, as Scheuvens and Kandler (2014) point out, there is a certain degree of overlap between different PSAs and source identification cannot be based on clay-mineral ratios alone.

Additionally, bulk samples are often analysed for their isotopic composition (e.g. Grousset et al., 1992; Grousset and Biscaye, 2005). Especially the neodymium ($\frac{^{143}Nd}{^{144}Nd}$) and strontium ($\frac{^{87}Sr}{^{86}Sr}$) isotope ratios have been found characteristic for PSAs, (e.g. Grousset and Biscaye,2005, see also figure 19b).

As variations in $\frac{^{143}\text{Nd}}{^{144}\text{Nd}}$ are very small the ϵ-notation has been introduced. Similar to the δ-notation used to report isotopic values of precipitation (see section 3.4.1), the ϵ-notation describes the relative deviation with respect to a standard, in this case the Chondritic Uniform Reservoir (CHUR). Scheuvens and Kandler (2014) hasten to qualify that interregional variation in isotopic ratios can be larger than inter-source variability, rendering also the isotopic analysis' practicality merely supplementary.

Finally, the elemental ratios of rare earth and other trace elements can to some extend be used for source fingerprinting (e.g. Banta et al., 2008). However, Svensson et al. (2000) find only little variance in the elemental composition of 12 glacial samples despite variations in mineralogy. That many major elements cannot be used is also supported by Scheuvens and Kandler (2014), they see however, some potential for source characterisation in the potassium, manganese and titanium levels relative to Al, which is uniformly distributed in the earth's crust (Bowen, 1979). (Scheuvens et al., 2013) has demonstrated the benefit of the ratio $\frac{Ca+Mg}{Fe}$ for discrimination of African sources.

Provenance Greenlandic dust Several provenance studies on bulk samples of dust deposited on the Greenlandic ice sheet have been conducted (e.g. Svensson et al., 2000; Bory et al., 2002). In the first study carried out by Biscaye et al. (1997), it was found that Eastern Asia was the most likely source for dust deposited in the period 23-26ka b2k. It is important to note one exception (see chapter 8), when during an interstadial with relatively low concentrations the dusts composition resembled slightly more southern PSA samples.

Recently, the hypothesis of a sole Asian source was challenged by Muhs (2013), who criticises the few PSA samples used by Biscaye et al. and, invoking Mahowald et al. (2006), contests that '[i]t certainly seems possible that sources other than Asia could have provided dust to Greenland or at least that multiple sources are involved'.

However, the findings by Biscaye et al. were confirmed by Svensson et al. (2000), whose complete set of samples turnt out to be very homogeneous and of Asian provenance. Bory et al. (2002; 2003) were able to show that Asian provenance extends to the resent day and to identify the Takla Makan as the dominant source responsible for the spring time maxima. As dominant source of dust deposited in autumn, however, he suggested either the Tengger or the Mu Us figures 19 and 59.

Figure 20 shows modelled provenance studies by Mahowald et al. (2011). For the LGM the model - in remarkable accordance with Biscaye et al. (1997) and Svensson et al. (2000) - predicts East Asia to be virtually the only source for GISP2 and GRIP, where Biscaye

Present   **LGM**

(a) Fraction from North America ↑

(b) Fraction from East Asia ↑

(c) Fraction from North Africa ↑

(d) Fractions from 'other' sources (LGM) and Europe (present)
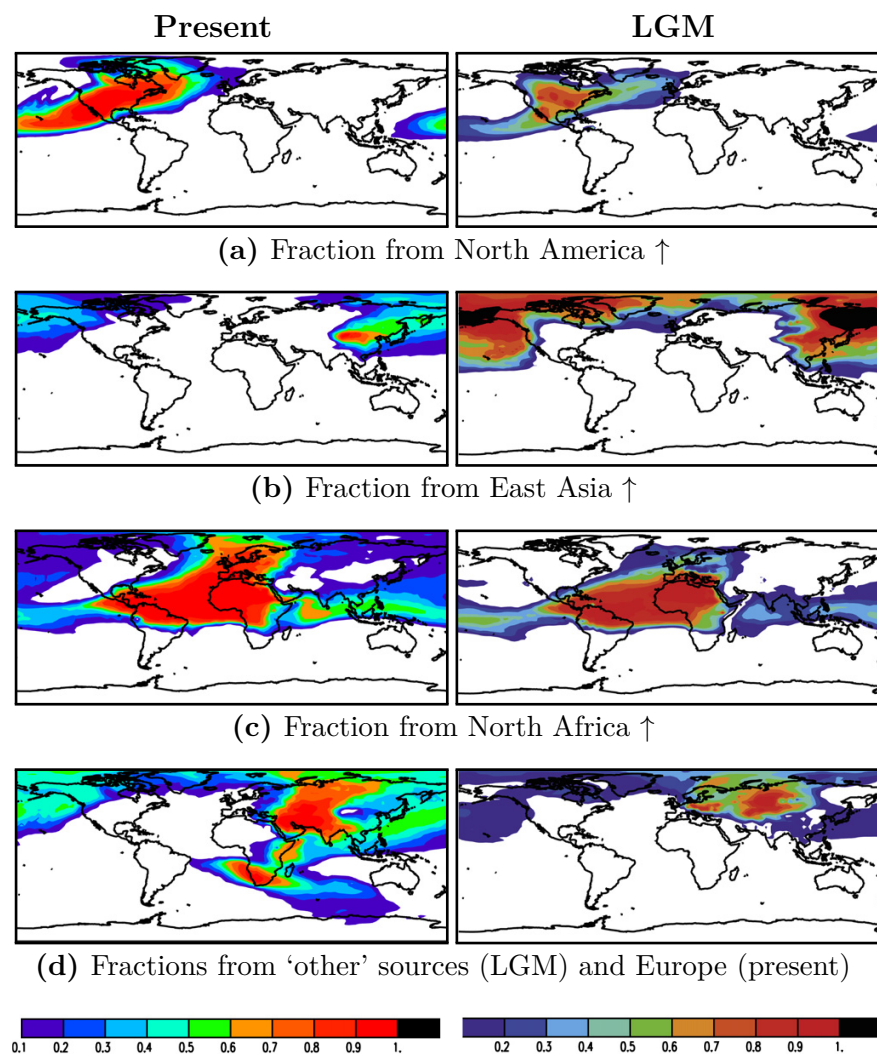
Figure 20: Dust provenance in Greenland at present and during LGM, modified, from Mahowald et al. (2011)

et al. and Svensson et al. carried out their studies. In the present day run, however, the model would assume a second source in North Africa (figure 20c), rather than in East Asia, as the data published by Bory et al. (2003; also figure 19b) suggests.

The claim by Bory et al. (2003) is backed by an analysis of modelled back trajectories evaluated by Kahl et al. (1997), who find basically no ten-day back trajectory staring in North Africa ending up at Summit. Mosher et al. (1993) and VanCuren et al. (2012), however, were able to detect aerosols at Dye 3 and Summit, respectively, and also an isotopic study conducted by Lupker et al. (2010) has identified Northern Africa as a second potential source next to Takla Makan, Gobi or the Ordos plateau in Asia.

Antarctic sources Grousset et al. (1992) were the first to conduct isotopic analysis on Antarctic dust bulk samples and identified Patagonia to be major source for dust at Dome C during the LGM. This result was found to be true also at Vostok and Talos Dome, as well as for previous glaciations (Basile et al., 1997; Delmonte et al., 2004a, 2010). However, evaluating the last eight glacial cycles in the EDC core (EPICA members, 2004), Delmonte et al. (2008a) found a slightly reduced Patagonian contribution in ancient glaciations.

(a) Fraction from South America ↑

(b) Fraction from Australia ↑

Figure 21: Dust deposition in Antarctica for present and LGM climate
as presented by Mahowald et al. (2011)

As is apparent from figure 21a, (Mahowald et al., 2011) convincingly reproduce the South American provenance of dust in Antarctica during LGM. During interglacials, Revel-Rolland et al. (2006) reported a significant contribution from Australia to the dust load above Antarctica. Gaiero (2007) taking into account strontium's isotopic fractionation in the finest particles, suggesting Puna-Altiplano to contribute to Antarctic dust. Delmonte et al. (2008b) readily accepted that, proposing the high-altitude sight might gain relative importance on the high latitude one during interglacials.

4.2.3 Deposition

Mineral dust can be removed from the atmosphere by either dry or wet deposition. Wet deposition is defined as the fraction of dust removal taking place during precipitation events by either in-cloud scavenging ('rain-out') or 'wash-out', i.e. below cloud scavenging (e.g. Mahowald et al., 2011). Dry deposition, on the other hand, occurs by gravitational settling,

diffusion or impaction and is, just as wet deposition, size-dependent (Bergametti and Foret, 2014).

This difference is important when the aerosol load above the ice sheet (and its deposition) are to be reconstructed (Mahowald et al., 1999). Mahowald et al. point out that concentration is a better estimate for the aeolian load over the ice pack if wet deposition dominates (as is currently the case over Greenland), but that fluxes are a better proxy for dustiness in case of dry deposition.

(a) Wet deposition at present   **(b)** Wet deposition during LGM
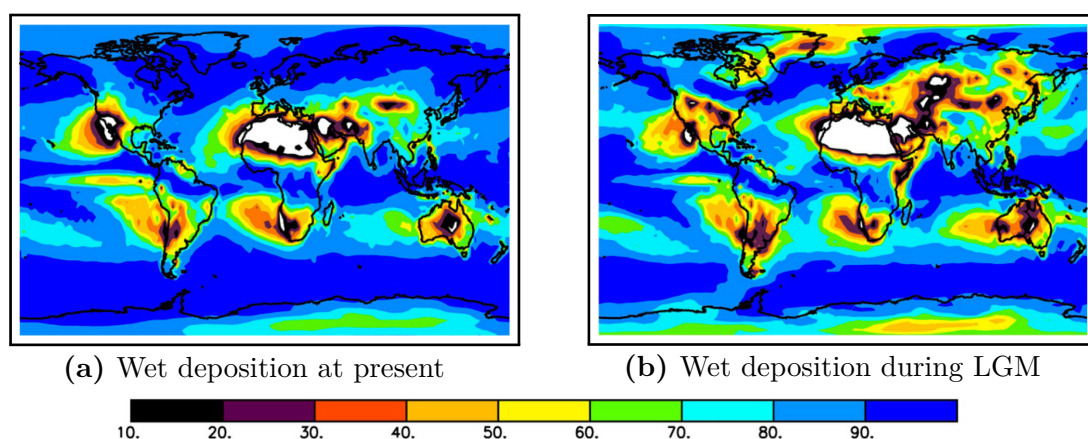
Figure 22: Fraction of wet deposition for current and LGM climates, modified from Mahowald et al. (2011)

Often the flux is considered a function of dry and wet deposition

$$J_{ice} = J_{dry} + J_{wet} = v_{dry}C_{air} + \epsilon A C_{air}$$

Where J are fluxes, v_{dry} is the settling velocity, ϵ the scavenging coefficient and A the accumulation rate (Fischer et al., 2007). While Mahowald et al. (2011) accuse this model for oversimplification, it does demonstrate that, at high accumulation rates wet deposition dominates.

Figure 22 shows the fraction of deposition that comes from wet deposition as modelled by Mahowald et al. (2011). While Mahowald et al. suspect their model to overestimate dry deposition during the LGM, others, acknowledging a drop in accumulation rate by a factor of two during the LGM relative to present day (Johnsen et al., 1992; Andersen et al., 2006), still believe wet deposition to dominate (e.g. Alley et al., 1995; Fuhrer et al., 1999). Depositional patterns on Greenland during the LGM are thus uncertain.

Chapter 5

Aeolian Dust Detection in Ice Cores

Summary   *Prior to the integration of continuously operating particle sensors into CFA systems continuous dust records had to be inferred from impurity records proxy measurements. These proxies (mainly Ca^{2+}, but also Fe or Al) however, estimate only a fraction of the total dust load, as they are not contained by all mineral aerosols and cannot reveal changes in particle sizes.*

Until now, two different detection techniques have been used to characterise particulate aerosols in Greenlandic ice cores, i.e. ccs, based on electrical impedance and laser light attenuation. While the former is widely appreciated for its reliable and accurate sizing, the latter does not require discrete samples and can thus constitute a CFA detection line.

Nonetheless, as size distributions detected by multiple attenuation sensors on an identical sample only show a limited degree of resemblance, it has to be concluded that continuous particle sizing does not fulfil scientific requirements. This implies that current dust detection techniques do not allow for maximum extraction of the preserved information.

5.1 Coulter Principle

Classically, particle sizing is done using a principle introduced by Wallace Coulter (1956). Initially developed for the US navy (Robinson, 2013), the Coulter counter rapidly spread in the medical sector and beyond after its commercialisation.

The basic principle of a Coulter counter is depicted in figure 23. An aperture connects two otherwise electronically isolated, electrolyte-filled chambers. Electrodes are placed on either side of the aperture and during a particle's passage through the orifice it displaces a volume of the electrolyte equal to its own, which is recorded as an increase in the electrical resistance between the two electrodes.

$$\Delta R = \left(\frac{4\rho_m d_p^3}{\pi D_t^4} \right) F \left(\frac{d_p^3}{D_t^3} \right) \tag{21}$$

De Blois and Bean (1970) derive equation (21) (their numbering), with D_t and d_p the diameters of the orifice and the particle, respectively, ρ_m the resistivity of the electrolyte, and F a correction term needed to account for a non-homogeneous electric field.
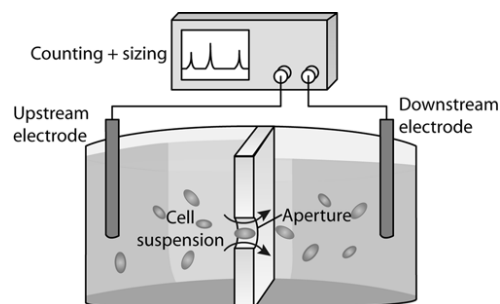
Figure 23: Working principle of a Coulter counter, taken from Gawad et al. (2010)

The detector's sensitivity is thus inversely proportional to the orifice's diameter. This highlights the trade-off that has to be made between sensitivity and functionality. While small apertures are desired to lower the detectors detection limit, care needs to be taken to avoid clogging of the orifice. When measuring dust in ice cores, orifices between $20\mu m$ and $30\mu m$ are usually chosen (Steffensen, 1997; Wegner, 2008).

Sensitivities of resistive pulse detectors are usually denoted by its volume fraction, i.e. the ratio of the volume of a detectable particle and the electric field's volume. Current commercial Coulter counters have a volume fraction of .0037% (Zhang et al., 2009), and are widely appreciated not only for their sensitivity, but also for their reproducibility both within the ice core community (e.g. Petit et al., 1981; Steffensen, 1997; Ruth et al., 2002) and beyond (e.g. Hayakawa et al., 1995; Shapiro, 2004; Zhang et al., 2009).

Coulter counters are, however, missing out on the specific opportunities that ice cores offer, being high resolution archives. The detection technique as outlined above and shown in figure 23 does not allow for continuous sample feeding, making it incompatible with CFA systems, resulting in time consuming sample preparation and a lower the resolution of the eventually obtained data set compared to those of soluble aerosols for which CFA techniques exist.

5.2 Attenuation Measurement

Therefore, Ruth et al. (2002) introduced an optical flow-through detector for microparticles to CFA. When light hits a particle, some of it will pass through, some of it will be reflected and a third fraction will be scattered. Optical detection techniques are generally better suited for detecting larger or concentrated particles (Zhang et al., 2009), and due to the

improved signal-to-noise ratio scattering detectors are more sensitive than attenuation sensors (Ateya et al., 2008).

However, attenuation sensors are widely used when detecting insolubles in water (Zhang et al., 2009), and in cooperation with the German manufacturer Klotz GmbH the Institut für Umweltphysik of the University of Heidelberg modified a detector based on the attenuation of laser light (Saey, 1998). After the Heidelberg group's successful adaptation of the Klotz detector to applications in ice cores several groups have purchased similar laser particle detectors (LPD) and integrated them into their CFA systems (see e.g Kaufmann et al., 2008; Bigler et al., 2011).
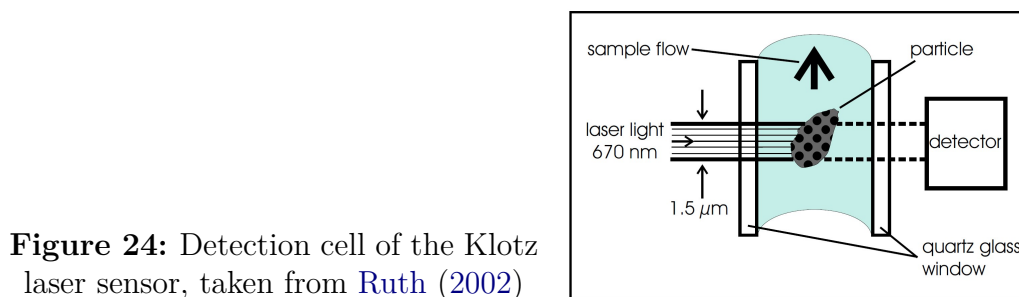
Figure 24: Detection cell of the Klotz laser sensor, taken from Ruth (2002)

Figure 24 schematically shows the detection cell of the LPD. A $1.5{\times}250\mu m$ wide beam hits the particles flowing through a cell with a cross section of $230{\times}250\mu m$. Particles are identified by a decrease in the detected intensity and events are binned according to minimum intensity levels. Due to the relatively large flow cell the flow should be kept above $2\ ml\ min^{-1}$ in order to minimize dispersion (Ruth et al., 2002), which is about twice as much as allocated other CFA detection lines, see chapter 2.

Attenuation detectors rely on the geometric shadowing as main part of the signal. However, as Ruth et al. (2003) points out, geometric shadowing becomes dominant only for particles of at least $7\mu m$ in diameter, a dimension well above the lognormal distribution's modes in both, glacial and interglacial periods (Steffensen, 1997). Below that limit both, small angle scattering (see section 6.3.2) and geometric shadowing contribute to the signal and the former cannot be simulated with latex beads. To circumvent this problem an indirect calibration was used, linking the attenuation sensor to a Coulter counter by measuring identical samples with both instruments and adjusting the bin edges of the optical sensor such that the resistive pulse and the attenuation detector yield identical results (Ruth et al., 2003; Wegner, 2008).

5.3 Re-calibration of Attenuation Sensors

The first column of figure 25 shows the size distributions detected in the same depth interval of the NEEM core, using (a) the German *Alfred-Wegener-Institut's* (AWI), (b) the Danish *Centre for Ice and Climate's* (CIC) and (c) the Bernese *Institut für Klima- und Umweltphysik's* (KUP) attenuation sensors (LS), as well as (d) the French *Laboratoire de Glaciologie et Géophysique de l'Environnement's* (LGGE) Coulter counter (CC).

Each LS yields size distributions with characterising features. The AWI sensor (blue line) seems to only detect particles larger than the mode and assigns unexpectedly few counts to the size interval between $2.1\mu m$ and $2.2\mu m$; the Danish detector (red) finds surprisingly many counts half way the distribution's tail between $4.7\mu m$ and $6.1\mu m$ and the Swiss LPD (black) shows a sawtooth pattern on the size distribution's rising flank and allocates conspicuously many event to the interval between $4\mu m$ and $4.5\mu m$. At least for the German and Swiss detectors, these deviations from the LGGE CC are systematic, see figure 43.
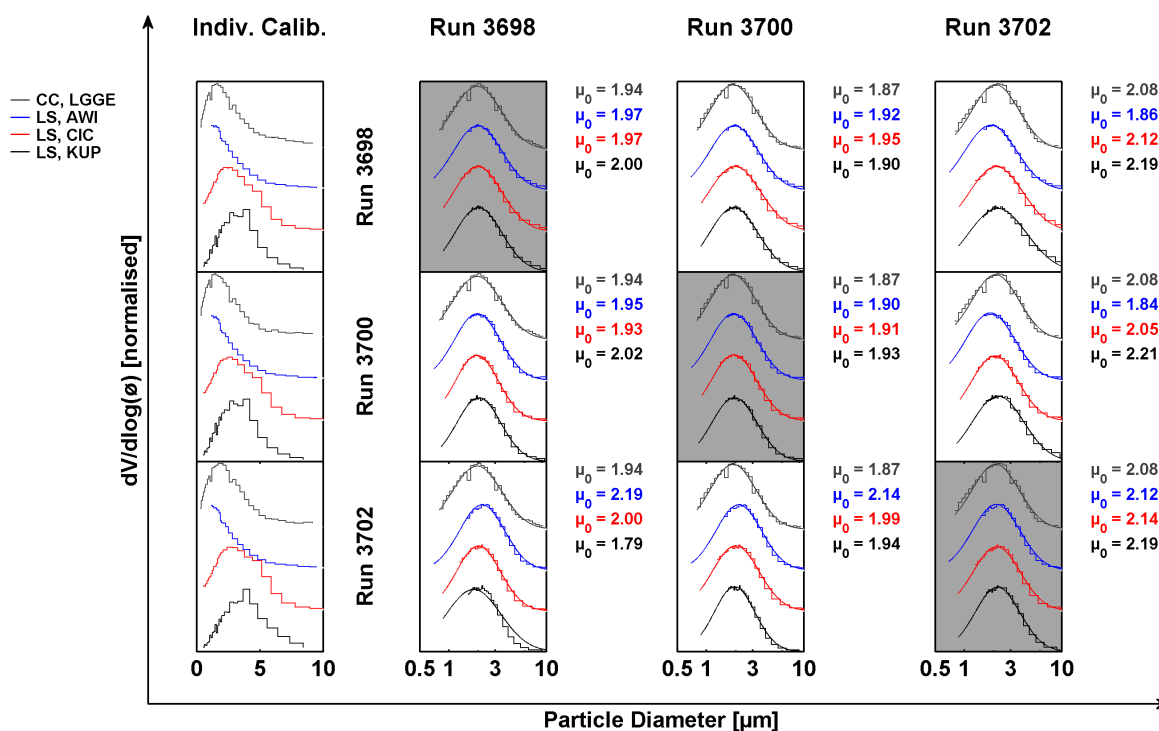
Figure 25: Size distributions based on Factory Settings (left) and bin size adjustment following Ruth et al. (2002)

Publishing the first LS-acquired data set, Ruth et al. (2002; 2003) already reported a mismatch between size distributions obtained with LPDs and CCs, and the inconsistency of LS data series has also been mentioned before (Bigler et al., 2011; Lambert et al., 2012). Addressing this mismatch, various corrections methods for continuous dust data series have been proposed. These are either based on mapping the continuous data set onto a discretely obtained size distribution (Ruth et al., 2002; Lambert et al., 2012), or on smoothing the lognormal distribution by adjusting the bin's edges (Grinsted, 2013) or by re-allocating counts from one bin to another (Erhardt, 2013).

5.3.1 Mapping to simultaneously acquired Coulter counter data

Ruth et al. (2002) proposed to keep the upper limit of the largest bin fixed, and to iteratively alter the edges of the smaller bins. The lower limit of the next smaller bin is found by linear interpolation towards either larger or smaller x-values, such that the total number of counts in the newly defined bin equals the number of counts in the corresponding interval of the CC-obtained size distribution.

As measurements with LPDs and CCs might result in unequal number concentrations (particles ml^{-1}), the possibility for an 'efficiency correction' is provided. The LS detected number concentration can be adjusted by selecting one channel in the LS data series and multiplying the continuously detected distribution with the scaling factor needed to match the number of counts in the selected channel and the corresponding interval in the electrically acquired size distribution.

This method has been applied to one of three consecutive runs performed during the 2011 NEEM field season, and the effect of the newly determined bin edges on the other two runs has been investigated. The results are presented in columns two to four of figure 25. Grey-shaded axes denote the data sets from which the new bin edges were derived by mapping to LGGE CC data, and the adjacent white axes in the same row are the resulting size distributions applying these new edges to the previous or subsequent runs.

It can be concluded that relative changes in the modes of the lognormal distribution, identified after correcting the LS data using this correction method, have to be interpreted with care. The three modes yielded by the LGGE data set start out at $1.94\mu m$, to decrease by 3% and eventually rise again by 11% to $2.19\mu m$. The AWI sensor shows consistently decreasing modes suggesting the smallest mode in the same run the LGGE data has measured the largest one. While the pattern of a decrease preceding an increase can be reproduced by the corrected CIC data set, the relative decrease is consistently underestimated. The

corrected KUP data though, seems follows the trend identified by the CC nicely, with the only exception of run 3698 when bin edges are adjusted to run 3702.

Lambert et al. (2012) used a two-sided regression analysis to match CC data from the EPICA Dome C core to data acquired with the Swiss and the Danish LPDs. Regression was performed on the logarithm of dust fluxes (i.e. the concentration multiplied with the accumulation rate, see section 4.2.3) and the errors of the fitted slope and offset were estimated by performing a Monte Carlo simulation. Their reported results

$$log_{10}(CC) = (0.9084 \pm 0.0309) \times log_{10}(KUP_{LPD}) - (1.3276 \pm 0.1076)$$

$$log_{10}(CC) = (1.633 \pm 0.089) \times log_{10}(CIC_{LPD}) - (3.136 \pm 0.128)$$

differ significantly and highlight the inconsistency of LPD-obtained size distributions.

5.3.2 Smoothing of Detected Size Distribution

Erhardt (2013) developed a correction algorithm independent of CC measurements on the same sample. Instead, he assumed an underlying uniform distribution as well as an erroneous determination of the bin edges on the manufacturers's side and attributed each bin an error Δb.
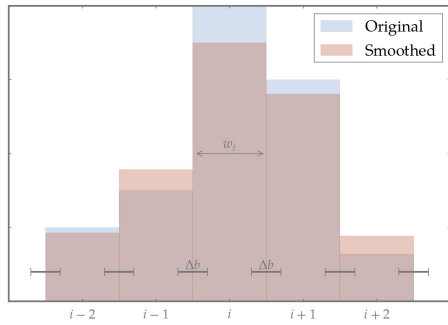
(a) Illustration of the correction proposed by Erhardt (2013)
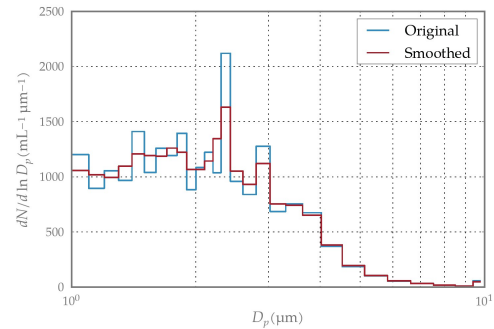
(b) Mean size distribution of the upper 600m of the NEEM core

Figure 26: Abakus correction after Tobias Erhardt, both figures 26a and 26b taken from Erhardt (2013)

Figure 26a illustrates the correction mechanism constructed by Erhardt (2013). The counts (cts) allocated to the ith bin with width w_i are spread out over the interval $[w_i - \Delta b, w_i + \Delta b]$ and counts now outside of the original bins, as derived from the manufacturer's calibration, were reallocated to neighbouring bins.

In this approach, the original bin edges were this kept unmodified (see figure 26b), but the size distribution was smoothed by altering the counts allocated to each bin via

$$cts'_i = \frac{cts_i}{w_i + 2\Delta b} + \Delta b \left(\frac{cts_{i-1}}{w_{i-1} + 2\Delta b} + \frac{cts_{i+1}}{w_{i+1} + 2\Delta b} \right)$$

Grinsted (2013) decided, similar to Erhardt (2013), not to experimentally correct the acquired data but to assume a smooth underlying size distribution and an unchanged systematic error introduced by erroneous bin edges. The algorithm leaves both, the largest bin's upper boundary and the smallest bin's lowest one unchanged. Bin edges in between are determined statistically (on size distributions representing 250 to 500sec measurement intervals) to eventually return as many monotonically decreasing *number* distributions as possible. The factory-set bin edges are still assumed to be to some extend correct, in that a penalty for large deviations between old and new bin edges is introduced and minimised.
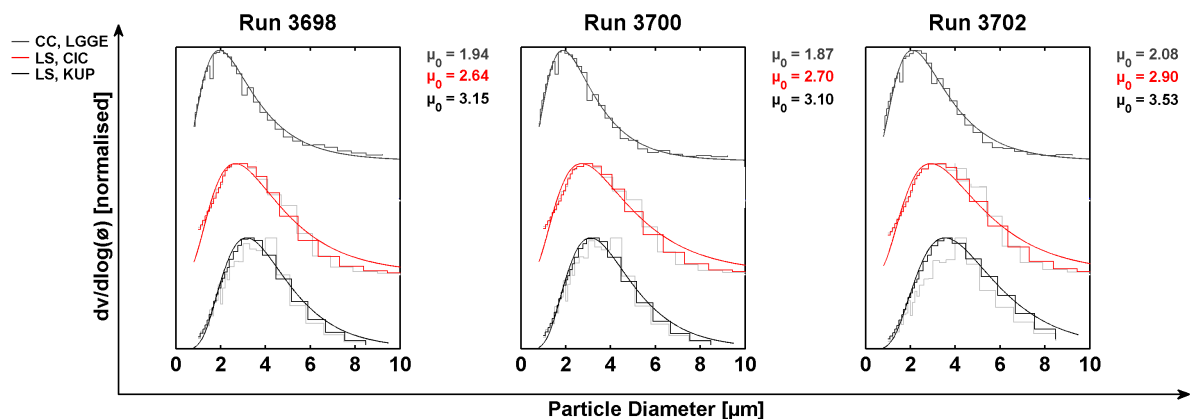
Figure 27: Statistically re-calibrated size distributions

As this approach is based on a large number of size distributions this correction could not be applied to the AWI LPD, as it only squired run means during the entire NEEM campaign - and yielded consequently too little data for statistical corrections.

In this approach the counts are thus kept constant, and the results for the CIC and the KUP LPDs are shown in figure 27. The trend of a 3% decrease in the distribution's mode followed by an 11% increase set by the LGGE CC is almost exactly reproduced by the Swiss LPD, while the CIC sensor seems to underestimate relative particle sizes in run 3698. Still, these bin edges have been used for figure 55 and further size distributions presented in chapter 8 acquired with any of the two LPDs. In absolute mode values, however, the CIC LPD is only 50% off the LGGE CCs results, while the Swiss instrument differs by up to 75%.

5.4 Aeolian Dust Load Proxies

5.4.1 Calcium

As mentioned in section 2.3.1, in Greenlandic cores the calcium's continental source dominates its marine one (Legrand and Mayewski, 1997), such that '[t]he dust concentration usually followed the Ca^{2+} variability' (Ruth et al., 2002). Indeed, based on for its marine fraction corrected calcium records ($nssCa$, see equation (2.2)), many studies have aimed at the reconstruction of paleoatmospheric transport paths and implicitly or explicitly at the identification of source areas (Fuhrer et al., 1999; Röthlisberger et al., 2002; Fischer et al., 2007; see also section 4.2.2).

However, it has to be born in mind that only the Ca^{2+} containing fraction of the dust will be detected. While it can safely be assumed that largest soluble fraction of dust consists of $CaCO_3$ (Ruth, 2002) or other Ca^{2+} containing carbonates (Scheuvens and Kandler, 2014), the soluble fraction of dust detected in ice cores is not constant over climatic transitions (e.g. Ruth et al., 2002). Further will the dust's mineralogical composition vary with changing source areas (Bory et al., 2002; Mahowald et al., 2011), and so too will the Ca bearing fraction of the soluble dust deposited.

5.4.2 Trace Elements using ICPMS

Whereas the calcium content of mineral dust is known to be largely dependent on the dust's source region, the aluminium (Al) content of crustal material is more homogeneous (Bowen, 1979; Scheuvens and Kandler, 2014), and thus less deceptive to variation in dust input due to source changes. Consequently, the Al content is more representative than Ca for the aeolian dust load and has indeed been used as a proxy (e.g. Ruth et al., 2002; Banta et al., 2008). Aluminium is commonly detected using inductively coupled plasma mass spectrometry (ICPMS), as are other crustal constituents that are - albeit less homogeneously distributed in the earth's crust - also used to approximate the atmospheric dust content above the ice. Iron, silicon, manganese or potassium are but a few trace metals that have been used to this end (e.g. Knüsel et al., 2003; Osterberg et al., 2006).

The dust's elemental composition is, to some extent (see section 4.2.2), representative for its source area (Scheuvens and Kandler, 2014). Comparing multiple proxies, Ruth et al. (2008) noted that the pronounced concentration changes of two orders of magnitude over a glacial-interglacial transition could not be reproduced by any of the elemental proxies and attributed that to changes in source area(s) simultaneously to the concentration decrease.
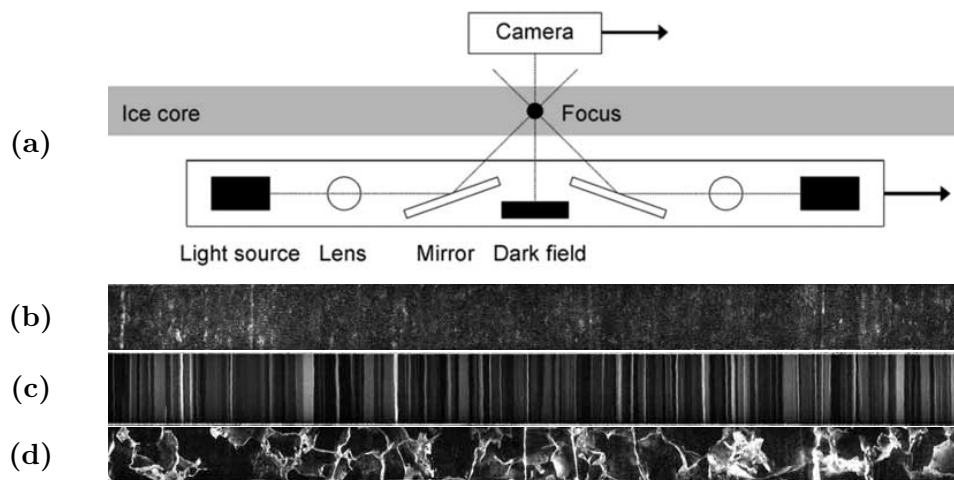
Figure 28: Line scan instrument (a) and sample images of (b) Holocene, (c) glacial and (d) basal ice; modified from Svensson et al. (2005)

Restrictions to data sets acquired with ICPMS are that (1) prior to injection into the ICPMS, the melt water stream needs to be acidified, and (2) only the fraction of aeolian dust containing the trace metal in question is quantified. Acid digestion is usually performed with hydrofluoric (HF) or nitric (HNO_3) acid (e.g. Osterberg et al., 2006; Banta et al., 2008). Incomplete dissolution, to which the sample is especially subjected when the ICPMS is connected to an CFA melthead (e.g. Knüsel et al., 2003), can lead to an underestimation of the trace element containing dust fraction. The limitations due to the selectivity to only a subset of the insolubles is highlighted by Banta et al. (2008), who identify different trends in the carbonate and aluminous dust particles, meaning that a decrease in one of the two fractions does not allow conclusions to be drawn for the entirety of the deposited insolubles.

5.4.3 Visual Stratigraphy

Ram and Koenig (1997) have used the VS dating the GISP2 core, and interpreted the counted cloudy bands as a dust signal. As alternative or further causes of the VS microbubbles forming around impurities were suggested (Alley et al., 1997; Dahl-Jensen et al., 1997). Observing a controlled melting process through a microscope, however, (Svensson et al., 2005), have been able to diffuse that claim. Svensson et al. thus concluded that the scatter is not due to the presence of solubles and the observed high degree of correlation with the NGRIP dust record (Ruth et al., 2003) has lead to the general acceptance of VS as another dust proxy (e.g. Winstrup et al., 2012).

Figure 28 depicts the instrument with which the visual stratigraphy (VS) of the NGRIP core was recorded (Svensson et al., 2005). Light enters a 3*cm* thick slab of ice from below and, if not scattered does not hit the lens of the camera mounted on top. Therefore clear ice is represented by black pixels in the images obtained and shown below the schematic.
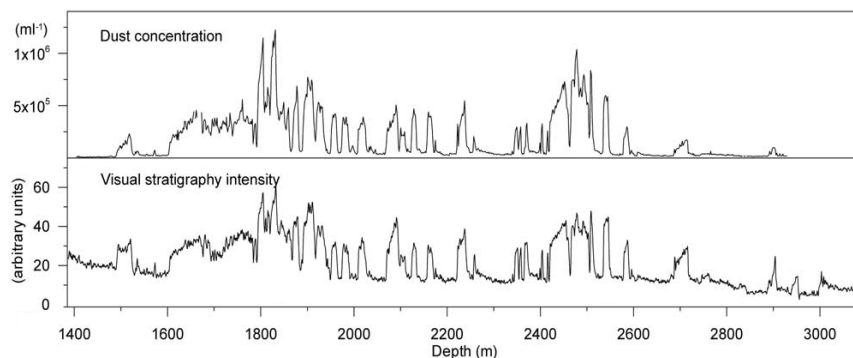
Figure 29: Rel. line scan intensity and number concentration acquired with the KUP LPD (Ruth et al., 2003); modified after (Svensson et al., 2005)

Additionally to the the inability to provide information on the insolubles size distribution, which is common to all proxies, the VS cannot be used to quantify the dust load or volume concentration of the deposited mineral dust. For dating purposes, however, being a CFA-independent time series with maxima in spring (Winstrup et al., 2012), it has been part of the data set used to construct the GICC05 time scale via layer counting in a multi-proxy approach (Andersen et al., 2006; Rasmussen et al., 2006; ; see also section 2.1).

The interval within which the VS record can be used to annual layer recognition is, as the line scan images in figure 28 shows, limited. During the Holocene, as can be seen from figure 28b, annual layers are not preserved, presumably due to the relatively low dust load and high accumulation rate. Also in the basal part annual layers are, if they had been present, disturbed by the basal heat flow into the ice, see figure 28d. The information that can be obtained on insolubles is limited to *relative* concentrations and no knowledge on grain size can be obtained.

Chapter 6

Optical Flow Cytometry

Summary   *Flow cytometres are designed to analyse individual cells or organisms and to classify them based on multiple, simultaneously obtained parameters. These include commonly small (FSC) and wide angel (SSC) scatter and often fluorescence, be it autofluorecsence or dye-induced.*

The instrument used in this study features two photo multiplier tubes: One to detect wide angle scatter to identify particles passing through the detector and another one at a small angle to investigate to which degree that signal is a measure for the scattering insoluble's size.

Relating the small angle scatter intensity to particle size was found impossible. While narrowly confined intervals in the scattered light's intensity could be attributed to measurements on monodispersed latex beads, a calibration curve incorporating several standard measurements was found impossible to obtain.

Subsequent attempts to calibrate the instrument indirectly, linking them to independent measurements of the same sample or directly by using the pulse width (the time-of-flight) were found to be of little mitigating potential. Classical flow cytometric analysis in multiple dimensions (i.e. FSC and SSC) did not yield any indications for a fundamentally changing particle morphology over the interval examined.

6.1 The Evolution of Flow Cytometry

Flow cytometry (FCM) was developed within analytical cytology (Shapiro, 2003, 2004), but has since been widely accepted as an analytical method in an array of other fields, where counting, identification and characterisation of cells or particles in suspension is of interest. Applications of FCM can be found in palaeontology, ecology, botany, microbiology, molecular biology, physiology and - most prominently - in oceanography, where it has been introduced in the early 1980s (Legendre and Yentsch, 1989) and subsequently seen a tremendous proliferation (Legendre et al., 2001; Yentsch and Yentsch, 2008).

   Shapiro locates the bifurcation in the previously common genealogy of cytometers and microscopes in the Stockholm of the 1930s, where Caspersson (1950, cited by Shapiro, 2004)

made use of the intrinsic absorption of cellular nucleic acid to characterise individual cells. In 1953 Crosland-Taylor presented 'a device for counting small particles suspended in fluid through a tube', which lined up particles contained in the sample stream in a single file. This was achieved by letting a faster flowing sheath liquid narrow the sample stream's diameter down to one comparable to the the particles' cross section. The single-file stream of particles was subsequently led through the interrogation region, i.e. the common focal point of the lens focussing the light source and the one collecting the scattered light for detection.

Gradually flow cytometers grew in complexity. The number of light sources was increased by Kamentsky et al. (1965), to simultaneously detect scattering of visible light (as did Crosland-Taylor, 1953) and UV-absorption of nucleic acids (as did Caspersson, 1950) and additional sensors to also detect fluorescence light were designed by the companies Los Alamos in the United States (Van Dilla et al., 1969) and Partec in Münster, Germany (Dittrich and Göhde, 1969, cited by Picot et al., 2012) . By applying logical gates, i.e. structuring the wealth of data that could be collected for each particle, different cell types could be distinguished more reliably.

Accurate sizing, however, was impossible. Indeed, as Shapiro (2004) notes, 'correlations between particle sizes and signal amplitudes were not particularly strong', so that cytologists resorted to the apparatus developed by Wallace Coulter (1956), making use of the electrical impedance of cells (see section 5.1). If information on cell size was to be obtained from flow cytometric measurements, researches usually used attenuation measurements (see Shapiro, 2004).

Once established, FCM saw a trend towards flow cytometers that were portable and easier to operate. Air-cooled lasers and bench-top computers enabled the manufacturing of smaller instruments and the emergence of AIDS created a demand for on-site analysis in the 1980s (Shapiro, 2004). The trend toward miniaturisation continued and culminated in attempts to place all components needed on a chip (e.g. Blankenstein and Larsen, 1998) and using microfluidic techniques. Since then, many ideas have been floated how to improve and miniaturise components for fluid handling, the optics or the electrical signal detection (see e.g. the review by Ateya et al., 2008).

6.2 Partec's CyFlow SL

In their review of 2008, Ateya et al. pointed out that the microfluidic devices' 'commercial availability is on the horizon'. However, this is cutting edge technology and was not available

at the start of this project, such that Partec's benchtop model *CyFlow SL* was chosen.

Partec enjoys a good reputation in the literature (e.g. Shapiro, 2003), is a pioneer in commercialising flow cytometry (Picot et al., 2012) and have scientists working on continuously improving their instruments in order to ensure their instruments are always state-of-the-art (e.g. Shapiro, 2004). Their model *SL BLue* (for Single Laser) is a slightly upgraded version of the *SL Green* that was designed in the 1980s for HIV detection in the field.

Another argument for Partec was that FCM had not been used in ice core science before, and since '[m]ost babies aren't born in supermarkets', as Shapiro (2003, p.466) points out in his 'Fourth Law of Flow Cytometry', technical assistance from the vendor is essential in the early stages. Both hardware and software modifications according to our needs were part of the agreement that could be reached with Partec. This included *inter alia* continuous rather than discrete analysis, batch processing of large amounts of big data files and a tailor made software to convert the instrument output files from the flow cytometry standard (.fcs) to text files that allow for subsequent analysis in custom made software.

(a) Flow cell and hydrodynamic focussing

(b) Optical bench and dichroic mirrors
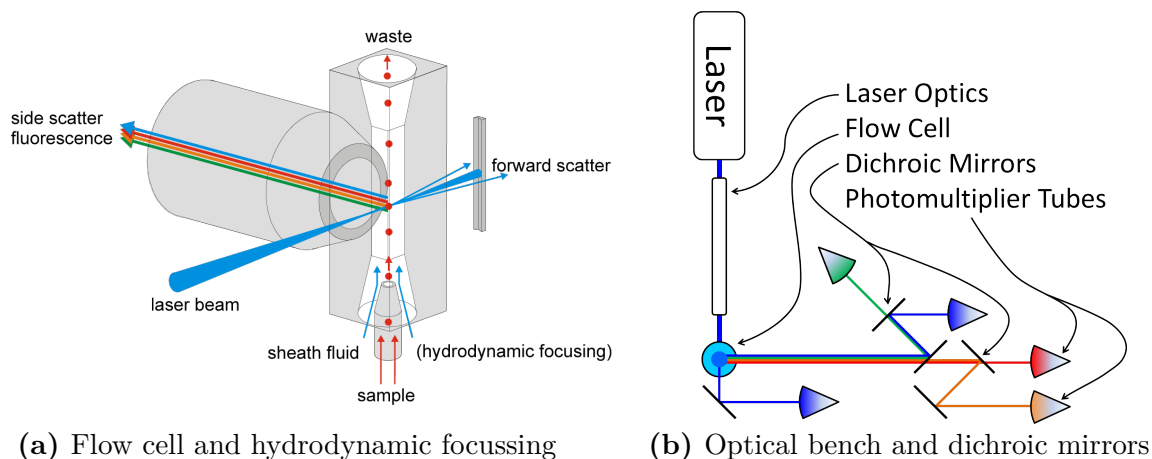
Figure 30: Key Components of Partec's CyFlow SL

The CyFlow SL's light source is an air-cooled $150mW$ solid state laser with a wavelength of $488nm$. In the early stage of the project it was hoped that by adding commercially available cell stains to the sample stream and subsequently applying gates on the obtained fluorescence signal, cells could be distinguished from dust and living cells from dead ones. Similar work has been published on discrete samples by Miteva et al. (2009), and the stains used in their study (Invitrogen's SYTO 13 and their Live/Dead kit) would fluoresce if excited at $488nm$.

Figure 30 shows the flow cell and the optical bench of the CyFlow SL. Hydrodynamical focusing of the sample stream is done in a quartz cuvette. The ensheathing flow is a pressure-driven stream of de-mineralised water. An adjustable overpressure drives the sheath flow from one reservoir, through the flow cell into another one. This set-up could easily be installed in the CFAlab erected at NEEM where the required sheath flow could be produced on-site.

Signal detection is performed at a small angle for the forward scatter (FSC), and at 90° for the side scatter (SSC) and emitted fluorescence. The different wavelengths collected at 90° are separated by means of dichroic mirrors, placed in the optical path behind the collection lens as indicated in figure 30b. Once separated, the different wavelengths are, just as the FSC signal, reflected into photomultiplier tubes (PMT), which can all be configured independently.

Each PMT has its own adjustable gain voltage and amplification mode. The latter is set to let the 2^{15} channels the instrument offers reflect a linear scale or to cover three or four decades logarithmically. Signal detection in all PMTs is triggered as soon as the signal in an appointed detector exceeds an customisable threshold. Individual amplification comes in handy, because the gain of the non-triggering PMTs can be set to higher levels without need to worry about noise amplification as the noise is filtered out by the triggering detector.

Figure 31 shows the mathematically approximated scattering light's intensity (see section 6.3.2) at a wide angle (SSC, 90°) and a narrow angle (FSC, 12°). It becomes apparent that the SSC is much less sensitive to noise than a equally amplified FSC signal. Therefore, when detecting small cells, usually a SSC threshold is chosen to trigger data acquisition.

Partec's acquisition software allows for the simultaneous recording of several quantitative measurements. These include next to the peak height also the peak width or the area under the peak. Further can each event caused by a particle passing through the interrogation volume be assigned a time stamp, which increases by one after a predefined interval - usually one second or $500msec$ - has passed.

Apart from two PMTs to record scattered FSC and SSC signals, the Cyflow SL could accommodate three PMTs for fluorescence detection. Since an adaptation of the method used by Miteva et al. (2009) was aimed for, only two (red and green) fluorescence PMTs were needed. It turnt out, however, that the incubation time needed for the dye to penetrate cells of the type that Miteva et al. found, could not be decreased sufficiently to facilitate in-flow staining. Consequently, the idea of distinguishing dust the biotic and the abiotic
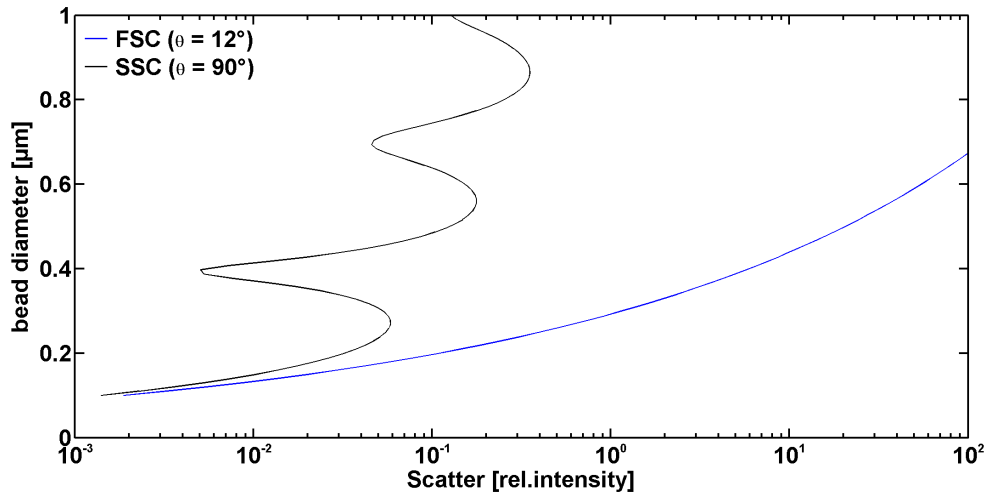
Figure 31: To small particles, SSC is less sensitive than FSC

fraction of the insolubles was given up and the two fluorescence detectors became de facto superfluous.

6.3 Direct calibration

Exploring the potential to identify the detected insolubles' biogenic fraction was of secondary importance only. Primarily it was to be investigated to what extend a flow cytometer could be used to improve sizing of particles in a continuously flowing sample stream, as the Abakus - the only instrument capable of doing so - was known to leave room for improvement (e.g. Ruth et al.,2002, 2003; see also section 5.2).

6.3.1 Forward Scatter Amplitude

Calibration Procedure   In order to calibrate a partec CyFlow SL cytometer, attempts were made to link the relative scatter intensities detected at small angles (FSC) to the scattering particle's equivalent diameter, i.e. the diameter a sphere of identical refractive index causing the same signal would have. The SSC signal was used for triggering as it is less sensitive to noise (see figure 31), which results in a lower detection limit and a higher resolution in the FSC, whose gain can be set higher.

A calibration consists of multiple standard measurements with latex beads of different diameters, all of whom have a refractive index of 1.19. Standard solutions are prepared beforehand to contain about as many particles as the subsequently measured sample and are one after the other injected into the instrument's flow cell.
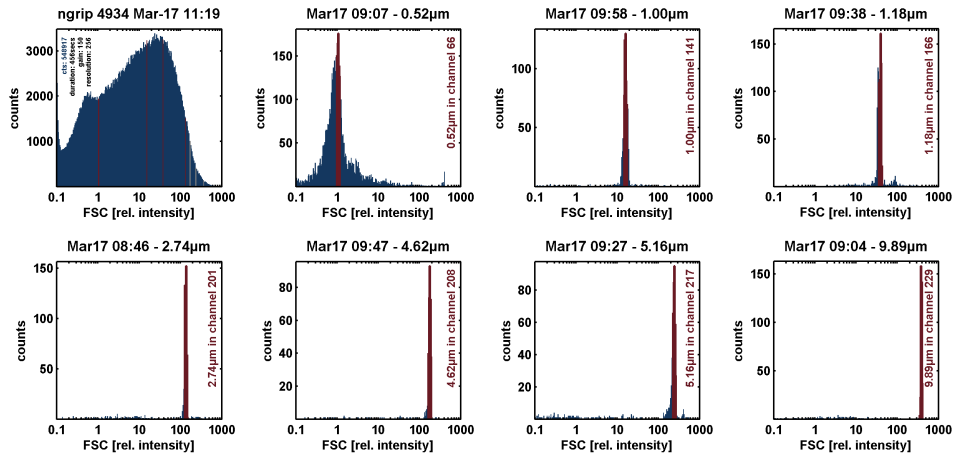
Figure 32: Data from a 2m section from GS22 and its preceding calibration

Laboratory NGRIP campaign   The presented calibration attempts using the FSC as size estimate are performed on data acquired during a measurement campaign conducted in the lab in Copenhagen in March 2011. The laboratory was temperature controlled, which prevented the laser from overheating as it did at NEEM in 2009. Further was the cytometer placed on a separate table to ensure, that the instrument is subjected to physical shocks with a lower frequency than it the case at NEEM in 2010, where vibrations resulted in a frequent misalignment of the cytometer's flow cell, see also figure 47b.

For presentation purposes, the instrument's initial resolution of 2^{15} has been down-sampled to 256 channels, so that all histograms presented in figure 32 are in a lower resolution than the actual data set. During the NGRIP GS22 campaign the FSC's amplification mode was to 'log4', meaning that the whole detection range spans four decades. Consequently, a particle in channel 128 of a 256 bin histogram has not caused a signal that was half as strong as one from the maximum channel, but only $\frac{1}{100}$.

In the axes to the upper left in figure 32, raw data obtained during that campaign is shown, while the other axes display the standard runs constituting the calibration that was performed shortly before the data was acquired. The channel with the most counts for each standards is also superimposed on the raw data histogram, fine standard ($<5\mu m$) in red and coarse ones in grey. This calibration was selected because it was the nicest calibration ever obtained, meaning that larger standards consistently caused higher intensities in the FSC signals (which is an exceptional case, see section 6.3.2) and the individual standard measurements' coefficients of variation ($\frac{\sigma}{\mu}$) are very small.

In figures 33 and 34 it is assumed that the FSC is a function of the particles' size

Parameters	
x-value	FSC
y-value	diameter
dynamic range	.5-15 μm

(a) Calibration parameters and curves

(b) Derived size distributions
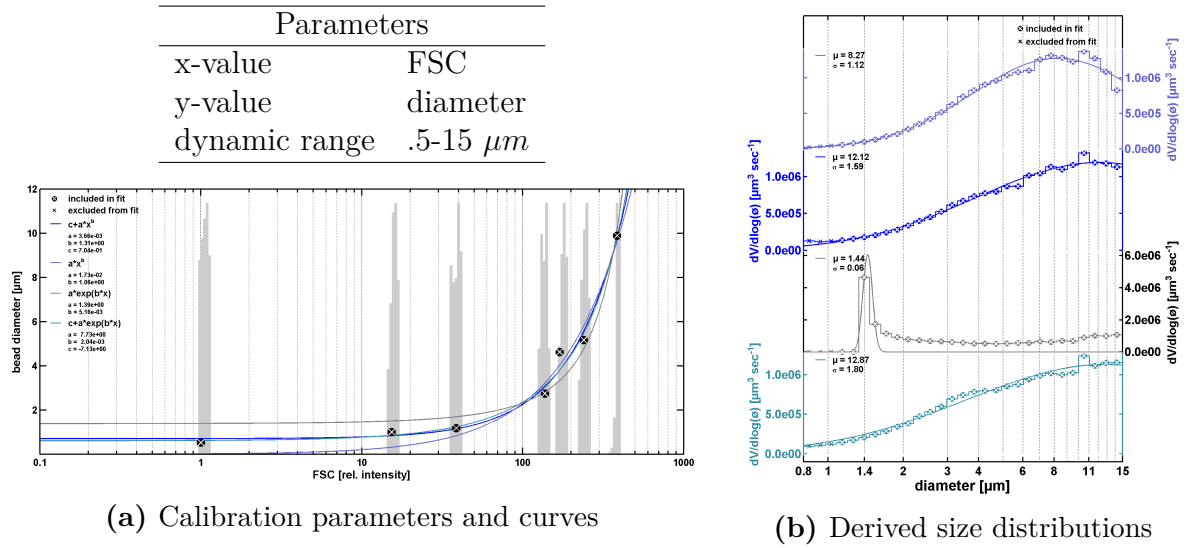
Figure 33: GS22 Full Range Log

first order, and the beads' diameters are plotted against the FSC signal they caused. The maxima in the standard runs shown in figure 32 are denoted in grey and gave raise to a set of (FSC,diameter) pairs to which exponential (ae^{bx} and $c + ae^{bx}$) as well as power functions (ax^b and $c + ax^b$) are fitted (figures 33a and 34a).

The calibration functions obtained this way are then use to assign all events constituting the raw data histogram in figure 32 an equivalent bead radius. Eventually, the volume distribution over diameter is calculated and shown in figures 33b and 34b as $\frac{dV}{dlog(r)}$. Colours are chosen such that a calibration function's colour matches the size distribution it results in.

Full range analysis The calibration functions shown in figure 33a yield size distributions whose modes are either shifted to larger values with respect to the modes previously reported by Steffensen (1997) and Ruth et al. (2003), or in the case of $c + ae^{bx}$ being used as calibration function, place the vast majority of the volume derived from equivalent radii in a single bin.

For the calibration model ae^{bx}, a relatively large y-intercept is needed in order to capture the steep increase demanded by the larger standards. As the slope of this model is very small well into the third decade, the sheer amount of particles assigned an equivalent diameter close to this calibration function's amplitude $A = 1.39\mu m$. This is the reason why the majority of the volume is due to those particles, rather than the $10\mu m+$ ones which are still found in similar numbers as by the other three models.

(a) Calibration parameters and curves

(b) Analysis with reduced dynamic range
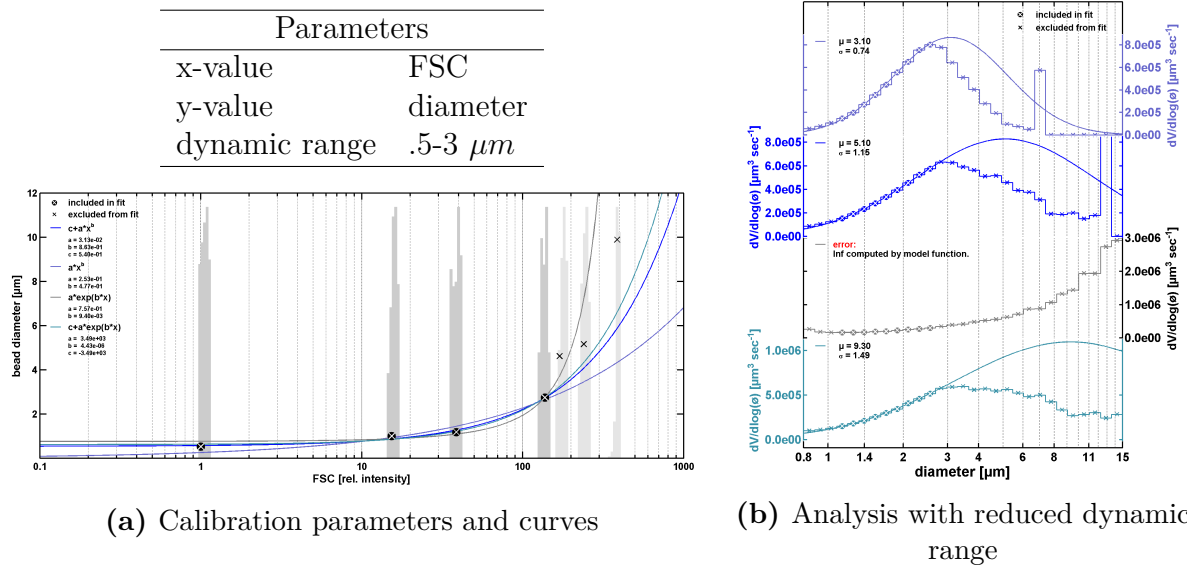
Figure 34: Analysis with reduced dynamic range

From the raw data histogram in figure 32, it becomes apparent that there are many counts in bins with edges of $10\mu m$ and larger. These weigh heavily on the volume distribution. Stronger, as a consequence of the calibration functions derivatives' high values in the upper end of the dynamic range, are the (relatively many) events at FSC intensities larger than the intensity calibrated to represent $10\mu m$ assigned extremely large radii. This results in a volume contribution of those $>10\mu m$ particles exceeding that of the bins in the fine fraction ($<5\mu m$). The large volume contributed by a single event in the larger bins is also the reason for the noisy high end of the distribution.

Presumably reduced dynamic range   The core of the problem - the many events with FSC intensities comparable to or larger than that of $9.89\mu m$ standard - can be circumvented by assuming those signals lie outside the flow cytometer's dynamic range. Reducing the dynamic range allows for the high intensities to be omitted, a solid physical basis for this measure, however, is missing. Larger standards give rise to peaks so well defined, see figure 32, that there is no good reason to omit them. Further are there flow cytometers on the market using similar electronics and optics with dynamic ranges of 5, 7 or even 8 decades.

Disregarding all of the above, figure 34 shows what the same measurement would look like if all standards larger than $3\mu m$ and events with intensities larger than the one caused by the $2.74\mu m$ standard were to be omitted. The power functions ax^b and $c + ax^b$ constrain particle sizes to below 7.2 and $13.2\mu m$ respectively μm. This explains the large volume
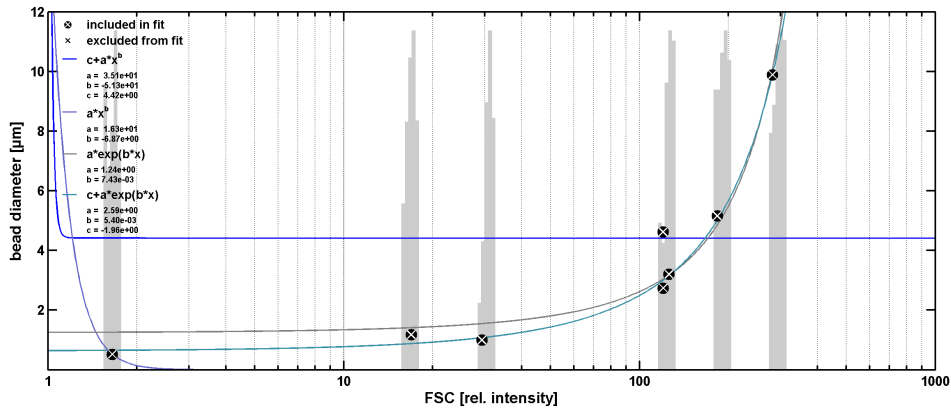
(a) Calibration of June 7th, 2010, 03:53h ↑
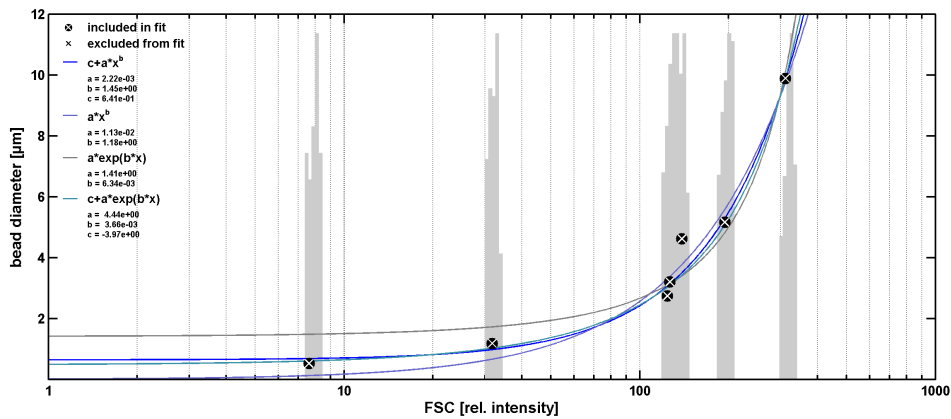
(b) Calibration performed at 04:09h on June 14th, 2010 ↑

Figure 35: Best and worst calibration obtained during the NEEM 2010 field season

placed in the respective bins.

Fits to the obtained size distributions are unconstrained for diameters larger than the mode, if a mode could be found by fitting a lognormal distribution. This was not the case for ae^{bx}, while the distributions derived after calibrating with $c + ae^{bx}$ and $c + ax^b$ are still larger than anything ever reported before. Judging only from the final result - the mode - assuming a reduced dynamic range and the function ax^b to reproduce the FSC signal of all particles $<2.74\mu m$ might be the best way of data treatment. However, as mentioned above, there is no sound basis to do so.

Results from NEEM 2010 As mentioned before, the calibration presented above was obtained under optimal conditions in the laboratory. Figure 35 shows the best and the worst calibration obtained during the field campaign in 2010. NThe FSC detector's amplification

FORWARD SCATTER →
(LINEAR)

NUMBER OF EVENTS →

3μ
4μ
6μ 5μ 8μ 7μ

3μ
4μ
5μ 6μ 7μ 8μ
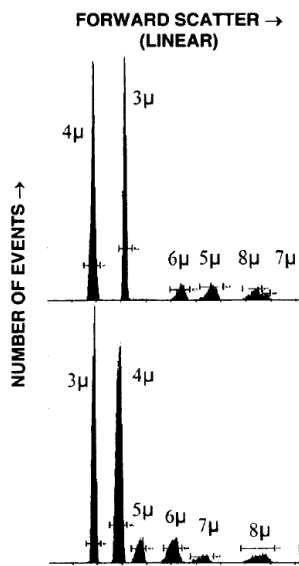
Figure 7-I. Forward scatter does not measure particle size
(courtesy of Kevin Becker, Phoenix Flow Systems).

Standard pairs with $\text{FSC}(\emptyset_1) > \text{FSC}(\emptyset_2)$:			
$\emptyset_1$		$\emptyset_2$	
1.00	and	1.18	μm
2.74	and	3.20	μm
2.74	and	4.62	μm
3.20	and	4.62	μm
4.62	and	9.89	μm
5.16	and	9.89	μm

" [. . .] And these are beads; their diameters can be and have been measured accurately by electron microscopy, and their refractive indices are pretty much all the same, so we can't find any way to wiggle out of accepting the fact that forward scatter does not measure size."

Shapiro (2003, p.276)

Figure 36: Flow cytometric bead size determination, histogram in Shapiro (2003, p.275)

mode was set to 'log3' during that campaign to deliberately reduce the sensitivity, as a source of noise was present that could only be excluded by this measure.

During the whole campaign the standards with respective bead diameters of $2.74 \mu m$ $3.20 \mu m$ and $5.16 \mu m$ showed very similar FSC signals. Occasionally, they would even swap position such that the signs of their size and FSC signal differences respectively would be opposing each other, see figure 35a. The same happened, albeit less frequently, for the standards with bead diameters of $1.00 \mu m$ and $1.18 \mu m$, and both occurred during the calibration presented in figure 35a.

Smaller standards causing larger signals than larger standards are not unusual in FCM (Tzur et al., 2011; Shapiro, 2003, p.275). In figure 36 a complete list of standard pairs that have been found to occasionally swap positions in the course of this project is presented. Even pairs with relative diameter difference of more than 100% are amongst those. The theoretical explanation for this was provided by Gustav Mie (1908) and figure 36 further contains a plot directly taken from Shapiro's Practical flow cytometry and the accompanying quote from his text.

6.3.2 Mie Scattering

> " [...] [n]ot only can't we compare apples and oranges; we can't, strictly speaking, always compare apples and apples, because theory predicts, and experiments confirm, that, even for uniform particles, forward scatter amplitude will not be a monotonic function of particle size."

<div align="right">Shapiro (2003, p.275)</div>

Having shown the experiments confirming that FSC is not a monotonic function of particle size, in the following the theory behind is briefly sketched. The non-monotonic behaviour can be approximated making use of a theory developed by Gustav Mie in 1908, which was comprehensively reformulated in the authoritative book by Bohren and Huffman (1983). As their derivation is reported here, the equation tags refer to either their numbering or the page number in their work.

For the scattered irradiance at angle θ relative to the incident perpendicularly polarised light

$$\frac{I_s}{I_i} \propto (S_{11} + S_{12}) \tag{p.113}$$

holds, where I_s and I_i are the intensities of the incident and scattered electric fields. S_{11} and S_{12} are given by

$$\begin{aligned} S_{11} &= \frac{1}{2}(|S_2|^2 + |S_1|^2) \\ S_{12} &= \frac{1}{2}(|S_2|^2 - |S_1|^2) \end{aligned} \tag{4.77}$$

which derives from the Stokes parameters and relation between the amplitudes of the incident electric field and the one scattered by a spherical object in the far field approximation

$$\begin{pmatrix} E_{\|s} \\ E_{\perp s} \end{pmatrix} = \frac{e^{ik(r-z)}}{-ikr} \begin{pmatrix} S_2 & 0 \\ 0 & S_1 \end{pmatrix} \begin{pmatrix} E_{\|i} \\ E_{\perp i} \end{pmatrix} \tag{4.75}$$

where S_1 and S_2 are functions of $cos(\theta)$ to which the transverse components of the scattered electric field are proportional. They are expressed in terms of spherical Bessel functions evaluated at x and mx
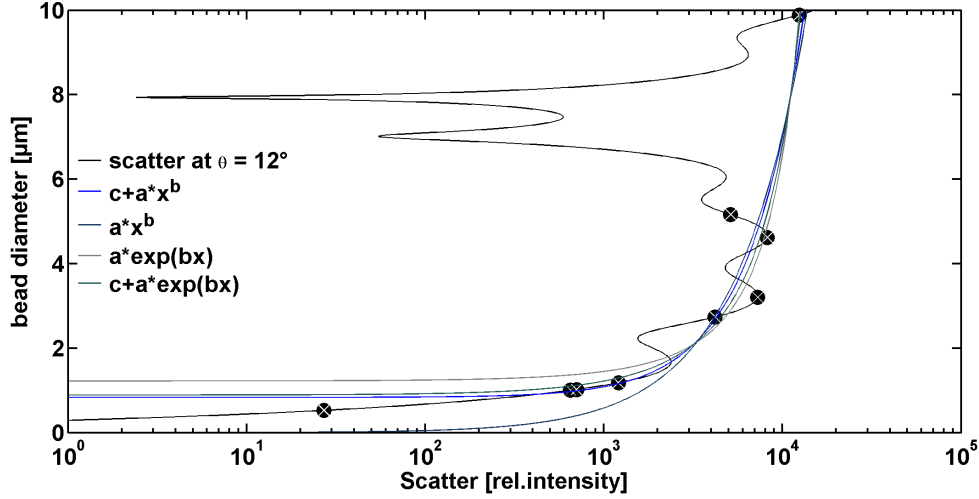
Figure 37: Computed FSC intensity at 12° and calibration attempts

$$
\begin{aligned}
S_1(cos\theta) &= \sum_n \frac{2n+1}{n(n+1)}(a_n\pi_n(cos\theta) + b_n\tau_n(cos\theta)) \\
S_2(cos\theta) &= \sum_n \frac{2n+1}{n(n+1)}(a_n\tau_n(cos\theta) + b_n\pi_n(cos\theta))
\end{aligned}
\tag{4.74}
$$

by means of a_n and b_n - the Mie scattering coefficients,

$$
a_n = \frac{\mu m^2 j_n(mx)[xj_n(x)]' - \mu_1 j_n(x)[mxj_n(mx)]'}{\mu m^2 j_n(mx)[xh_n^{(1)}(x)]' - \mu_1 h_n^{(1)}(x)[mxj_n(mx)]'}
$$

$$
\tag{4.53}
$$

$$
b_n = \frac{\mu_1 j_n(mx)[xj_n(x)]' - \mu j_n(x)[mxj_n(mx)]'}{\mu_1 j_n(mx)[xh_n^{(1)}(x)]' - \mu h_n^{(1)}(x)[mxj_n(mx)]'}
$$

with m the refractive index of the sphere relative to the ambient medium, $x = ka$ the size parameter, a the radius of the sphere, $k = 2\pi/\lambda$ the wave number and μ and μ_1 the magnetic permeability of the ambient medium and the sphere, respectively. $h_n^{(1)}$ are spherical Hankel functions,

$$
h_n^{(1)}(\rho) = j_n(\rho) + iy_n(\rho)
\tag{4.13}
$$

which are linear combinations of spherical Bessel functions j_n and y_n of order n. The functions $\pi_n(cos\theta)$ and $\tau_n(cos\theta)$ in equation (4.74) describe the angular scattering patterns of the spherical harmonics

$$\pi_n = \frac{P_n^1}{sin\theta}; \qquad \tau_n = \frac{dP_n^1}{d\theta} \tag{4.46}$$

with P_n^1 the Legendre polynomial of order n.

Calculated calibration curve Figure 37 shows the scattered light's intensity as a function of diameter, albeit with reversed x- and y-axes. Calculations were performed using the 'MieCalc' software provided by Michel (2011). The parameters for the specific calculation yielding figure 37 were 488 nm for the light source's wavelength and 1.33 and 1.19 for the refractive indices of the medium (water) and the scattering sphere (latex) respectively. Theoretical FSC signals for all standard measured during this project - and thus used in calibration attempts - are also highlighted.
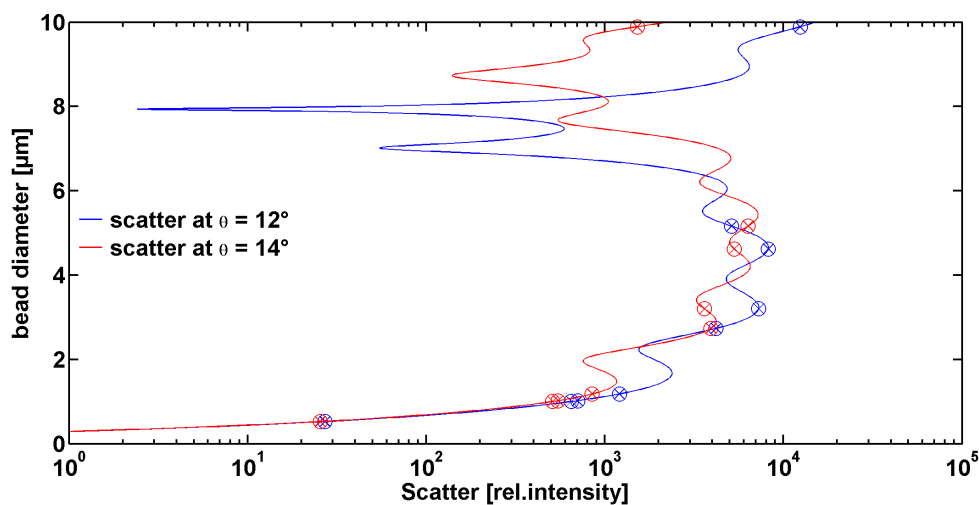
Figure 38: Computed FSC intensity at 12° and 14°

It becomes clear that the calibration curves attempted to fit to the measured standards in section 6.3.1 are a poor representations of the calculated signal. It is further underlined that from the FSC intensity no clear conclusion on the scattering particles size can be drawn. Spheres identical in composition would cause the same signal, regardless of being 0.78, 6.88, 7.18, 7.76 or 8.08 μm in diameter. From figure 37 it is safe to conclude that no particle detector, based on the scattering signal of insolubles cannot be used for range 1-10μm.

Angle-dependence of FSC As mentioned above, during the 2010 NEEM field season frequent misalignment of the flow cell was caused by vibrating tables and further physical shocks. Using the same software as before7, a widening in FSC by 2° resulting from a slight movement of the cell was simulated. The results are shown in figure 38 and lead to the conclusion that the signal is too sensitive to the scattering angle to ignore variations or to even to simply increase the error margin when analysing the data.

For example, a FSC signal of 3300 would, after misalignment by 2° be caused by a bead with a diameter of $3.45\mu m$. Assuming a precise knowledge of the calibration curve, this could be interpreted as a particle of diameter 2.60, 6.41 or $8.75\mu m$. The error bar would thus need to allow for an error of at least $1.85\mu m$, which is more than any change in mode on glacial-interglacial time scales ever reported. After misalignment not even climatic transitions could be identified any more based on particle size (e.g. Steffensen, 1997; Ruth et al., 2003).

> " [...] one cannot reliably estimate the relative sizes of two cells of different types from small-angle light scatter signals"

Shapiro (2003, p.275)
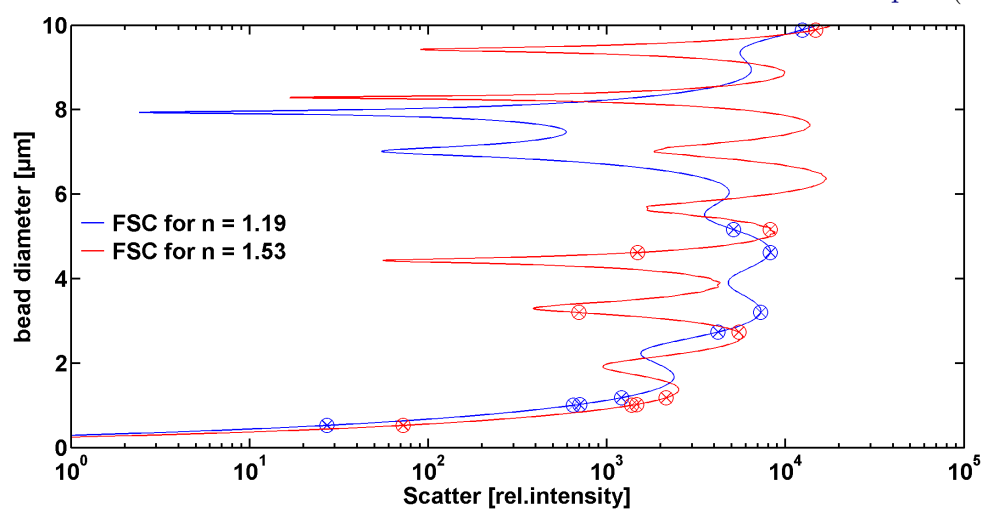
Figure 39: Computed FSC intensity at 12° for latex beads and hypothetical sperical dust

Varying refractive indices An additional problem arises due to the fact that the latex beads all have a refractive index of 1.19, which is not the case for dust. Depending on its source region the refractive index may vary (e.g. Claquin et al.,1998; Sokolik and Toon,1999, see also section 4.1.3). As Tegen (2003) points out, the refractive index for Sahara is

darker than for Asia, both regions possibly contributing to the dust load deposited on the Greenlandic ice sheet at present (Lupker et al., 2010; VanCuren et al., 2012).

In figure 39 the refractive index of hypothetical dust is assumed to be 1.53 to investigate to what extend a latex bead is representing an assumed spherical dust particle; the result is telling in itself. One should avoid attributing a diameter to a detected particle because another particle with different (figure 39) or identical (figure 37) refractive index, but different diameter, might have caused an identical signal. Therefore, Shapiro (2003) emphasizes that FSC signals should not even be used for relative sizing.

6.3.3 Time of flight

Taking advantage of the very stable fluidic system in a flow cytometer, time-of-flight (TOF) measurements are sometimes used to estimate cell size with higher accuracy than obtainable when using the FSC (e.g. Leary et al., 1979; Galbraith et al., 1988; Tzur et al., 2011). As the flow cytometer is connected to a CFA system working with peristaltic pumps, the flow rate is too volatile for TOF measurements, see figure 40. Therefore, the flow cytometer's fluidics were decoupled from the sample supplying peristaltic pump, as shown in figure 40a. The overpressure in the blank water (mQ) was created by a syringe pump, and the pressure driven flow lead through the flow cell. Figure 40b shows the constant and adjustable flow at two different pump pressure settings in red.
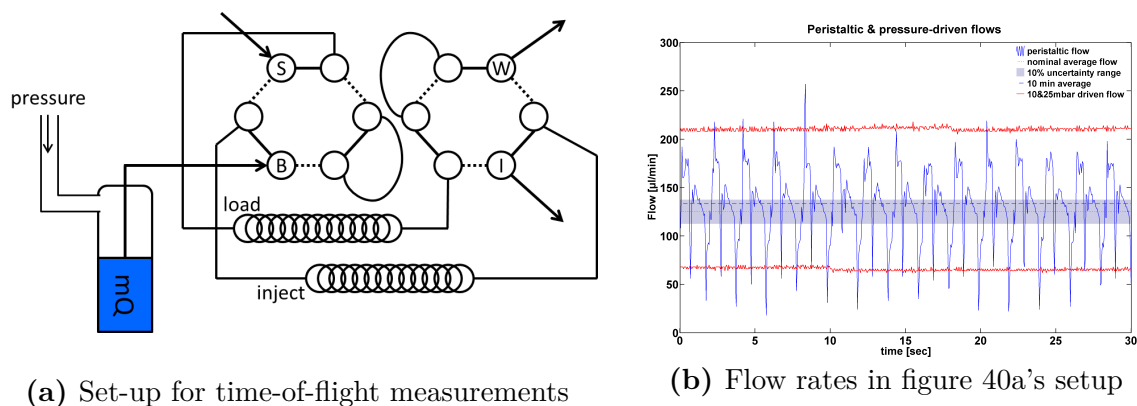
(a) Set-up for time-of-flight measurements

(b) Flow rates in figure 40a's setup

Figure 40: Decoupling pulsatile and pressure-driven flow

Technically, the flow cytometer can be set such as to acquire the pulse width of any PMT. However, the instruments resolution is only 2^{15} and even at a sheath flow driving overpressure of only 25mbar, the instrument would assign a $2.74\mu m$ bead a mean value of 7 in FSC width. Therefore, a National Instruments I/O-card (USB-6216) was connected to the FSC PMT with a sampling rate of $400^{kS}/_{sec}$.
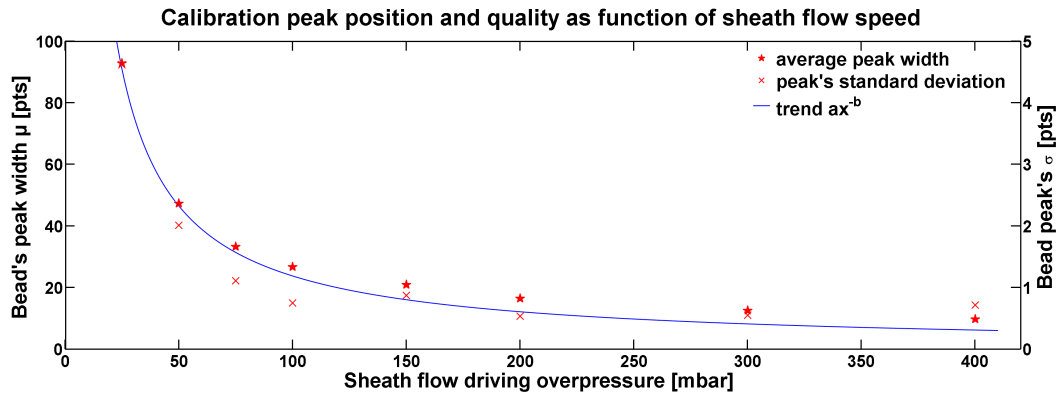
Figure 41: Peak width caused by the time of flight of $3\mu m$ beads

Results of this experiment are shown in figure 41. The y-units, labelled [pts] correspond thus to $(400ksec)^{-1}$ and it becomes apparent that the lower the sheath flow, the longer the TOF. However, as mentioned in section 6.1, the sheath flow needs to reduce the sample streams diameter to the same order of magnitude as the particles detected. Else there might be coincidences leading to an overestimation in size or particles not passing centred thorough the laser beam, leading to their sizes underestimation. These two effects are reflected in the eventually recorded distribution that the standard measurements yielded.

It becomes clear that an overpressure of $200mbar$ does not need to be exceeded in order to reduce the standard histogram's σ. At this pressure the TOF is about 20pts, which is too low a resolution for the particle sizes expected based on results by Steffensen (1997) and Ruth et al. (2003). An I/O-card with a sampling rate of $2.5^{MS}/_{sec}$ might remedy this, but is has to be kept in mind that a $35min$ measurement would yield impractically large data files.

6.4 Indirect calibration

The obtained histograms based on FSC data are thus only loosely related to particle size. As this (to an admittedly less dramatic extend) is also the case for optical attenuation measurements (Ruth et al., 2003; Lambert et al., 2012), the same techniques that are used to mitigate the attenuation problem could be applied here.

This was attempted using the approach suggested by Ruth et al. (2002) discussed in section 5.3.1. Initial bin sizes were assigned by fitting a function of the type ax^b to a series of measured standards as shown for other calibrations in figures 33 and 34.

Subsequently, an 'efficiency correction' was carried out for the $2\mu m$ bin and then the previously fitted bin edges were adjusted to make the cytometric data match the size
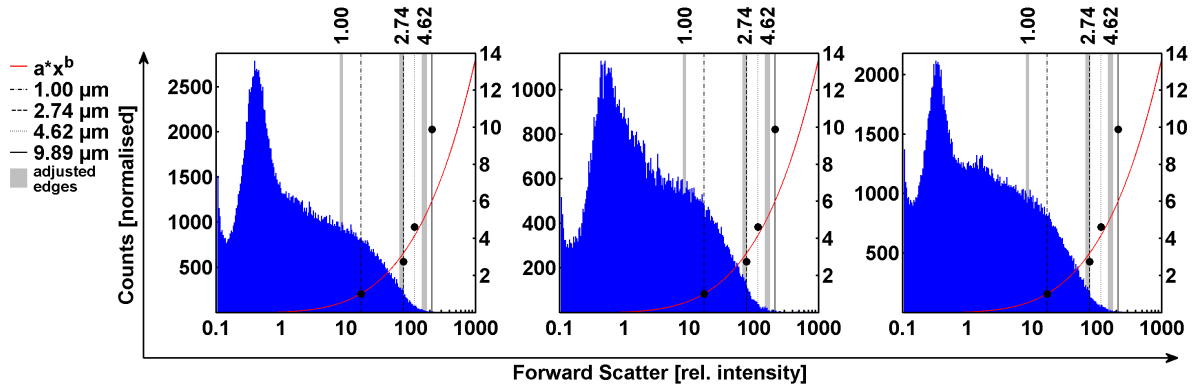
Figure 42: NEEM raw data, detected and corrected standards

distribution independently collected by Coulter counter measurements of the same run performed at LGGE.

The results are presented in figures 42 and 43. In the former it is examined which effect this correction method has on the position of the measured beads. Bead measurements are denoted in black, the fitted calibration curve is shown in red and the adjusted positions of the bins to which the standard would be allocated are shaded in grey. The correction method propose by Ruth et al. (2002) requires one fix point in the high end of the distribution, for which the bin in which the $9.89\mu m$ standard fell was chosen. Therefore, by design, this standard would not change position.

It can be concluded that the ratio of counts in the bins at the higher end to those in the lower end is much lower in the flow cytometer data. More importantly, the results show that the optical alignment did not change during those three runs and that the 'offset' between the two detectors is constant.

This becomes also apparent from figure 43. Here is, in the same manner as for the LS detectors in figure 25, evaluated how the correction based on one run, alters the results of preceding or following runs. Interestingly, if flow cytometer data corrected in this way, the general trend and very closely if the position of the mode as identified by the LGGE CC data can be reproduced.

However, this approach was based on the assumption that bigger particles trigger larger signals. As shown before (e.g. figures 35a and 37) and present in the literature (e.g. Tzur et al., 2011; Shapiro, 2003, p.275), this assumption is unreasonable.
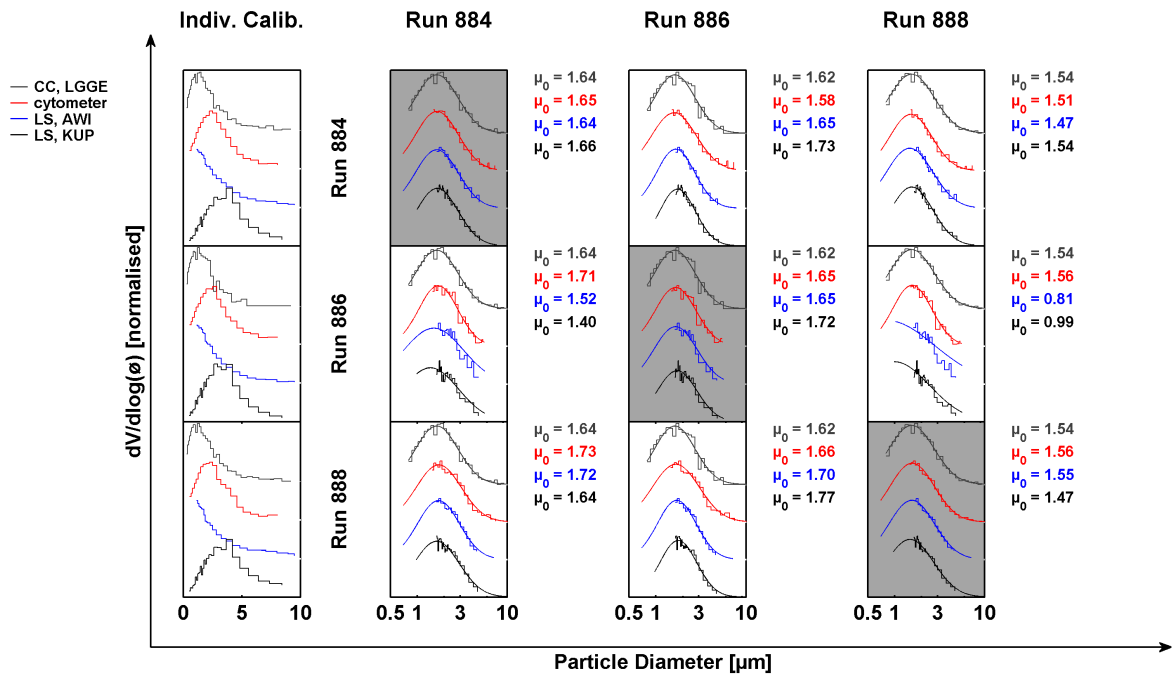
Figure 43: Linking flow cytometric data to LGGE's Coulter counter. Calibration function used was ax^b

6.5 Flow Cytometric Analysis

Time series As opposed to cell sizing, for which microbiologists usually refer to Coulter counters (Shapiro, 2004), time series are occasionally acquired to study reaction kinetics (Nolan et al., 1995; Graves et al., 2002). Figure 44 shows dust time series obtained measuring $3m$ of NEEM Holocene ice during the 2009 field season.

The upper two curves show the normalised number concentration, the lower ones the volume concentration. In the case of the cytometer, sizes are attributed to the individual events as described above. Preliminary bin edges were found fitting ax^b to series of standard measurements and using the correction method developed by Ruth et al. (2002) the data was matched to the LGGE's Coulter counter. In red and blue, the data acquired with the flow cytometer and the Swiss attenuation counter, respectively, is smoothed over $1cm$.

It becomes clear that the cytometer data shows more dispersion due to the lower flow rate (0.150 $^{ml}/_{min}$ vs 1.800 $^{ml}/_{min}$) and the much longer transmission line from the debubbler to the detector. The grey curves show the data in $1mm$ resolution. Due to the low flow rate the cytometer data series is slightly noisier, as the lower count rate results in an increased signal to noise ration.
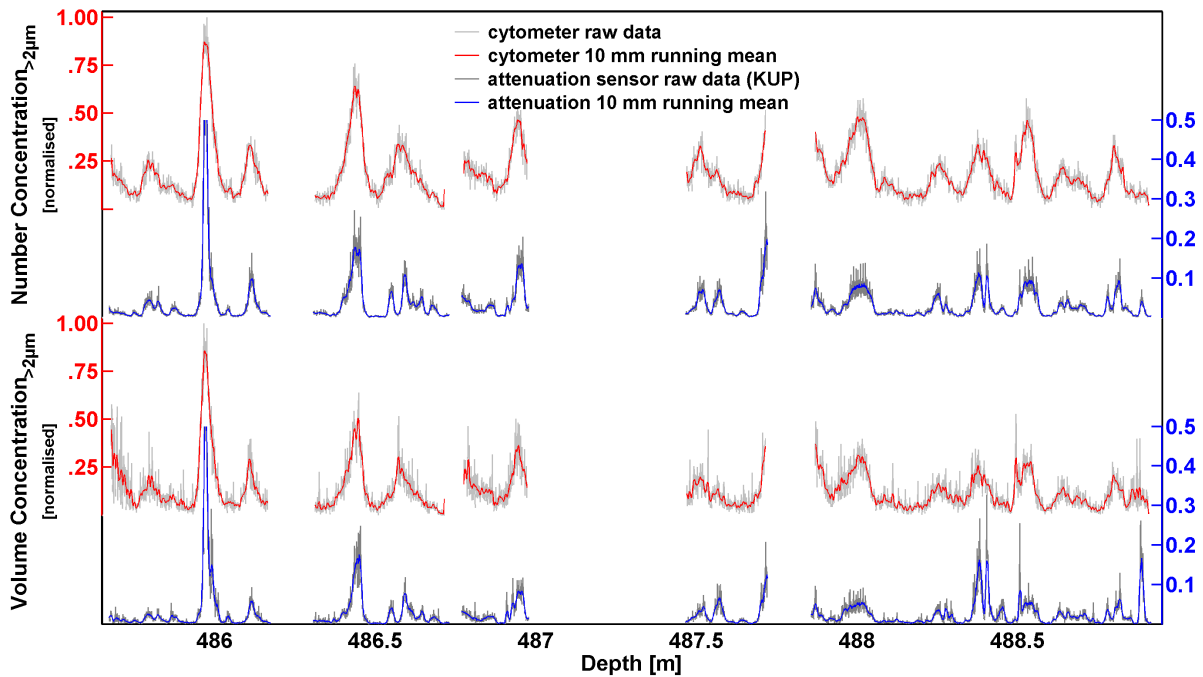
Figure 44: Number Concentration of NEEM Holocene section and volume concentration obtained by linking to discrete Coulter counter measurements performed at LGGE

Transmission lines of different lengths, on the other hand, are responsible for unequal y-values in the LS and cytometer data. The former shows a very prominent and sharp peak at $486m$ depth, which is smoothed out by the detection set-up before it reaches the cytometer. Normalisation of the profiles then results in low y-values for the LS series.

That said, the curves look remarkably similar. This suggests that the cytometer could be the instrument of choice aiming for continuously obtained number concentration records, as in a flow cytometer, coincidences can virtually be excluded by adjusting the sheath flow's magnitude.

Logical gating Much more common in microbiology than the collection of time series, is the construction of logical gates based on one or two parameters, and the combination of multiple gates (Loken et al., 1990; Mandy et al., 1992; Tzur et al., 2011). The potential of theses techniques, used in other disciplines to successfully distinguish between different types of cells or organisms was investigated on data obtained in laboratory NGRIP campaign also used for evaluation of the flow cytometer's potential to produce particle size distributions (see section 6.3).

This campaign was conducted in March 2011 on the Greenland stadial 22 (GS22).
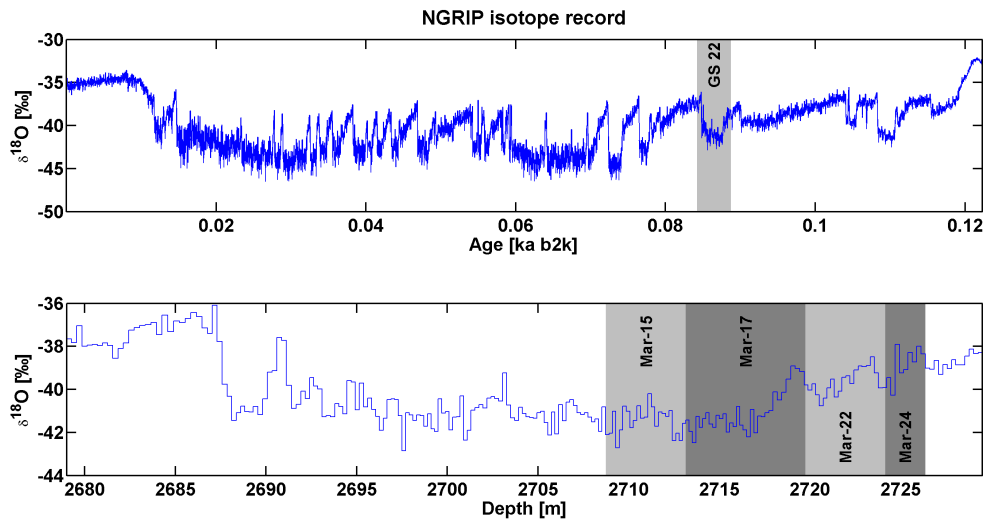
Figure 45: Isotopic record of the entire NGRIP core and the Stadial 22 within

All data collected with the flow cytometer is shown in figure 46. Each row represents a measurement day, also highlighted in the axes zooming in on GS22 in figure 45, the columns are the chronologically ordered quartiles of data acquired that particular day.

Superimposed on the FSC histograms in figure 46a are the standard measurements conducted prior to data acquisition. It can be seen that during the last four days of the GS22 campaign no single monotonically increasing calibration curve could be obtained. However, this is not surprising (see section 6.3.2) and sizing the insolubles was not the aim at the end of this campaign.

Generally speaking, the histograms do not change very much during a day, but considerably on a daily basis. This suggests that the FSC is first and foremost a function of the alignment of the optical path which was optimised prior to any calibration.

One notable exception was March 17th, where the FSC changes drastically in the third run and the scatter plot again during the last run. As the onset of GS22 was measured in those runs (see figure 45), there was a chance that this was a climate signal. Run 17-Mar-D is examined close in figure 47b.

As becomes clear from the SSC-FSC scatter plots in figure 46b, variations in SSC appear to be more pronounced than in the FSC. The reason for this is not clear, sometimes the scatter plot is interpreted as an indicator for the cells or organisms morphology (e.g. Benson et al., 1984; Shapiro, 2003, p.276). Since SSC is set as the trigger for data acquisition (see section 6.2), no data with a relative SSC intensity lower than three is stored, which explains the white bands in the lower part of the 16 scatter plots.
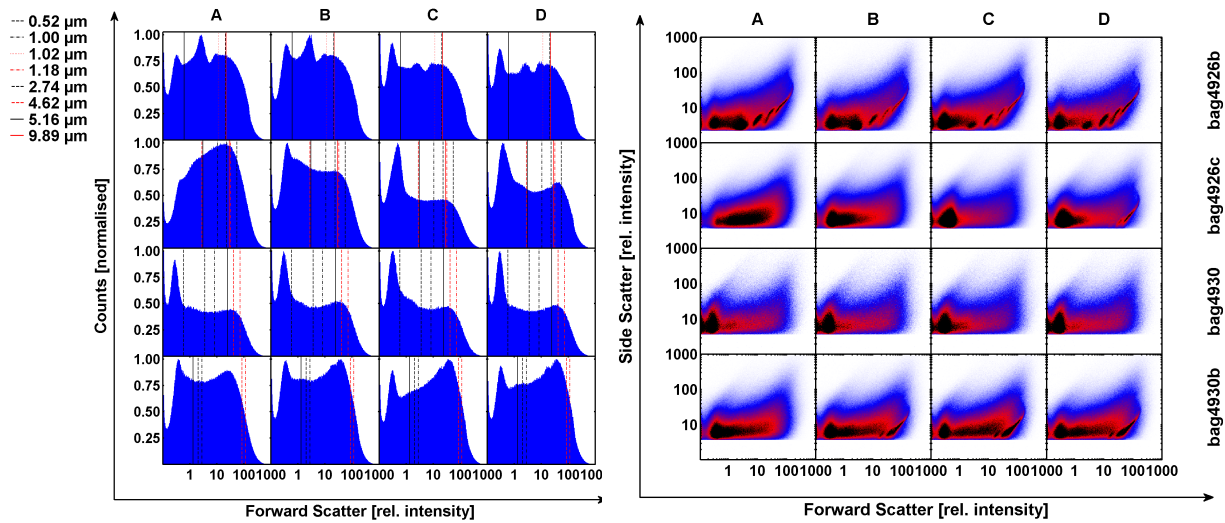
(a) FSC Histograms of GS 22 data   **(b)** SSC vs FSC scatter plots of GS 22 data

Figure 46: Cytometric analysis of GS 22 in NGRIP core

The cytometer data in figures 47 and 48 is linked to the dust record obtained with the CIC LS as it was published by Vallelonga et al. (2012). Depth scale synchronisation was achieved by visually selecting tie points in on average 10cm intervals, and subsequently interpolating both the depth as provided by Vallelonga et al. and the normalised counts as detected.

In figure 47a, the three striking maxima in the FSC histogram of the 15-Mar-C run are gated out and their respective percentage is compared to the normalised count rate. As it is unknown what exactly these maxima represent, any interpretation is difficult. Gate 1, however, exhibits a striking periodicity only loosely related to over all concentration changes. Gates 2 and three, on the other hand, are fairly constant apart from one interval at around $2711.85 m$ depth where both seem to be subjected to noise.

The scatter plot of run 17-Mar-D shows surprisingly many counts at moderate FSC and low SSC intensities. Gating these events out, as indicated by the black envelope in figure 46b's scatter plot, it becomes apparent that there is indeed a sudden increase in particles causing such a signal. Interestingly they seem to coincide with an increase in heavy oxygen isotopes (see figure 45). However, as no other aerosol record simultaneously collected by Vallelonga et al. (2012) reacts to an increase in temperature in neither the bag preceding the step in gated events neither in the following one, it cannot be excluded that the increase is due to a physical shock the instrument received.

Gating in figure 48 is done on prominent features in the number concentration, and
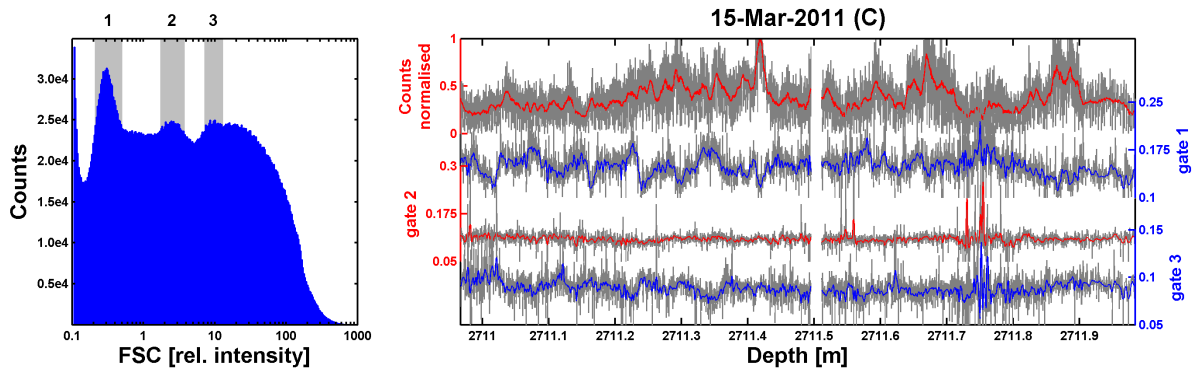
(a) Run 15 March C and gating on FSC signal
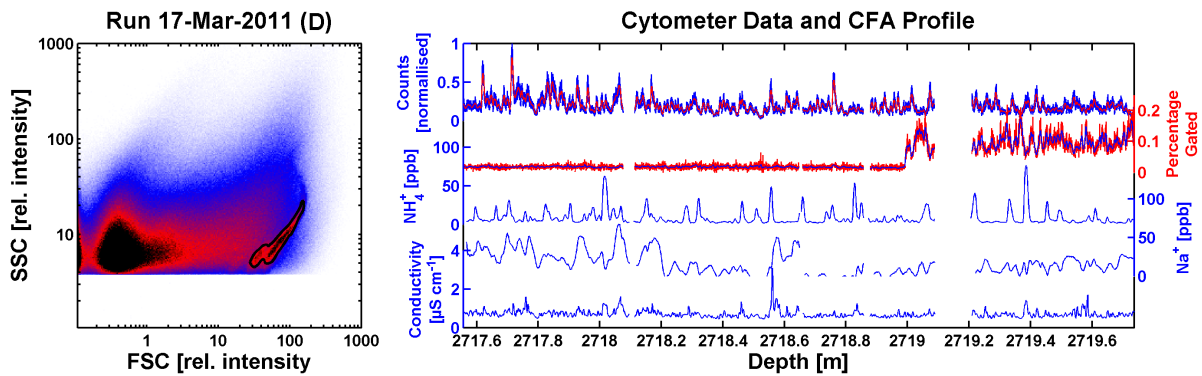
(b) Run 17 March D and gate in the FSC|SSC scatter plot

Figure 47: Cytometric analysis of GS 22 in NGRIP core

then it is investigated to what extend the scatter plot, possibly somehow related to the dust grains' morphology, looks in those sub-samples. I seems that the maxima 2, 5 and 6 resemble each other more than the minima 3 and 4, who have more events in the region gated out before, in figure 47b. These remain, however, vast speculations as long as it is not clear what these scatter plots actually represent.

Conclusion

Cytometers were found to work reliably when the number concentration is the record of interest (figure 44). If the diameter of the sample stream is not much larger than the particles diameter, coincidences can be precluded and a very accurate measure can be obtained.

As soon as quantitative information is to be obtained, however, FCM falls short. For
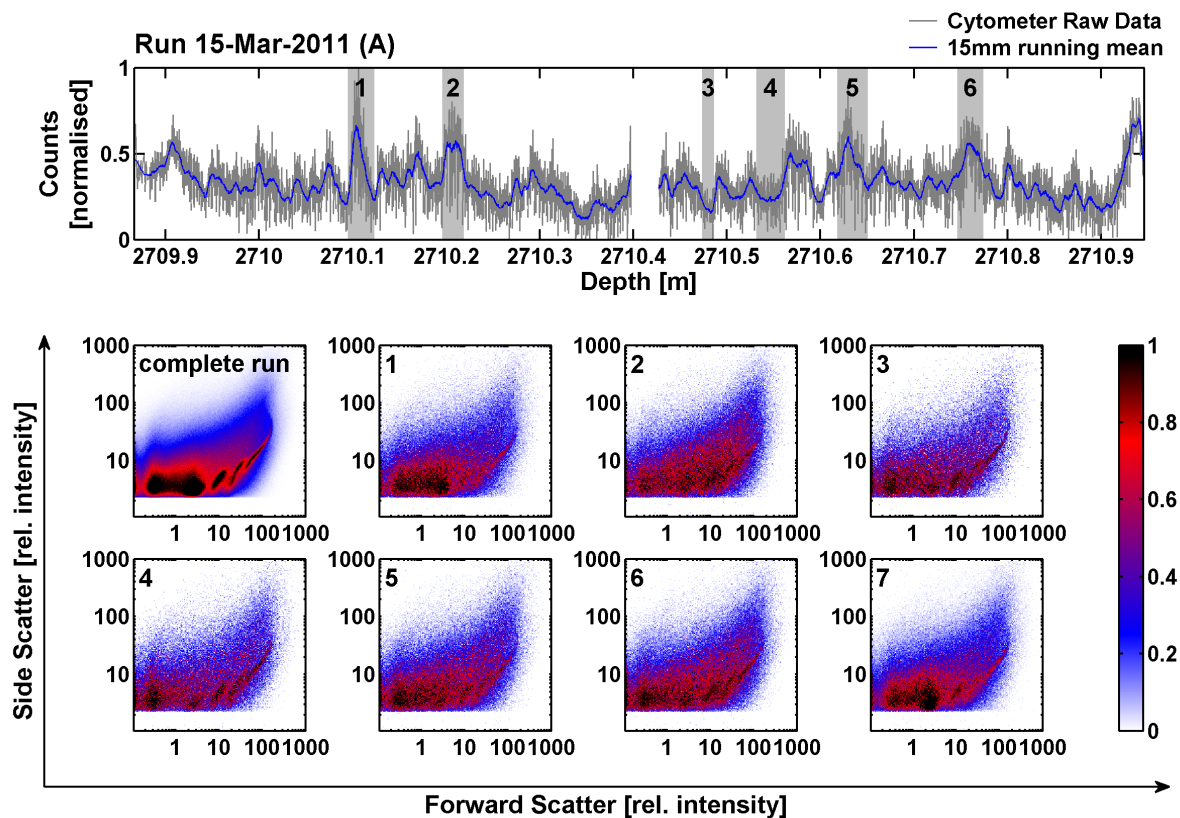
Figure 48: Scatter plots of selected time gates

(1), the incubation time to dye the sample for induced fluorescence is too long to be incorporated into a CFA system, (2) the scattering on particles of sizes commonly found in ice cores is neither geometric nor elastic (section 6.3.2) and (3) the peristaltic pumps used in CFA systems produce a too pulsatile flow to allow for time-of-flight measurements (figure 40b). Dying was therefore abandoned and Shapiro's (2003) advice, to 'avoid thinking of the small angle scatter signal as an accurate measure of cell size', was also followed.

The small difference in particle size and the scattered light's wavelength lead to prevailing Mie scattering, a phenomenon mathematically approached with Bessel functions and Legendre polynomials, i.e. differential equations, consequently incorporating a plethora of sines and cosines in the expected signal (see figure 37). As a matter of fact, if the 'size discrimination of particles with a diameter ratio of 1:2 was accomplished' (Pamme et al., 2003), it might have been a result worth telling the scientific community.

Additionally, FCM suffers from being an optical technique *as such*. The disadvantages of optical techniques - although allowing for continuous operation - are threefold. In addition

to being impossible to calibrate in the range of interest, optical techniques have a lower sensitivity and thus a higher detection limit (Zhang et al., 2009). Also, they do not directly measure volume - the quantity usually reported (Steffensen, 1997; Ruth et al., 2003) - but instead yield a signal dependent on the particle's cross section and surface, from which volume needs to be inferred.

The problem of the pulsatile flow prohibiting TOF analysis could be solved though, by replumbing the fluidic system as sketched in figure 40a. Unfortunately, the CyFlow's maximum resolution of 2^{15} channels is insufficient to derive size from pulse width during time-of-flight measurements. Experiments have been performed using a NI I/O card with a sampling rate of 400kS/sec. Even this has not yielded sufficiently resolvable wide peaks figure 41, which will need to be addressed hardware replacement. This approach can then be expected to result in extremely large data files, but is nonetheless proposed as a more promising was than using the FSC.

Constructing logical gates and analyse only subsets of the collected data might have some quantitative potential. Especially the sudden increase in events gated out in figure 47b and the possibly different morphology of particles found during spring maxima and those in the background figure 48 merits further investigation. However, these results are difficult to interpret as long as it is unclear what they actually represent. Therefore it is suggested to combine further multi-angle scatter experiments with optical imaging.

Chapter 7

Impedance-Based Flow Cytometry

Summary   *When aiming for accurate sizing of particles suspended in a liquid, impedance measurements are superior to optical methods. Impedance measurements are a direct measure of the particle's volume, while for scatter or attenuation detectors the volume has to be inferred from a signal that standard particles with different shape and different optical properties have caused.*

However, until now electrical volumetric measurements had the drawback to allow for discrete measurements only, making them incompatible with CFA systems. This has changed over the last decade with the development of microfluidic Coulter counters and impedance cytometers.

It is found that before integrating this technique into existing CFA systems some problems have to be addressed. (1) When mixing electrolyte into the sample more care needs to be taken to avoid sample dispersion (2) the throughput needs to be increased or multiple detectors are to be connected in parallel and (3) the cytometer's sensitivity was found to be insufficient for particles in the size range present in ice cores, a problem best tackled by the addition of a low conducting sheath flow. Despite these challenges, continuous volumetric measurements based on electrical impedance measurements are believed to be the best way to enhance the quality of aeolian dust data from ice cores, simultaneously yielding information on concentration and size.

7.1 Microfluidic Impedance Cytometry

As mentioned in chapter 5 and frequently reiterated in the literature (Hayakawa et al., 1995; Ruth et al., 2002; Shapiro, 2004; Zhang et al., 2009; Tzur et al., 2011), are resistive pulse measurements superior to laser attenuation (as in the Klotz particle counter, see section 5.2) or laser scatter measurements (as in an optical flow cytometer, see chapter 6) in terms of sensitivity and reproducibility. The disadvantage of these measurements has always been that (1) the instruments were too bulky for transport and that (2) analysis needed to be performed on discrete samples.

These problems have been solved over the last decade by a miniaturisation trend toward so-called microfluidic Coulter counters (μCC) and microfluidic impedance cytometers reviewed by Sun and Morgan (2010), similar and parallel to the miniaturisation trend within the field of optical flow cytometry (see e.g. Ateya et al., 2008; and section 6.1). Taking advantage of the advance in micro-fabrication since the late 1990s (sketched by Rogers and Nuzzo, 2005), resistive pulse detectors could be built to characterise particles flowing through a microchannel.

(a) Detection channel and typical signal   **(b)** Picture of the cytometer chip
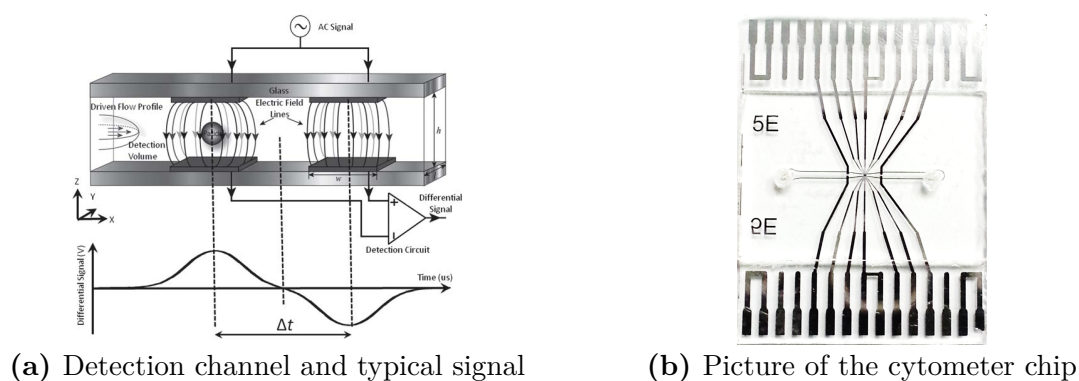
Figure 49: The Impedance Cytometer described by Spencer and Morgan (2011)

In μCCs electrodes are placed on either side of the channel and pores in the channel walls (corresponding to the orifice in classical Coulter counters) allow for a current to pass from one electrode to the other. State-of-the art micro Coulter counters using sophisticated noise reduction techniques (e.g. Wu et al., 2008) have been shown to reach significantly higher sensitivities than classical Coulter counters (Zhang et al., 2009).

From μCCs microfluidic impedance cytometry (MIC) evolved. Ayliffe et al. (1999) presented a chip with electrodes integrated into the channel walls and demonstrated the ability to detect single particles flowing through a femtoliter sized detection cell. As is the case for classical Coulter counters (see section 5.1), an electrolyte (mostly phosphate-buffered sulphate, PBS) is added to the sample before the measurement to increase the signal to noise ratio.

7.2 The Southampton impedance cytometer

Figure 49 shows the design of the impedance cytometer that was developed by Spencer (2013) and connected to the Copenhagen CFA system. Into the walls of the $300\mu m$ long channel with a cross section of $40\mu m^2$, two sets of $30\mu m$ wide electrodes were fabricated with a centre distance of $70\mu m$. An AC voltage was applied to the upper electrodes and

particles passing one-by-one through the interrogation volumes between the electrodes caused a voltage peak proportional to their volume, detected at the lower electrodes.

The signal eventually recorded is the voltage difference between the two bottom electrodes - a typical signal of a particle passing through the channel is also shown in figure 49. This is done with a sample frequency of 230 $^{kS}/_{sec}$, and each event is subsequently found by a signal processing software identifying the symmetrical shape around the central inversion point marked in figure 49a. Due to this distinct shape, the software is to some extend capable of identifying particles that cause signals with amplitudes of the same order as the the noise's.
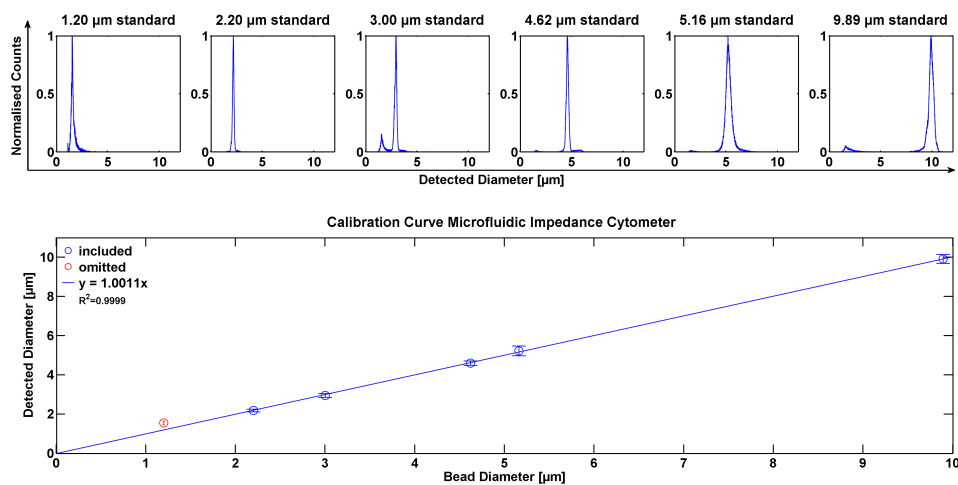
Figure 50: Calibration of the impedance cytometer employed

Calibrations were performed using latex beads of known diameter, which were diluted in demineralised water and final concentrations resembled the expected concentrations of the ice core sample. After adding PBS in a ratio 1:9, the beads were injected into the MIC and the obtained histograms are shown in the top axes of figure 50. The bottom axis displays the calibration curve relating particle size to the cube root of the impedance, with error estimates being equal to the standard deviations of Gaussians fitted to the histograms above.

The calibration curve proves to be linear at least down to a diameter of $2.20\mu m$. At $1.2\mu m$, however, the impedance's cube root seems to overestimate particle size, such that the detection limit for this experiment lay above $1\mu m$ in radius. However, figure 50 also shows that this offset is highly reproducible such that a careful calibration with multiple latex standards of diameters below $2\mu m$ can deal with this problem.

7.3 Impedance cytometry as CFA detection line

When connected to the C CFA, the sample preparation, i.e. the mixing with PBS, had to be done in-flow. Figure 51b shows a the mixing coil utilised in this experiment. The serpentine channel had chevron shaped ridges to aid mixing, were $1mm$ wide and $200\mu m$. The distances of the sample and PBS inlet to the junction of the two flows were arranged such that it both liquids are entering the unit driven by identical pressures, the mixing ratio would always be 1:9 (Spencer, 2013). However, for the sake of simplicity, the flows of sample and PBS were driven by peristaltic pump, assuring a workable mixing ratio by proper pump tube diameter selection.

(a) Experimental set-up   **(b)** The Sample-Electrolyte Mixing Unit
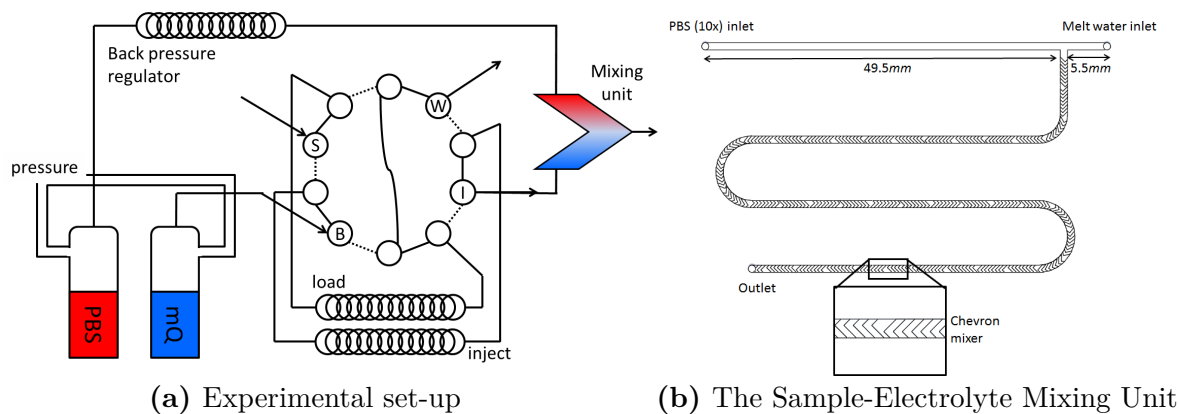
Figure 51: Flow scheme for integration of an impedance cytometer in CFA systems

The first results of impedance cytometry performed on an ice core sample are presented in figure 52. They were obtained while melting a $20cm$ section of the shallow NM2007-I core at roughly $60m$ depth. Additionally, data obtained with a standard particle detector based on laser attenuation is shown. Comparing the standard CFA line to the proposed change in figure 52a highlights the fundamental drawbacks of the tested MIC line.

For one, the count rate of the impedance cytometer was too low, resulting in a very noisy time series (compare figure 44), masking the preserved natural variations in the dust concentration that are detectable by the attenuation sensor. The attenuation sensor's capability stems mainly from the fact that the flow in that line was with 2.1 $^{ml}/_{min}$ more than 20 times that of the MIC with 80 $^{\mu l}/_{min}$. Secondly, the dispersion of the sample is too large to satisfy the pursued high resolution in the C CFA.

Figure 52b finally draws attention to the fact that, despite the highly workable calibration curve (figure 50), particle sizing still seems to be flawed. Apart from the previously

(a) Volume and number concentrations   **(b)** Size distributions
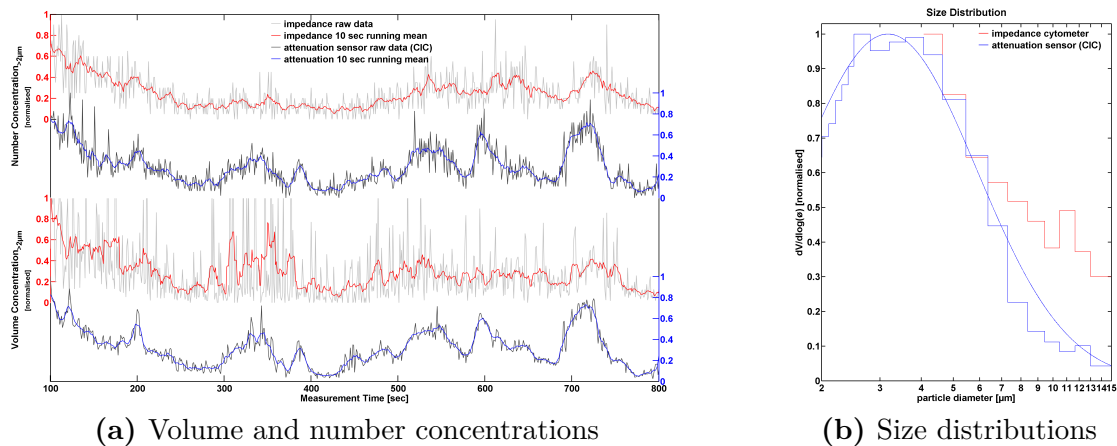
Figure 52: First results of impedance cytometry on an ice
core sample, compared to the AWI attenuation sensor

mentioned unsatisfactory high detection limit (above the mode of an assumed mono-modal
lognormal distribution), it seems that particle sizes are systematically overestimated.

To summarise, in order to engineer a new CFA analysis line, four challenges need to be
addressed. (1) As obvious from figure 50, the limit of detection is too high to capture the
mode of grain size histograms of dust deposited on Greenland. (2) The obtained time series
is too noisy and the smoothing when processing the data should be limited. This is shown
in figure 52a, just as that (3), even the detected signal is being smoothed out. Finally (4),
the MIC seems to overestimate the volumes of also the larger particles (figure 52b).

7.4 Outlook

Grain size overestimation   The apparent overestimation might be a consequence of
the detection limit. Figure 52b shows the *normalised* size distributions, and as the two
obtained distributions do not have their maximum in the same bin, this alters the picture.
If all the y-values of the MIC-obtained curve are lowered by 95% the difference is reduced.
Further, as has been shown before (section 5.3), is the attenuation-obtained curve only an
indication, not an absolute reference. Additionally, the flow profile caused by a peristaltic
pump is highly volatile (see figure 40b), and this effect has not yet been investigated either.
Decoupling the sample stream to the debubbler from the one into the MIC as proposed in
figure 51a could, however, rule possible effects out.

Signal convolution   The reduction of mixing volumes is a challenge omnipresent in Con-
tinuous Flow Analysis, and could consequently be addressed drawing from CFA experience.

The mixing unit depicted in figure 51b is likely to contribute significantly to the signal's smoothing. Its length has not been minimised and the effect of the chevron mixing in flow direction has not yet been investigated. Technically, the unit could be replaced by mixing coils used in classical CFA, those are knotted cautiously to maximize lateral and minimize longitudinal mixing. However, using standard CFA equipment, i.e. HPFE tubing with an inner diameter of no less than $1/16$", this would ask for an increased flow rate to reduce the mixing length, see equation (1.2).

Detection limit A higher flow speed through the detection channel, on the other hand, compromises the limit of detection. Doubling the flow rate results in only half as many data points per event in the recorded voltage signal, therefore the convolution fit is less constrained and the detection limit increases (Spencer, 2013). However, lowering the detection limit is desirable for a plethora of applications and a considerable amount of research has focussed on increasing the MIC's sensitivity.

Gascoyne et al. (2004, cited by Spencer and Morgan, 2011) , for example, point out that the impedance signal caused by a given particle is not solely a function of its volume, but also of its trajectory through the cytometer's interrogation volume. To many applications this does not constitute an unworkable situation. As Spencer and Morgan (2011) show, this dependence is of limited effect over the largest part of the channel area and only close to the electrodes the signal might double.

Gawad et al. (2004) found that additionally, the opacity (i.e. the ratio of the impedances at a high and a low frequency) can be used to correct for the particles position with respect to the electrodes and thus increase the cytometer's sensitivity. Multi-frequency measurements are widely used in impedance cytometry, since higher frequencies cause the capacitance of the cell membrane to decrease (Höber, 1910). Morgan et al. (2007) have developed chips that simultaneously measure the impedance at several hundred frequencies to classify cells based on their size as well as membrane and intracellular properties. Opacity correction seems therefore to be a way to further increase sensitivity.

However, if sensitivity is to be pushed to the limit positional control of the sample stream is desirable. As is the case for optical flow cytometry, the sample streams trajectory can be controlled by ensheathing it in a flow of a particle free liquid. Initially introduced to micro Coulter counting by Nieuwenhuis et al. (2004) as a 'liquid aperture' to avoid channel clogging, a sheath flow was found to be beneficial in multiple respects. Not only does it allow for positional control, but - if of lower conductance than the sample - to also increase the density of electrical field lines in the sample stream (Larsen et al., 1997). Indeed,

insulating sheath flows have been demonstrated to increase the cytometer's sensitivity down to a volume fraction of 0.007% (e.g. Rodriguez-Trujillo et al., 2007; Bernabini et al., 2011).

Furthermore, Wu et al. (2008) demonstrated that the sensitivity can be significantly improved by using sophisticated signal amplification and noise reduction techniques. They demeonstrated the ability to detect particles with a diameter of $520nm$, corresponding to a volume fraction of 0.0004%, one order of magnitude lower than currently available Coulter counters.

(a) Multi-aperture design (taken from Jagtiani et al., 2006)

(b) Multi-channel design (after Zhe et al., 2007)
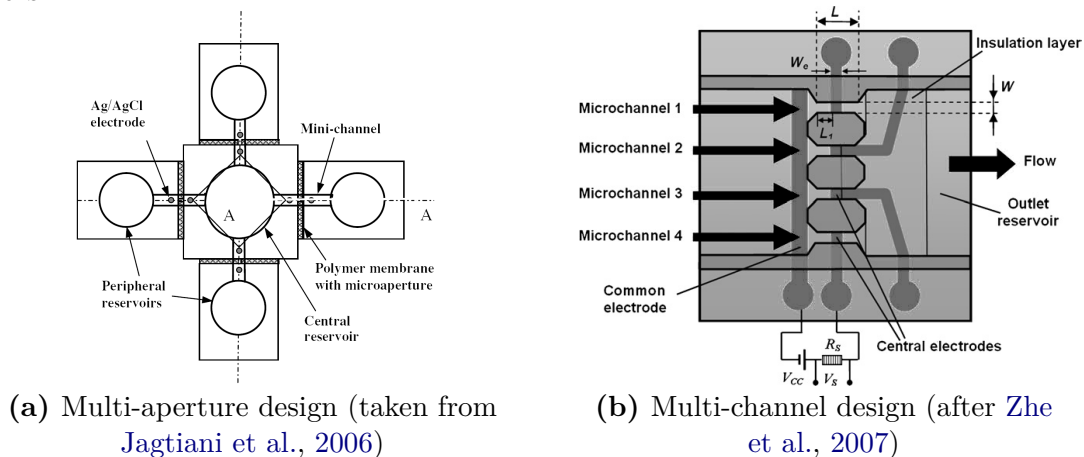
Figure 53: Impedance cytometers designed to increase sample throughput

Sample throughput Next to lowering the detection limit, increasing the throughput is a desire common to multiple impedance cytometer applications (Zhang et al., 2009; Sun and Morgan, 2010; Cheung et al., 2010). Any cytometer's maximal throughput is proportional to its channel's diameter (Zhang et al., 2009) and could therefore be easily increased. However, as mentioned above (section 5.1), an increase in the channel's cross section will inevitably come at the expense of the instrument's sensitivity. To increase the throughput and simultaneously leaving the sensitivity uncompromised, multi-aperture and multi-channel designs have been proposed by Jagtiani et al. (2006) and Zhe et al. (2007), see figure 53.

Jagtiani et al. designed a chip with a central reservoir from which sample is forced into one of four independent detection channels, while Zhe et al. proposed to split an incoming sample stream into four sub-streams, flowing through four parallel channels that share one common electrode. As an increased flow through a CFA mixing coil could supply multiple impedance cytometers with sample, multiple parallel measurements could be performed rather easily on multiple chips.

Chapter 8

A Highly Resolved Dust Size Record

Working Hypothesis *The Aeolean dust deposited on Greenland stems from multiple - in the Holocene and interstadials distinguishable - source areas. Particles entrained above the more productive primary source is responsible for the prominent annual concentration maxima and dominate the signal if averaged over multiple seasons. On sub-seasonal time scales however, a secondary source in closer proximity to the drilling site can be identified by an increased coarse particle percentage (CPP).*

Distinct inputs from this postulated closer source are shown in multiple maxima of the CPP and result in no (little) correlation of the CPP with the number concentration during the Holocene (interstadials). During the last glacial maximum, the primary source's productivity increased relative to the secondary's. Due to the high correlation between all impurities during the last glacial, the secondary source, if present, cannot be identified.
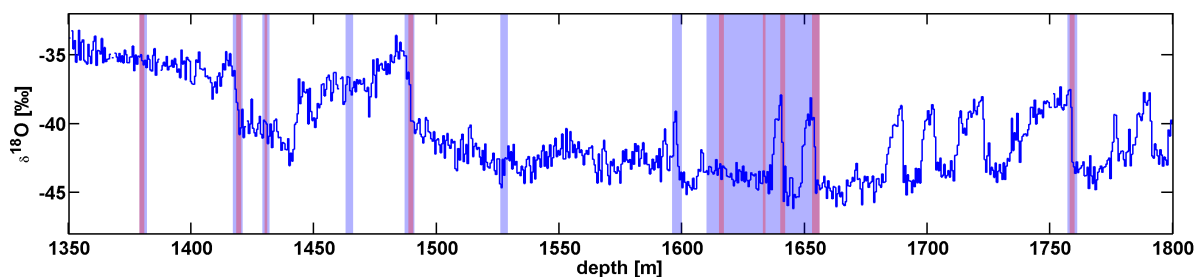
Figure 54: Sections with available (highlighted in blue) and evaluated data (red)

Logical gating, commonly used when processing flow cytometric data (see section 6.5), can also be used on attenuation (Abakus) data, albeit on less parameters. Gating possibilities are limited to information on the binned attenuation (section 5.2) to some extend related to size (section 5.3), the concentration in a given core interval and the time of detection, transferable to core depth and climatic conditions.

'Gating' on these parameters has been done before: Steffensen (1997) and Zielinski et al. (1997) implicitly gated their Coulter counter data on depth. Ruth et al. (2003) and Lambert et al. (2008) additionally gated out a coarse particle fraction from their respective NGRIP and EDC time series. However, the dust time series obtained with the Bernese Abakus connected to the B CFA during the NEEM field seasons 2009 to 2012 has been acquired in much higher temporal resolution and can, at least, confirm or falsify previous findings, if not reveal hitherto unknown information.

8.1 The phase shift between mode and number concentration
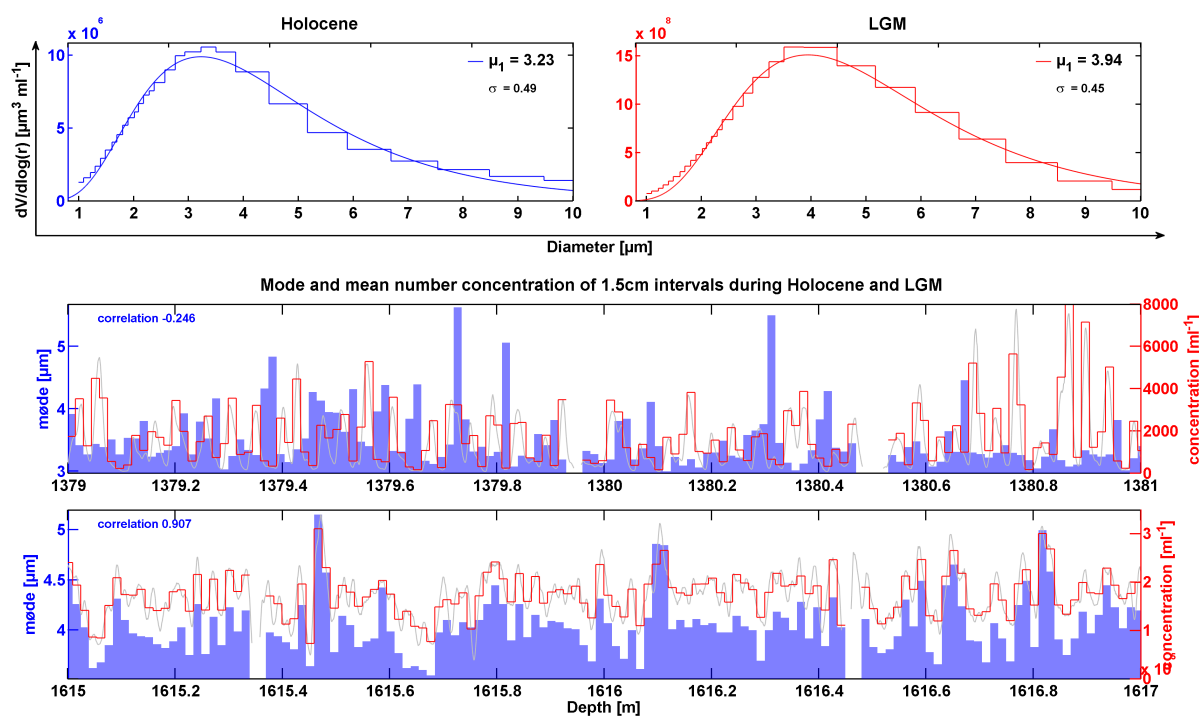
Figure 55: Mode and number concentration in 2m long NEEM core sections from the Holocene & the LGM resp. The time series' resolution is 1.5cm

Figure 55 shows the grain size frequency histograms of all insoluble aerosols detected in a 2m long segment of the NEEM core representative for the early Holocene and the last glacial maximum (LGM), respectively. The size distribution was smoothed using a statistical adjustment of the bin's edges, as described in section 5.3.2. As the data is of previously unavailable high temporal resolution, however, it allows for a more fine scaled

analysis than obtainable when processing $2m$ means. The time series in figure 55 show the mean number concentration (counts ml^{-1}) of $1.5cm$ intervals, along with the modes of the lognormal distributions best representing the observed size distribution.

The size distributions could thus reproduce earlier results, in that insolubles deposited during glacials are more abundant - findings true for Antarctica (Petit et al., 1981; De Angelis et al., 1983) and Greenland (Steffensen, 1997; Ruth et al., 2003). Assuming the preserved size distribution to be represented by a mono-modal lognormal distribution, the data presented in figure 55 further confirms previous findings that the mode lies at larger particle sizes during glacial periods than during the Holocene, while the lognormal distribution's standard deviation is larger in Holocene samples (e.g. Steffensen, 1997; Delmonte et al., 2004b).
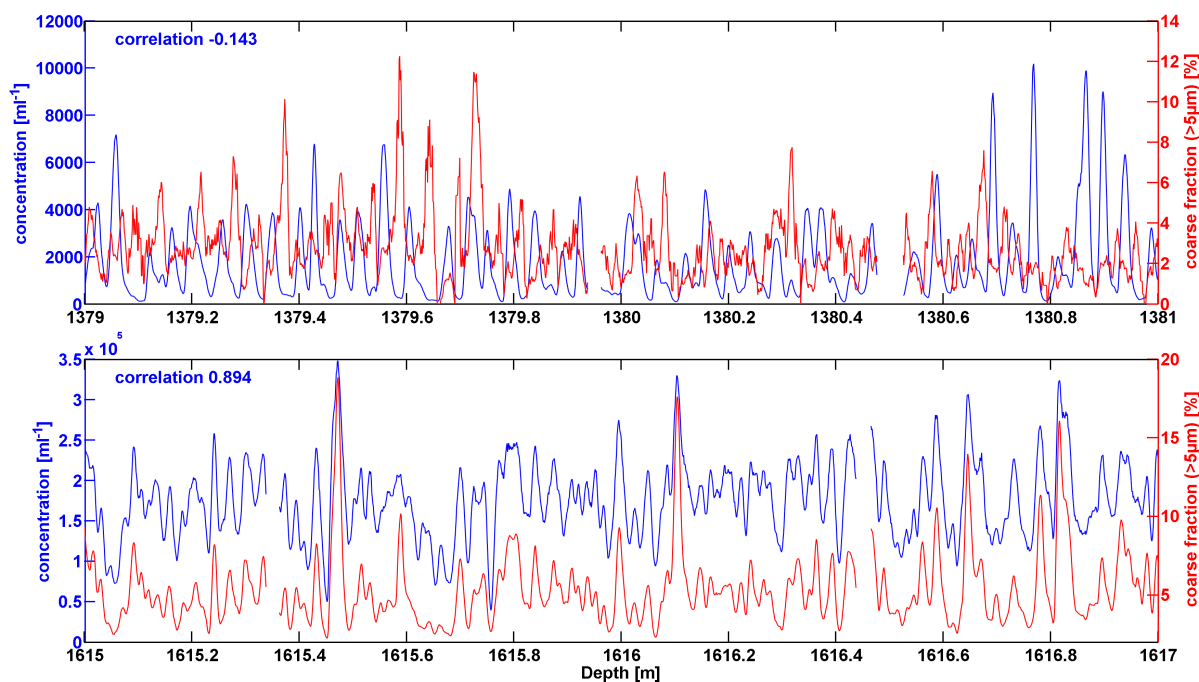
Figure 56: Number concentration and its coarse fraction during Holocene & LGM

Phasing and mutual interrelations of various parameters such as the number concentration, the volume concentration, the mode, the coarse particle percentage (CPP), the 'mean number diameter' or the 'mean volume diameter' have been briefly addressed by Zielinski and Mershon (1997) and (Ruth et al., 2003). The NEEM record with $1.5cm$ resolution demonstrates that the size distribution's mode and the number concentration, highly correlated during the LGM, are slightly anti-correlated in the early Holocene.

As larger modes are a consequence of an increased CPP, the pattern shown in figure 55 is reflected in figure 56. The CPP series, however, offers the advantage that it can be analysed in a higher resolution than the modes, the latter requiring binning over a certain depth interval. Therefore, subsequent analysis is based on the CPP.

8.2 The proximate source's input during the Holocene
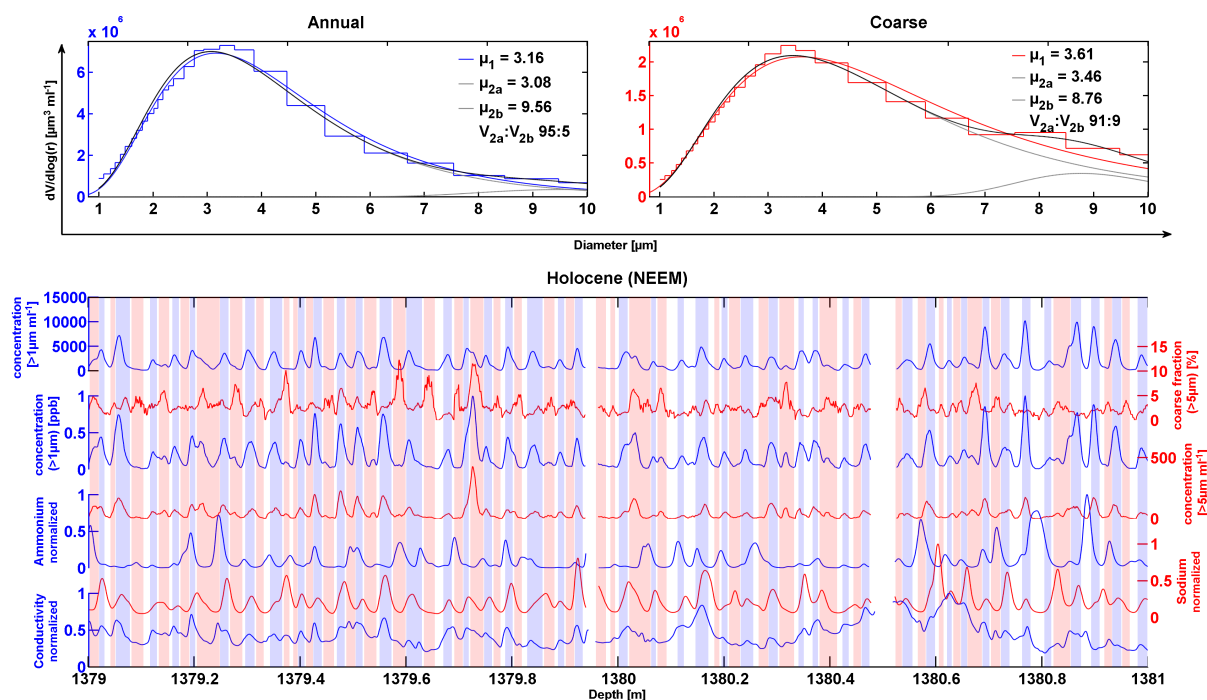
Figure 57: Possible existence of weaker (peaks occasionally invisible in number concentration) proximate (larger mode) source

Figure 57 zooms in on the Holocene section of the NEEM core shown in figure 55. The high resolution of the CFA data set allows for a sub-seasonal analysis of changes in the dust's size distribution. Spikes in the number concentration occur annually (Andersen et al., 2006; Rasmussen et al., 2006), consist primarily of particles entrained in Asia (Bory et al., 2002) and, at least in the very recent past, are deposited during spring (Whitlow et al., 1992; Mosher et al., 1993). These maxima are gated out in figure 57 and their cumulative size distribution is shown in blue.

In between the annual dust spikes, the CPP is found to peak multiple times. This pattern is neither site, nor detection system dependent, as a look at figure 58 reveals. Here

a section of the Holocene NGRIP ice, analysed in the C CFA system optimised for high temporal resolution (Bigler et al., 2011) is presented.

CPP maxima are also gated out in figure 57 and figure 58 and their size distributions are shown in red. The size distribution of particles deposited during those intervals cannot be represented by a mono-modal distribution.

Multi-modal size distributions with modes in the size range capable of long-range transport (i.e. $<10\mu m$, see section 4.1.2) are indicative of multiple sources (Pye, 1987, p.129). In fact, since the size distribution of a dust plume is not significantly altered any after a few days of transport (ca. $1000km$, Scheuvens and Kandler, 2014), the mode might be characteristic for the source region (Maher et al., 2010). The relatively small number of particles deposited during secondary input indicates a weaker source than the primary one, whereas the larger modes indicate a shorter atmospheric residence time.
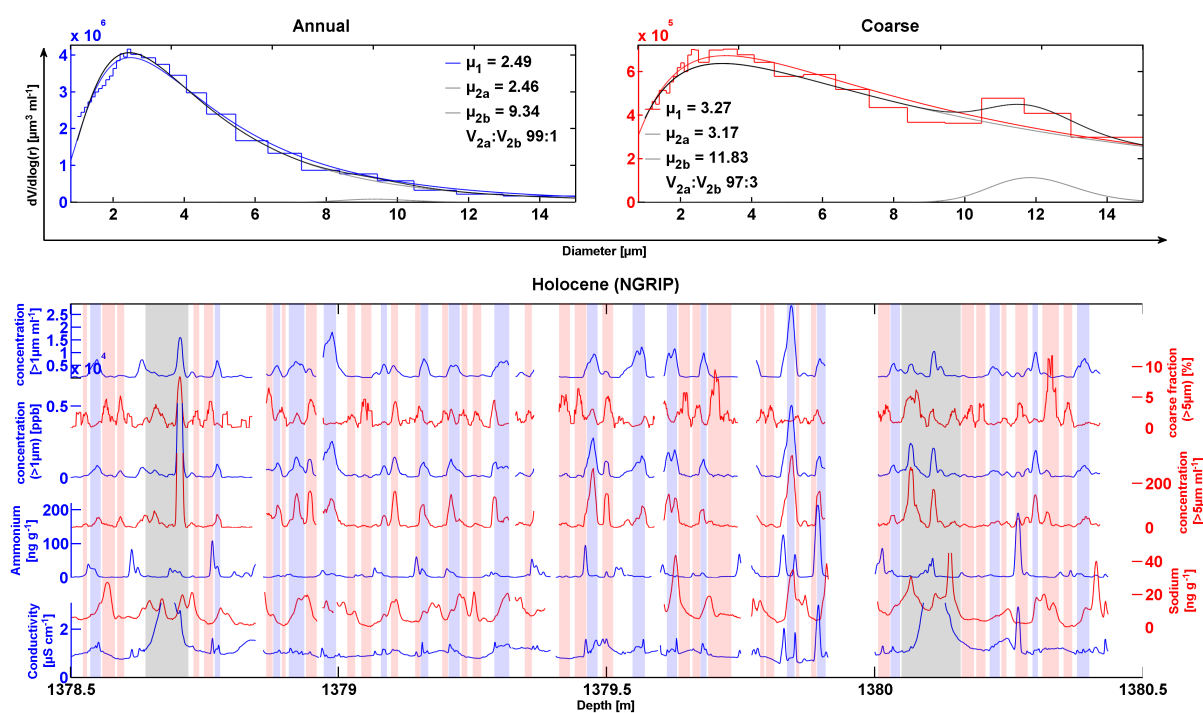
Figure 58: Asynchronous peaks are also present in NGRIP ice and even more prominent in higher resolution

Distinction between different sources by attributing maxima in the number concentration to one, and maxima in CPP to the other becomes problematic when analysing events where maxima in both series almost coincide, as is the case at 1379.72m or 1380.03m in the interval shown in figure 57. The strength of the proposed litmus test, i.e. differentiation

of sources by their CPP, would be weakened by frequent occurrences of such events and could culminate in the rejection of the hypothesis of a secondary source.

However, the high resolution analysis of a 2m segment from the NGRIP core shown in figure 58 diffuses these concerns. Asynchronous peaks in number concentration and CPP are even more prominent in higher resolution and might even suggest that the coincidences in the NEEM record are measurement artefacts.

Intervals have been selected in the same way as the analysis of the NEEM section with the exception of the intervals highlighted in grey, during which grain sizes might have been influenced by a volcano. Figure 57 and figure 58 both show the ammonium and sodium profile obtained by CFA simultaneously with the presented dust records in an attempt to identify the seasonality of the secondary input. Maxima in the NH_4^+ concentration mark summer (Legrand and Mayewski, 1997; Rasmussen et al., 2006) and maxima in Na^+ mark winter (Wolff et al., 2003; Fischer et al., 2007) intervals. These maxima coincide only sporadically with those in CPP (highlighted in red) such that determination of the local source's periodicity remains difficult.

8.3 Potential Source Areas for Greenlandic dust

The high correlation of particle size and number concentration during the glacial depicted in figure 56 supports earlier findings of Svensson et al. (2000). Based on the mineralogical and isotopical composition, Svensson et al. contest that the dust deposited on Greenland during the last glacial originates almost exclusively from one major source area or multiple sources in each others proximity.

Steffensen (1997) already hinted at the annual patterns depicted in the top axes figure 56. Analysing firn samples covering 5 years, Steffensen found the CPP to be significantly higher during autumn|winter, when concentrations are lower. An observation he attributed to the increased relative importance of another source.

This source was further hinted at by Bory et al. (2002), who, analysing snow pit samples, also noted that a second noted that a second source area, 'plays a role during most of year, and during the low-dust season [. . .] in particular'. Figure 59 shows the results of their isotopic analysis of the dust grains, based on which Bory et al. conclude that a the identified secondary source must also be Asian. The resemblance of the respective phasings of (1) the dashed Ca^{2+} curve (a proxy for mineral dust, see section 2.3.1 or 5.4.1) and the *reversed* steplike ϵNd_0 and (2) the number concentration and CPP in figure 56 is remarkable.

The isotopic analysis of the snow pit sample collected by Bory et al. (2003) is shown in
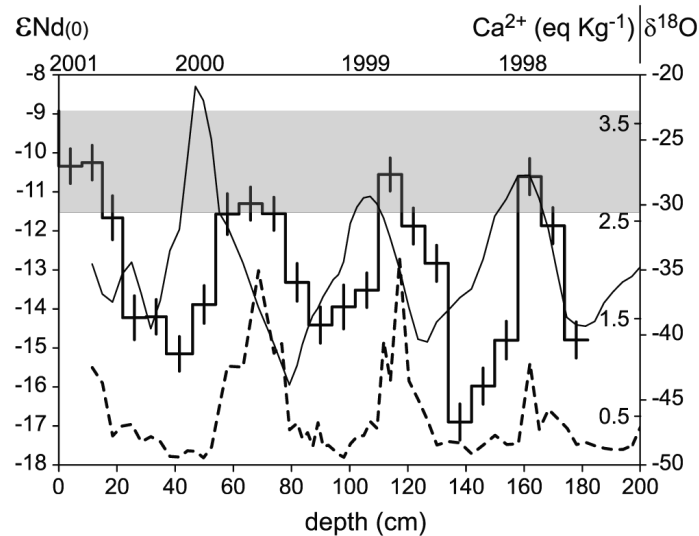
Figure 59: Extending pattern from Holocene ice to present day seasonal variation in the distribution of isotopically distinguishable sources, taken from Bory et al. (2003)

figure 19b. Bory et al. conclude that the secondary source is also Asian, likely the Tengger or the Mu Us, but not the Gobi desert.

However, the year round Asian provenance of dust deposited on Greenland is not uncontested, see section 4.2.2. Based on model results Mahowald et al. (2011) suggest a Northern African source (see figure 20). Their study is supported by Saharan aerosols found in atmospheric samples at Dye 3 and Summit by Mosher et al. (1993) and VanCuren et al. (2012), respectively. Lupker et al. (2010) have extended evidence for a Saharan input back to the eighteenth, conducting isotopic studies on dust in the upper part of the Dye 3 core.

As the mode of a grain size histogram derived from a bulk sample, apart from being source specific (Maher et al., 2010), remains function of transport path (e.g. Ruth et al., 2003), and the secondary modes shown in figures 57 and 58 indicate significantly differing atmospheric residence times, the findings here also suggest a non-Asian source.

8.4 The secondary source during interstadials

In figure 60 the $\delta^{18}O$ - indicating the timing of the warming - and the CPP's correlation with the number concentration are shown. The observed decrease in correlation over stadial-interstadial transitions could indicate a relative increase in the contribution of the secondary source to the total dust load deposited during interstadials.

By zooming in on stadial-interstadial transitions and the last two abrupt warmings at the onset of the Holocene, the rapidity with which these changes occur is investigated. The
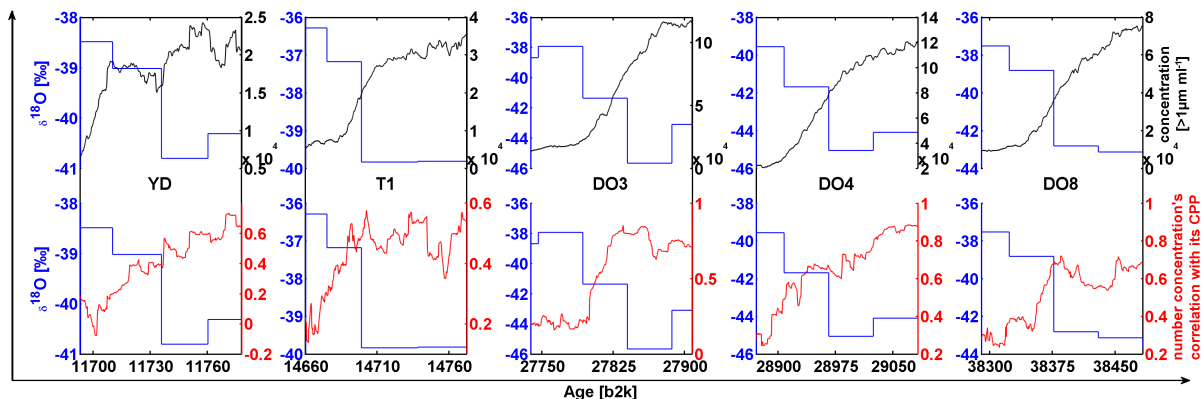
Figure 60: δ^{18}O and the number concentration's correlation
with its coarse fraction over DO's 2|3|4 and in the YD

correlation shown in figure 60 is calculated within a running window of 55cm width. As opposed to the Holocene, a correlation between the number concentration and its CPP is still existing, albeit significantly weakened during the interstadials and the Younger Dryas. The underlying resurgence of a multi-source pattern is too abrupt to explain the dominance of the primary source during the LGM by a shut-off of the secondary source, i.e. due to ice coverage.

Table 2 shows results when a bimodal lognormal distribution is fitted to the smoothed grain size histogram cumulated over a 1m interval of ice representing different climatic periods. Generally, when fitting (monomodal) lognormal distributions to ice core dust data, the fit is constrained to the finer particles detected (Steffensen, 1997; Ruth et al., 2003). Here the whole data set was used, but based on the fits to the maxima in the coarse fractions (i.e. the red histograms in figures 57 and 58), the secondary mode was constrained to be not smaller than $8\mu m$.

The a priori expectations were fulfilled, with larger primary modes in stadials, and smaller modes in interstadial, the Younger Dryas and the Holocene. As the secondary source has a significant share of the deposited dust volume only during the Holocene, its source strength relative to the primary source's must have either decreased, or the atmospheric circulation must have shifted and deposited the secondary's aerosol load elsewhere.

Such varying responses of different source areas over glacial-interglacial transitions are not unknown in the literature. Inspired by Gaiero (2007), who suggested that the Puna-Altiplano might have contributed to Antarctic dust in addition to the long-known Patagonian source, Delmonte et al. (2008b) proposed the former to strengthen while the latter

interval (m)	climatic period	primary input mode (μm)	primary input volume (%)	secondary input mode (μm)	secondary input volume (%)	CPP's correlation
1379|80	Holocene	3.23	95.3	8.57	4.7	-0.042
1430|31	YD	3.19	99.6	9.65	0.4	0.347
1616|17	LGM	3.88	100.0	8.00	0.0	0.864
1633|34	GS3	3.49	100.0	8.00	0.0	0.746
1640|41	IS3	3.18	100.0	8.00	0.0	0.144
1648|49	GS4	3.47	99.6	8.00	0.4	0.705
1653|54	IS4	3.22	100.0	8.00	0.0	0.293
1655|56	GS5	3.54	100.0	8.00	0.0	0.829

Table 2: Characteristics of the primary and secondary input, lower limits for modes set to $1\mu m$ & $8\mu m$ resp.

weakens transitioning into the Eemian or the Holocene.

Further is their a general decreasing correlation between CPP and number concentration with temperature visible in table 2. This could lead to the suspicion that, in the words of Biscaye et al. (1997), in 'a brief period during an interstadial, when dust transport [is] exceptionally low' and the CPP is not, the sample might have an isotopic signature, different from the main source's. As Biscaye et al. (1997) in their prominent study indeed did find such a sample, I would speculate, that during interstadials multiple sources deposit dust on the Greenlandic ice sheet.

8.5 The mode-concentration correlation during stadials

Aerosol records with coinciding maxima during stadials, but source and component dependent seasonality during the Holocene have been reported before (e.g. Rasmussen et al.,2006; Svensson et al.,2006; see figure 61). The relationship between the levels of Ca^{2+} (primary terrestrial origin) and Na^+ (with its major source being marine) in polar ice cores has been analysed by Fischer et al. (2007). They concluded that either their source strengths changed relative to one another or that the atmospheric transport pattern changed, altering the relative life time of the two aerosols.

Shifts in transport pathways to Greenland have often been attributed to the height of the Laurentide ice sheet (Stuiver et al., 1995; Bromwich et al., 2004). If the ice sheet is high enough (Peltier, 1994), the westerly jet stream might split into a western and

(a) Holocene, modified from Rasmussen et al. (2006)

(b) GS8, taken from Andersen et al. (2006)

(c) IS5, taken from Andersen et al. (2006)
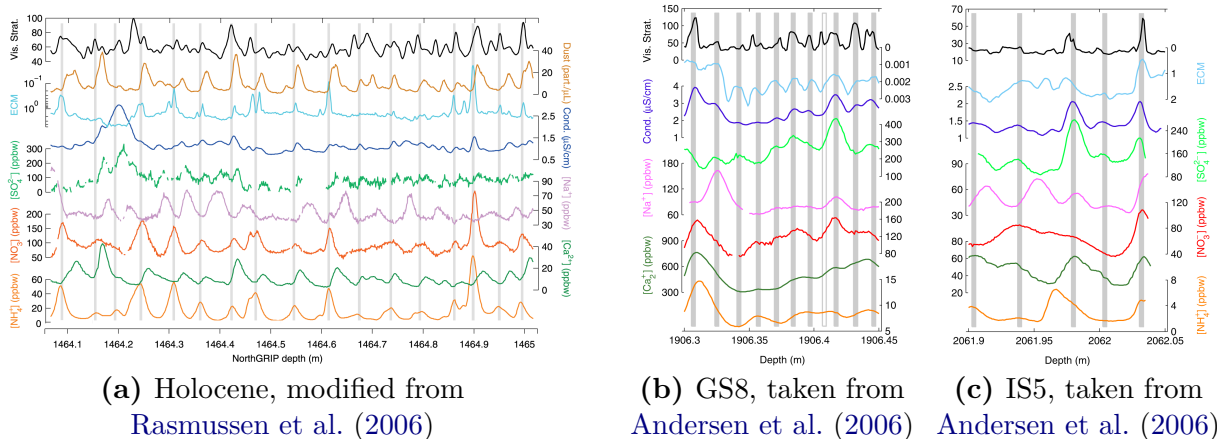
Figure 61: CFA profiles of Holocene, stadial and interstadial NGRIP sections

northern stream around it, significantly alter the transport paths from various sources and disturb the seasonal signal (De Angelis et al., 1997; Andersen et al., 2006). However, Fuhrer et al. (1999) found this explanation unlikely to be accountable for shifts that, as shown by Andersen et al. (2006), can happen on a year-to-year basis.

Another theory is based on model results and suspect depositional processes to be the explanation. Suggesting an increased seasonality of precipitation, substantially decreased in winter (Krinner et al., 1997; Werner et al., 2000), it is hypothesised that most components were deposited in summer. This was rejected by Andersen et al. (2006), who pointed out that species carrying a summer or autumn signal should still be separated from aerosols that are deposited in spring.

Thus, the former hypothesis cannot explain the rapid changes in correlation between CPP and number concentration shown in figure 60 and according to the latter, maxima in the two time series discussed here should still be distinguishable, which they are not. Therefore, a third explanation is proposed, also building on the results reported by (Krinner et al., 1997) and Werner et al. (2000), but unlike earlier invocations of their findings, a dominant dry deposition is assumed in accordance with Mahowald et al. (2011).

The sporadic precipitation events during stadials are not scavenging the impurity content from the atmosphere above the ice sheet. Instead, it is argued, they merely separate layers of previously dry deposited mineral dust. This can also explain the at times very sharp intensity increases and decreases during stadial as presented by Svensson et al. (2005; see also figure 28c). Soluble aerosols are in turn deposited adhering to mineral dust, as it is known for phosphate irrespective of climatic stage (e.g. Kjær et al., 2013). Studies conducted by e.g. Shi et al. (2008) and Li and Shao (2009) have shown, that further solubles

commonly detected by CFA, such as NO_3^- and SO_4^{2-}, readily coat aeolian dust if contemporaneously air-borne.

8.6 Tentative conclusion

The input of a second source in addition to the dominant Asian one (Biscaye et al., 1997) is uncontested in the literature. Bory et al. (2003) have shown the differing seasonality of these two sources determining the dust samples' $\frac{^{143}Nd}{^{144}Nd}$ ratios. This phase shift between ϵNd_0 and dust concentration is likely to coincide with the seasonality between CPP and concentration.

Opposed to the existence of secondary dust input, its provenance is contested between being Asian (e.g. Kahl et al., 1997; Bory et al., 2003) or Saharan (e.g. Lupker et al., 2010; VanCuren et al., 2012). The large difference between the two modes of the bimodal lognormal distribution, fitted to size distributions representing periods of detectable secondary input, seems to support the latter's findings.
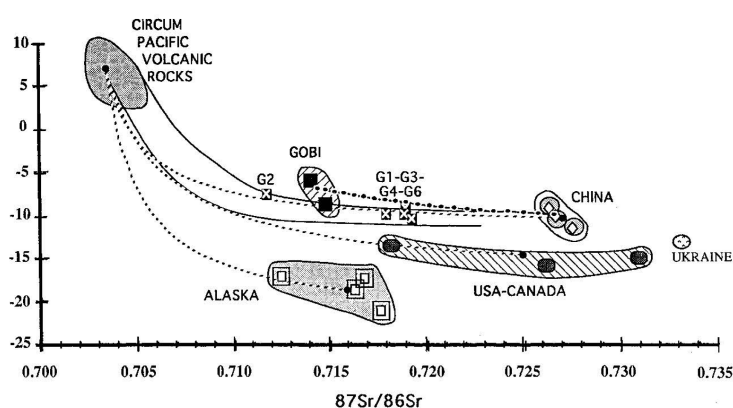
Figure 62: Results of the isotopic analysis by Biscaye et al.,
taken from Biscaye et al. (1997)

Isotopic studies cannot reproduce the high resolution of CFA systems. The presented CFA record suggests a secondary input also during interstadials, inferior to the present day's in relative dust load contribution. In their work identifying eastern Asia as primary source, Biscaye et al. (1997) reported one outlier in the isotopic analysis' $\frac{^{87}Sr}{^{86}Sr}$ versus ϵNd_0 scatter plot (i.e. point G2 in figure 62). That sample represented an interval of low concentration during an interstadial - thus exactly the conditions under which one could expect to identify a secondary input.

Fischer et al. (2007) present indication that the atmospheric circulation patterns during

interstadials and the Holocene resemble each other. This stands in slight contradiction to the findings reported here, as the outlier in the data set obtained by Biscaye et al. (1997), and the autumn source in the work of Bory et al. (2003) show differing isotopic signatures. Owing to the second source's marginal contribution to the dust volume archived, it is impossible to determine its output's size distribution and to present assumptions on the transport path length or atmospheric residence time relative to the primary source's.

The relative importance of the primary source during the glacial is increased, as witnessed by a narrower size distribution (Pye, 1987, p.129). This, and the general pattern of coinciding maxima in concentration profiles of aerosol ejected from their sources with differing seasonality, render the secondary source invisible. It should be noted, though, that as transport patterns can change rapidly (Steffensen et al., 2008) and might alter across stadial-interstadial transitions, the secondary source might not contribute to the Greenlandic dust load at all during stadials.

However, one should be careful to exclude the presence of further dust sources (Muhs, 2013) during stadials. Sources of soluble aerosols with different seasonality at present day can be distinguished as they deposit qualitatively different aerosols and none has been effectively shut off. A complete muting of the secondary source is further unlikely as the maxima in the CPP and number concentration loose their strong correlation quickly with warming temperatures.

These warming temperatures also imply a shift towards more wet deposition (Mahowald et al., 2011) and it is this shift that is speculated to be responsible for the observed phase differences between the various sources. Whereas during warmer stages frequent precipitation scavenges the polar atmosphere and archives also seasonal differences in source strengths, during stadials precipitation might merely be the isolating layer between horizons of accumulated dry deposition horizons. In other words, the degree of correlation between various sources contributing to the aerosol load above Greenland could be a function of dry deposition.

Conclusion

A **Continuous Flow Analysis** (CFA) system was constructed and optimised for high resolution (Bigler et al., 2011). Major improvements were accomplished by **(A1)** redesigning the melthead that now features engraved channels to reduce dispersion on the melter's surface, **(A2)** a drastically reduced flow rate allowing for **(A3)** the reduction of the debubbler's volume by more than a factor of three.

Since the reduced melt rate leads to a diminished amount of sample, the number of analysis lines needed to be reduced. In order to optimally transfer the system's temporal resolution, the choice was made for ammonium (a biospheric summer signal), sodium (marine, winter) and aeolian dust (terrestrial, spring). Further were new detection lines constructed. In particular a classical line for phosphate (Kjær et al., 2011, 2013) and interfaces to couple laser spectrometers detecting CH_4 mixing ratios (Stowasser et al., 2012) and $\delta^{18}O$ and δD-values (Gkinis et al., 2010, 2011).

The attenuation-based laser sensor (LS) commonly integrated into CFA systems (Ruth et al., 2002) was sought to be replaced by a flow cytometer, thus by employing a scattering technique. Due to inconsistent results and the LSs incapability to reproduce volumetric Coulter counter (CC) measurements, dissatisfaction about continuous dust data is mutually shared (e.g. Ruth et al., 2003). However, owing to the grain size of aeolian dust deposited on the polar ice sheets, the scattering signal is best approximated using Gustav Mie's (1908) theory. This means that - in the words of Howard M. Shapiro (2004) - 'although larger particles, in general, produced larger signals than smaller ones, correlations between particle sizes and signal amplitudes were not particularly strong'.

Remedy to the continuous data set's poor quality is believed to be found in the employment of a chip-sized **micro impedance flow cytometer** (MIC, Spencer and Morgan, 2011). MICs combine the electronic volume measurements with the continuous sample stream needed for CFA. However, issues that need to be addressed before integrating MICs as a fully-fledge detection line are **(B1)** the detection limit and **(B2)** the throughput, but solutions for both challenges have been suggested. These proposals are likely to mitigate the other two obstacles mentioned, namely the possible overestimation of particle sizes (figure 52b) and the unacceptably high signal dispersion.

While LS data has been shown (and known) not to be robust enough for quantitative

analysis, the qualitative information that can be obtained from LS obtained CFA profiles has not yet been fully exploited. An **analysis of $10m$ LS data** on selected intervals of the NEEM core could, confirm that **(C1)** multiple sources contribute to the total dust load above the Greenlandic ice sheet at present (e.g. Bory et al., 2003).

Andersen et al. (2006) and Rasmussen et al. (2006) reported a high degree of covariation among aerosols records from various sources in stadials and less (no) correlation in interstadials (the Holocene). While many exhibit differing seasonal variation during the Holocene and interstadials, they are archived in the same stratigraphic layers during stadials. The data analysed here reveals that also the correlation between the number concentration and the coarse particle percentage (CPP) is a function of climatic stage, following the same pattern.

Further could **(C2)** the dominance of a single source during stadials, results presented earlier by Biscaye et al. (1997) and Svensson et al. (2000), be seen in the data. The primary source's relatively (and thus absolutely) largest increase strength was mirrored in a, relative to Holocene samples, narrower grain size distribution in sections representing stadials. That is further supported by a marginalised secondary contribution to the dust load during the glacial (table 2).

Thus, being rooted in the credible reproduction of expected patterns, further claims could be made taking advantage of the higher temporal resolution over several climatic stages, compared to the studies by Biscaye et al., Svensson et al. and Bory et al. mentioned above. In the debate concerning the geographical location of the secondary source, the data indicates that **(C3)** the secondary source is not in the proximity of the primary one. This is mirrored in a significant difference in the mean particles size between those stemming from the primary and those being ejected by secondary source (figures 57 and 58).

It is finally suggested the correlation's decrease with increasing temperatures is due to **(C4)** dominant dry deposition during stadials and a shift to more (dominant) wet deposition during interstadials (the Holocene). This is done acknowledging the increased seasonality of precipitation reported by, for example, Krinner et al. (1997) and following Mahowald et al. (2011) in their conviction of little wet deposition during the LGM (and, by extrapolation any stadial). Thus, it is proposed that the different 'modes of deposition' (Andersen et al., 2006) are a measure the relative importance of dry and wet deposition to the ice sheet.

List of Figures

5 Aeolian Dust Detection in Ice Cores

6 Optical Flow Cytometry

References

Abbott, P. M. and Davies, S. M. (2012). Volcanism and the Greenland ice-cores: the tephra record. *Earth Science Reviews*, 115(3):173–191. (pg. 11, 23, 31, 54)

Alley, R., Finkel, R., Nishiizumi, K., Anandakrishnan, S., Shuman, C., Mershon, G., Zielinski, G., and Mayewski, P. (1995). Changes in continental and sea-salt atmospheric loadings in central Greenland during the most recent deglaciation: Model-based estimates. *Journal of Glaciology*, 41(139):503–514. (pg. 65)

Alley, R., Saltzman, E., Cuffey, K., and Fitzpatrick, J. (1990). Summertime formation of depth hoar in Central Greenland. *Geophysical Research Letters*, 17(12):2393–2396. (pg. 24)

Alley, R., Shuman, C., Meese, D., Gow, A., Taylor, K., Cuffey, K., Fitzpatrick, J., Grootes, P., Zielinski, G., Ram, M., Spinelli, G., and Elder, B. (1997). Visual-stratigraphic dating of the GISP2 ice core: Basic, reproducibility, and application. *Journal of Geophysical Research*, 102(C12):26367–26382. (pg. 24, 74)

Andersen, K. K., Svensson, A., Rasmussen, S. O., Steffensen, J. P., Johnsen, S. J., Bigler, M., Röthlisberger, R., Ruth, U., Siggaard-Andersen, M.-L., Dahl-Jensen, D., Vinther, B. M., and Clausen, H. B. (2006). The Greenland Ice Core Chronology 2005, 15-42 ka. Part 1: Constructing the time scale. *Quaternary Science Reviews*, 25(23-24):3246–3257. (pg. 10, 16, 39, 59, 65, 75, 110, 116, 120)

Anklin, M., Bales, R., Mosley-Thompson, E., and Steffen, K. (1998). Annual accumulation at two sites in northwest Greenland during recent centuries. *Journal of Geophysical Research*, 103(D22):28775–8784. (pg. 24, 25, 28, 29, 30, 33, 34, 38)

APHA (2005). *Standard methods for the examination of water and wastewater*. American Public Health Association. Eaton, A.D., Clesceri, L.C., and Greenberg, A.E. (eds). (pg. 34)

Ateya, D. A., Erickson, J. S., Howell, Jr., P. B., Hilliard, L. R., Golden, J. P., and Ligler, F. S. (2008). The good, the bad, and the tiny: A review of microflow cytometry. *Analytical and Bioanalytical Chemistry*, 391(5):1485–1498. (pg. 68, 77, 101)

Ayliffe, H., Bruno Frazier, A., and Rabbitt, R. (1999). Electric impedance spectroscopy using microchannels with integrated metal electrodes. *Journal of Microelectromechanical Systems*, 8(1):50–57. (pg. 101)

Bagnold, R. (1941). *The Physics of Blown Sand and Desert Dunes*. Methuen, New York. (pg. 57)

Bagnold, R. (1960). The re-entrainment of settled dusts. *International journal of air pollution*, 2:357–363. (pg. 57)

Balkanski, Y., Schulz, M., Claquin, T., and Guibert, S. (2007). Reevaluation of Mineral aerosol radiative forcings suggests a better agreement with satellite and AERONET data. *Atmospheric Chemistry and Physics*, 7(1):81–95. (pg. 55, 58)

Banta, J. R., McConnell, J. R., Edwards, R., and Engelbrecht, J. P. (2008). Delineation of carbonate dust, aluminous dust, and sea salt deposition in a Greenland glaciochemical array using positive matrix factorization. *Geochemistry Geophysics Geosystems*, 9:19. (pg. 61, 62, 73, 74)

Barnes, P. R. F., Wolff, E. W., Mader, H. M., Udisti, R., Castellano, E., and Röthlisberger, R. (2003). Evolution of chemical peak shapes in the Dome C, Antarctica, ice core. *Journal of Geophysical Research*,

108(D3). (pg. 39)

Basile, I., Grousset, F., Revel, M., Petit, J.-R., Biscaye, P., and Barkov, N. (1997). Patagonian origin of glacial dust deposited in East Antarctica (Vostok and Dome C) during glacial stages 2, 4 and 6. *Earth and Planetary Science Letters*, 146:573–589. (pg. 64)

Baumgartner, M., Schilt, A., Eicher, O., Schmitt, J., Schwander, J., Spahni, R., Fischer, H., and Stocker, T. F. (2012). High-resolution interpolar difference of atmospheric methane around the last glacial maximum. *Biogeosciences*, 9(10):3961–3977. (pg. 52)

Bazin, L., Landais, A., Lemieux-Dudon, B., Toyé Mahamadou Kele, H., Veres, D., Parrenin, F., Martinerie, P., Ritz, C., Capron, E., Lipenkov, V., Loutre, M.-F., Raynaud, D., Vinther, B., Svensson, A., Rasmussen, S. O., Severi, M., Blunier, T., Leuenberger, M., Fischer, H., Masson-Delmotte, V., Chappellaz, J., and Wolff, E. (2013). An optimized multi-proxy, multi-site Antarctic ice and gas orbital chronology (AICC2012): 120-800 ka. *Climate of the Past*, 9(4):1715–1731. (pg. 16, 39)

Beer, J., Finkel, R., Bonani, G., Gäggeler, H., Görlach, U., Jacob, P., Klockow, D., Langway, J. C., Neftel, A., Oeschger, H., Schotterer, U., Schwander, J., Siegenthaler, U., Suter, M., Wagenbach, D., and Wölfli, W. (1991). Seasonal variations in the concentration of ^{10}Be, Cl^-, NO_3^-, SO_4^{2-}, H_2O_2, ^{210}Pb, ^3H, mineral dust, and $\delta^{18}O$ in Greenland snow. *Atmospheric Environment*, 25A(5/6):899–904. (pg. 33)

Begley, I. S. and Scrimgeour, C. M. (1996). On-line reduction of H_2O for δ^2H and $\delta^{18}O$ measurement by continuous-flow isotope ratio mass spectrometry. *Rapid Communications in Mass Spectrometry*, 10(8):969–973. (pg. 47)

Bendschneider, K. and Robinson, R. (1952). A new spectrophotometric determination of nitrite in sea water. *Journal of Marine Research*, 11:87–96. (pg. 34, 35)

Benson, M. C., McDougal, D. C., and Coffey, D. S. (1984). The application of perpendicular and forward light scatter to assess nuclear and cellular morphology. *Cytometry*, 5(5):515–522. (pg. 95)

Bergametti, G. and Foret, G. (2014). Dust deposition. In Stuut, J.-B. and Knippertz, P., editors, *Mineral dust - A key player in the earth system.* Springer. *in preparation.* (pg. 65)

Bernabini, C., Holmes, D., and Morgan, H. (2011). Micro-impedance cytometry for detection and analysis of micron-sized particles and bacteria. *Lab on a Chip*, 11(3):407–412. (pg. 106)

Bigler, M. (2008). *CFA Dokumentation.* personal communication. (pg. 21, 33)

Bigler, M., Röthlisberger, R., Lambert, F., Stocker, T., and Wagenbach, D. (2006). Aerosol deposited in East Antarctica over the last glacial cycle: Detailed apportionment of continental and sea-salt contributions. *Journal of Geophysical Research*, 111(D8):D08205. (pg. 27)

Bigler, M., Svensson, A., Kettner, E., Vallelonga, P., Nielsen, M. E., and Steffensen, J. P. (2011). Optimization of high-resolution continuous flow analysis for transient climate signals in ice cores. *Environmental Science & Technology*, 45(10):4483–4489. (pg. vi, 11, 13, 24, 25, 28, 36, 37, 38, 68, 70, 111, 119, 121)

Bigler, M., Svensson, A., Steffensen, J. P., and Kaufmann, P. (2007). A new continuous high-resolution detection system for sulphate in ice cores. *Annals of Glaciology*, 45:178–182. (pg. 21, 31, 32, 33, 121)

Bigler, M., Wagenbach, D., Fischer, H., Kipfstuhl, J., Miller, H., Sommer, S., and Stauffer, B. (2002). Sulphate record from a northeast Greenland ice core over the last 1200 years based on continuous flow analysis. *Annals of Glaciology*, 35:250–256. (pg. 32)

Biscaye, P., Grousset, F., Revel, M., Van der Gaast, S., Zielinski, G., Vaars, A., and Kukla, G. (1997). Asian provenance of glacial dust (stage 2) in the Greenland Ice Sheet Project 2 ice core, Summit, Greenland.

Journal of Geophysical Research, 102(C12):26765–26781. (pg. 61, 62, 115, 117, 118, 120)

Blankenstein, G. and Larsen, U. D. (1998). Modular concept of a laboratory on a chip for chemical and biochemical analysis. *Biosensors and Bioelectronics*, 13(3-4):427 – 438. (pg. 77)

Blunier, T. and Brook, E. J. (2001). Timing of millennial-scale climate change in Antarctica and Greenland during the last glacial period. *Science*, 291(5501):109–112. (pg. 49)

Blunier, T., Chappellaz, J., Schwander, J., Dllenbach, A., Stauffer, B., Stocker, T., Raynaud, D., Jouzel, J., Clausen, H., Hammer, C., and Johnsen, S. (1998). Asynchrony of Antarctic and Greenland climate change during the last glacial period. *Nature*, 394(6695):739–743. (pg. 24, 50)

Blunier, T., Chappellaz, J., Schwander, J., Stauffer, B., and Raynaud, D. (1995). Variations in atmospheric methane concentration during the Holocene epoch. *Nature*, 374(6517):46–49. (pg. 9)

Bohren, C. F. and Huffman, D. R. (2004[1983]). *Absorption and scattering of light by small particles.* Wiley, Winheim. (pg. 86)

Bory, A.-M., Biscaye, P., Piotrowski, A., and Steffensen, J. (2003). Regional variability of ice core dust composition and provenance in Greenland. *Geochemistry, Geophysics, Geosystems*, 4(12):1107. (pg. 61, 62, 63, 112, 113, 117, 118, 120)

Bory, A.-M., Biscaye, P. E., Svensson, A., and Grousset, F. E. (2002). Seasonal variability in the origin of recent atmospheric mineral dust at NorthGRIP, Greenland. *Earth and Planetary Science Letters*, 196:123–134. (pg. 61, 62, 73, 110, 112)

Bourgeois, J. C. (2000). Seasonal and interannual pollen variability in snow layers of arctic ice caps. *Review of Palaeobotany and Palynology*, 108(1-2):17–36. (pg. 11)

Bowen, H. J. M. (1979). *Environmental Chemistry of the Elements.* Academic Press, London. (pg. 27, 62, 73)

Boyd, P. W. and Ellwood, M. J. (2010). The biogeochemical cycle of iron in the ocean. *Nature Geoscience*, 3(10):675–682. (pg. 55, 56)

Boyd, P. W., Jickells, T., Law, C. S., Blain, S., Boyle, E. A., Buesseler, K. O., Coale, K. H., Cullen, J. J., de Baar, H. J. W., Follows, M., Harvey, M., Lancelot, C., Levasseur, M., Owens, N. P. J., Pollard, R., Rivkin, R. B., Sarmiento, J., Schoemann, V., Smetacek, V., Takeda, S., Tsuda, A., Turner, S., and Watson, A. J. (2007). Mesoscale iron enrichment experiments 1993-2005: synthesis and future directions. *Science*, 315(5812):612–617. (pg. 56)

Bromwich, D., Toracinta, E., Wei, H., Oglesby, R., Fastook, J., and Hughes, T. (2004). Polar MM5 simulations of the winter climate of the Laurentide Ice Sheet at the LGM. *Journal of Climate*, 17(17):3415–3433. (pg. 115)

Brook, E., Harder, S., Severinghaus, J., Steig, E., and Sucher, C. (2000). On the origin and timing of rapid changes in atmospheric methane during the last glacial period. *Global Biogeochemical Cycles*, 14(2):559–572. (pg. 9, 49)

Buizert, C., Martinerie, P., Petrenko, V. V., Severinghaus, J. P., Trudinger, C. M., Witrant, E., Rosen, J. L., Orsi, A. J., Rubino, M., Etheridge, D. M., Steele, L. P., Hogan, C., Laube, J. C., Sturges, W. T., Levchenko, V. A., Smith, A. M., Levin, I., Conway, T. J., Dlugokencky, E. J., Lang, P. M., Kawamura, K., Jenk, T. M., White, J. W. C., Sowers, T., Schwander, J., and Blunier, T. (2012). Gas transport in firn: multiple-tracer characterisation and model intercomparison for NEEM, Northern Greenland. *Atmospheric Chemistry and Physics*, 12(9):4259–4277. (pg. 9, 52)

Burakham, R., Higuchi, K., Oshima, M., Grudpan, K., and Motomizu, S. (2004). Flow injection spectrophotometry coupled with a crushed barium sulfate reactor column for the determination of sulfate ion in water samples . *Talanta*, 64(5):1147 – 1150. (pg. 33)

Caspersson, T. O. (1950). *Cell growth and cell function*. Norton, New York. (pg. 76, 77)

Chappellaz, J., Barnola, J., Raynaud, D., Korotkevich, Y., and Lorius, C. (1990). Ice-core record of atmospheric methane over the past 160,000 years. *Nature*, 345(6271):127–131. (pg. 49, 50)

Chappellaz, J., Blunier, T., Kints, S., Barnola, J.-M., Raynaud, D., and Stauffer, B. (1997). Changes in the atmospheric CH_4 gradient between Greenland and Antarctica during the Holocene. *Journal of Geophysical Research*, 102(D13):15987–15997. (pg. 24, 50)

Chappellaz, J., Blunier, T., Raynaud, D., Barnola, J., Schwander, J., and Stauffer, B. (1993). Synchronous changes in atmospheric CH_4 and Greenland climate between 40 and 8 kyr BP. *Nature*, 366(6454):443–445. (pg. 9, 49)

Chappellaz, J., Stowasser, C., Blunier, T., Baslev-Clausen, D., Brook, E. J., Dallmayr, R., Faïn, X., Lee, J. E., Mitchell, L. E., Pascual, O., Romanini, D., Rosen, J., and Schüpbach, S. (2013). High-resolution glacial and deglacial record of atmospheric methane by continuous-flow and laser spectrometer analysis along the NEEM ice core. *Climate of the Past Discussions*, 9:2517–2556. (pg. 21)

Cheung, K. C., Di Berardino, M., Schade-Kampmann, G., Hebeisen, M., Pierzchalski, A., Bocsi, J., Mittag, A., and Tarnok, A. (2010). Microfluidic impedance-based flow cytometry. *Cytometry A*, 77A(7):648–666. (pg. 106)

Claquin, T., Roelandt, C., Kohfeld, K., Harrison, S., Tegen, I., Prentice, I., Balkanski, Y., Bergametti, G., Hansson, M., Mahowald, N., Rodhe, H., and Schulz, M. (2003). Radiative forcing of climate by ice-age atmospheric dust. *Climate Dynamics*, 20(2-3):193–202. (pg. 55)

Claquin, T., Schulz, M., Balkanski, Y., and Boucher, O. (1998). Uncertainties in assessing radiative forcing by mineral dust. *Tellus B*, 50(5):491–505. (pg. 55, 58, 89)

Clarke, R., Coates, J., and Fincoin, S. (1988). A fluorescence stopped-flow kinetic study of the displacement of 2-[(2-bis[carboxymethyl]amino-5-methylphenoxy)methyl]-6-methoxy-8-bis[carboxymethyl]aminoquinoline (QUIN2) from its Ca^{2+}, Pr^{3+}, Tb^{3+}, Dy^{3+} and Yb^{3+} complexes by ethylenedinitrilotetraacetate (EDTA) in aqueous solution. *Inorganica Chimica Acta*, 153:21–24. (pg. 30)

Cole-Dai, J. H., Budner, D. M., and Ferris, D. G. H. (2006). High speed, high resolution, and continuous chemical analysis of ice cores using a melter and ion chromatography. *Environmental Science & Technology*, 40(21):6764 – 6769. (pg. 22)

Colovos, G., Panesar, M. R., and Parry, E. P. (1976). Linearizing the calibration curve in determination of sulfate by the methylthymol blue method. *Analytical Chemistry*, 48(12):1693–1696. (pg. 32)

Coulter, W. H. (1956). High speed automatic blood cell counter and cell size analyzer. *Proceedings of the National Electronics Conference*, 12:1034–1042. (pg. 66, 77)

Craig, H., Gordon, L. I., and Horibe, Y. (1963). Isotopic exchange effects in evaporation of water 1: Low-temperature experimental results. *Journal of Geophysical Research*, 68:5079. (pg. 47)

Crosland-Taylor, P. (1953). A device for counting small particles suspended in fluid through a tube. *Nature*, 171(4340):37–38. (pg. 77)

Crosson, E. (2008). A cavity ring-down analyzer for measuring atmospheric levels of methane, carbon

dioxide, and water vapor. *Applied Physics B*, 92(3):403–408. (pg. 44)

Dahl-Jensen, D., Thorsteinsson, T., Alley, R., and Shoji, H. (1997). Flow properties of the ice from the Greenland Ice Core Project ice core: The reason for folds? *Journal of Geophysical Research*, 102(C12):26831–26840. (pg. 74)

Dansgaard, W. (1964). Stable isotopes in precipitation. *Tellus*, 16(4):436–468. (pg. 10, 24, 46)

Dansgaard, W. and Johnsen, S. (1969). A flow model and a time scale for the ice core from Camp Century, Greenland. *Journal of Glaciology*, 8(53):215–223. (pg. 39)

Dansgaard, W., Johnsen, S., Clausen, H., Dahl-Jensen, D., Gundestrup, N., Hammer, C., Hvidberg, C., Steffensen, J., Sveinbjörnsdottir, A., Jouzel, J., and Bond, G. (1993). Evidence for general instability of past climate from a 250-kyr ice-core record. *Nature*, 364(6434):218–220. (pg. 27)

Dansgaard, W., White, J., and Johnsen, S. (1989). The abrupt termination of the Younger Dryas climate event. *Nature*, 339(6225):532–534. (pg. 47)

Davies, S. M., Wastegard, S., Abbott, P. M., Barbante, C., Bigler, M., Johnsen, S. J., Rasmussen, T. L., Steffensen, J. P., and Svensson, A. (2010). Tracing volcanic events in the NGRIP ice-core and synchronising North Atlantic marine records during the last glacial period. *Earth and Planetary Science Letters*, 294(1-2):69–79. (pg. 23, 31)

De Angelis, M., Fehrenbach, L., Jehanno, C., and Maurette, M. (1985). Micrometre-sized volcanic glasses in polar ices and snows. *Nature*, 317(6032):52–54. (pg. 11, 31)

De Angelis, M., Legrand, M., Petit, J., Barkov, N., Korotkevitch, Y., and Kotlyakov, V. (1983). Soluble and insoluble impurities along the 950 m deep Vostok ice core (Antarctica) - climatic implications. *Journal of Atmospheric Chemistry*, 1(3):215–239. (pg. 109)

De Angelis, M., Steffensen, J., Legrand, M., Clausen, H., and Hammer, C. (1997). Primary aerosol (sea salt and soil dust) deposited in Greenland ice during the last climatic cycle: Comparison with east Antarctic records. *Journal of Geophysical Research*, 102(C12):26681–26698. (pg. 116)

De Blois, R. and Bean, C. (1970). Counting and sizing of submicron particles by the resistive pulse technique. *Review of Scientific Instruments*, 41:909–916. (pg. 66)

Delmas, R. and Boutron, C. (1980). Are the past variations of the stratospheric sulfate burden recorded in central Antarctic snow and ice layers? *Journal of Geophysical Research*, 85(C10):5645–5649. (pg. 31)

Delmas, R., Legrand, M., Aristarain, A., and Zanolini, F. (1985). Volcanic deposits in Antarctic snow and ice. *Journal of Geophysical Research*, 90(D7):2901–2920. (pg. 30, 31)

Delmonte, B., Andersson, P., Schöberg, H., Hansson, M., Petit, J., Delmas, R., Gaiero, D., Maggi, V., and Frezzotti, M. (2010). Geographic provenance of aeolian dust in East Antarctica during Pleistocene glaciations: preliminary results from Talos Dome and comparison with East Antarctic and new Andean ice core data. *Quaternary Science Reviews*, 29(1-2):256 – 264. (pg. 64)

Delmonte, B., Andersson, P. S., Hansson, M., Schöberg, H., Petit, J. R., Basile-Doelsch, I., and Maggi, V. (2008a). Aeolian dust in East Antarctica (EPICA-Dome C and Vostok): Provenance during glacial ages over the last 800 kyr. *Geophysical Research Letters*, 35(7):L07703. (pg. 64)

Delmonte, B., Basile-Doelsch, I., Petit, J.-R., Maggi, V., Revel-Rolland, M., Michard, A., Jagoutz, E., and Grousset, F. (2004a). Comparing the EPICA and Vostok dust records during the last 220,000 years: Stratigraphic correlation and provenance in glacial periods. *Earth Science Reviews*, 66:63–87. (pg. 64)

Delmonte, B., Delmas, R. J., and Petit, J. R. (2008b). Comment on 'Dust provenance in Antarctic ice

during glacial periods: From where in southern South America?' by D. M. Gaiero. *Geophysical Research Letters*, 35(8):L08707. (pg. 64, 114)

Delmonte, B., Petit, J. R., Andersen, K. K., Basile-Doelsch, I., Maggi, V., and Lipenkov, V. Y. (2004b). Dust size evidence for opposite regional atmospheric circulation changes over east Antarctica during the last climatic transition. *Climate Dynamics*, 23(3-4):427–438. (pg. 109)

Delmotte, M., Chappellaz, J., Brook, E., Yiou, P., Barnola, J. M., Goujon, C., Raynaud, D., and M., V. I. L. (2004). Atmospheric methane during the last four glacial-interglacial cycles: Rapid changes and their link with Antarctic temperature. *Journal of Geophysical Research*, 109(D12):D12104. (pg. 49)

Dittrich, W. and Göhde, W. (1969). Impulsfluorometrie bei Einzelzellen in Suspensionen. *Zeitschrift für Naturforschung*, 24b:360–361. (pg. 77)

Dong, S. and Dasgupta, P. K. (1987). Fast fluorometric flow injection analysis of formaldehyde in atmospheric water. *Environmental Science & Technology*, 21:581–588. (pg. 19, 28)

Edwards, R., McConnell, J. R., and Banta, J. R. (2007). Atmospheric deposition of iron and phosphorus to Greenland over the 20th-Century. *AGU Fall Meeting Abstract*, pages B1154+. (pg. 41)

EPICA members (2004). Eight glacial cycles from an Antarctic ice core. *Nature*, 429(6992):623–628. (pg. 64)

Epstein, S. and Mayeda, T. (1953). Variation of the ^{18}O content of waters from natural sources. *Geochimica et Cosmochimica Acta*, 4:213–224. (pg. 47)

Erhardt, T. (2013). A 3000 year high resolution dust record from the NEEM ice core. Master's thesis, University of Bern. (pg. 70, 71, 72, 122)

Etheridge, D., Steele, L., Langenfelds, R., Francey, R., Barnola, J.-M., and Morgan, V. (1996). Natural and anthropogenic changes in atmospheric CO_2 over the last 1000 years from air in Antarctic ice firn. *Journal of Geophysical Research*, 101(D2):4115–4128. (pg. 9)

Fabre, A., Barnola, J.-M., Arnaud, L., and Chappellaz, J. (2000). Determination of gas diffusivity in polar firn: Comparison between experimental measurements and inverse modeling. *Geophysical Research Letters*, 27(4):557–560. (pg. 50)

Falkowski, P. G., Barber, R. T., and Smetacek, V. (1998). Biogeochemical controls and feedbacks on ocean primary production. *Science*, 281(5374):200–206. (pg. 39, 56)

Faria, S. H., Freitag, J., and Kipfstuhl, S. (2010). Polar ice structure and the integrity of ice-core paleoclimate records. *Quaternary Science Reviews*, 29(1-2):338 – 351. (pg. 39)

Federer, U., Kaufmann, P. R., Manuel, H. A., Simon, S., and Stocker, T. (2008). Continuous flow analysis of total organic carbon in polar ice cores. *Environmental Science & Technology*, 42:8039–8043. (pg. 21, 28)

Filippelli, G. M. (2008). The global phosphorus cycle: Past, present, and future. *Elements*, 4(2):89–95. (pg. 39, 41, 56)

Fischer, H., Behrens, M., Bock, M., Richter, U., Schmitt, J., Loulergue, L., Chappellaz, J., Spahni, R., Blunier, T., Leuenberger, M., and Stocker, T. F. (2008). Changing boreal methane sources and constant biomass burning during the last termination. *Nature*, 452(7189):864–867. (pg. 49)

Fischer, H., Siggaard-Andersen, M.-L., Ruth, U., Röthlisberger, R., and Wolff, E. (2007). Glacial/interglacial changes in mineral dust and sea-salt records in polar ice cores: Sources, transport, and deposition. *Reviews of Geophysics*, 45:RG1002. (pg. 9, 27, 29, 60, 65, 73, 112, 115, 117)

Flückiger, J., Blunier, T., Stauffer, B., Chappellaz, J., Spahni, R., Kawamura, K., Schwander, J., Stocker, T. F., and Dahl-Jensen, D. (2004). N_2O and CH_4 variations during the last epoch: insight into global processes. *Global Biogeochemical Cycles*, 18:GB1020. (pg. 9, 50)

Formenti, P., Schütz, L., Balkanski, Y., Desboeufs, K., Ebert, M., Kandler, K., Petzold, A., Scheuvens, D., Weinbruch, S., and Zhang, D. (2011). Recent progress in understanding physical and chemical properties of African and Asian mineral dust. *Atmospheric Chemistry and Physics*, 11(16):8231–8256. (pg. 61)

Fuhrer, K., Neftel, A., Anklin, M., and Maggi, V. (1993). Continuous measurements of hydrogen peroxide, formaldehyde, calcium and ammonium concentrations along the new GRIP ice core from Summit, Central Greenland. *Atmospheric Environment*, A27(12):1873–1880. (pg. 25, 28)

Fuhrer, K., Neftel, A., Anklin, M., Staffelbach, T., and Legrand, M. (1996). High-resolution ammonium ice core record covering a complete glacial-interglacial cycle. *Journal of Geophysical Research*, 101(D2):4147–4164. (pg. 25)

Fuhrer, K., Wolff, E., and Johnsen, S. (1999). Timescales for dust variability in the Greenland Ice Core Project (GRIP) ice core in the last 100,000 years. *Journal of Geophysical Research*, 104(D24):31043–31052. (pg. 29, 60, 65, 73, 116)

Gaiero, D. (2007). Dust provenance in Antarctic ice during glacial periods: From where in southern South America? *Geophysical Research Letters*, 34(17):L17707. (pg. 64, 114)

Galbraith, D. W., Harkins, K. R., and Jefferson, R. A. (1988). Flow cytometric characterization of the chlorophyll contents and size distributions of plant protoplasts. *Cytometry*, 9(1):75–83. (pg. 90)

Gascoyne, P. R. C., Anderson, T., Vykoukal, J., and Becker, F. (2004). Particle impedance sensor. US Patent 6703819. (pg. 105)

Gawad, S., Cheung, K., Seger, U., Bertsch, A., and Renaud, P. (2004). Dielectric spectroscopy in a micromachined flow cytometer: Theoretical and practical considerations. *Lab on a Chip*, 4(3):241–251. (pg. 105)

Gawad, S., Holmes, D., Benazzi, G., Renaud, P., and Morgan, H. (2010). Impedance spectroscopy and optical analysis of single biological cells and organisms in microsystems. In Hughes, M. P. and Hoettges, K. F., editors, *Microengineering in Biotechnology*. Springer, New York, NY. (pg. 67)

Genfa, Z. and Dasgupta, P. K. (1989). Fluorometric measurement of aqueous ammonium ion in a flow injection system. *Analytical Chemistry*, 61(5):408–412. (pg. 15, 19, 26)

Gibson, E. R., Hudson, P. K., and Grassian, V. H. (2006). Aerosol chemistry and climate: Laboratory studies of the carbonate component of mineral dust and its reaction products. *Geophysical Research Letters*, 33(13):L13811. (pg. 55)

Gillette, D. A. (1974). On the production of soil wind erosion aerosols having the potential for long range transport. *Journal de Recherches Atmosphériques*, 8:735–744. (pg. 57)

Gillette, D. A. (1978). A wind tunnel simulation of the erosion of soil: Effect of soil texture, sandblasting, wind speed, and soil consolidation on dust production . *Atmospheric Environment (1967)*, 12(8):1735–1743. (pg. 58)

Giné, M., F, H. B., Zagatto, E., and Reis, B. (1980). Simultaneous determination of nitrate and nitrite by flow injection analysis. *Analytica Chimica Acta*, 114:191 – 197. (pg. 35)

Gkinis, V., Popp, T. J., Blunier, T., Bigler, M., Schüpbach, S., Kettner, E., and Johnsen, S. J. (2011).

Water isotopic ratios from a continuously melted ice core sample. *Atmospheric Measurement Techniques*, 4:2531 – 2542. (pg. 11, 49, 119)

Gkinis, V., Popp, T. J., Johnsen, S. J., and Blunier, T. (2010). A continuous stream flash evaporator for the calibration of an IR cavity ring-down spectrometer for the isotopic analysis of water. *Isotopes in Environmental and Health Studies*, 46:463–475. (pg. 44, 46, 49, 119)

Güllük, T., Wagner, H. E., and Slemr, F. (1997). A high-frequency modulated tunable diode laser absorption spectrometer for measurements of CO_2, CH_4, N_2O, and CO in air samples of a few cm^3. *Review of Scientific Instruments*, 68(1):230–239. (pg. 52)

Graves, S. W., Nolan, J. P., Jett, J. H., Martin, J. C., and Sklar, L. A. (2002). Nozzle design parameters and their effects on rapid sample delivery in flow cytometry. *Cytometry*, 47(2):127–137. (pg. 93)

Grinsted, A. (2013). *newedges.m.* personal communication. (pg. 70, 72)

Grousset, F., Biscaye, P., Revel, M., Petit, J., Pye, K., Joussaume, S., and Jouzel, J. (1992). Antarctic (Dome C) ice-core dust at 18 ky BP: Isotopic constraints on origins. *Earth and Planetary Science Letters*, 111:175–182. (pg. 61, 63)

Grousset, F. and Biscaye, P. E. (2005). Tracing dust sources and transport patterns using Sr, Nd and Pb isotopes. *Chemical Geology*, 222:149–167. (pg. 61)

Hammer, C. (1977). Past volcanism revealed by Greenland ice sheet impurities. *Nature*, 270(5637):482–486. (pg. 10, 30, 31)

Hammer, C. (1980). Acidity of polar ice cores in relation to absolute dating, past volcanism, and radio-echoes. *Journal of Glaciology*, 25(93):359–372. (pg. 23, 31)

Hammer, C., Clausen, H., and Dansgaard, W. (1980). Greenland ice sheet evidence of post-glacial volcanism and its climatic impact. *Nature*, 288(5788):230–235. (pg. 30)

Hammer, C., Clausen, H., Dansgaard, W., Gundestrup, N., Johnsen, S., and Reeh, N. (1978). Dating of Greenland ice cores by flow models, isotopes, volcanic debris, and continental dust. *Journal of Glaciology*, 20(82):3–26. (pg. 23)

Hayakawa, O., Nakahira, K., and Tsubaki, J. (1995). Evaluation of fine ceramics raw powders with particle size analysers having different measurement principle and its problem. *Journal of the Ceramic Society of Japan*, 10(6):586–592. (pg. 67, 100)

Haywood, J. and Boucher, O. (2000). Estimates of the direct and indirect radiative forcing due to tropospheric aerosols: A review. *Reviews of Geophysics*, 38(4):513–543. (pg. 55)

Höber, R. (1910). Eine Methode die elektrische Leitfähigkeit im Innern von Zellen zu messen. *Pflüger's Archiv für die gesamte Physiologie des Menschen und der Tiere*, 133:237–259. (pg. 105)

Herron, M. (1982). Impurity Sources of F^-, Cl^-, NO_3^- and SO_4^{2-} in Greenland and Antarctic Precipitation. *Journal of Geophysical Research*, 87(C4):3052–3060. (pg. 30, 31, 33)

Huber, C. and Leuenberger, M. (2003). Fast high-precision on-line determination of hydrogen isotope ratios of water or ice by continuous-flow isotope ratio mass spectrometry. *Rapid Communications in Mass Spectrometry*, 17(12):1319–325. (pg. 22, 43, 46, 47)

Huber, C. and Leuenberger, M. (2004). Measurements of isotope and elemental ratios of air from polar ice with a new on-line extraction method. *Geochemistry, Geophysics, Geosystems*, 5(10):Q10002. (pg. 44)

Huber, C. and Leuenberger, M. (2005). On-line systems for continuous water and gas isotope ratio measurements. *Isotopes in Environmental and Health Studies*, 41(3):189–205. (pg. 43, 44, 49)

Huber, C., Leuenberger, M., and Zumbrunnen, O. (2003). Continuous extraction of trapped air from bubble ice or water for on-line determination of isotope ratios. *Analytical Chemistry*, 75(10):2324–2332. (pg. 22, 46)

IPCC (2007). Changes in Atmospheric Constituents and in Radiative Forcing. In Solomon, S., Qin, D., Manning, M., Chen, Z., Marquis, M., Averyt, K., M.Tignor, and Miller, H., editors, *Climate Change 2007: The Physical Science Basis. Contribution of Working Group I to the Fourth Assessment Report of the Intergovernmental Panel on Climate Change*. Cambridge University Press, Cambridge. (pg. 55)

Jagtiani, A. V., Zhe, J., Hu, J., and Carletta, J. (2006). Detection and counting of micro-scale particles and pollen using a multi-aperture Coulter counter. *Measurement Science and Technology*, 17:1706–1714. (pg. 106)

Jickells, T. D., An, Z. S., Andersen, K. K., Baker, A. R., Bergametti, G., Brooks, N., Cao, J. J., Boyd, P. W., Duce, R. A., Hunter, K. A., Kawahata, H., Kubilay, N., laRoche, J., Liss, P. S., Mahowald, N., Prospero, J. M., Ridgwell, A. J., Tegen, I., and Torres, R. (2005). Global iron connections between desert dust, ocean biogeochemistry, and climate. *Science*, 308(5718):67–71. (pg. 56)

Johnsen, S., Clausen, H., Dansgaard, W., Fuhrer, K., Gundestrup, N., Hammer, C., Iversen, P., Steffensen, J., Jouzel, J., and Stauffer, B. (1992). Irregular glacial interstadials recorded in a new Greenland ice core. *Nature*, 359(6393):311–313. (pg. 24, 65)

Johnsen, S., Dansgaard, W., and White, J. (1989). The origin of Arctic precipitation under present and glacial conditions. *Tellus B*, 41(4):452–468. (pg. 10, 47)

Johnsen, S. J., Clausen, H. B., Cuffey, K. M., Hoffmann, G., Schwander, J., and Creyts, T. (2000). Diffusion of stable isotopes in polar firn and ice: The isotope effect in firn diffusion. In Hondoh, T., editor, *Physics of Ice Core Records*, pages 121–140. Hokkaido University Press, Sapporo. (pg. 17)

Johnsen, S. J., Dahl-Jensen, D., Gundestrup, N., Steffensen, J. P., Clausen, H. B., Miller, H., Masson-Delmotte, V., Sveinbjornsdottir, A. E., and White, J. (2001). Oxygen isotope and palaeotemperature records from six Greenland ice-core stations: Camp Century, Dye-3, GRIP, GISP2, Renland and North-GRIP. *Journal of Quaternary Science*, 16(4):299–307. (pg. 16, 39)

Johnsen, S. J., Dahljensen, D., Dansgaard, W., and Gundestrup, N. (1995). Greenland paleotemperatures derived from GRIP borehole temperature and ice core isotopic profiles. *Tellus Series B-Chemical and Physical Meteorology*, 47(5):624–629. (pg. 46)

Jouzel, J., Alley, R., Cuffey, K., Dansgaard, W., Grootes, P., Hoffmann, G., Johnsen, S., Koster, R., Peel, D., Shuman, C., Stievenard, M., Stuiver, M., and White, J. (1997). Validity of the temperature reconstruction from water isotopes in ice cores. *Journal of Geophysical Research*, 102(C12):26471–26487. (pg. 46)

Jouzel, J., Masson-Delmotte, V., Cattani, O., Dreyfus, G., Falourd, S., Hoffmann, G., Minster, B., Nouet, J., Barnola, J. M., Chappellaz, J., Fischer, H., Gallet, J. C., Johnsen, S., Leuenberger, M., Loulergue, L., Luethi, D., Oerter, H., Parrenin, F., Raisbeck, G., Raynaud, D., Schilt, A., Schwander, J., Selmo, E., Souchez, R., Spahni, R., Stauffer, B., Steffensen, J. P., Stenni, B., Stocker, T. F., Tison, J. L., Werner, M., and Wolff, E. W. (2007). Orbital and millennial Antarctic climate variability over the past 800,000 years. *Science*, 317(5839):793–796. (pg. 9)

Jouzel, J. and Merlivat, L. (1984). Deuterium and oxygen-18 in precipitation: Modeling of the isotopic effects during snow formation. *Journal of Geophysical Research*, 89(D7):11749–11757. (pg. 10, 24, 46)

Kagenow, H. and Jensen, A. (1983). Kinetic determination of magnesium and calcium by stopped-flow injection analysis. *Analytica Chimica Acta*, 145:125 – 133. (pg. 19, 29, 30)

Kahl, J., Martinez, D., Kuhn, H., Davidson, C., Jaffrezo, J.-L., and Harris, J. (1997). Air mass trajectories to Summit, Greenland: A 44-year climatology and some episodic events. *Journal of Geophysical Research*, 102(C12):26861–26875. (pg. 63, 117)

Kamentsky, L. A., Melamed, M., and Derman, H. (1965). Spectrophotometer: New instrument for ultrarapid cell analysis. *Science*, 150(3696):630–631. (pg. 77)

Kaufmann, P. R., Federer, U., Hutterli, M. A., Bigler, M., Schüpbach, S., Ruth, U., Schmitt, J., and Stocker, T. (2008). An improved continuous flow analysis system for high-resolution field measurements on ice cores. *Environmental Science & Technology*, 42(21):8044–8050. (pg. vi, 10, 13, 15, 20, 21, 22, 25, 27, 28, 32, 33, 37, 38, 43, 68, 121)

Kawamura, K., Parrenin, F., Lisiecki, L., Uemura, R., Vimeux, F., Severinghaus, J. P., Hutterli, M. A., Nakazawa, T., Aoki, S., Jouzel, J., Raymo, M. E., Matsumoto, K., Nakata, H., Motoyama, H., Fujita, S., Goto-Azuma, K., Fujii, Y., and Watanabe, O. (2007). Northern Hemisphere forcing of climatic cycles in Antarctica over the past 360,000 years. *Nature*, 448(7156):912–U4. (pg. 9)

Kerstel, E. R. T., van Trigt, R., Reuss, J., and Meijer, H. A. J. (1999). Simultaneous determination of the ^{2}H/^{1}H, ^{17}O/^{16}O, and ^{18}O/^{16}O iotope abundance ratios in water by means of laser spectrometry. *Analytical Chemistry*, 71(23):5297–5303. (pg. 44, 47)

Kjær, H. A., Svensson, A., Vallelonga, P., Kettner, E., Schüpbach, S., Bigler, M., Steffensen, J. P., and Hansson, M. E. (2011). First continuous phosphate record from Greenland ice cores. *Climate of the Past Discussions*, 7(6):3959–3989. (pg. 11, 41, 43, 119)

Kjær, H. A., Vallelonga, P., Svensson, A., Kristensen, M. E. L., Tibuleac, C., and Bigler, M. (2013). Continuous flow analysis method for determination of dissolved reactive phosphorus in ice cores. *Environmental Science & Technology*. (pg. 11, 41, 43, 116, 119)

Kjær, H. A. (2013). *An optical method for continuous determination of pH in ice cores*. personal communication. (pg. 31)

Knippertz, P. (2014). Meteorological aspects of dust emission and transport. In Stuut, J.-B. and Knippertz, P., editors, *Mineral dust - A key player in the earth system*. Springer. *in preparation*. (pg. 58)

Knüsel, S., Piguet, D. E., Schwikowski, M., and Gäggeler, H. W. (2003). Accuracy of continuous ice-core trace-element analysis by Inductively coupled plasma sector field mass spectrometry. *Environmental Science & Techonlogy*, 37(10):2267 – 2273. (pg. 22, 73, 74)

Kohfeld, K. and Harrison, S. P. (2001). DIRTMAP: The geological record of dust. *Earth Science Reviews*, 54:81–114. (pg. 59)

Kondo, O., Miyata, H., and Tôei, K. (1982). Determination of sulfate in river water by flow injection analysis. *Analytica Chimica Acta*, 134:353 – 358. (pg. 33)

Krinner, G., Genthon, C., and Jouzel, J. (1997). GCM analysis of local influences on ice core δ signals. *Geophysical Research Letters*, 24(22):2825–2828. (pg. 116, 120)

Kumar, P., Sokolik, I. N., and Nenes, A. (2011). Measurements of cloud condensation nuclei activity and droplet activation kinetics of fresh unprocessed regional dust samples and minerals. *Atmospheric Chemistry and Physics*, 11(7):3527–3541. (pg. 55)

Lambert, F., Bigler, M., Steffensen, J. P., Hutterli, M., and Fischer, H. (2012). Centennial mineral dust

variability in high-resolution ice core data from Dome C, Antarctica. *Climate of the Past*, 8(2):609–623. (pg. 70, 71, 91)

Lambert, F., Delmonte, B., Petit, J. R., Bigler, M., Kaufmann, P. R., Hutterli, M. A., Stocker, T. F., Ruth, U., Steffensen, J. P., and Maggi, V. (2008). Dust-climate couplings over the past 800,000 years from the EPICA Dome C ice core. *Nature*, 452(7187):616–619. (pg. 58, 108)

Landais, A., Barnola, J., Kawamura, K., Caillon, N., Delmotte, M., Ommen, T. V., Dreyfus, G., Jouzel, J., Masson-Delmotte, V., Minster, B., Freitag, J., Leuenberger, M., Schwander, J., Huber, C., Etheridge, D., and Morgan, V. (2006). Firn-air $\delta^{15}N$ in modern polar sites and glacial-interglacial ice: A model-data mismatch during glacial periods in Antarctica? *Quaternary Science Reviews*, 25(1-2):49 – 62. (pg. 50)

Landais, A., Caillon, N., Goujon, C., Grachev, A. M., Barnola, J. M., Chappellaz, J., Jouzel, J., Masson-Delmotte, V., and Leuenberger, M. (2004). Quantification of rapid temperature change during DO event 12 and phasing with methane inferred from air isotopic measurements. *Earth and Planetary Science Letters*, 225:221–232. (pg. 9)

Larsen, U., Blankenstein, G., and Branebjerg, J. (1997). *Microchip Coulter particle counter*. Technical digest of the international conference on solid-state sensors and actuators, Chicago, IL. (pg. 105)

Lazarus, A. L., Kok, G. L., Gitlin, S. N., and Lind, J. A. . (1985). Automated fluorometric method for hydrogen peroxide in atmospheric precipitation. *Analytical Chemistry*, 57:917–922. (pg. 19, 28)

Leary, J., Todd, P., Wood, J., and Jett, J. (1979). Laser flow cytometric light scatter and fluorescence pulse width and pulse rise-time sizing of mammalian cells. *Journal of Histochemistry and Cytochemistry*, 27(1):315–320. (pg. 90)

Legendre, L., Courties, C., and Troussellier, M. (2001). Flow cytometry in oceanography 1989-1999: Environmental challenges and research trends. *Cytometry*, 44(3):164–172. (pg. 76)

Legendre, L. and Yentsch, C. M. (1989). Overview of flow cytometry and image analysis in biological oceanography and limnology. *Cytometry A*, 10(5):501–510. (pg. 76)

Legrand, M., De Angelis, M., Staffelbach, T., Neftel, A., and Stauffer, B. (1992). Large perturbations of ammonium and organic acids content in the Summit-Greenland ice core. Fingerprint from forest fires? *Geophysical Research Letters*, 19(5):473–475. (pg. 25)

Legrand, M. and Delmas, R. (1984). The ionic balance of Antarctic snow: A 10-year detailed record. *Atmospheric Environment*, 18:1867–1874. (pg. 27)

Legrand, M. and Delmas, R. (1987). A 220-year continuous record of volcanic H_2SO_4 in the Antarctic ice sheet. *Nature*, 327(6124):671–676. (pg. 10, 31)

Legrand, M., Ducroz, F., Wagenbach, D., Mulvaney, R., and Hall, J. (1998). Ammonium in coastal Antarctic aerosol and snow: Role of polar ocean and penguin emissions. *Journal of Geophysical Research*, 103(D9):11043–1056. (pg. 25, 30)

Legrand, M. and Kirchner, S. (1990). Origins and variations of nitrate in South Polar precipitation. *Journal of Geophysical Research*, 95(D4):3493–3507. (pg. 33, 34)

Legrand, M., Lorius, C., Barkov, N., and Petrov, V. (1988). Vostok (Antarctica) ice core: Atmospheric chemistry changes over the last climatic cycle (16,000 years). *Atmospheric Environment*, 22(2):317–331. (pg. 26)

Legrand, M. and Mayewski, P. A. (1997). Glaciochemistry of polar ice cores: A review. *Reviews of Geophysics*, 35(3):219–243. (pg. 9, 25, 26, 27, 28, 29, 31, 33, 35, 37, 38, 73, 112)

Leuenberger, M. and Huber, C. (2002). On-line determination of oxygen isotope Rratios of water or ice by mass spectrometry. *Analytical Chemistry*, 74(18):4611–4617. (pg. 22, 43, 47)

Li, W. J. and Shao, L. Y. (2009). Observation of nitrate coatings on atmospheric mineral dust particles. *Atmospheric Chemistry and Physics*, 9(6):1863–1871. (pg. 116)

Littot, G., Mulvaney, R., Röthlisberger, R., Udisti, R., Wolff, E. W., Castellano, E., de Angelis, M., Hansson, M., Sommer, S., and Steffensen, J. P. (2002). Comparison of analytical methods used for measuring major ions in the EPICA Dome C (Antarctica) ice core. *Annals of Glaciology*, 35:299–305. (pg. 10, 16, 24)

Lohmann, U. and Feichter, J. (2005). Global indirect aerosol effects: A review. *Atmospheric Chemistry and Physics*, 5(3):715–737. (pg. 56)

Loken, M. R., Brosnan, J. M., Bach, B. A., and Ault, K. A. (1990). Establishing optimal lymphocyte gates for immunophenotyping by flow cytometry. *Cytometry*, 11(4):453–459. (pg. 94)

Loulergue, L., Schilt, A., Spahni, R., Masson-Delmotte, V., Blunier, T., Lemieux, B., Barnola, J. M., Raynaud, D., Stocker, T. F., and Chappellaz, J. (2008). Orbital and millennial-scale features of atmospheric CH_4 over the past 800,000 years. *Nature*, 453(7193):383–386. (pg. 49)

Lupker, M., Aciego, S., Bourdon, B., Schwander, J., and Stocker, T. (2010). Isotopic tracing (Sr, Nd, U and Hf) of continental and marine aerosols in an 18th century section of the Dye-3 ice core (Greenland). *Earth and Planetary Science Letters*, 295(1-2):277–286. (pg. 63, 90, 113, 117)

Madsen, B. and Murphy, R. (1981). Flow-injection and photometric determination of sulfate rainwater with methythymol blue. *Analytical Chemistry*, 8(12):1924–1926. (pg. 20, 31, 32)

Maher, B. A., Prospero, J. M., Mackie, D., Gaiero, D., Hesse, P. P., and Balkanski, Y. (2010). Global connections between aeolian dust, climate and ocean biogeochemistry at the present day and at the last glacial maximum. *Earth Science Reviews*, 99(1-2):61–97. (pg. 55, 57, 58, 111, 113)

Mahowald, N., Albani, S., Engelstaedter, S., Winckler, G., and Goman, M. (2011). Model insight into glacial-interglacial paleodust records. *Quaternary Science Reviews*, 30(7-8):832–854. (pg. 59, 62, 63, 64, 65, 73, 113, 116, 118, 120)

Mahowald, N., Jickells, T. D., Baker, A. R., Artaxo, P., Benitez-Nelson, C. R., Bergametti, G., Bond, T. C., Chen, Y., Cohen, D. D., Herut, B., Kubilay, N., Losno, R., Luo, C., Maenhaut, W., McGee, K. A., Okin, G. S., Siefert, R. L., and Tsukuda, S. (2008). Global distribution of atmospheric phosphorus sources, concentrations and deposition rates, and anthropogenic impacts. *Global Biogeochemical Cycles*, 22(4):GB4026. (pg. 39, 41, 56)

Mahowald, N., Kohfeld, K., Hansson, M., Balkanski, Y., Harrison, S. P., Prentice, I. C., Schulz, M., and Rodhe, H. (1999). Dust sources and deposition during the last glacial maximum and current climate: A comparison of model results with paleodata from ice cores and marine sediments. *Journal of Geophysical Research*, 104(D13):15895–15916. (pg. 59, 65)

Mahowald, N. M., Baker, A. R., Bergametti, G., Brooks, N., Duce, R. A., Jickells, T. D., Kubilay, N., Prospero, J. M., and Tegen, I. (2005). Atmospheric global dust cycle and iron inputs to the ocean. *Global Biogeochemical Cycles*, 19(4):GB4025. (pg. 56, 57, 58)

Mahowald, N. M., Muhs, D. R., Levis, S., Rasch, P. J., Yoshioka, M., Zender, C. S., and Luo, C. (2006). Change in atmospheric mineral aerosols in response to climate: Last glacial period, preindustrial, modern, and doubled carbon dioxide climates. *Journal of Geophysical Research*, 111(D10):L20705. (pg. 58,

59, 60, 62)

Mandy, F. F., Bergeron, M., Recktenwald, D., and Izaguirre, C. A. (1992). A simultaneous three-color T cell subsets analysis with single laser flow cytometers using T cell gating protocol comparison with conventional two-color immunophenotyping method. *Journal of Immunological Methods*, 156(2):151 – 162. (pg. 94)

Martin, J. H. (1990). Glacial-interglacial CO_2 change: The Iron Hypothesis. *Paleoceanography*, 5(1):1–13. (pg. 56)

Masoom, M. and Townshend, A. (1985). Determination of glucose in blood by flow injection analysis and an immobilized glucose oxidase column. *Analytica Chimica Acta*, 166:111 – 118. (pg. 28)

Masson-Delmotte, V., Jouzel, J., Landais, A., Stiévenard, M., Johnsen, S. J., White, J. W. C., Werner, M., Sveinbjörnsdóttir, A., and Fuhrer, K. (2005). GRIP deuterium excess reveals rapid and orbital-scale changes in Greenland moisture origin. *Science*, 309(5731):118–121. (pg. 10, 46)

Mayewski, P., Lyons, W., Spencer, M., Twickler, M., Dansgaard, W., Koci, B., Davidson, C., and Honrath, R. (1986). Sulfate and nitrate concentrations from a South Greenland ice core. *Science*, 232(4753):975–977. (pg. 30, 33)

McConnell, J., Edwards, R., Kok, G., Flanner, M., Zender, C., Saltzman, E., Banta, J., Pasteris, D., Carter, M., and Kahl, J. (2007). 20th-century industrial black carbon emissions altered Arctic climate forcing. *Science*, 317(5843):1381–1384. (pg. 11, 22, 28, 30)

McConnell, J. R., Lamorey, G. W., Lambert, S. W., and Taylor, K. C. (2002). Continuous ice-core chemical analyses using inductively coupled plasma mass spectrometry. *Environmental Science & Technology*, 36(1):7 – 11. (pg. 22, 25, 37)

McCormack, T., David, A., Worsfold, P., and Howland, R. (1994). Flow injection determination of nitrate in estuarine and coastal waters. *Analytical Proceedings*, 31(3):81–83. (pg. 20)

Meese, D., Gow, A., Alley, R., Zielinski, G., Grootes, P., Ram, M., Taylor, K., Mayewski, P., and Bolzan, J. (1997). The Greenland Ice Sheet Project 2 depth-age scale: Methods and results. *Journal of Geophysical Research*, 102(C12):26411–26423. (pg. 10, 24)

Michel, B. (2011). MieCalc - freely configurable program for light scattering calculations (Mie theory). Accessible at `http://www.lightscattering.de/MieCalc/eindex.html`, last accessed 15 Sep 2013. (pg. 88)

Mie, G. (1908). Beiträge zur Optik trüber Medien speziell kolloidaler Metallösungen. *Annalen der Physik*, 25:377–445. (pg. 85, 86, 119)

Mitchell, L. E., Brook, E. J., Sowers, T., McConnell, J. R., and Taylor, K. (2011). Multidecadal variability of atmospheric methane, 1000-1800 C.E. *Journal of Geophysical Research*, 116(G2):G02007. (pg. 52)

Miteva, V., Teacher, C., Sowers, T., and Brenchley, J. (2009). Comparison of the microbial diversity at different depths of the GISP2 Greenland ice core in relationship to deposition climates. *Environmental Microbiology*, 11(3):640–656. (pg. 11, 54, 78, 79)

Moore, J., Paren, J., and Oerter, H. (1992). Sea salt dependent electrical conduction in polar ice. *Journal of Geophysical Research*, 97(B13):19803–19812. (pg. 31)

Morgan, H., Sun, T., Holmes, D., Gawad, S., and Green, N. G. (2007). Single cell dielectric spectroscopy. *Journal of Applied Physics*, 40(1):61–70. (pg. 105)

Mosher, B., Winkler, P., and Jaffrezo, J.-L. (1993). Seasonal trends in aerosol chemistry at Dye 3, Green-

land. *Atmospheric Environment*, 27A(17-18):2761–2772. (pg. 63, 110, 113)

Muhs, D. R. (2013). The geologic records of dust in the Quaternary. *Aeolian Research*, 9:3–48. (pg. 54, 55, 58, 59, 60, 61, 62, 118)

Murphy, J. and Riley, J. (1962). A modified single solution method for the determination of phosphate in natural waters. *Analytica Chimica Acta*, 27(0):31 – 36. (pg. 43)

NEEM members (2013). Eemian interglacial reconstructed from a Greenland folded ice core. *Nature*, 493(7433):489 – 494. (pg. 9)

Neftel, A., Beer, J., Oeschger, H., Zürcher, F., and Finkel, R. (1985). Sulphate and nitrate concentrations in snow from South Greenland 1895-1978. *Nature*, 314(6012):611–613. (pg. 30, 33)

NGRIP members (2004). High-resolution record of Northern Hemisphere climate extending into the last interglacial period. *Nature*, 431(7005):147–151. (pg. 39, 60)

Niedermeier, D., Hartmann, S., Clauss, T., Wex, H., Kiselev, A., Sullivan, R. C., DeMott, P. J., Petters, M. D., Reitz, P., Schneider, J., Mikhailov, E., Sierau, B., Stetzer, O., Reimann, B., Bundke, U., Shaw, R. A., Buchholz, A., Mentel, T. F., and Stratmann, F. (2011). Experimental study of the role of physicochemical surface processing on the IN ability of mineral dust particles. *Atmospheric Chemistry and Physics*, 11(21):11131–11144. (pg. 56)

Nieuwenhuis, J., Kohl, F., Bastemeijer, J., Sarro, P., and Vellekoop, M. (2004). Integrated Coulter counter based on 2-dimensional liquid aperture control. *Sensors and Actuators B: Chemical*, 102(1):44 – 50. (pg. 105)

Nolan, J. P., Posner, R. G., Martin, J. C., Habbersett, R., and Sklar, L. A. (1995). A rapid mix flow cytometer with subsecond kinetic resolution. *Cytometry*, 21(3):223–229. (pg. 93)

Okin, G. S., Mahowald, N., Chadwick, O. A., and Artaxo, P. (2004). Impact of desert dust on the biogeochemistry of phosphorus in terrestrial ecosystems. *Global Biogeochemical Cycles*, 18(2):GB2005. (pg. 56)

Okin, G. S., Mladenov, N., Wang, L., Cassel, D., Caylor, K. K., Ringrose, S., and Macko, S. A. (2008). Spatial patterns of soil nutrients in two southern African savannas. *Journal of Geophysical Research: Biogeosciences*, 113(G2):G02011. (pg. 55)

Osterberg, E. C., Handley, M. J., Sneed, S. B., Mayewski, P. A., and Kreutz, K. J. (2006). Continuous ice core melter system with discrete sampling for major ion, trace element, and stable isotope analyses. *Environmental Science & Technology*, 40:3355–3361. (pg. 22, 73, 74)

Pamme, N., Koyama, R., and Manz, A. (2003). Counting and sizing of particles and particle agglomerates in a microfluidic device using laser light scattering: Application to a particle-enhanced immunoassay. *Lab on a Chip*, 3:187–192. (pg. 98)

Pasteris, D. R., McConnell, J. R., and Edwards, R. (2012). High-resolution, continuous method for measurement of acidity in ice cores. *Environmental Science & Technology*, 46(3):1659–1666. (pg. 31)

Paytan, A. and McLaughlin, K. (2007). The oceanic phosphorus cycle. *Chemical Reviews*, 107(2):563–576. (pg. 41)

Peltier, W. R. (1994). Ice Age Paleotopography. *Science*, 265(5169):195–201. (pg. 115)

Petit, J., Basile, I., Leruryuet, A., Raynaud, D., Lorius, C., Jouzel, J., Stievenard, M., Lipenkov, V., Barkov, N., Kudryashov, B., Davis, M., Saltzman, E., and Kotlyakov, V. (1997). Four climate cycles in Vostok ice core. *Nature*, 387(6631):359–360. (pg. 46)

Petit, J.-R., Briat, M., and Royer, A. (1981). Ice age aerosol content from East Antarctic ice core samples and past wind strength. *Nature*, 293(5831):391–394. (pg. 10, 12, 59, 67, 109)

Picot, J., Guerin, C. L., Kim, C. L. V., and Boulanger, C. M. (2012). Flow cytometry: retrospective, fundamentals and recent instrumentation. *Cytotechnology*, 64(2):109–130. (pg. 77, 78)

Prospero, J. M. (1999). Long-range transport of mineral dust in the global atmosphere: Impact of African dust on the environment of the southeastern United States. *Proceedings of the National Academy of Sciences*, 96(7):3396–3403. (pg. 58)

Prospero, J. M., Charlson, R. J., Mohnen, V., Jaenicke, R., Delany, A. C., Moyers, J., Zoller, W., and Rahn, K. (1983). The atmospheric aerosol system: An overview. *Reviews of Geophysics*, 21(7):1607–1629. (pg. 54)

Pye, K. (1987). *Aeolian dust and dust deposits.* Academic Press, San Diego, Calif. (pg. 11, 54, 57, 58, 111, 118)

Quiles, R., Fernández-Romero, J. M., Fernández, E., de Castro, M. D. L., and Valcárcel, M. (1993). Automated enzymatic determination of sodium in serum. *Clinical chemistry*, 39:500–503. (pg. 20, 21, 27, 28)

Ram, M. and Koenig, G. (1997). Continuous dust concentration profile of pre-Holocene ice from the Greenland Ice Sheet Project 2 ice core: Dust stadials, interstadials, and the Eemian. *Journal of Geophysical Research*, 102(C12):26641–26648. (pg. 74)

Rasmussen, S., Andersen, K., Johnsen, S., Bigler, M., and McCormack, T. (2005). Deconvolution-based resolution enhancement of chemical ice core records obtained by continuous flow analysis. *Journal of Geophysical Research*, 110(D17):D17304. (pg. 16, 17)

Rasmussen, S., Andersen, K., Svensson, A., Steffensen, J., Vinther, B., Clausen, H., Siggaard-Andersen, M.-L., Johnsen, S., Larsen, L., Dahl-Jensen, D., Bigler, M., Röthlisberger, R., Fischer, H., Goto-Azuma, K., Hansson, M., and Ruth, U. (2006). A new Greenland ice core chronology for the last glacial termination. *Journal of Geophysical Research*, 111(D6):D06102. (pg. 24, 39, 75, 110, 112, 115, 116, 120)

Rea, D. K. (1994). The paleoclimatic record provided by eolian deposition in the deep sea: The geologic history of wind. *Reviews of Geophysics*, 32(2):159–195. (pg. 58, 61)

Revel-Rolland, M., De Dekker, P., Delmonte, B., Hesse, P., Magee, J., Basile-Doelsch, I., Grousset, F. E., and Bosch, D. (2006). Eastern Australia: A possible source of dust in East Antarctica interglacial ice. *Earth and Planetary Science Letters*, 249:1–13. (pg. 64)

Robinson, E. A. and Treitel, S. (1980). *Geophysical Signal Analysis.* Prentice-Hall, Old Tappan, NJ. Chapter 4. (pg. 16)

Robinson, J. P. (2013). Wallace H. Coulter: Decades of invention and discovery. *Cytometry Part A*, 83A(5):424–438. (pg. 66)

Rodriguez-Trujillo, R., Mills, C., Samitier, J., and Gomila, G. (2007). Low cost micro-Coulter counter with hydrodynamic focusing. *Microfluidics and Nanofluidics*, 3(2):171–176. (pg. 106)

Rogers, J. A. and Nuzzo, R. G. (2005). Recent progress in soft lithography. *Materials Today*, 8(2):50 – 56. (pg. 12, 101)

Roth, M. (1971). Fluorescence reaction for amino acids. *Analytical Chemistry*, 43(7):880–882. (pg. 26)

Rousseau, D., Duzer, D., Cambon, G., Jolly, D., Poulsen, U., Ferrier, J., Schevin, P., and Gros, R. (2003). Long distance transport of pollen to Greenland. *Geophysical Research Letters*, 30(14):ASC12. (pg. 11)

Röthlisberger, R., Bigler, M., Hutterli, M., Sommer, S., Stauffer, B., Junghans, H., and Wagenbach, D. (2000). Technique for continuous high-resolution analysis of trace substances in firn and ice cores. *Environmental Science & Technology*, 34(2):338–342. (pg. vi, 10, 13, 15, 19, 20, 21, 24, 27, 28, 29, 30, 31, 32, 34, 35, 121)

Röthlisberger, R., Mulvaney, R., Wolff, E. W., Hutterli, M. A., Bigler, M., Sommer, S., and Jouzel, J. (2002). Dust and sea salt variability in central East Antarctica (Dome C) over the last 45 kyrs and its implications for southern high-Iatitude climate. *Geophysical Research Letters*, 29(20):1963. (pg. 26, 29, 73)

Ruth, U. (2002). *Concentration and size distribution of microparticles in the NGRIP ice core (Central Greenland) during theLLast glacial period*. PhD thesis, Universität Bremen. (pg. 68, 73)

Ruth, U., Barbante, C., Bigler, M., Delmonte, B., Fischer, H., Gabrielli, P., Gaspari, V., Kaufmann, P., Lambert, F., Maggi, V., Marino, F., Petit, J.-R., Udisti, R., Wagenbach, D., Wegner, A., and Wolff, E. W. (2008). Proxies and Measurement Techniques for Mineral Dust in Antarctic Ice Cores. *Environmental Science & Technology*, 42(15):5675–5681. (pg. 58, 60, 73)

Ruth, U., Bigler, M., Röthlisberger, R., Siggaard-Andersen, M.-L., Kipfstuhl, S., Goto-Azuma, K., Hansson, M., Johnsen, S., Lu, H., and Steffensen, J. (2007). Ice core evidence for a very tight link between North Atlantic and east Asian glacial climate. *Geophysical Research Letters*, 34(3):L03706. (pg. 36)

Ruth, U., Wagenbach, D., Bigler, M., Steffensen, J. P., Röthlisberger, R., and Miller, H. (2002). High resolution microparticle profiles at NGRIP: Case studies of calcium-dust relationship. *Annals of Glaciology*, 35:237–242. (pg. 12, 25, 28, 67, 68, 69, 70, 73, 80, 91, 92, 93, 100, 119)

Ruth, U., Wagenbach, D., Steffensen, J. P., and Bigler, M. (2003). Continuous record of microparticle concentration and size distribution in the central Greenland NGRIP ice core during the last glacial period. *Journal of Geophysical Research*, 108(D3):4098. (pg. 21, 60, 68, 70, 74, 75, 80, 82, 89, 91, 99, 108, 109, 113, 114, 119)

Saey, P. (1998). Konzentration und Grössenverteilung von Mikropartikeln in alpinen und polaren Eisbohrkernen. Master's thesis, Universität Heidelberg. (pg. 68)

Sassen, K., DeMott, P. J., Prospero, J. M., and Poellot, M. R. (2003). Saharan dust storms and indirect aerosol effects on clouds: CRYSTAL-FACE results. *Geophysical Research Letters*, 30(12):1633. (pg. 56)

Scheuvens, D. and Kandler, K. (2014). On composition, morphology and size distribution of airborne mineral dust. In Stuut, J.-B. and Knippertz, P., editors, *Mineral dust - A key player in the earth system*. Springer. *in preparation*. (pg. 55, 58, 61, 62, 73, 111)

Scheuvens, D., Schütz, L., Kandler, K., Ebert, M., and Weinbruch, S. (2013). Bulk composition of northern African dust and its source sediments : A compilation . *Earth-Science Reviews*, 116:170 – 194. (pg. 62)

Schüpbach, S., Federer, U., Kaufmann, P. R., Hütterli, M. A., Buiron, D., Blunier, T., Fischer, H., and Stocker, T. F. (2009). A new method for high-resolution methane measurements on polar ice cores using continuous flow analysis. *Environmental Science & Technology*, 43(14):5371–5376. (pg. 21, 22, 50, 52)

Schütz, L. and Sebert, M. (1987). Mineral aerosols and source identification. *Journal of Aerosol Science*, 18(1):1–10. (pg. 61)

Schüpbach, S., Federer, U., Bigler, M., Fischer, H., and Stocker, T. F. (2011). A refined TALDICE-1a age scale from 55 to 112 ka before present for the Talos Dome ice core based on high-resolution methane measurements. *Climate of the Past*, 7(3):1001–1009. (pg. 24, 50)

Schwander, J., Sowers, T., Barnola, J.-M., Blunier, T., Fuchs, A., and Malaizé, B. (1997). Age scale of the air in the Summit ice: Implication for glacial-interglacial temperature change. *Journal of Geophysical Research*, 102(D16):19483–19493. (pg. 9)

Schwander, J. and Stauffer, B. (1984). Age difference between polar ice and the air trapped in its bubbles. *Nature*, 311(5981):45–47. (pg. 9)

Severinghaus, J., Sowers, T., Brook, E. J., Alley, R. B., and Bender, M. L. (1998). Timing of abrupt climate change at the end of the Younger Dryas interval from thermally fractionated gases in polar ice. *Nature*, 391(6663):141–146. (pg. 9, 49)

Severinghaus, J. P., Albert, M. R., Courville, Z. R., Fahnestock, M. A., Kawamura, K., Montzka, S. A., Mühle, J., Scambos, T. A., Shields, E., Shuman, C. A., Suwa, M., Tans, P., and Weiss, R. F. (2010). Deep air convection in the firn at a zero-accumulation site, central Antarctica. *Earth and Planetary Science Letters*, 293(3-4):359 – 367. (pg. 9)

Shapiro, H. M. (2003). *Practical flow cytometry*. John Wiley & Sons, Hoboken, NJ. (pg. 76, 78, 85, 86, 87, 89, 90, 92, 95, 98, 122)

Shapiro, H. M. (2004). The evolution of cytometers. *Cytometry A*, 58A(1):13–20. (pg. 67, 76, 77, 78, 93, 100, 119)

Shi, Z., Zhang, D., Hayashi, M., Ogata, H., Ji, H., and Fujiie, W. (2008). Influences of sulfate and nitrate on the hygroscopic behaviour of coarse dust particles. *Atmospheric Environment*, 42(4):822 – 827. (pg. 116)

Shine, K. P. and de Forster, P. M. (1999). The effect of human activity on radiative forcing of climate change: a review of recent developments. *Global and Planetary Change*, 20(4):205 – 225. (pg. 55)

Sigg, A., Fuhrer, K., Anklin, M., Staffelbach, T., and Zurmühle, D. (1994). A continuous analysis technique for trace species in ice cores. *Environmental Science & Technology*, 28(2):204 – 209. (pg. vi, 10, 13, 14, 15, 16, 17, 18, 19, 20, 22, 24, 26, 28, 29, 30, 34, 38, 121)

Sigg, A. and Neftel, A. (1991). Evidence for a 50% increase in H_2O_2 over the last 200 years from a Greenland ice core. *Nature*, 351(6327):557–559. (pg. 28)

Sigman, D. M. and Boyle, E. A. (2000). Glacial/interglacial variations in atmospheric carbon dioxide. *Nature*, 407(6806):859–869. (pg. 56)

Sokolik, I. and Toon, O. (1999). Incorporation of mineralogical composition into models of the radiative properties of mineral aerosol from UV to IR wavelengths. *Journal of Geophysical Research*, 104(D8):9423–9444. (pg. 58, 89)

Sowers, T., Alley, R., and Jubenville, J. (2003). Ice core records of atmospheric N_2O covering the last 106,000 years. *Science*, 301(5635):945–948. (pg. 9)

Sowers, T., Bender, M., and Raynaud, D. (1989). Elemental and isotopic composition of occluded O_2 and N_2 in polar ice. *Journal of Geophysical Research*, 94(D4):5137–5150. (pg. 9)

Sowers, T., Brook, E., Etheridge, D., Blunier, T., Fuchs, A., Leuenberger, M., Chappellaz, J., Barnola, J. M., Wahlen, M., Deck, B., and Weyhenmeyer, C. (1997). An interlaboratory comparison of techniques for extracting and analyzing trapped gases in ice cores. *Journal of Geophysical Research*, 102(C12):26527–26538. (pg. 50)

Spahni, R., Chappellaz, J., Stocker, T. F., Loulergue, L., Hausammann, G., Kawamura, K., Fluckiger, J., Schwander, J., Raynaud, D., Masson-Delmotte, V., and Jouzel, J. (2005). Atmospheric methane and nitrous oxide of the late Pleistocene from Antarctic ice cores. *Science*, 310(5752):1317–1321. (pg. 49)

Spencer, D. C. (2013). *Advanced microfluidic impedance cytometry for point-of-care analysis*. PhD thesis, University of Southampton. (pg. 101, 103, 105)

Spencer, D. C. and Morgan, H. (2011). Positional dependence of particles in microfludic impedance cytometry. *Lab on a Chip*, 11:1234–1239. (pg. 101, 105, 119, 123)

Stauffer, B. and Berner, W. (1978). CO_2 in natural ice. *Journal of Glaciology*, 21(85):291–300. (pg. 9, 15)

Stauffer, B., Blunier, T., Dällenbach, A., Indermühle, A., Schwander, J., Stocker, T., Tschumi, J., Chappellaz, J., Raynaud, D., Hammer, C., and Clausen, H. (1998). Atmospheric CO2 concentration and millennial-scale climate change during the last glacial period. *Nature*, 392(6671):59–62. (pg. 9)

Steffensen, J. (1997). The size distribution of microparticles from selected segments of the Greenland Ice Core Project ice core representing different climatic periods. *Journal of Geophysical Research*, 102(C12):26755–26763. (pg. 12, 58, 59, 60, 67, 68, 82, 89, 91, 99, 108, 109, 112, 114)

Steffensen, J. P. (1988). Analysis of the seasonal variation in dust, Cl^-, NO_3^-, and SO_4^{2-} in two Central Greenland firn cores. *Annals of Glaciology*, 10:171–177. (pg. 59)

Steffensen, J. P., Andersen, K. K., Bigler, M., Clausen, H. B., Dahl-Jensen, D., Fischer, H., Goto-Azuma, K., Hansson, M., Johnsen, S. J., Jouzel, J., Masson-Delmotte, V., Popp, T., Rasmussen, S. O., Röthlisberger, R., Ruth, U., Stauffer, B., Siggaard-Andersen, M.-L., Sveinbjörnsdóttir, r. E., Svensson, A., and White, J. W. C. (2008). High-resolution Greenland ice core data show abrupt climate change happens in few years. *Science*, 321(5889):680–684. (pg. 47, 118)

Stowasser, C. (2013). *Continuous greenhouse gas measurements from ice cores*. PhD thesis, Centre for Is og Klima, Københavns Universitet. (pg. 50)

Stowasser, C., Buizert, C., Gkinis, V., Chappellaz, J., Schüpbach, S., Bigler, M., Faïn, X., Sperlich, P., Baumgartner, M., Schilt, A., and Blunier, T. (2012). Continuous measurements of methane mixing ratios from ice cores. *Atmospheric Measurement Techniques*, 5(5):999–1013. (pg. 11, 21, 44, 46, 50, 52, 119)

Stuiver, M., Grootes, P. M., and Braziunas, T. F. (1995). The GISP2 $\delta^{18}O$ Climate Record of the Past 16,500 Years and the Role of the Sun, Ocean, and Volcanoes. *Quaternary Research*, 44:341–354. (pg. 115)

Sugimae, A. (1984). Elemental constituents of atmospheric particulates and particle density. *Nature*, 307(5947):145–147. (pg. 58)

Sun, T. and Morgan, H. (2010). Single cell microfluidic impedance cytometry - A review. *Microfluidics and Nanofluidics*, 8:423–443. (pg. 101, 106)

Svensson, A., Andersen, K. K., Bigler, M., Clausen, H. B., Dahl-Jensen, D., Davies, S. M., Johnsen, S. J., Muscheler, R., Parrenin, F., Rasmussen, S. O., Röthlisberger, R., Seierstad, I., Steffensen, J. P., and Vinther, B. M. (2008). A 60 000 year Greenland stratigraphic ice core chronology. *Climate of the Past*, 4:47–57. (pg. 36, 39, 59)

Svensson, A., Andersen, K. K., Bigler, M., Clausen, H. B., Dahl-Jensen, D., Davies, S. M., Johnsen, S. J., Muscheler, R., Rasmussen, S. O., Röthlisberger, R., Steffensen, J. P., and Vinther, B. M. (2006). The Greenland Ice Core Chronology 2005, 15-42 ka. Part 2: comparison to other records. *Quaternary Science Reviews*, 25(23-24):3258–3267. (pg. 10, 24, 115)

Svensson, A., Bigler, M., Kettner, E., Dahl-Jensen, D., Johnsen, S., Kipfstuhl, S., Nielsen, M., and Steffensen, J. P. (2011). Annual layering in the NGRIP ice core during the Eemian. *Climate of the Past*, 7(4):1427–1437. (pg. 16, 39)

Svensson, A., Biscaye, P. E., and Grousset, F. E. (2000). Characterization of late glacial continental dust in the Greenland Ice Core Project ice core. *Journal of Geophysical Research*, 105(D4):4637–4656. (pg. 62, 63, 112, 120)

Svensson, A., Nielsen, S. W., Kipfstuhl, S., Johnsen, S. J., Steffensen, J. P., Bigler, M., Ruth, U., and Röthlisberger, R. (2005). Visual stratigraphy of the North Greenland Ice Core Project (NorthGRIP) ice core during the last glacial period. *Journal of Geophysical Research*, 110(D2):D02108. (pg. 24, 39, 74, 75, 116)

Taylor, K., Mayewski, P., Twickler, M., and Whitlow, S. (1996). Biomass burning recorded in the GISP2 ice core: A record from eastern Canada? *The Holocene*, 6(1):1–6. (pg. 25)

Tegen, I. (2003). Modeling the mineral dust aerosol cycle in the climate system. *Quaternary Science Reviews*, 22:1821–1834. (pg. 55, 58, 89)

Thompson, A. M. (1992). The Oxidizing Capacity of the Earth's Atmosphere: Probable Past and Future Changes. *Science*, 256(5060):1157–1165. (pg. 28)

Tobo, Y., DeMott, P. J., Raddatz, M., Niedermeier, D., Hartmann, S., Kreidenweis, S. M., Stratmann, F., and Wex, H. (2012). Impacts of chemical reactivity on ice nucleation of kaolinite particles: A case study of levoglucosan and sulfuric acid. *Geophysical Research Letters*, 39(19):L19803. (pg. 56)

Toon, O. B. (2003). Atmospheric science: African dust in Florida clouds. *Nature*, 424(6949):623–624. (pg. 55)

Traversi, R., Becagli, S., Castellano, E., Migliori, A., Severi, M., and Udisti, R. (2002). High-resolution fast ion chromatography (FIC) measurements of chloride, nitrate and sulphate along the EPICA Dome C ice core. *Annals of Glaciology*, 35(1):291–298. (pg. 22)

Tsien, R. Y., Pozzan, T., and Rink, T. J. (1982). Calcium homeostasis in intact lymphocytes: cytoplasmic free calcium monitored with a new, intracellularly trapped fluorescent indicator. *Journal of Cell Biology*, 94(2):325–334. (pg. 20, 30)

Twomey, S. (1977). The Influence of Pollution on the Shortwave Albedo of Clouds. *Journal of Atmospheric Sciences,*, 34(7):1149–1154. (pg. 55)

Tzur, A., Moore, J., Jorgensen, P., Shapiro, H., and Kirschner, M. (2011). Optimizing optical flow cytometry for cell volume-based sorting and analysis. *Plos One*, 6(1):e16053. (pg. 85, 90, 92, 94, 100)

Vallelonga, P., Bertagna, G., Blunier, T., Kjær, H. A., Popp, T. J., Rasmussen, S. O., Steffensen, J. P., Stowasser, C., Svensson, A. S., Warming, E., Winstrup, M., Bigler, M., and Kipfstuhl, S. (2012). Duration of Greenland stadial 22 and ice-gas Δage from counting of annual layers in Greenland NGRIP ice core. *Climate of the Past*, 8(6):1839–1847. (pg. 96)

Vallelonga, P. and Svensson, A. (2014). Ice core archives of mineral dust. In Stuut, J.-B. and Knippertz, P., editors, *Mineral dust - A key player in the earth system*. Springer. *in preparation.* (pg. 60)

Van Dilla, M., Trujillo, T., Mullaney, P., and Coulter, J. (1969). Cell microfluorometry: A method for rapid fluorescence measurement. *Science*, 163(3872):1213–1214. (pg. 77)

VanCuren, R. A., Cahill, T., Burkhart, J., Barnes, D., Zhao, Y., Perry, K., Cliff, S., and McConnell, J. (2012). Aerosols and their sources at Summit Greenland - First results of continuous size- and time-resolved sampling. *Atmospheric Environment*, 52:82 – 97. (pg. 63, 90, 113, 117)

Vaughn, B. H., White, J. W. C., Delmotte, M., Trolier, M., Cattani, O., and Stievenard, M. (1998). An automated system for hydrogen isotope analysis of water. *Chemical Geology*, 152(3-4):309–319. (pg. 47)

Vinther, B., Clausen, H., Johnsen, S., Rasmussen, S., Andersen, K., Buchardt, S., Dahl-Jensen, D., Seierstad, I., Siggaard-Andersen, M.-L., Steffensen, J., Svensson, A., Olsen, J., and Heinemeier, J. (2006). A synchronized dating of three Greenland ice cores throughout the Holocene. *Journal of Geophysical Research*, 111(D13):D13102. (pg. 24, 47)

Wagenbach, D., Ducroz, F., Mulvaney, R., Keck, L., Minikin, A., Legrand, M., Hall, J. S., and Wolff, E. W. (1998). Sea-salt aerosol in coastal Antarctic regions. *Journal of Geophysical Research*, 103(D9):10961–10974. (pg. 27)

Washington, R., Todd, M. C., Lizcano, G., Tegen, I., Flamant, C., Koren, I., Ginoux, P., Engelstaedter, S., Bristow, C. S., Zender, C. S., Goudie, A. S., Warren, A., and Prospero, J. M. (2006). Links between topography, wind, deflation, lakes and dust: The case of the Bodélé Depression, Chad. *Geophysical Research Letters*, 33(9):L09401. (pg. 57)

Wegner, A. (2008). *Sources and transport characteristics of mineral dust in Dronning Maud Land, Antarctica.* PhD thesis, Universität Bremen. (pg. 67, 68)

Werner, M., Mikolajewicz, U., Heimann, M., and Hoffmann, G. (2000). Borehole versus isotope temperatures on Greenland: Seasonality does matter. *Geophysical Research Letters*, 27(5):723–726. (pg. 116)

Whitlow, S., Mayewski, P., and Dibb, J. (1992). A comparison of major chemical species seasonal concentration and accumulation at the South Pole and Summit, Greenland. *Atmospheric Environment*, 26A(11):2045–2054. (pg. 29, 59, 110)

Whitlow, S., Mayewski, P., Dibb, J., Holdsworth, G., and Twickler, M. (1994). An ice core based record of biomass burning in the Arctic and Subarctic 1750-1980. *Tellus B*, 46(3):234–242. (pg. 25)

Wilhelms, F., Kipfstuhl, J., Miller, H., Heinloth, K., and Firestone, J. (1998). Precise dielectric profiling of ice cores: A new device with improved guarding and its theory. *Journal of Glaciology*, 44(146):171–174. (pg. 31)

Winckler, G. and Fischer, H. (2006). 30,000 years of cosmic dust in Antarctic ice. *Science*, 313(5786):491–491. (pg. 11, 54)

Winstrup, M., Svensson, A. M., Rasmussen, S. O., Winther, O., Steig, E. J., and Axelrod, A. E. (2012). An automated approach for annual layer counting in ice cores. *Climate of the Past*, 8(6):1881–1895. (pg. 74, 75)

Wolff, E., Rankin, A., and Rothlisberger, R. (2003). An ice core indicator of Antarctic sea ice production? *Geophysical Research Letters*, 30(22):2158. (pg. 26, 27, 112)

Wolff, E. W., Chappellaz, J., Blunier, T., Rasmussen, S. O., and Svensson, A. (2010). Millennial-scale variability during the last glacial: The ice core record. *Quaternary Science Reviews*, 29(21-22):2828–2838. (pg. 39)

Wolff, E. W., Fischer, H., Fundel, F., Ruth, U., Twarloh, B., Littot, G. C., Mulvaney, R., Rothlisberger, R., de Angelis, M., Boutron, C. F., Hansson, M., Jonsell, U., Hutterli, M. A., Lambert, F., Kaufmann, P., Stauffer, B., Stocker, T. F., Steffensen, J. P., Bigler, M., Siggaard-Andersen, M. L., Udisti, R., Becagli, S., Castellano, E., Severi, M., Wagenbach, D., Barbante, C., Gabrielli, P., and Gaspari, V. (2006). Southern Ocean sea-ice extent, productivity and iron flux over the past eight glacial cycles. *Nature*, 440(7083):491–496. (pg. 54)

Wolff, E. W., Legrand, M. R., and Wagenbach, D. (1998). Coastal Antarctic aerosol and snowfall chemistry. *Journal of Geophysical Research*, 103(D9):10927–10934. (pg. 33)

Wood, E. D., Armstrong, F. A. J., and Richards, F. A. (1967). Determination of nitrate in sea water by cadmium-copper reduction to nitrite. *Journal of the Marine Biological Association*, 47:23–31. (pg. 34)

Wu, X., Chon, C. H., Wang, Y.-N., Kang, Y., and Li, D. (2008). Simultaneous particle counting and detecting on a chip. *Lab on a Chip*, 8:1943–1949. (pg. 101, 106)

Yang, Y., Zhang, X.-X., Korenaga, T., and Higuchi, K. (1997). Determination of passive-sampled sulphur dioxide in ambient air as sulphate ion by flow injection analysis with an in-line reaction column. *Talanta*, 45(2):445 – 450. (pg. 33)

Yentsch, C. S. and Yentsch, C. M. (2008). Single cell analysis in biological oceanography and its evolutionary implications. *Journal of Plankton Research*, 30(2):107–117. (pg. 76)

Zhang, H., Chon, C. H., Pan, X., and Li, D. (2009). Methods for counting particles in microfluidic applications. *Microfluidics and Nanofluidic*, 7:729–749. (pg. 67, 68, 99, 100, 101, 106)

Zhang, J., Fischer, C., and PB, O. (1999). Optimization of performance and minimization of silicate interference in continuous flow phosphate analysis. *Talanta*, 49(2):293–304. (pg. 43)

Zhang, J.-Z. and Chi, J. (2002). Automated analysis of nanomolar concentrations of phosphate in natural waters with liquid waveguide. *Environmental Science & Technology*, 36(5):1048–1053. (pg. 41)

Zhe, J., Jagtiani, A. V., Dutta, P., Hu, J., and Carletta, J. (2007). A micromachined high throughput Coulter counter for bioparticle detection and counting. *Journal of Micromechanics and Microengineering*, 17:304–313. (pg. 106)

Zielinski, G., Mayewski, P., Meeker, D., Grönvold, K., Germani, M., Whitlow, S., Twickler, M., and Taylor, K. (1997). Volcanic aerosol records and tephrachronology of the Summit, Greenland, ice cores. *Journal of Geophysical Research*, 102(C12):26625–26640. (pg. 23, 31, 108)

Zielinski, G., Mayewski, P., Meeker, L., Whitlow, S., Twickler, M., Morrison, M., Meese, D., Gow, A., and Alley, R. (1994). Record of volcanism since 7000 B.C. from the GISP2 Greenland ice core and implications for the volcano-climate system. *Science*, 264(5161):948–952. (pg. 31)

Zielinski, G. and Mershon, G. (1997). Paleoenvironmental implications of the insoluble microparticle record in the GISP2 (Greenland) ice core during rapidly changing climate of the Pleistocene-Holocene transition. *Geological Society of America Bulletin*, 109(5):547–559. (pg. 109)

Zimmermann, F., Weinbruch, S., Schütz, L., Hofmann, H., Ebert, M., Kandler, K., and Worringen, A. (2008). Ice nucleation properties of the most abundant mineral dust phases. *Journal of Geophysical Research*, 113(D23):D23204. (pg. 56)

Appendices

Appendix A

Bigler et al. (2011):

Optimisation of High-Resolution CFA

The student's contribution to the paper:
At the start of my PhD project there was no Continuous Flow Analysis system in Copenhagen. This publication describes the system I set up with Matthias Bigler after his design. My main tasks included (1) reliable heat control of both the melt head and those detection lines that needed temperature regulation for kinetics improvement and (2) ensuring the low volume debubbler's functionality by testing different geometries and materials. The flow scheme described is the result of minor modifications I undertook, in order to integrate a Near Infra Red Cavity Ring Down Spectrometer for continuous methane detection.
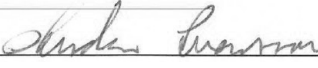
16/10-2013	Maibritt Nielsen	
18/10-13	ANDERS SVENSSON	
10.10.2013	BIGLER Matthias	
25/10/2013	Joergen Peder Steffensen	
28/10/13	Paul Vallelonga	
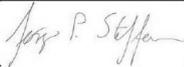
Optimization of High-Resolution Continuous Flow Analysis for Transient Climate Signals in Ice Cores

Matthias Bigler,*,[†,‡] Anders Svensson,[†] Ernesto Kettner,[†] Paul Vallelonga,[†] Maibritt E. Nielsen,[†] and Jørgen Peder Steffensen[†]

[†]Centre for Ice and Climate, Niels Bohr Institute, University of Copenhagen, Juliane Maries Vej 30, DK-2100 Copenhagen Ø, Denmark

[‡]Climate and Environmental Physics, Physics Institute, and Oeschger Centre for Climate Change Research, University of Bern, Sidlerstrasse 5, CH-3012 Bern, Switzerland

ABSTRACT: Over the past two decades, continuous flow analysis (CFA) systems have been refined and widely used to measure aerosol constituents in polar and alpine ice cores in very high-depth resolution. Here we present a newly designed system consisting of sodium, ammonium, dust particles, and electrolytic meltwater conductivity detection modules. The system is optimized for high-resolution determination of transient signals in thin layers of deep polar ice cores. Based on standard measurements and by comparing sections of early Holocene and glacial ice from Greenland, we find that the new system features a depth resolution in the ice of a few millimeters which is considerably better than other CFA systems. Thus, the new system can resolve ice strata down to 10 mm thickness and has the potential of identifying annual layers in both Greenland and Antarctic ice cores throughout the last glacial cycle.

INTRODUCTION

Ice core drilling projects in Greenland and Antarctica have demonstrated the great value of the polar ice caps as sensitive archives of atmospheric composition and climatic variability over the late Pleistocene. In Greenland, the GRIP, GISP2, and NGRIP drilling projects have demonstrated the regularity and extent of Dansgaard−Oeschger cycles and have provided a glimpse of the climate of the Northern Hemisphere during the Eemian.[1] In Antarctica, drilling projects at Vostok, Dome Fuji, Dome Concordia,[2] and Dronning Maud Land[3] have shown the extent of variability between each glacial-interglacial cycle and indicated the importance of climate transitions such as the mid Brunhes−Matuyama event.

Recent and current drilling projects in Antarctica (TalDICE, WAIS Divide) and Greenland (NEEM) offer further insights into the Earth's late Pleistocene climate, particularly through the employment of new high-resolution analytical techniques. Emphasis is placed on these techniques because of the low annual snow accumulation at some drilling sites, as well as the subsequent thinning of those ice layers with compression and glacial flow. At NGRIP, it is calculated that glacial thinning has reduced the thickness of annual snow layers to just 1 cm in the deeper part of the core.[1] Similar annual layer thicknesses have been reported in the deepest part of the EPICA Dronning Maud Land (EDML) ice core.[4] A recent study of Greenland ice has shown that definitive shifts in precipitation sources can occur within a few years,[5] underlining the need to determine important climate parameters at annual resolution.

The past decade has seen extensive development in continuous flow analysis (CFA) techniques, permitting the efficient use of ice core samples for a multitude of studies. The analysis of climatic signals in ice cores traditionally employed the division of each core section into discrete pieces dedicated to individual, often destructive, analysis for gases, water isotopes, aeolian dust, chemistry, and so on. For contamination-prone analytes, these pieces then required further decontamination and preparation, resulting in a substantial loss of ice core material (refs 6 and 7 and references therein). The cost of ice core recovery and the great number of participants in ice coring projects is driving a trend toward continuous techniques, greater collaboration and integration of analytical methods, all optimized for the introduction of the sample as a continuous water stream. Continuous methods for the determination of gas concentrations, water isotopes and many chemical species have been reported in the literature in recent years. An early design[8] featured a debubbler that was open to air, and determined eight analytes (electrolytic meltwater conductivity, formaldehyde, sodium, hydrogen peroxide, ammonium, calcium, nitrate, and sulfate). This system has been significantly improved, with additional analytical channels and a sealed debubbler allowing the separation of air bubbles from the melt stream and subsequent analysis of the air trapped in the ice.[9] This technique has proven successful for the online determination of methane concentrations in Antarctic ice from Talos Dome.[10] The CFA technique has also been extended to a variety of analytical challenges, including the determination of water and gas isotopes,[11,12] carbon compounds,[13,14] trace elements,[6,7] and
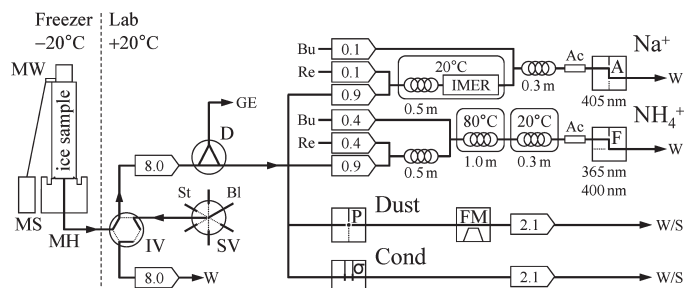
Figure 1. Scheme of the C CFA setup with melthead (MH), melting speed sensor (MS), melting weight (MW), injection (IV), and selection (SV) valves for standard (St) and blank (Bl), debubbler (D), line to the gas extraction unit (GE), reagents (Re), buffers (Bu), waste (W), and optional discrete sampling (S) lines, Accurel membrane debubblers (Ac), immobilized enzyme reactor (IMER), absorption (A), fluorescence (F), particle (P), and conductivity (σ) detectors, flow meter (FM). Flow rates of the peristaltic pump tubes (in mL/min), reaction coil lengths, temperatures and detector light wavelengths are given in the scheme.

polycyclic aromatic hydrocarbons,[15] but also for efficient discrete sampling tasks or the coupling to ion chromatographs.[16−18]

This work presents a CFA system developed at the Centre for Ice and Climate at the University of Copenhagen (in the following denoted as C CFA) which has been optimized for high-resolution determination of transient signals in thin ice strata, with the specific aim of resolving the annual signal in thin layers of deep polar ice cores. The improved resolution is obtained by avoiding or minimizing mixing volumes, in particular at the melthead and in the debubbler unit, and by running the system at low melt speed. The latter has the drawback that only few components can be measured due to the decreased available sample amount. The current system determines the mass concentration of water-soluble sodium (Na^+), ammonium (NH_4^+), the electrolytic meltwater conductivity (σ), and the number of insoluble dust particles (dust). To first order, the system thus provides proxies of marine (Na^+), terrestrial (dust), and biogenic (NH_4^+) environments, whereas σ is a sum parameter of all ionic constituents in the ice. The analytical depth resolution in the ice is evaluated by comparing measurements of standard solutions with the CFA system developed at the Physics Institute of the University of Bern (here called B CFA) and by analyzing sections of early Holocene and glacial ice from the Greenland NGRIP ice core that is compared to existing Greenland records.

■ MATERIALS AND METHODS

The C CFA system described here consists primarily of a melting unit in a freezer, sample/standard valves, a debubbler and various analytical modules in a lab at normal room temperature (Figure 1). While this configuration is similar to that already reported for the B CFA,[9] though not specifically designed for field deployment, the system has been optimized to achieve better measuring resolution through new melthead and debubbler designs and shorter sample distribution lines with appropriate flow rates.

Melting Unit. The melthead is located in an upright freezer at −20 °C and is heated with four 125 W heating cartridges, one with an embedded thermocouple (type "J", Mickenhagen). The temperature, in our case ∼30 °C, is controlled by a temperature regulator (dTRON 308, Jumo) to maintain the desired ice melting speed. A removable rectangular plexiglass sample holder is affixed on a centering frame above the melthead to
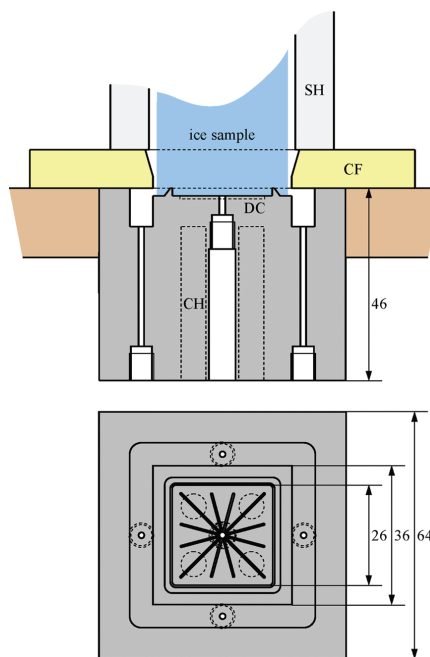
Figure 2. Melthead with drain channels (DC) and holes, $^1/_4$−28 standard flat-bottom ports, cartridge heaters (CH), centering frame (CF), and removable rectangular plexiglass sample holder (SH); measures are in mm.

guide the ice sample of 34 mm × 34 mm cross section and 55 cm length. It was cut either in a cold lab or already in the field, however, both ends, and if present, core breaks within a sample section were carefully cleaned with a microtome knife before melting. Within the core holder, a 200 g stainless steel cylinder with PTFE endpieces is maintaining a constant downward force on the sample during analysis which leads to a more

stable melting speed. A hook attached to the top of the weight and connected to a draw wire position transducer (SX80, WayCon) located alongside the melthead is used for depth registration during melting.

The melthead (Figure 2) features a square cross-section composed of an inner and outer collection area which are separated by a 2 mm high triangular ridge. In a first version (used for the measurements in this pilot study) the melthead was produced from a solid block of aluminum without surface coating. In a second version it is made of copper (higher thermal conductivity) with a chemically inert 2 μm gold surface coating on a 5 μm layer of electroless nickel. In contrast to the B CFA melthead[9] with its slightly conical inner area and six concentrically arranged drain off holes, a squared and flat inner area with starring drain channels (0.75 mm deep, 0.4 mm wide) and only one central drainage point minimizes the mixing at the melthead and utilizes the maximal amount of the available sample. This central hole is 1.6 mm in diameter and allows a 1.6 mm OD and 0.5 mm ID PEEK tube (polyetheretherketone) to be located approximately 1 mm below the melthead surface to remove meltwater from the inner area of the melthead without being plugged by the melting ice. Four drainage channels are in the outer area to remove meltwater from the contaminated, surface of the ice sample.

Compared to the B CFA system with a typical ice melting rate of 3−4 cm/min[9] the C CFA system runs at a lower melt rate of 1.5 cm/min, while keeping the inner area of the melthead with 26 mm × 26 mm in the same order of magnitude. This gives ∼9 mL/min meltwater for the C CFA system including 10% air. In order to prevent contamination, an overflow from the inner to the outer melthead area of >10% is created by pumping only ∼8 mL/min sample to the warm lab (Figure 1).

Pumping, Sample and Standard Selection. Pumping is carried out with peristaltic pumps (Ismatech IPC with Tygon tubing) and the manifold consists of Teflon tubing (PFA HP plus, Upchurch). Immediately after the melthead is an automated 6-port injection valve (medium pressure, DC gear motor actuator, Upchurch) which is used to toggle between the sample meltwater stream and blank or standards. An additional line is used to maintain pumping from the melthead when blank or standards are fed into the analytical modules before or after a melting run (Figure 1). An automated 6-port selection valve (Upchurch) is used to switch between ultrapure blank water (Milli-Q, ≥ 18.2 MΩ/cm, Millipore Advantage) and various Na^+ and NH_4^+ standard solutions.

In order to minimize mixing volumes, a setup without pump tube between the melthead and the debubbler was tested. Instead, pumping was applied at the overflow of the debubbler. Given this pump rate and the pump rates of the four analytical modules, the total flow rate from the melthead is determined as well. However, due to the segmented flow of water and air between the melthead and the debubbler, the signal dispersion in this part of the system is already very low and did not improve significantly. Furthermore, pressure problems caused strong baseline fluctuations in the Na^+ module and the implementation of a unit separating air from water for measurements of atmospheric gases was impossible. Therefore, a pump tube between the melt head and the debubbler is indispensable.

Debubbler. The debubbler has the function of removing air bubbles from the ice core meltwater, preventing air entering into the analytical modules, which might be stuck and will cause false signals. Its new design features a closed flat triangular cell with one inlet and two outlets: one for the debubbled meltwater and the other for the air
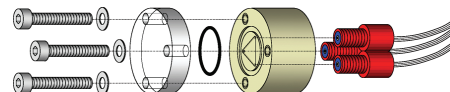
Figure 3. New debubbler design with a flat triangular cell.
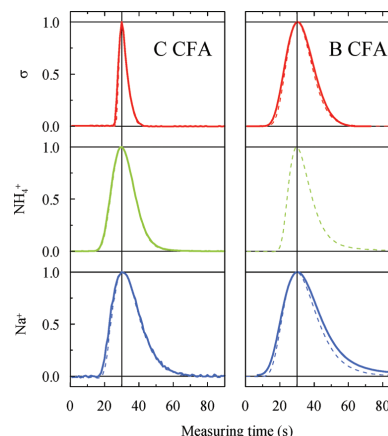
Figure 4. Standardized peaks of short multicomponent standard pulses switched via injection valve (thin dashed lines) or applied between Milli-Q-ice cubes (thick lines; no data available for B CFA NH_4^+ and dust).

bubbles and excess meltwater (Figure 3). The debubbler body made of PEEK is sealed to a transparent FEP (fluorinated ethylene propylene) cap with an O-ring allowing visual inspection of the debubbling. Different cell designs and variations were tested, with the best separation of air and water achieved by an equilateral triangular cell with side length 10 mm and depth of 2 mm resulting in a very low mixing volume of ∼90 μL at a sample flow of ∼8 mL/min. The debubbler is oriented such that the air outlet is in the topmost vertical position. The amount of meltwater directed to the analytical channels is 6 mL/min, consisting of σ (2.1 mL/min), dust (2.1 mL/min), Na^+ (0.9 mL/min), and NH_4^+ (0.9 mL/min), resulting in a debubbler overflow of ∼2 mL/min (∼25% of the sample) containing all the air (∼0.8 mL/min) to ensure reliable debubbling.

Analytical Systems. Similar to a previous work,[9] a conductivity meter (3082 with micro flow cell 829, Amber Science) is used to determine σ, and a laser particle detector (Abakus with LDS 23/25bs sensor, Klotz) is operated in series with a liquid flow meter (ASL-1600-20, Sensirion) to produce sensitive flow-calibrated measurements of particle size and concentrations. NH_4^+ concentrations are determined using a fluorescence method[8] with a photomultiplier-based detector (PMT-FL, FIAlab instruments), while Na^+ is measured following an absorption method[8] using one channel of a three-channel fiberoptic spectrometer (USB2000, Ocean Optics) and a deuterium halogen light source (DT-Mini-2-GS, Ocean Optics) coupled to a microvolume flow cell with 10 mm path length (SMA-Z-microV-10, FIAlab instruments). Detection limits and analytical ranges are in the same order of magnitude as in the initial publication.[9]

Data Acquisition and Processing. A self-made control and data acquisition (DAQ) software (based on LabVIEW 8.5
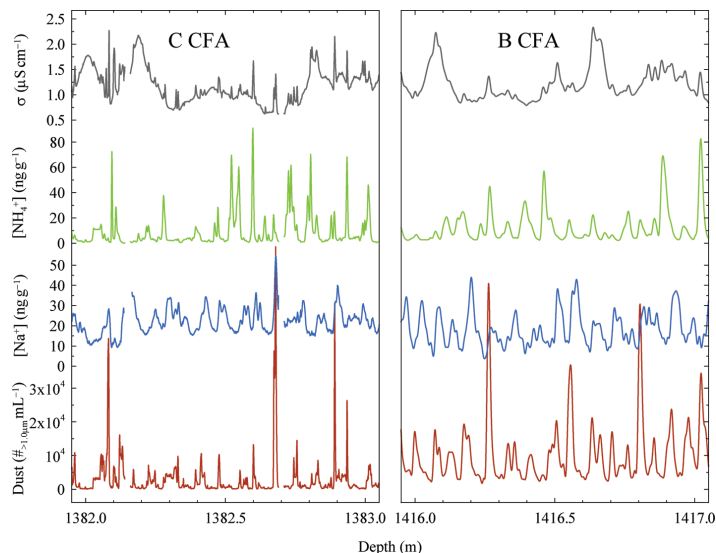
Figure 5. NGRIP data sections from the early Holocene obtained with the new C CFA and the established B CFA system.
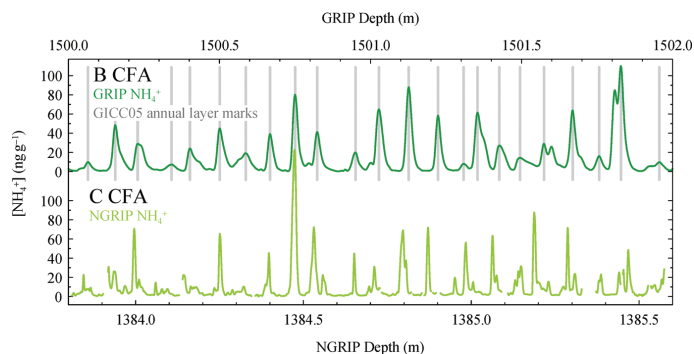
Figure 6. Comparison of GRIP and NGRIP NH_4^+ profiles from the early Holocene on depth scales from the same time interval. Peaks from the two cores can easily be paired one-to-one. The gray vertical lines in the GRIP profile show the annual layer marks applied for the Greenland Ice Core Chronology 2005 (GICC05).[21]

from National Instruments) is used and the devices are connected via RS232-to-USB converter (Digi International) or DAQ device (USB-6216 from National Instruments) to the measuring computer. Drivers were either provided by the manufacturer (OOIBase32 and OOILVD from Ocean Optics) or are self-made (particle detector, conductivity meter, fluorescence detector, actuated valves). The data processing software is based on MATLAB routines. They transform the detector signals to, for example, concentrations and the measuring time to depth by using calibration measurements and the melt speed recordings plus the different analytical delay-times of each component, respectively. Furthermore, measurements of contaminated ice due to breaks and at the beginning and the end of a measuring run can be removed.

■ RESULTS AND DISCUSSION

To demonstrate the resolution enhancement of the new C CFA system compared to the existing B CFA system independently of the chosen melting speed, we carried out tests with high-concentration multicomponent standard pulses (without dust) injected into the system for ∼0.5 s. We found that peak shapes and durations are independent of the concentration and peak height, respectively. Therefore, we can compare standardized peaks (amplitude scaled to 1) as shown in Figure 4 (thin dashed lines). This method is straightforward, however, it does not account for possible signal dispersion between the melthead and the injection valve. To overcome this, we carried out a second set of tests by applying

4486

dx.doi.org/10.1021/es200118j |*Environ. Sci. Technol.* 2011, 45, 4483–4489

our multicomponent standard between Milli-Q-ice cubes which we melted under similar conditions as real ice samples, thus, accounting for the total signal dispersion of the examined systems (Figure 4, thick lines). For the C CFA system, we find almost identical signal peaks for both approaches. As the meltwater stream in this section is still segmented by the air contained in the ice which limits signal dispersion, it can be concluded that the newly designed melthead introduces almost no dispersion. In contrast, the B CFA system shows small differences, as the debubbler is placed within this section and the melthead is not optimized in terms of depth resolution.

Now comparing the C CFA with the B CFA system shows that the peaks are narrower in the new C CFA system, especially for σ, but only slightly for NH_4^+. It is apparent that the higher flow rate through the conductivity flow cell (and also through the dust detector, not shown) increases depth resolution. Unfortunately, it is not an option for the NH_4^+ and Na^+ detection systems to increase the flow rate, as most of the signal dispersion for those components takes place in temperature-controlled mixing coils and reaction columns, respectively, and the corresponding reaction times and reagent mixing ratios are already optimized.[8] To give a measure of the individual time resolutions we calculated the mean value of the duration of a signal increase from 10% above the baseline to 90% of the signal maximum and the corresponding decrease. For the C CFA (and B CFA) we find 5 s (14 s) for σ, 11 s (12 s) for NH_4^+, and 14 s (20 s) for Na^+. Considering a melting speed of 1.5 cm/min as applied for the C CFA system (4 cm/min for the B CFA) this would be equivalent to a depth resolution of ~1.5 mm (~9 mm) for σ, ~3 mm (~8 mm) for NH_4^+, and ~3.5 mm (~13 mm) for Na^+.

NGRIP Early Holocene measurements. To demonstrate the performance of the new setup on real samples, we analyzed 11 m of early Holocene ice from the Greenland NGRIP ice core[1] measuring NH_4^+, Na^+, dust and σ. The samples cover the depth interval from 1378.3 to 1389.3 m and have an age close to 10.0 ka.[19] This section is almost adjacent to the NGRIP ice that was analyzed by the B CFA system[8,20] which allows comparing temporal resolution and absolute concentrations as adjacent Holocene ice sections are expected to show similar values. A selected section of the results is shown in Figure 5. The mean annual layer thickness is around 7.5 cm at this depth and, as expected, annual cycles are resolved in the measurements. Due to the higher resolution of the C CFA system, multiple peaks within one year emerge even more clearly in all series. Generally, a separation of the seasons is observed with NH_4^+ summer peaks, Na^+ winter peaks, and dust spring peaks.[21]

NH_4^+ shows a rather clear annual cycle often with multiple summer peaks overlaying a background level below 10 ng/g (Figure 5). The average NH_4^+ concentrations is with 10.7 ng/g somewhat lower than in the adjacent section measured by the B CFA system (16.4 ng/g) and a contemporaneous GRIP CFA section (13.5 ng/g), calculated on equally long sections. Part of the temporal overlap of NH_4^+ in NGRIP with GRIP[22] is shown in Figure 6. Annual peaks can easily be paired year by year.[21] This shows that NH_4^+ has a rather common signature on a quite widespread geographical area (GRIP and NGRIP are separated by more than 315 km) and gives confidence that the two analytical setups produce consistent NH_4^+ profiles.

Na^+ has a background level of 10−20 ng/g (Figure 5) and winter peaks of up to more than 100 ng/g (not shown). The average concentration level of 18.6 ng/g corresponds well to that
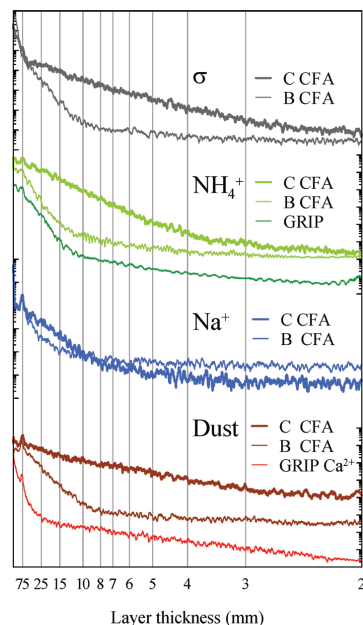
Figure 7. Comparison of Holocene power spectra from the new C CFA system (thick lines) with existing CFA data from NGRIP obtained with the B CFA system (thin lines) and from GRIP obtained with an older version of the B CFA.[22] As the dust profile from GRIP is not available from this interval, Ca^{2+} often used as a dust proxy, is shown instead. Most spectra show a clear annual spike around 75 mm layer thickness. For the C CFA data series (except for Na^+), the power corresponding to a layer thickness of 10 mm is well above the noise level, showing that the setup can resolve annual layers of that thickness. The spectra have been shifted vertically in order to separate them, but they are shown on equidistant scales. Data gaps have been linearly interpolated for the analysis which is based on ~10 m ice sections.

obtained by the B CFA system (16.5 ng/g) on slightly older NGRIP ice.

Dust has a very low background level of less than 1000 particles per mL with very sharply defined spring peaks of highly variable amplitude (Figure 5). Furthermore, peaks occurring at other seasons are not uncommon, an observation which is enabled by the much higher depth resolution of the new C CFA setup compared to the setup of the B CFA system.[23] As both laser systems (Abakus) used different sensors with different detection limits and thus did not cut at the same place of the particle size distribution, the dust concentration level of the new C CFA data is about a factor of 4 lower than that obtained by B CFA on adjacent NGRIP ice. Additional calibration and flow rate measurement errors cannot be excluded. Apart from the absolute deviation, however, the relative accordance of the two records is good.

The σ profile expresses a rather weak annual cycle in the smooth continuous background level of around 1−2 $\mu S/cm$ which is superimposed by very distinct spikes (Figure 5) that may reach up to more than 5 $\mu S/cm$ (not shown). This detailed pattern is not resolved in the lower-resolution B CFA data. The spikes often, but
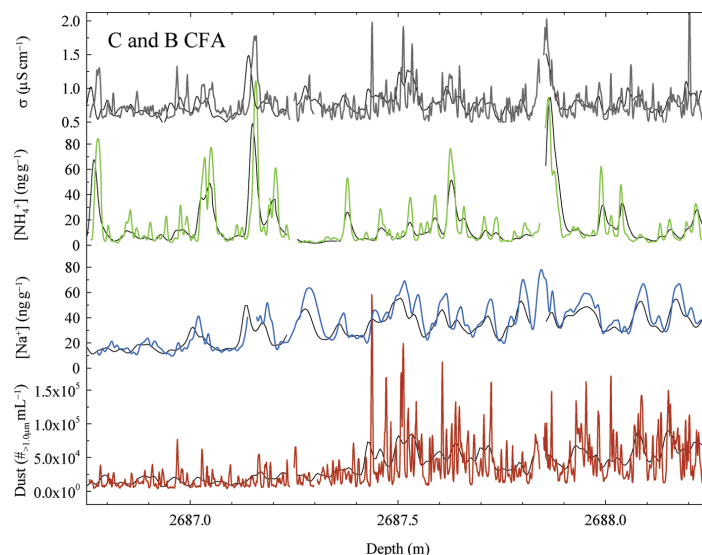
Figure 8. NGRIP data section from the last glacial period showing a Greenland stadial-interstadial transition obtained with the new C CFA (thick colored lines) demonstrating that ~1 cm thick layers are preserved/resolved in dust and σ. For the purpose of comparison, data measured with the established B CFA system are given as well (thin black lines).

not always, coincidence with large NH_4^+ and/or dust peaks. We note that σ represents the sum of all ions in the meltwater including those not analyzed in the present study, for example, sulfate and nitrate, which can contribute significantly to the meltwater conductivity.[24] The measured σ level of 1.19 μS/cm is very consistent with that obtained on adjacent NGRIP ice by the B CFA system (1.22 μS/cm).

Depth Resolution Derived from Holocene Ice Samples. To estimate the depth resolution of the new C CFA setup based on ice samples, power spectra of the measured Holocene data series are considered (Figure 7). They show a rather well-defined background or noise level, where the spectra are flattening out, a clear signal several orders of magnitude above the background,[25] and a clear peak at the annual layer thickness of around 75 mm. σ shows only a weak peak at around 75 mm, as the different contributing ions peak at different times during the year and that diffusion may have occurred for some ions. For dust, NH_4^+, and σ the power corresponding to a layer thickness of 10 mm is at least 2 orders of magnitude above the noise level, whereas the corresponding power of sodium is about 1 order of magnitude above noise. Based on this, and in agreement with the depth resolution estimates derived from multicomponent standard pulse measurements (see above), we conclude that the C CFA setup easily has the potential to resolve 10 mm thin annual layers at least for dust, NH_4^+ and σ, provided the signal is preserved in the ice. We further compare our results with existing CFA profiles from adjacent NGRIP and contemporaneous GRIP Holocene ice (Figure 7). As all three data sets are obtained from periods and locations with very similar climate conditions and annual layer thicknesses, the power spectra are directly comparable and reflect mostly differences in the depth resolution to which the applied melting speed contributes. The power spectra

show that the new C CFA setup clearly has a superior depth resolution in all parameters.

Glacial Ice Samples with Thin Annual Layers. In order to demonstrate directly that the new C CFA system is able to resolve layers of ~1 cm thickness (e.g., in ice which underwent strong thinning) and also to show that such layers can be preserved in the ice, we analyzed an additional 1.5 m long section from the glacial part of the NGRIP ice core from a depth of around 2687.50 m containing a Greenland stadial-interstadial transition (Figure 8). We observe that dust and σ data are in very good agreement with visual stratigraphy data (not shown). According to the NGRIP time scale,[1] the age of this section is around 85 ka and the expected annual layer thickness is ~1.3 cm which should result in ~110 annual layers in the analyzed ice. Indeed, such a number of layers can be found in the dust and σ record, whereas the signal seems not to be preserved in the case of NH_4^+ and Na^+ in ice of this depth. As at least NH_4^+ would have the potential to resolve such layers (see section above), we conclude that this species is affected by diffusion in deep ice. This topic is further discussed in the context of even deeper ice from the last interglacial period, the Eemian, in a following manuscript.[26]

■ AUTHOR INFORMATION

Corresponding Author
*Phone: +41 (0) 631 8673; fax: +41 (0) 631 8742; e-mail: bigler@climate.unibe.ch.

152 | page

■ REFERENCES

(1) North Greenland Ice Core Project members. High-resolution record of Northern Hemisphere climate extending into the last interglacial period. *Nature* **2004**, *431*, 147-151.

(2) EPICA community members. Eight glacial cycles from an Antarctic ice core. *Nature* **2004**, *429*, 623-628.

(3) EPICA community members. One-to-one coupling of glacial climate variability in Greenland and Antarctica. *Nature* **2006**, *444*, 195-198.

(4) Ruth, U.; Barnola, J.-M.; Beer, J.; Bigler, M.; Blunier, T.; Castellano, E.; Fischer, H.; Fundel, F.; Huybrechts, P.; Kaufmann, P.; Kipfstuhl, S.; Lambrecht, A.; Morganti, A.; Oerter, H.; Parrenin, F.; Rybak, O.; Severi, M.; Udisti, R.; Wilhelms, F.; Wolff, E. "EDML1": A chronology for the EPICA deep ice core from Dronning Maud Land, Antarctica, over the last 150000 years. *Clim. Past* **2007**, *3*, 475–484.

(5) Steffensen, J. P.; Andersen, K. K.; Bigler, M.; Clausen, H. B.; Dahl-Jensen, D.; Fischer, H.; Goto-Azuma, K.; Hansson, M.; Johnsen, S. J.; Jouzel, J.; Masson-Delmotte, V.; Popp, T.; Rasmussen, S. O.; Röthlisberger, R.; Ruth, U.; Stauffer, B.; Siggaard-Andersen, M.-L.; Sveinbjornsdottir, A. E.; Svensson, A.; White, J. W. C. High-resolution Greenland ice core data show abrupt climate change happens in few years. *Science* **2008**, *321*, 680–684.

(6) McConnell, J. R.; Lamorey, G. W.; Lambert, S. W.; Taylor, K. C. Continuous ice-core chemical analyses using inductively coupled plasma mass spectrometry. *Environ. Sci. Technol.* **2002**, *36*, 7–11.

(7) Knüsel, S.; Piguet, D. E.; Schwikowski, M.; Gäggeler, H. W. Accuracy of continuous ice-core trace-element analysis by inductively coupled plasma sector field mass spectrometry. *Environ. Sci. Technol.* **2003**, *37*, 2267–2273.

(8) Röthlisberger, R.; Bigler, M.; Hutterli, M.; Sommer, S.; Stauffer, B.; Junghans, H. G.; Wagenbach, D. Technique for continuous high-resolution analysis of trace substances in firn and ice cores. *Environ. Sci. Technol.* **2000**, *34*, 338–342.

(9) Kaufmann, P. R.; Federer, U.; Hutterli, M. A.; Bigler, M.; Schüpbach, S.; Ruth, U.; Schmitt, J.; Stocker, T. F. An improved continuous flow analysis system for high-resolution field measurements on ice cores. *Environ. Sci. Technol.* **2008**, *42*, 8044–8050.

(10) Schüpbach, S.; Federer, U.; Kaufmann, P. R.; Hutterli, M. A.; Buiron, D.; Blunier, T.; Fischer, H.; Stocker, T. F. A new method for high-resolution methane measurements on polar ice cores using continuous flow analysis. *Environ. Sci. Technol.* **2009**, *43*, 5371–5376.

(11) Huber, C.; Leuenberger, M. On-line systems for continuous water and gas isotope ratio measurements. *Isot. Environ. Health Stud.* **2005**, *41*, 189–205.

(12) Gkinis, V.; Popp, T. J.; Johnsen, S. J.; Blunier, T. A continuous stream flash evaporator for the calibration of an IR cavity ring-down spectrometer for the isotopic analysis of water. *Isot. Environ. Health Stud.* **2010**, *46*, 463–475.

(13) Federer, U.; Kaufmann, P. R.; Hutterli, M. A.; Schüpbach, S.; Stocker, T. F. Continuous flow analysis of total organic carbon in polar ice cores. *Environ. Sci. Technol.* **2008**, *42*, 8039–8043.

(14) McConnell, J. R.; Edwards, R.; Kok, G. L.; Flanner, M. G.; Zender, C. S.; Saltzman, E. S.; Banta, J. R.; Pasteris, D. R.; Carter, M. M.; Kahl, J. D. W. 20th-century industrial black carbon emissions altered arctic climate forcing. *Science* **2007**, *317*, 1381–1384.

(15) Gabrieli, J.; Vallelonga, P.; Cozzi, G.; Gabrielli, P.; Gambaro, A.; Sigl, M.; Decet, F.; Schwikowski, M.; Gäggeler, H.; Boutron, C.; Cescon, P.; Barbante, C. Post 17th-century changes of European PAH emissions recorded in high-altitude alpine snow and ice. *Environ. Sci. Technol.* **2010**, *44*, 3260–3266.

(16) Udisti, R.; Becagli, S.; Castellano, E.; Mulvaney, R.; Schwander, J.; Torcini, S.; Wolff, E. Holocene electrical and chemical measurements from the EPICA-Dome C ice core. *Ann. Glaciol.* **2000**, *30*, 20–26.

(17) Cole-Dai, J.; Budner, D. M.; Ferris, D. G. High speed, high resolution, and continuous chemical analysis of ice cores using a melter and ion chromatography. *Environ. Sci. Technol.* **2006**, *40*, 6764–6769.

(18) Osterberg, E. C.; Handley, M. J.; Sneed, S. B.; Mayewski, P. A.; Kreutz, K. J. Continuous ice core melter system with discrete sampling for major ion, trace element, and stable isotope analyses. *Environ. Sci. Technol.* **2006**, *40*, 3355–3361.

(19) Vinther, B. M.; Clausen, H. B.; Johnsen, S. J.; Rasmussen, S. O.; Andersen, K. K.; Buchardt, S. L.; Dahl-Jensen, D.; Seierstad, I. K.; Siggaard-Andersen, M.-L.; Steffensen, J. P.; Svensson, A.; Olsen, J.; Heinemeier, J. A synchronized dating of three Greenland ice cores throughout the Holocene. *J. Geophys. Res.* **2006**, *111*, D13102.

(20) Bigler, M. Hochauflösende Spurenstoffmessungen an polaren Eisbohrkernen: Glazio-chemische und klimatische Prozessstudien. PhD, Physikalisches Institut, Universität Bern, 2004.

(21) Rasmussen, S. O.; Andersen, K. K.; Svensson, A. M.; Steffensen, J. P.; Vinther, B. M.; Clausen, H. B.; Siggaard-Andersen, M.-L.; Johnsen, S. J.; Larsen, L. B.; Dahl-Jensen, D.; Bigler, M.; Röthlisberger, R.; Fischer, H.; Goto-Azuma, K.; Hansson, M. E.; Ruth, U. A new Greenland ice core chronology for the last glacial termination. *J. Geophys. Res.* **2006**, *111*, D06102.

(22) Fuhrer, K.; Neftel, A.; Anklin, M.; Maggi, V. Continous measurements of hydrogen peroxide, formaldehyde, calcium and ammonium concentrations along the new GRIP ice core from Summit, Central Greenland. *Atmos. Environ.* **1993**, *27A*, 1873–1880.

(23) Ruth, U.; Wagenbach, D.; Steffensen, J. P.; Bigler, M. Continuous record of microparticle concentration and size distribution in the central Greenland NGRIP ice core during the last glacial period. *J. Geophys. Res.* **2003**, *108*, 4098.

(24) Legrand, M.; Mayewski, P. Glaciochemistry of polar ice cores: A review. *Rev. Geophys.* **1997**, *35*, 219–243.

(25) Rasmussen, S. O.; Andersen, K. K.; Johnsen, S. J.; Bigler, M.; McCormack, T. Deconvolution-based resolution enhancement of chemical ice core records obtained by continuous flow analysis. *J. Geophys. Res.* **2005**, *110*, D17304.

(26) Svensson, A.; Bigler, M.; Kettner, E.; Dahl-Jensen, D.; Johnsen, S.; Kipfstuhl, S.; Nielsen, M.; Steffensen, J. P. Annual layering in the NGRIP ice core during the Eemian. *Clim. Past* submitted.

Appendix B

Svensson et al. (2011):
Annual Layers in Basal NGRIP Ice

The student's contribution to the paper:
This publication evaluates the implications of data obtained during the first CFA-measurement campaign. Next to demonstrating the mere functionality of the newly designed system, this campaign aimed at clarifying whether annual layers are present at greater depths and, if so, at the verification or falsification of values of their thicknesses previously calculated. My contribution consisted of the measurements preparation as well as subsequent participation and on-the-fly adjustments to the system.
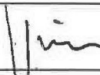
16/10-2013	Maibritt Nielsen	
18/10-13	ANDERS SVENSSON	
10.10.2013	BIGLER MATTHIAS	
6.11.2013	SEPP KIPFSTUHL	
20 nov 2013	DORTHE DAHL-JENSEN	
21 nov 2013	JØRGEN PEDER STEFFENSEN	

Climate of the Past
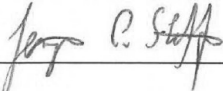
Annual layering in the NGRIP ice core during the Eemian

A. Svensson[1], **M. Bigler**[2], **E. Kettner**[1], **D. Dahl-Jensen**[1], **S. Johnsen**[1], **S. Kipfstuhl**[3], **M. Nielsen**[1], and **J. P. Steffensen**[1]

[1]Centre for Ice and Climate, Niels Bohr Institute, University of Copenhagen, Juliane Maries Vej 30,
2100 Copenhagen Ø, Denmark
[2]Climate and Environmental Physics, Physics Institute, and Oeschger Centre for Climate Change Research,
University of Bern, Sidlerstrasse 5, 3012 Bern, Switzerland
[3]Alfred Wegener Institute, Glaciology, Columbusstrasse, 27568 Bremerhaven, Germany

Abstract. The Greenland NGRIP ice core continuously covers the period from present day back to 123 ka before present, which includes several thousand years of ice from the previous interglacial period, MIS 5e or the Eemian. In the glacial part of the core, annual layers can be identified from impurity records and visual stratigraphy, and stratigraphic layer counting has been performed back to 60 ka. In the deepest part of the core, however, the ice is close to the pressure melting point, the visual stratigraphy is dominated by crystal boundaries, and annual layering is not visible to the naked eye. In this study, we apply a newly developed setup for high-resolution ice core impurity analysis to produce continuous records of dust, sodium and ammonium concentrations as well as conductivity of melt water. We analyzed three 2.2 m sections of ice from the Eemian and the glacial inception. In all of the analyzed ice, annual layers can clearly be recognized, most prominently in the dust and conductivity profiles. Part of the samples is, however, contaminated in dust, most likely from drill liquid. It is interesting that the annual layering is preserved despite a very active crystal growth and grain boundary migration in the deep and warm NGRIP ice. Based on annual layer counting of the new records, we determine a mean annual layer thickness close to 11 mm for all three sections, which, to first order, confirms the modeled NGRIP time scale (ss09sea). The counting does, however, suggest a longer duration of the climatically warmest part of the NGRIP record (MIS5e) of up to 1 ka as compared to the model estimate. Our results suggest that stratigraphic layer counting is possible basically throughout the entire NGRIP ice core, provided sufficiently highly-resolved profiles become available.

1 Introduction

The previous interglacial period, Marine Isotope Substage 5e (MIS5e) or the Eemian period in the European Pleistocene stratigraphy, approximately covers the time interval 130–115 kyr BP (Shackleton et al., 2003; Cheng et al., 2009; Brauer et al., 2007), although the first sign of Termination II may have appeared as early as 141 ka BP (Drysdale et al., 2009). The Eemian is known to have had warmer climate than present day climate (Turney and Jones, 2010), and the Eemian sea level may have been as much as 6–8 m above present day sea level (Kopp et al., 2009). The Eemian climate may in some regards resemble a future climate, if global warming continues as predicted by IPCC, and a full understanding of the climate conditions during this "natural" warm interglacial period is, therefore, of great interest. Overall, the climate in MIS5e is thought to have been rather stable although some smaller fluctuations may have appeared (Couchoud et al., 2009).

The 3085 m long NGRIP ice core from Central Greenland continuously covers the past 123 kyr, and it thus contains several thousand years of ice deposited during the Eemian period (Dahl-Jensen et al., 2002; North Greenland Ice Core Project members, 2004). The NGRIP climate record is continuous all the way to bedrock (Landais et al., 2006), i.e. there are no large scale disturbances of the type observed in the deepest parts of the GRIP and GISP2 cores (Suwa et al.,

Correspondence to: A. Svensson
(as@gfy.ku.dk)
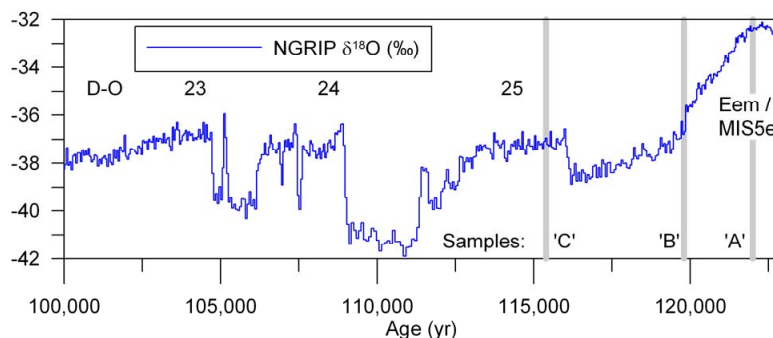
Fig. 1. The NGRIP δ^{18}O profile with indication of Dansgaard-Oeschger events (D-O) and the sampled ice core sections. The three 2.2 m sample sections are taken at the depths indicated by the gray vertical lines. The samples are referred to as "A", "B", and "C" as indicated. See Table 1 for further sample details.

2006). In the deepest part of the NGRIP core, the visual stratigraphy record is, however, dominated by ice crystal boundaries (Svensson et al., 2005) and annual banding is generally not visible to the naked eye. There is basal melting at the NGRIP site and the deepest part of the core is close to the pressure melting point (Dahl-Jensen et al., 2003). The annual layering may, therefore, be disturbed for example by micro folds or by rapid crystal growth in the warm environment (Faria et al., 2010).

High resolution records of impurities and visual stratigraphy have allowed for construction of a 60 ka chronology for the NGRIP ice core by annual layer counting (Svensson et al., 2008; Andersen et al., 2006). Pronounced annual banding in the visual stratigraphy profile beyond 60 ka suggests that the time scale can be further extended (Svensson et al., 2005), but at this depth annual layers are thin and difficult to identify based on available records. The NGRIP modeled time scale predicts annual layers are on the order of 1 cm thickness at around 115 ka, and the core may therefore provide an outstanding opportunity to establish an absolute time scale for the entire last glacial cycle if the annual layering is preserved in the oldest ice.

Recently, a new high-resolution continuous flow analysis (CFA) system for analysis of water soluble constituents and insoluble dust in ice cores has been developed at the University of Copenhagen (Bigler et al., 2011). The system determines the content of soluble sodium (mainly deriving from sea salt), soluble ammonium (related to biological processes and biomass burning events), insoluble dust particles (mostly transported from Asian deserts to Greenland), and the electrolytic melt water conductivity (which is a bulk signal for all ionic constituents). Measurements of early Holocene NGRIP ice on the new system show results compatible with existing NGRIP and GRIP CFA profiles (Bigler et al., 2011). The depth resolution of the new setup is, however, superior compared to existing systems and allows resolving annual lay-

ers of down to 1 cm thickness. With the new high-resolution CFA system, it may therefore be possible to identify annual layers throughout the NGRIP ice core if they are still present.

In this study, we apply the newly developed high-resolution CFA system to measure the impurity content of three 2.2 m NGRIP ice core sections from the Eemian and the glacial interception. We investigate if annual layers are detectable in this deep ice and we make comparisons to well-known impurity levels of the Holocene. Furthermore, we discuss ice core impurity diffusion and implications for the NGRIP time scale.

2 Samples and methods

In the glacial part of the NGRIP ice core, a number of records have been obtained, including the water isotope δ^{18}O, electrical conductivity measurement (ECM) on the ice surface, continuous flow analysis (CFA) of several chemical components, electrolytic conductivity and dust, as well as a visual stratigraphy (VS) profile. However, in the deepest 85 m of the core (3000–3085 m depth) that contains the Eemian ice, only measurements of δ^{18}O, ECM, and visual stratigraphy have been performed continuously.

The samples for the present study were selected based on the δ^{18}O climate proxy curve and from visual inspection of the core to obtain long unbroken pieces. The deepest ice was close to the pressure melting point in the bore hole, which made drilling difficult and the ice brittle when brought to surface. Therefore, many core breaks have occurred during drilling and subsequent core handling. The selected samples are some of the most well-preserved sections and they are of better quality than the average deep NGRIP ice. Three 2.2 m sections of NGRIP ice were selected around 2996, 3040, and 3070 m depth: respectively, one section from Greenland Interstadial 25 (GI-25), one section from the termination of the

Eemian, and one section from the warmest part of the Eemian in NGRIP from just 15 m above bedrock (Table 1 and Fig. 1). The samples have been stored in the Copenhagen ice core storage facility at a temperature of $-25°C$ and were cut to dimensions of $34 \times 34 \times 550\,mm^3$. End surfaces and breaks in the samples were removed before analysis.

An example of the samples visual stratigraphy is shown in Fig. 2. The NGRIP visual stratigraphy is obtained continuously by a dark field photography method, such that dark areas represent transparent (clean) ice whereas white areas indicate obstacles in the ice such as air bubbles or impurities (Svensson et al., 2005). The visual stratigraphy of the sampled ice is dominated by ice crystal boundaries. The crystals are large, in the 1–10 cm range, in particular in the deepest sample. Occasionally, a faint horizontal layering is visible within the crystals, but except for the crystal boundaries, the ice is very clean (transparent) as it is common for interglacial ice with low impurity content.

The samples were analyzed using a new setup for high-resolution CFA analysis of ice cores (Bigler et al., 2011). The setup measures the mass concentration of water soluble ammonium (NH_4^+), sodium (Na^+), the electrolytic conductivity of melt water (hereafter "conductivity"), and the amount of insoluble dust particles (hereafter "dust"). The setup has demonstrated a depth resolution that enables us to resolve features of down to 1 cm thickness.

3   Results

Results from the deepest sample "A" are shown in Fig. 3 and the complete measurement series are shown in Figs. S1–S3 in the Supplement. Whereas ammonium, sodium and conductivity show rather constant concentration levels, the dust concentrations occasionally show unusually elevated levels 5–20 times above the background level. Those strongly elevated dust peaks are most likely caused by contamination with drill liquid that may have entered the ice core through cracks in the ice, maybe produced during the drilling process. The dust contamination peaks are often but not consistently associated with the visible grain boundaries, which may have facilitated the formation of cracks. The contaminated dust sections can be discriminated not only from the elevated concentration levels but also from the dust size distribution (not shown) that shows a different pattern from that of the regular ice core dust. All contaminated dust sections have been removed for further discussions (Fig. 3). Fortunately, the other measured parameters show no sign of contamination in the sections of elevated dust.

4   Profile smoothing over 110 ka

Figure 4 compares power density spectra of 2.0 m impurity records of early Holocene NGRIP ice (data from Bigler et al., 2011) with 2.0 m of ice from the Eemian sample "A" and the
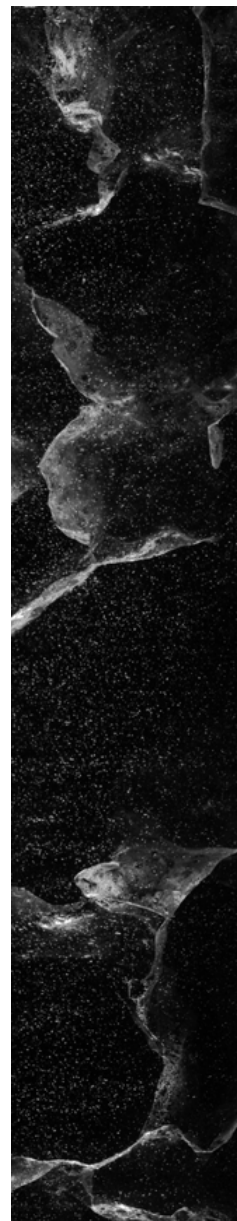
Fig. 2. Image of a section of sample "A" from 3070.10–3070.40 m depth (bag 5583). The slab is 3.4 cm thick and 6 cm wide. Ice crystals are rather large for Greenland: up to 10 cm across and grain boundaries are visible. This is due to the high temperature and very active crystal dynamics in the deepest part of the ice that is almost at the pressure melting point.

Table 1. List of samples. The sample length is after removal of breaks and end pieces.

Sample	Period	NGRIP Bag numbers	Depth interval (m)	Sample length (m)	Age ss09sea (kyr)	$\delta^{18}O$ (‰)
A	MIS5e/Eem	5581–5584	3069.00–3071.20	1.98	122.0	−32.4
B	MIS5e/GS-26	5528–5531	3039.85–3042.05	2.08	119.8	−36.2
C	GI-25	5447–5450	2995.30–2997.50	1.95	115.4	−37.0
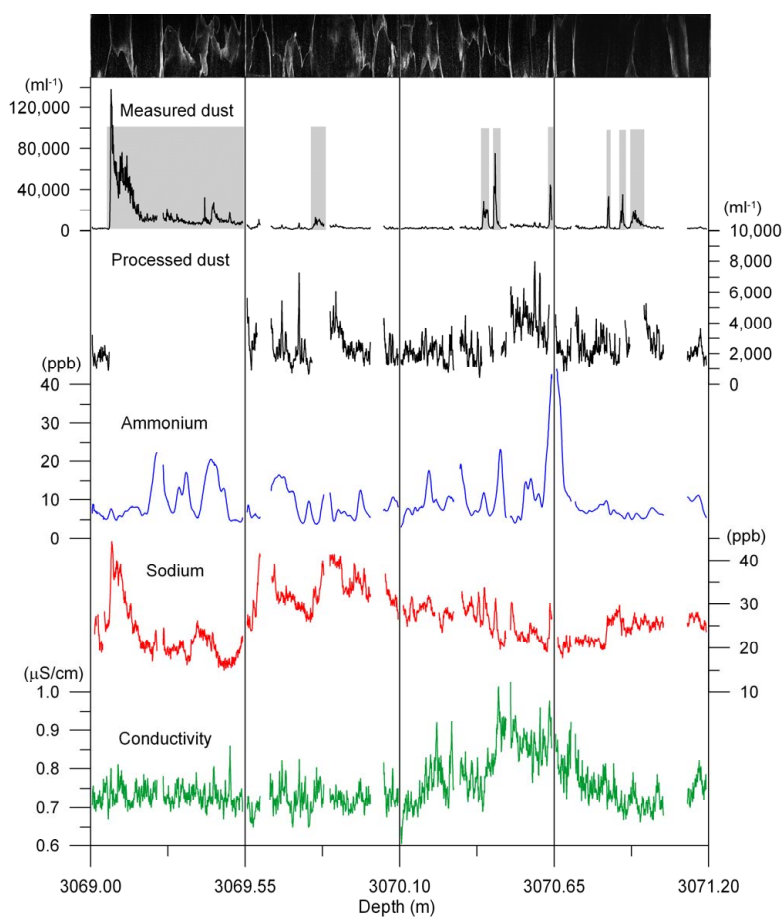
Fig. 3. Measured records of dust, ammonium, sodium, and conductivity from sample "A" shown together with the visual stratigraphy (top). The uppermost curve shows the measured dust profile including the contaminated sections that are indicated with gray bars. For the second dust curve, the contaminated sections are removed. Data gaps are caused by breaks in the core (that were removed), contamination issues (dust only), or analytical issues. Vertical lines indicate the 55 cm sections of the analyzed cores.
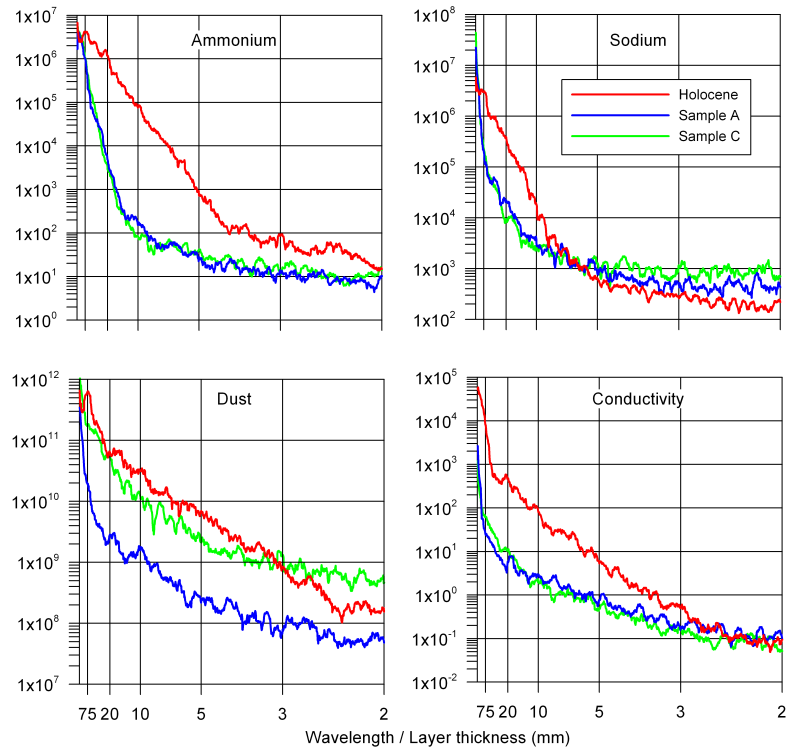
Fig. 4. Depth domain power density spectra comparing early Holocene, Eemian (sample "A"), and early glacial (sample "C") NGRIP records. The spectra are obtained by FFT of 2.0 m records in 1 mm depth resolution. The "wavelength/layer thickness" is calculated as 2.0 (m) times frequency. Holocene data are from Bigler et al. (2011). In the Holocene spectra a clear annual layer peak is visible at around 75 mm, whereas the Eemian and glacial spectra show no clear indication of an annual peak. Data gaps are linearly interpolated.

early glacial sample "C" of the present study. The spectra are composed of a "signal" at lower frequencies (left hand side of spectra) and a noise level where the spectra flatten out at higher frequencies (right hand side of spectra). The data sets are obtained by the same analytical technique and with the same depth resolution (sample melt speed), so from an analytical point of view the spectra are directly comparable. If we assume similar deposition patterns for impurities deposited during the Eemian and the early Holocene, the difference between the power spectra from the two periods reflects the effects of ice deformation and impurity diffusion over a 100 ka period. Obviously, all of the measured parameters are affected by both processes, but the parameters appear not to be influenced in the same way.

A pure vertical compression of the ice would result in a "stretching" of the power spectrum along the x-axis and thereby an amplification of the signal at all frequencies, whereas impurity diffusion in the ice will dampen higher

frequencies of the signal over time. The general change from Holocene to Eemian ice appears to be a dampening of signal at most frequencies, meaning that diffusion is the dominating process of the two, although ice layer thinning (compression) must be very important as well.

For dust, the power spectra of the Eemian and the early glacial have very similar shape, but the glacial sample has higher power at all frequencies due to the much stronger variability in dust concentration during the glacial period. As the influence of dust diffusion in the ice is likely to be low even over long periods, we would not expect the Eemian spectrum to be strongly influenced by diffusion as compared to the Holocene spectrum. The Eemian spectrum is, however, clearly influenced by some process that dampens the signal as compared to the Holocene. One mechanism that could explain this observation without involving dust diffusion would be rotation and deformation of ice crystals, which, to first order, would have an effect on the dust spectrum similar to that

of diffusion. Based on our data alone, we can, however, not distinguish between those different mechanisms.

As the conductivity signal is a composite signal that involves all of the ions in the ice, the interpretation of its development over time is likely to be complex. We do note, however, that the Eemain and the early glacial spectra are very similar, suggesting that time rather than climate is the important factor for the shape of the conductivity power spectrum.

Ammonium is the most affected parameter that has clearly undergone a significant diffusion over the 100 kyr period with a strong dampening of the signal. The effect is also evident from the record in depth space (Fig. 3), where the ammonium profile has been significantly smoothed as compared to a Holocene ammonium profile, which exhibits a prominent annual signal (Bigler et al., 2011). A similar effect has been observed for ammonium in old GRIP ice (Steffensen et al., 1997).

The Eemian sodium profile is also somewhat dampened as compared to its Holocene counterpart although apparently less than is the case for ammonium. A relatively low diffusivity of sodium and a strong binding of sodium in the ice lattice have also been observed for the Holocene section of the Antarctic Dome C ice core (Barnes et al., 2003).

5   Absolute concentration levels

The average concentration levels of the measured parameters are compared to early Holocene values from NGRIP obtained by the same analytical setup as applied in this study (Bigler et al., 2011) (Table 2).

Over the last glacial cycle, ammonium concentrations generally vary with climate, showing the highest concentrations during the MIS1 and MIS4 (Fuhrer et al., 1996; Mayewski et al., 1997). In this study, ammonium concentrations appear to be correlated with $\delta^{18}O$, but the level is consistently lower than the early Holocene value. For dust, the Eemian concentration level of this study (sample "A") is only slightly lower than that of the early Holocene, and the samples consistently show the well-known Greenland pattern of higher concentrations for colder climate (Ruth et al., 2003). The conductivity values of the present study are consistently lower than that of the early Holocene by about a factor of two. The Eemian and early glacial values vary consistently with climate ($\delta^{18}O$), showing the lower the values, the warmer the climate.

There is a whole range of possible reasons for the observed differences in the impurity concentration levels of the early Holocene, the Eemian, and the early glacial. Obviously, changes in source areas, transport routes, and deposition patterns are major players (Fischer et al., 2007). Another reason for differences may be related to elevation changes of the Greenland ice sheet from period to period, which may have been important (Vinther et al., 2009). Furthermore, slow chemical reactions in the ice over the 110 ka period or faster reactions in the deep warm ice may cause changes in the absolute levels. At this stage, however, we just note that, to first order, the Eemian levels are very comparable to those of the Early Holocene and that dust and ammonium appear to express a climatic dependence in concentrations.

6   Annual layering

In all of the analyzed ice, a clear stratigraphic signal is evident in both conductivity and dust records whenever they are available (Fig. 5 and Figs. S1–S3 in the Supplement). We associate the observed stratigraphy with annual layering.

The annual layers are counted following the scheme applied for the construction of the Greenland Ice Core Chronology 2005 (GICC05) (Rasmussen et al., 2006; Andersen et al., 2006): "certain" and "uncertain" annual layers are assigned along the profiles based on subjective evaluation for the likelihood of an annual layer. This quantitative error estimate has been applied systematically and successfully for the period 0–60 ka. In the present study, uncertain annual layers are counted as 0.5 ± 1.0 yr and introduce an uncertainty of about 14 % for the counting, which is somewhat higher than the 5 % generally found in the glacial NGRIP ice (Andersen et al., 2006). Note that because the layer counting is based on just one or two data series, the error estimate applied here is twice that of Andersen et al. (2006) where uncertain annual layers are counted as 0.5 ± 0.5 yr. The full data set and layer counting are shown in Fig. S1–S3 and the results are summarized in Table 3.

We determine annual layer thicknesses clustering around 11 mm, which is within the depth resolution of the analytical method for dust and conductivity (Bigler et al., 2011). Even for sodium, which is at the limit of its resolution to resolve those layers, the annual layering is occasionally observable. Unfortunately at this depth, the ammonium profile is too smoothed to reveal the seasonal pattern that is very pronounced in Holocene ice. Note that the low resolution of the ammonium profile is not due to limited resolution of the analytical technique.

Figure 6 shows power spectra of the impurity records in the time domain after applying the time scale resulting from the layer counting. In this domain, spectral peaks corresponding to the annual cycle are quite significant for all samples. In the Holocene, the annual spike is present for all four impurity records, whereas for the older samples there are no spikes for ammonium and sodium due to diffusion. In the Holocene, overtone peaks (at integer multiple frequencies) are seen for all components except sodium. Those are probably caused by (1) multiple annual peaks occurring for several components in high resolution in the Holocene and (2) the non-sinusoidal shape of the Holocene records in high depth resolution.

Table 2. Absolute concentration levels of the measured parameters compared to early Holocene values.

Sample	Age (kyr)	δ^{18}O (‰)	NH$_4$ (ppb)	Na (ppb)	Dust (ml^{-1})	Cond (μS cm^{-1})	Source reference
Holocene	10.0	−35.1	10.7	18.6	2716	1.19	Bigler et al. (2011)
A	122	−32.4	9.5	26.3	2516	0.75	This study
B	120	−36.2	6.3	34.9	5586	0.60	This study
C	116	−37.0	5.4	31.6	6015	0.51	This study

Table 3. Annual layer thicknesses (lambda) derived from the measured sections based on annual layer counting. The number of "certain" and "uncertain" annual layers results in total annual layers and error estimate. Lambdas of the modeled time scale ss09sea are shown for comparison.

Sample	Sample length (m)	Certain (yr)	Uncertain (yr)	Total (yr)	Lambda			
					mean	max	min	ss09sea
A	1.98	161	29	175.5 ± 29.0	11.3	13.5	9.7	14.7
B	2.08	183	20	193.0 ± 20.0	10.8	12.0	9.8	11.7
C	1.95	162	26	175.0 ± 26.0	11.1	13.1	9.7	11.1

In sections where annual layers are resolved in sodium, it is interesting to note the relative phasing among the measured parameters (Fig. 5): sodium spikes generally (but not consistently) fall between dust spikes, suggesting a seasonal pattern similar to that of the Holocene with sodium being a winter signal and dust arriving in spring (Rasmussen et al., 2006). Obviously, this conclusion is based on the assumption that the depth alignment of the different parameters is precise to the millimeter scale, which is probably pushing the precision a bit.

7 Implications for NGRIP time scale

The published time scale for the deepest part of the NGRIP ice core is the modeled ss09sea time scale that is based on the use of a fixed point at 110 ka and that takes into account the basal melt at NGRIP (Johnsen et al., 2001; Andersen et al., 2006). An alternative time scale for the early glacial period is based on comparison of Greenland and Antarctic gas records (Capron et al., 2010). Generally, the ss09sea chronology of the early glacial is confirmed by several independent records, such as U/Th dated stalagmite records from the alps (Drysdale et al., 2007; Boch et al., 2011) and China (Wang et al., 2008; Xia et al., 2007), but time scale uncertainties do allow for some flexibility in the exact timing of abrupt climate transitions.

Based on our data alone, we cannot evaluate the accuracy of the various time scales, but we can constrain the NGRIP annual layer thicknesses within the investigated period. Our derived annual layer thicknesses basically confirm the modeled NGRIP time scale (ss09sea) for the deepest part of the ice core, although it suggests that the duration of the MIS5e/Eemian section of the ice core may be somewhat longer than estimated by the model (Fig. 7 and Table 3). Assuming a rather constant annual layer thickness of the Eemian NGRIP ice as suggested by samples "A" and "B" implies a duration of the Eemian NGRIP section of 4 ka or up to 1 ka longer than according to the model.

A likely reason for a slightly biased annual layer thickness estimation in the ss09sea model during the Eemian would be an inaccurate estimate of basal melt rates at NGRIP that are quite poorly constrained. Another explanation for the discrepancy between our Eemian annual layer estimate and that of the model would be a partial breakdown of the δ^{18}O-accumulation relation in the Eemian period caused, for example, by significant elevation changes of the ice cap or by changes in the position of the ice divide over time. Such a breakdown is known to have occurred in MIS2 where ss09sea overestimates the annual layer thickness by some 20 % for a period of several thousands of years (Svensson et al., 2006).

8 Crystal boundaries and impurities

It has been suggested that very significant diffusion of soluble ice core impurities may appear under warm conditions similar to those found in the NGRIP Eemian ice (Rempel et al., 2001; Dash et al., 2006). The so-called anomalous diffusion appears in a water-vein system of the ice crystal grain boundaries. The possible existence of liquid veins in the ice sheets has important implications for microbiological and molecular analyses of ice cores (Miteva et al., 2009; Price, 2000). Recently, the occurrence of
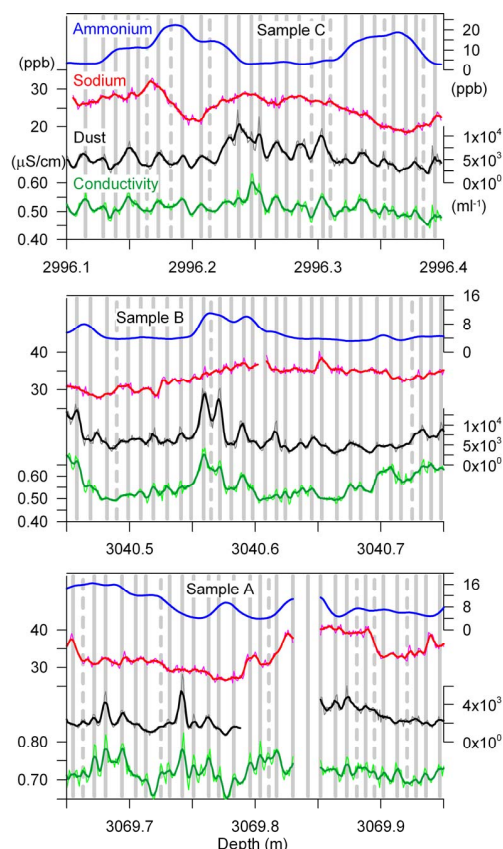
Fig. 5. Examples of annual layer counting in samples "A", "B", and "C", respectively. Annual layers are resolved in dust (black) and conductivity (green) and occasionally in sodium (red), whereas the ammonium signal (blue) is affected by post-depositional processes. "Certain" and "uncertain" annual layers are indicated with solid and dashed grey vertical lines, respectively. The measurements are shown in 1 mm resolution (thin light curves) as well as in 5 mm smoothed resolution (thick dark curves).

long-term post-depositional processes involving a rearrangement of impurities via migration in the vein network has been observed in the deepest part of the Antarctic Dome C record (Traversi et al., 2009).

Our results demonstrate that whereas there has been a significant displacement of ammonium ions in the deepest NGRIP ice, dust particles are not significantly affected by such processes. Indeed, the annual layering is preserved in dust across ice crystals that are tens of centimeters across (Fig. 2), and there are no elevated impurity concentrations within the ice crystal boundaries (except for dust

contamination presumably caused by drilling fluid). Not even the strongly diffused ammonium appears to have concentrated in grain boundaries, which challenges the ideas of an active liquid vein system in the deep central Greenland ice. As the power signal of the Eemian dust has a somewhat different shape as compared to Holocene (Fig. 4), it is likely that large impurities such as dust are displaced during deformation and rotation of ice crystals. The ice crystal boundaries migration that is active within the entire ice sheet and that the Eemian ice has experienced for 120 ka, has, however, not resulted in any significant displacement of the solid impurities in the Greenland ice.

Whereas the preservation of annual layers could be anticipated for the large and non-diffusive dust particles, it is not so obvious why a seasonal cycle is also observed in the conductivity record and even occasionally in the sodium record. One can speculate whether this signal in the Eemian records is derived from the original annual signal that was deposited with the snow or if diffusion and rearrangement of impurities over long time scales may have favored soluble impurities to cluster around solid particles in the ice. Indeed, the lack of a strong annual peak in the early Holocene conductivity power spectra (Figs. 4 and 6) suggests that the annual signal observed for the Eemian conductivity record may be a result of long-term post-depositional processes. On the other hand, if sodium shows a seasonal winter peak between the dust peaks, this suggests that we still see the original sodium signal in the Eemian ice. This finding is consistent with that of Ohno et al. (2005), who observed in ice from the Antarctic Dome F core that certain soluble impurities can form salts that stay fixed in the ice lattice.

9 Conclusions

Three sections of ice from the Eemian and the glacial interception in the deepest part of the NGRIP ice core have been analyzed by a new high-resolution CFA system for concentrations of sodium, ammonium, dust, and melt water conductivity. The absolute levels of all measured components are very comparable to those of early Holocene NGRIP ice.

Surprisingly, it is possible to identify annual layers in the records of dust and conductivity in all of the analyzed ice except for sections where dust is contaminated by drill liquid. It is the first time annual layers have been identified in ice from the last interglacial period in Greenland, and our results suggest that annual layering is likely to be preserved throughout the NGRIP ice core despite very active crystal dynamics and temperatures close to the melting point near bedrock. Continuous analysis and stratigraphic dating of the very deepest NGRIP ice may, however, not be feasible due to a rather poor ice core quality and a pronounced dust contamination. The samples selected for this study were high-quality ice core pieces but still the contamination issue is significant.
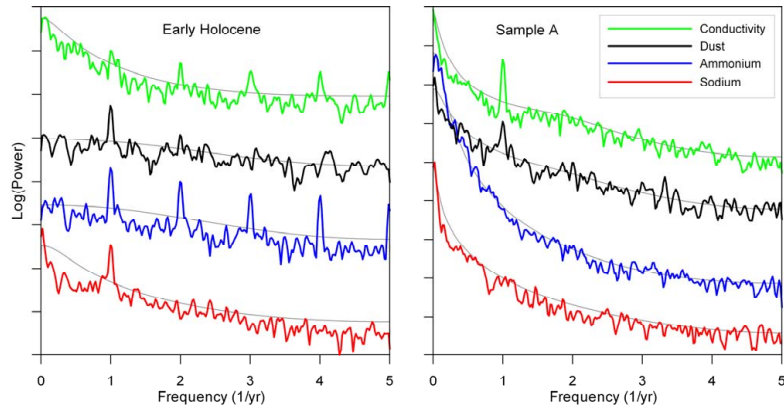
Fig. 6. Time domain power density spectra comparing early Holocene and Eemain (sample "A") NGRIP impurity records. The records were placed on a floating time scale based on annual layer counting. The early Holocene sample covers a 11.0 m ice core section (1378.30–1389.30 m depth about 10 b2k) in which 148 certain annual layers were identified (from Bigler et al., 2011). Sample "A" covers a 2.2 m core section in which 190 annual layers have been identified (Table 3). Both 'certain' and 'uncertain' annual layers are included. Grey lines indicate 95 % confidence limits from simulation of noise spectra. The spectra have been shifted vertically for clarity, but all spectra have comparable units. Larger missing sample sections were skipped, whereas shorter data gaps have been linearly interpolated.
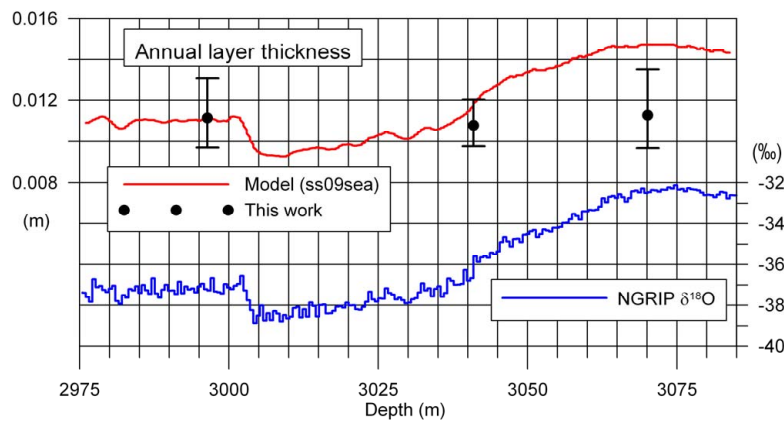
Fig. 7. NGRIP δ^{18}O and annual layer thicknesses of ss0sea compared to those of the present study.

To first order, our analyses confirm the modeled NGRIP time scale (ss09sea) in the deepest part of the NGRIP ice core. The determination of mean annual layer thicknesses around 11 mm in all three samples does, however, suggest that the MIS5e section of the core may be longer than predicted by the model by up to 1 ka.

The preservation of annual layers in the deep and warm NGRIP ice somehow challenges the ideas of an active liquid vein system in warm glacier ice that is put forward in several mainly theoretical papers. In our data, we see no sign

of elevated impurity concentrations in the grain boundaries, not even for ammonium that has clearly undergone a very significant diffusion over the glacial period.

The determination of annual layers of down to 1 cm thickness in deep Greenland ice opens the possibility for stratigraphic dating of a wide range of ice cores from both Greenland and Antarctica. In Greenland, annual layer thicknesses in most of the early glacial section of the NGRIP ice core exceed 1 cm. In Antarctica, the EDML ice core has centimeter thick annual layers throughout most of the glacial period,

whereas both Dome F and Dome C are believed to have annual layers exceeding 1 cm during MIS 5e. Potentially, stratigraphic ice core dating of the entire last glacial cycle should be possible in both Hemispheres.

Supplementary material related to this article is available online at: http://www.clim-past.net/7/1427/2011/ cp-7-1427-2011-supplement.pdf.

References

Andersen, K. K., Svensson, A., Rasmussen, S. O., Steffensen, J. P., Johnsen, S. J., Bigler, M., Röthlisberger, R., Ruth, U., Siggaard-Andersen, M.-L., Dahl-Jensen, D., Vinther, B. M., and Clausen, H. B.: The Greenland Ice Core Chronology 2005, 15–42 ka. Part 1: constructing the time scale, Quaternary Sci. Rev., 25, 3246–3257, 2006.

Barnes, P. R. F., Wolff, E. W., Mader, H. M., Udisti, R., Castellano, E., and Röthlisberger, R.: Evolution of chemical peak shapes in the Dome C, Antarctica, ice core, J. Geophys. Res., 108, 4126, doi:4110.1029/2002JD002538, 2003.

Bigler, M., Svensson, A., Kettner, E., Vallelonga, P., Nielsen, M. E., and Steffensen, J. P.: Optimization of High-Resolution Continuous Flow Analysis for Transient Climate Signals in Ice Cores, Environ. Sci. Technol., 45, 4483–4489, doi:10.1021/es200118j, 2011.

Boch, R., Cheng, H., Spötl, C., Edwards, R. L., Wang, X., and Häuselmann, Ph.: NALPS: a precisely dated European climate record 120-60 ka, Clim. Past Discuss., 7, 1049–1072, doi:10.5194/cpd-7-1049-2011, 2011.

Brauer, A., Allen, J. R. M., Mingram, J., Dulski, P., Wulf, S., and Huntley, B.: Evidence for last interglacial chronology and environmental change from Southern Europe, Proc. Natl. Acad. Sci., 104, 450–455, 2007.

Capron, E., Landais, A., Lemieux-Dudon, B., Schilt, A., Masson-Delmotte, V., Buiron, D., Chappellaz, J., Dahl-Jensen, D., Johnsen, S., Leuenberger, M., Loulergue, L., and Oerter, H.: Synchronising EDML and NorthGRIP ice cores using delta O-18 of atmospheric oxygen (delta O-18(atm)) and CH4 measurements over MIS5 (80–123 kyr), Quaternary Sci. Rev., 29, 222–234, doi:10.1016/j.quascirev.2009.07.014, 2010.

Cheng, H., Edwards, R. L., Broecker, W. S., Denton, G. H., Kong, X. G., Wang, Y. J., Zhang, R., and Wang, X. F.: Ice Age Termi-

nations, Science, 326, 248–252, doi:10.1126/science.1177840, 2009.

Couchoud, I., Genty, D., Hoffmann, D., Drysdale, R., and Blamart, D.: Millennial-scale climate variability during the Last Interglacial recorded in a speleothem from south-western France, Quaternary Sci. Rev., 28, 3263–3274, 2009.

Dahl-Jensen, D., Gundestrup, N., Miller, H., Watanabe, O., Johnsen, S. J., Steffensen, J. P., Clausen, H. B., Svensson, A., and Larsen, L. B.: The NorthGRIP deep drilling program, Ann. Glaciol., 35, 1–4, 2002.

Dahl-Jensen, D., Gundestrup, N., Gorgineni, S. P., and Miller, H.: Basal melt at NorthGRIP modeled from borehole, ice-core and radio-echo sounder observations, Ann. Glaciol., 37, 207–212, 2003.

Dash, J. G., Rempel, A. W., and Wettlaufer, J. S.: The physics of premelted ice and its geophysical consequences, Rev. Mod. Phys., 78, 695–741, doi:10.1103/RevModPhys.78.695, 2006.

Drysdale, R. N., Zanchetta, G., Hellstrom, J. C., Fallick, A. E., McDonald, J., and Cartwright, I.: Stalagmite evidence for the precise timing of North Atlantic cold events during the early last glacial, Geology, 35, 77–80, 2007.

Drysdale, R. N., Hellstrom, J. C., Zanchetta, G., Fallick, A. E., Goni, M. F. S., Couchoud, I., McDonald, J., Maas, R., Lohmann, G., and Isola, I.: Evidence for Obliquity Forcing of Glacial Termination II, Science, 325, 1527–1531, doi:10.1126/science.1170371, 2009.

Faria, S. H., Freitag, J., and Kipfstuhl, S.: Polar ice structure and the integrity of ice-core paleoclimate records, Quaternary Sci. Rev., 29, 338–351, doi:10.1016/j.quascirev.2009.10.016, 2010.

Fischer, H., Siggaard-Andersen, M.-L., Ruth, U., Röthlisberger, R., and Wolff, E.: Glacial/interglacial changes in mineral dust and sea-salt records in polar ice cores: Sources, transport, and deposition, Rev. Geophys., 45, RG1002, doi:1010.1029/2005RG000192, 2007.

Fuhrer, K., Neftel, A., Anklin, M., Staffelbach, T., and Legrand, M.: High-resolution ammonium ice core record covering a complete glacial-interglacial cycle, J. Geophys. Res.-Atmos., 101, 4147–4164, 1996.

Johnsen, S. J., Dahl-Jensen, D., Gundestrup, N., Steffensen, J. P., Clausen, H. B., Miller, H., Masson-Delmotte, V., Sveinbjörnsdottir, A. E., and White, J.: Oxygen isotope and palaeotemperature records from six Greenland ice-core stations: Camp Century, Dye-3, GRIP, GISP2, Renland and NorthGRIP, J. Quaternary Sci., 16, 299–307, 2001.

Kopp, R. E., Simons, F. J., Mitrovica, J. X., Maloof, A. C., and Oppenheimer, M.: Probabilistic assessment of sea level during the last interglacial stage, Nature, 462, 863-U851, doi:10.1038/nature08686, 2009.

Landais, A., Masson-Delmotte, V., Jouzel, J., Raynaud, D., Johnsen, S., Huber, C., Leuenberger, M., Schwander, J., and Minster, B.: The glacial inception as recorded in the NorthGRIP Greenland ice core: Timing, structure and associated abrupt temperature changes, Clim. Dynam., 26, 273–284, 2006.

Mayewski, P. A., Meeker, L. D., Twickler, M. S., Whitlow, S., Yang, Q., Lyons, W. B., and Prentice, M.: Major features and forcing of high-latitude Northern Hemisphere atmospheric circulation using a 110,000-year-long glaciochemical series, J. Geophys. Res., 102, 26345–26366, 1997.

Miteva, V., Teacher, C., Sowers, T., and Brenchley, J.: Comparison

of the microbial diversity at different depths of the GISP2 Greenland ice core in relationship to deposition climates, Environ. Microbiol., 11, 640–656, doi:10.1111/j.1462-2920.2008.01835.x, 2009.

North Greenland Ice Core Project members: High-resolution record of Northern Hemisphere climate extending into the last interglacial period, Nature, 431, 147–151, 2004.

Ohno, H., Igarashi, M., and Hondoh, T.: Salt inclusions in polar ice core: Location and chemical form of water-soluble impurities, Earth Planet. Sci. Lett., 232, 171–178, 2005.

Price, P. B.: A habitat for psychrophiles in deep Antarctic ice, Proc. Natl. Acad. Sci. USA, 97, 1247–1251, 2000.

Rasmussen, S. O., Andersen, K. K., Svensson, A. M., Steffensen, J. P., Vinther, B. M., Clausen, H. B., Siggaard-Andersen, M.-L., Johnsen, S. J., Larsen, L. B., Dahl-Jensen, D., Bigler, M., Röthlisberger, R., Fischer, H., Goto-Azuma, K., Hansson, M. E., and Ruth, U.: A new Greenland ice core chronology for the last glacial termination, J. Geophys. Res., 111, D06102, doi:06110.01029/02005JD006079, 2006.

Rempel, A. W., Waddington, E. D., Wettlaufer, J. S., and Worster, M. G.: Possible displacement of the climate signal in ancient ice by premelting and anomalous diffusion, Nature, 411, 568–571, 2001.

Ruth, U., Wagenbach, D., Steffensen, J. P., and Bigler, M.: Continuous record of microparticle concentration and size distribution in the central Greenland NGRIP ice core during the last glacial period, J. Geophys. Res., 108, 4098, doi:4010.1029/2002JD002376, 2003.

Shackleton, N. J., Sánchez-Goñi, M. F., Pailler, D., and Lancelot, Y.: Marine Isotope Substage 5e and the Eemian Interglacial, Global Planet. Change, 36, 151–155, 2003.

Steffensen, J. P., Clausen, H. B., Hammer, C. U., Legrand, M., and De Angelis, M.: The chemical composition of cold events within the Eemian section of the Greenland Ice Core Project ice core from Summit, Greenland., J. Geophys. Res., 102, 26747–26754, 1997.

Suwa, M., von Fischer, J. C., Bender, M. L., Landais, A., and Brook, E. J.: Chronology reconstruction for the disturbed bottom section of the GISP2 and the GRIP ice cores: Implications for Termination II in Greenland, J. Geophys. Res., 111, D02101, doi:02110.01029/02005JD006032, 2006.

Svensson, A., Nielsen, S. W., Kipfstuhl, S., Johnsen, S. J., Steffensen, J. P., Bigler, M., Ruth, U., and Röthlisberger, R.: Visual stratigraphy of the North Greenland Ice Core Project (North-GRIP) ice core during the last glacial period, J. Geophys. Res., 110, D02108, doi:02110.01029/02004JD005134, 2005.

Svensson, A., Andersen, K. K., Bigler, M., Clausen, H. B., Dahl-Jensen, D., Davies, S. M., Johnsen, S. J., Muscheler, R., Rasmussen, S. O., Röthlisberger, R., Steffensen, J. P., and Vinther, B. M.: The Greenland Ice Core Chronology 2005, 15-42 ka. Part 2: comparison to other records, Quaternary Sci. Rev., 25, 3258–3267, 2006.

Svensson, A., Andersen, K. K., Bigler, M., Clausen, H. B., Dahl-Jensen, D., Davies, S. M., Johnsen, S. J., Muscheler, R., Parrenin, F., Rasmussen, S. O., Röthlisberger, R., Seierstad, I., Steffensen, J. P., and Vinther, B. M.: A 60 000 year Greenland stratigraphic ice core chronology, Clim. Past, 4, 47–57, doi:10.5194/cp-4-47-2008, 2008.

Traversi, R., Becagli, S., Castellano, E., Marino, F., Rugi, F., Severi, M., de Angelis, M., Fischer, H., Hansson, M., Stauffer, B., Steffensen, J. P., Bigler, M., and Udisti, R.: Sulfate Spikes in the Deep Layers of EPICA-Dome C Ice Core: Evidence of Glaciological Artifacts, Environ. Sci. Technol., 43, 8737–8743, doi:10.1021/es901426y, 2009.

Turney, C. S. M. and Jones, R. T.: Does the Agulhas Current amplify global temperatures during super-interglacials?, J. Quaternary Sci., 25, 839–843, doi:10.1002/jqs.1423, 2010.

Vinther, B. M., Buchardt, S. L., Clausen, H. B., Dahl-Jensen, D., Johnsen, S. J., Fisher, D. A., Koerner, R. M., Raynaud, D., Lipenkov, V., Andersen, K. K., Blunier, T., Rasmussen, S. O., Steffensen, J. P., and Svensson, A. M.: Holocene thinning of the Greenland ice sheet, Nature, 461, 385–388, doi:10.1038/nature08355, 2009.

Wang, Y. J., Cheng, H., Edwards, R. L., Kong, X. G., Shao, X. H., Chen, S. T., Wu, J. Y., Jiang, X. Y., Wang, X. F., and An, Z. S.: Millennial- and orbital-scale changes in the East Asian monsoon over the past 224,000 years, Nature, 451, 1090–1093, doi:10.1038/nature06692, 2008.

Xia, Z., Kong, X., Jiang, X., and Cheng, H.: Precise dating of East-Asian-Monsoon D/O events during 95–56 ka BP: Based on stalagmite data from Shanbao Cave at Shennongjia, China, Sci. China Ser. D, 50, 228–235, 2007.

Appendix C

Gkinis et al. (2011):
Continuous Isotope Analysis in Ice Cores

The student's contribution to the paper:
My contribution to this publication was limited to the start-up phase of this project and to the peripheral work of this publication's focus. It consisted of getting the Copenhagen Continuous Flow Analysis (CFA) system running for testing the spectrometer set-up and integrating the Picarro-line into the Copenhagen CFA system. An introduction to the hardware used in CFA such as tubing, fittings and pumps was given, advantageous vendors were pointed out and a start-up kit of different components was provided. The very first continuous measurement on a rod of ice was done on a core I melted. When the system was shipped to the field for measurements on the NEEM core my contribution stopped.

Date	Name	Signature
16/10/2013	Simon Schüpbach	
20.10.2013	BIGLER Matthias	
23/10/2013	Vasileios Gkinis	
31/10/2013	Thomas Blunier	
13 Nov 2013	Trevor James Popp	
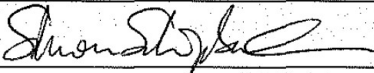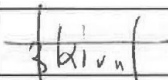
**Atmospheric
Measurement
Techniques**

Water isotopic ratios from a continuously melted ice core sample

V. Gkinis[1], T. J. Popp[1], T. Blunier[1], M. Bigler[2], S. Schüpbach[2], E. Kettner[1], and S. J. Johnsen[1,3]

[1]Centre for Ice and Climate, Niels Bohr Institute, University of Copenhagen, Juliane Maries Vej 30,
2100 Copenhagen, Denmark
[2]Physics Institute, Climate and Environmental Physics and Oeschger Centre for Climate Change Research University of Bern,
Sidlerstrasse 5, 3012 Bern, Switzerland
[3]Science Institute, University of Iceland, Dunhaga 3, 107, Iceland

Abstract. A new technique for on-line high resolution isotopic analysis of liquid water, tailored for ice core studies is presented. We built an interface between a Wavelength Scanned Cavity Ring Down Spectrometer (WS-CRDS) purchased from Picarro Inc. and a Continuous Flow Analysis (CFA) system. The system offers the possibility to perform simultaneuous water isotopic analysis of δ^{18}O and δD on a continuous stream of liquid water as generated from a continuously melted ice rod. Injection of sub µl amounts of liquid water is achieved by pumping sample through a fused silica capillary and instantaneously vaporizing it with 100 % efficiency in a home made oven at a temperature of 170 °C. A calibration procedure allows for proper reporting of the data on the VSMOW–SLAP scale. We apply the necessary corrections based on the assessed performance of the system regarding instrumental drifts and dependance on the water concentration in the optical cavity. The melt rates are monitored in order to assign a depth scale to the measured isotopic profiles. Application of spectral methods yields the combined uncertainty of the system at below 0.1 ‰ and 0.5 ‰ for δ^{18}O and δD, respectively. This performance is comparable to that achieved with mass spectrometry. Dispersion of the sample in the transfer lines limits the temporal resolution of the technique. In this work we investigate and assess these dispersion effects. By using an optimal filtering method we show how the measured profiles can be corrected for the smoothing effects resulting from the sample dispersion. Considering the significant advantages the technique offers, i.e. simultaneuous measurement of δ^{18}O and δD, potentially in combination with chemical components that are traditionally measured on CFA systems, notable reduction on analysis time and power consumption, we consider it as an alternative to traditional isotope ratio mass spectrometry with the possibility to be deployed for field ice core studies. We present data acquired in the field during the 2010 season as part of the NEEM deep ice core drilling project in North Greenland.

1 Introduction

Polar ice core records provide some of the most detailed views of past environmental changes up to 800 000 yr before present, in large part via proxy data such as the water isotopic composition and embedded chemical impurities. One of the most important features of ice cores as climate archives, is their continuity and the potential for high temporal resolution. Greenland ice cores are particularly well suited for high resolution paleoclimatic studies, because relatively high snow accumulation rates allow seasonal changes in proxy data to be identified more than 50 000 yr in the past (Johnsen et al., 1992; NGRIP members, 2004).

The isotopic signature of polar precipitation, commonly expressed through the δ notation[1] (Epstein, 1953; Mook,

---

[1]Isotopic abundances are typically reported as deviations of a sample's isotopic ratio relative to that of a reference water (e.g. VSMOW) expressed in per mil (‰) through the δ notation: $\delta^i = \left(\dfrac{^i R_{\text{sample}}}{^i R_{\text{SMOW}}} - 1 \right) \times 1000$ where $^2R = \dfrac{^2\text{H}}{^1\text{H}}$ and $^{18}R = \dfrac{^{18}\text{O}}{^{16}\text{O}}$

2000) is related to the temperature gradient between the evaporation and condensation site (Dansgaard, 1964) and has so far been used as a proxy for the temperature of the cloud at the time of condensation (Jouzel and Merlivat, 1984; Jouzel et al., 1997; Johnsen et al., 2001). One step further, the combined signal of δD and $\delta^{18}O$ commonly referred to as the deuterium excess (hereafter D_{xs}), constitutes a useful paleothermometer tool. Via its high correlation with the temperature of the evaporation source (Johnsen et al., 1989), it has been used to resolve issues related to changes in the location of the evaporation site (Cuffey and Vimeux, 2001; Kavanaugh and Cuffey, 2002). A relatively recent advance in the use of water isotope ratios as a direct proxy of firn temperatures, has been introduced by Johnsen et al. (2000). Assessment of the diffusivity of the water isotopologues in the porous medium of the firn column can yield a temperature history, provided a dating model is available.

The measurement of water stable isotopic composition is typically performed off-line via discrete sampling with traditional isotope ratio mass spectrometry (hereafter IRMS). While high precision and accuracy can routinely be achieved with IRMS systems, water isotope analysis remains an elaborate process, which is demanding in terms of sample preparation, power consumption, sample size, consumables, isotope standards and carrier gases. The analysis of a deep ice core at its full length in high resolution (typically 2.5 to 5 cm per sample) requires the processing of a vast amount of water samples and can take years to complete. Additionally, these procedures often come at the expense of not fully exploiting the temporal resolution available in the ice core.

Laser spectroscopy in the near and mid infrared region has been demonstrated as a potential alternative for water isotope analysis, presenting numerous advantages over IRMS (Kerstel et al., 1999; Kerstel, 2004). A major advantage of the technique is the ability to directly inject the sampled water vapour in the optical cavity of the spectrometer where both isotopic ratios $^{18}O/^{16}O$ and $^2H/^1H$ are measured simultaneously. In contrast, in the most common IRMS techniques water is not measured as such, but has to be converted to a different gas prior to measurement. For $\delta^{18}O$ analysis, the CO_2 equilibration method (Epstein, 1953) has been widely used, whereas δD analysis commonly involves the reduction of water to hydrogen gas over hot uranium (Bigeleisen et al., 1952; Vaughn et al., 1998; Huber and Leuenberger, 2003), or chromium (Ghere et al., 1996). However, the combined use of these two methods rules out simultaneous analysis of both water isotopologues on a given sample. More recently, in combination with the use of continuous flow mass spectrometers, conversion of water to CO and H_2 is performed in a pyrolysis furnice (Begley and Scrimgeour, 1997) and allows simultaneous δD and $\delta^{18}O$ measurement, but still on a single discrete sample. One of the drawbacks of this technique is the interference of NO , formed at the ion source by the reaction of N_2 and O_2 with the CO signal at $m/z = 30$ (Accoe, 2008). Nowadays, commercial IR spectrometers are available with a precision comparable to IRMS systems (Lis et al., 2008; Brand et al., 2009). These units typically receive a continuous stream of water vapour and offer ease of use and portability.

The analysis of another set of ice core proxies, that of chemical impurities, has similarly been an elaborate process, traditionally performed with liquid chromatography techniques. With the advent of Continuous Flow Analysis (heareafter CFA) from continuously melted ice core segments, the measurement of chemical impurities has reached the point of largely exploiting the high resolution available in the core while it is often performed in the field (Sigg et al., 1994; Röthlisberger et al., 2000; Kaufmann et al., 2008). The continuous, on-line nature of the technique has resulted in a considerable reduction in sample preparation and processing times. Recently, Schüpbach et al. (2009) demonstrated the measurement of CH_4 mixing ratios in an on-line semi continuous mode with the use of a gas chromatograph combined with a pulsed discharge and a thermal conductivity detector.

Here, we demonstrate the ability to perform continuous measurements of water isotope ratios from a stream of water vapor derived from a continuously melting ice rod by coupling a commercial IR spectrometer to a CFA system via a passive, low volume flash evaporation module. In the following, we assess the system's precision, accuracy, and efficient calibration. We then comment on issues related to sample dispersion in the sample transfer lines, the evaporation module and the optical cavity of the spectrometer itself in order to determine the expected smoothing imposed on the acquired data sets. Finally, isotopic analysis of ice core samples from the NEEM deep ice core are presented and compared to measurements performed in discrete mode.

2   Experimental

2.1   Continuous flow analysis

In the system described here, (Fig. 1) an ice rod measuring $3.2 \times 3.2 \times 110$ cm (hereafter CFA run) is continuously melted on a copper, gold-nickel coated melter at a regulated temperature of $20\,°C$. The concentric arrangement of the melter's surface facilitates the separation of the sample that originates from the outer and inner part of the core. Approximately 90 % of the sample from the inner part is transfered to the analytical system by means of a peristaltic pump with a flow rate of $16\,ml\,min^{-1}$. This configuration provides an overflow of ≈ 10 % from the inner to the outer part of the melter and ensures that the water sample that is introduced into the analytical system is not contaminated.

A stainless steel weight sitting on top of the ice rod enhances the stability and continuity of the melting process. An optical encoder connected to the stainless steel weight, records the displacement of the rod. This information is used
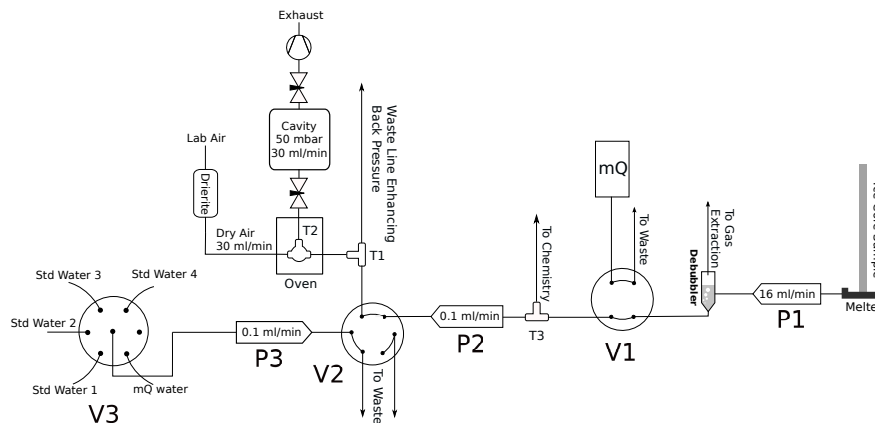
Fig. 1. Block diagram of the CFA-CRDS system.

to accurately define the depth scale of the produced water isotope data. Breaks in the ice rod are logged prior to the melting process and accounted for, during the data analysis procedure.

Gases included in the water stream originating from the air bubbles in the ice core are extracted in a sealed debubbler, with a volume of $\approx 300\,\mu l$. The melt rate of the present system is approximately $3.2\,cm\,min^{-1}$, thus resulting in an analysis time of $\approx 35\,min$ per CFA run. During the intervals between CFA runs, mQ^2 water is pumped through the system. A 4-port injection valve (V1 in Fig. 1) allows the selection between the mQ and sample water. The mQ water is spiked with isotopically enriched water containing 99.8 atom % deuterium, Cortecnet Inc.) in a mixing ratio of $\approx 1\,ppm$. In this way a distinction between sample and mQ water is possible, facilitating the identification of the beginning and end times of a CFA run.

For further details on the analysis of chemical components or the extraction of gases for greenhouse gas measurements the reader is refered to Kaufmann et al. (2008) and Schüpbach et al. (2009).

2.2 The water isotope measurement

We follow the same approach as previously presented in Gkinis et al. (2010) by coupling a commercially available Cavity Ring Down IR spectrometer (hereafter WS-CRDS) purchasecd from Picarro Inc. (Picarro L1102-i) (Crosson, 2008). The spectrometer operates with a gas flow rate of $30\,standard\,ml\,min^{-1}$. In the optical cavity the pressure is regulated at 47 mbar with two proportional valves in a feedback loop configuration up- and down-stream of the optical

[2]filtered and deionized water with a resistivity more than $18.2\,M\Omega\,cm$ and a total organic content less than 10 ppb.

cavity at a temperature of 80 °C. The high signal to noise ratio achieved with the Cavity Ring Down configuration in combination with fine control of the environmental parameters of the spectrometer, result in a performance comperable to modern mass spectrometry systems taylored for water stable isotope analysis.

A 6-port injection valve (V2 in Fig. 1) selects sample from the CFA line or a set of local water standards. The isotopic composition of the local water standards is determined with conventional IRMS and reported with respect to VSMOW standard. A 6-port selection valve (V3 in Fig. 1) is used for the switch between different water standards. A peristaltic pump (P3 in Fig. 1) in this line with variable speeds, allows adjustment of the water vapor concentration in the spectrometer's optical cavity, by varying the pump speed. In that way, the system's sensitivity to levels of different water concentration can be investigated and a calibration procedure can be implemented. We use high purity Perfluoroalkoxy (PFA) tubing for all sample transfer lines.

Injection of water sample into the evaporation oven takes place via a $\varnothing\,40\,\mu m$ fused silica capillary where immediate and 100 % evaporation takes place avoiding any fractionation effects. The setpoint of the evaporation temperature is set to 170 °C and is regulated with a PID controller. The amount of the injected water to the oven can be adjusted by the pressure gradient maintained between the inlet and waste ports of the T1 tee-split (Fig. 1). The latter depends on the ratio of the inner diameters of the tubes connected to the two ports as well as the length of the waste line. The total water sample consumption is $\approx 0.1\,ml\,min^{-1}$ maintained by the peristaltic pump P2 (Fig. 1). For a detailed description of the sample preparation and evaporation module the reader may reffer to Gkinis et al. (2010). A smooth and undisturbed sample delivery to the spectrometer at the level of $\approx 20\,000\,ppm$ results
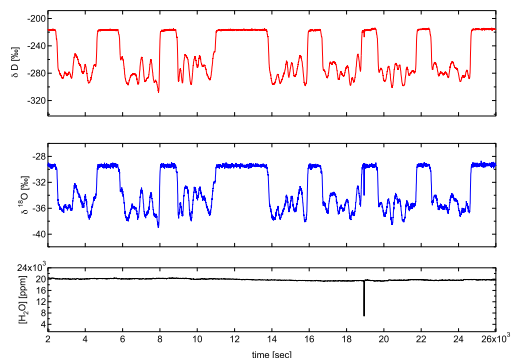
Fig. 2. Raw signals spanning 7 CFA runs on 29 May 2010.

in optimum performance of the system. Fluctuations of the sample flow caused by air bubbles or impurities are likely to result in a deteriorated performance of the measurement and are occasionally observed as extreme outliers on both δ^{18}O and δD measurements. The processes that control the occurence of these events are still not well understood.

3 Results and discussion – from raw data to isotope records

In this study we present data collected in the framework of the NEEM ice core drilling project. Measurements were carried out in the field during the 2010 field season and span 919.05 m of ice core (depth interval 1281.5–2200.55 m). Here we exemplify the performance of the system over a section of ice from the depth interval 1382.152–1398.607. The age of this section spans $\approx$411 yr with a mean age of 10.9 ka b2k [3]. The reported age is based on a preliminary time scale constructed by stratigraphic transfer of the GICC05 time scale (Rasmussen et al., 2006) from the NGRIP to the NEEM ice core.

In Fig. 2 we present an example of raw data as acquired by the system. This data set covers 7 CFA runs (7.70 m of ice). A clear baseline of the isotopically heavier mQ water can be seen in between CFA runs. At $t = 1.9 \times 10^4$ s one can observe a sudden drop in the signal of the water concentration due to a scheduled change of the mQ water tank. Adjacent to this, both δ^{18}O and δD signals present a clear spike, characteristic of the sensitivity of the system to the stability of the sample flow rates.

3.1 VSMOW – water concentration calibrations

Before any further processing we correct the acquired data for fluctuations of the water concentration in the optical

---

[3]thousand years before 2000 AD (ka b2k)

cavity. To a good approximation the δ^{18}O and δD signals show a linear response to differences in water concentrations around 20 000 ppmv (Brand et al., 2009; Gkinis et al., 2010). A correction is performed as:

$$\Delta\delta = \alpha(R_{20} - 1) \tag{1}$$

Here $R_{20} = \frac{[\text{H}_2\text{O}]}{20000}$, $\alpha_{18} = 1.94\,‰$ and $\alpha_D = 3.77\,‰$ as estimated in Gkinis et al. (2010). The estimation of these values has been performed several times during the period July 2009–October 2011. Based on compiled data from 6 calibrations we can report that these values do not appear to be drifting in the course of the two years. The values reported here are the ones estimated chronologically closer to the measurements we present here. These values are most likely instrument specific and should be used with caution for other analyzers. We typically operate the system in the area of 17 000–22 000 ppmv in which we observe no impact of the water concentration level on the precision of the isotopic signal. The mean and standard deviation of the water concentration signal in the course of aprroximately 7 h as seen in Fig. 2 is 19 939±306 ppmv. The water concentration correction is applied to the raw data, scaling all the isotopic values to the level of 20 000 ppmv.

Raw data are expressed in per mil values for both δ^{18}O and δD and ppmv for the water vapour concentration. These values are based on the slope and intercept values of the instrument's stored internal calibration line. Due to apparent instrumental drifts though, the latter are expected to deviate with time. To overcome this problem we perform frequent VSMOW calibrations by using 3 local water standards with well known δ^{18}O and δD values measured by conventional Isotope Ratio Mass Spectrometry combined with a pyrolysis glassy carbon reactor (Thermo DeltaV–TC/EA). The water standards are transported and stored in the field using the necessary precautions to avoid evaporation. We used amber glass bottles with silicon sealed caps. Two of the water standards are used to calculate the slope and the intercept of the calibration line and the third is used for a check of the linearity and the accuracy. The frequency of the VSMOW calibrations depends on the work flow of the overall CFA system. For the particular section we present here a VSMOW calibration was performed the same day.

In Fig. 3 we illustrate this calibration. Based on the measured and real values of the standards "−22" and "−40" the measurement of the "NEEM" standard can be used as a test for accuracy and linearity. In Table 1 we present the VSMOW calibrated values of the water standards as estimated with the IRMS system. The slope and intercept of the calibration lines are [1.002, −0.007] for δ^{18}O and [0.963, −8.214] for δD. Based on these values one can calculate the isotopic composition of the "NEEM" standard. The results we obtain are −33.4‰ and −256.99‰ for δ^{18}O and δD respectively. This results in a difference of 0.04‰ (0.31‰) for δ^{18}O (δD), giving an indication about the accuracy obtained by the system.
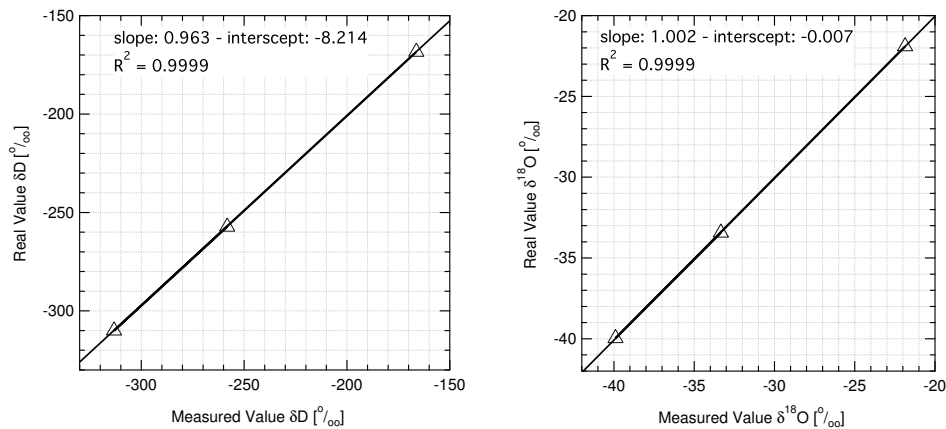
Fig. 3. VSMOW calibrations with three water standards "−22", "−40" and "NEEM"; Left – δD, right – δ^{18}O.

Table 1. Isotopic composition of the standards used for the VS-MOW calibrations in ‰.

	−22	NEEM	−40
δ^{18}O	−21.9	−33.44	−39.97
δD	−168.4	−257.3	−310

3.2 The depth scale

The melting process is recorded by an optical encoder connected to the top of the stainless steel weight that lies on top of the ice rod. The data acquired by the optical encoder allow for a conversion of the measurement time scale to a depth scale. In order to locate the beginning and end of every run we take advantage of the isotopic step observed during the transition between mQ baseline and sample water. A smoothed version of the discrete derivative of the acquired isotope data for both δ^{18}O and δD reveals a local minimum (maximum) for the beginning (end) of the measurement (Fig. 4). The logged depth of the top and the bottom of the CFA run is assigned to these points. Data that lie in the transition interval between mQ and sample water are manually removed from the series. Additional breaks within a CFA run that can possibly be created during the drilling or processing phase of the ice core, are taken into account at the last stage of the data analysis. If necessary and depending on their size, the gaps can be filled by means of some interpolation technique. Here, due to the small size of the gaps we use a linear interpolation scheme. The use of more advanced methods is also possible but is out of the scope of this work. The processed profiles presented in Fig. 4 are reported with

a nominal resolution of 5 mm. The interpolated sections are highlighted with gray bars. Their width indicates the length of the gaps.

3.3 Noise level – comparison with discrete data

An estimate of the noise level of the measurements can be obtained from the appropriately normalized power spectral density of the time series. Using the δ^{18}O and δD data of the section under consideration, we implement an autoregressive spectral estimation method developed by Burg (1975) by the use of the algorithm introduced by Andersen (1974). The order of the autoregressive model is $M = 300$. The standard deviation of the time series will be defined as:

$$\sigma^2 = \int_{-f_c}^{f_c} |\hat{\eta}(f)|^2 df \qquad (2)$$

where the Nyquist frequency is $f_c = 100\,\text{cycles m}^{-1}$ and $|\hat{\eta}(f)|^2$ can be obtained by a linear fit on the flat high frequency part of the spectrum (Fig. 5). By performing this analysis we obtain $\sigma_{18} = 0.055$ ‰ and $\sigma_{\text{D}} = 0.21$ ‰.

In order to validate the quality of the calibrations as well as the estimated depth scale we compare the CFA data with measurements performed in a discrete fashion using the same WS-CRDS spectrometer in combination with a sample preparation evaporator system (Gupta et al., 2009) and an autosampler. The discrete samples are cut in a resolution of 5 cm. The sample injection sequence takes into account apparent memory effects and results are reported on the VS-MOW scale by appropriate calibration using local water standards. The results are illustrated in Fig. 6 for δ^{18}O and δD. The comparison of the data sets demonstrates validity of the
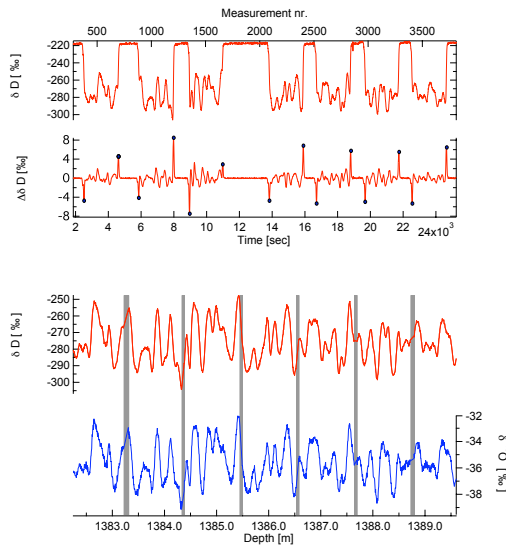
Fig. 4. The beginning and end of each CFA run is determined by the extrema of the 1st derivative of the isotopic signal, presented on the top graph. With gray bars we indicate the position and width of sections with data that are missing due to breaks in the ice, or removed in order to account for the transition from mQ water to sample and vice cersa.

Fig. 5. δ^{18}O and δD power spectral density based on the data of the interval 1382.152–1398.607 m.

followed calibration procedures. The benefits of the technique in terms of achieved resolution can be seen when one compares the two datasets over isotopic cycles with relatively small amplitude and higher frequency. Such an example can be seen at the depth of 1390.5 m where a sequence of 4 cycles is sampled relatively poorly with the discrete method when compared to the on-line system. This performance can benefit studies that look into the spectral properties of the signals by providing better statistics for the obtained measurements.

3.4 Obtained resolution – diffusive sample mixing

One of the advantages of the combined CFA–CRDS technique for water isotopic analysis of ice cores lies in the potential for higher resolution measurements relative to discrete sampling. However, diffusion effects in both the liquid and the vapor phase are expected to attenuate the obtained resolution.

Attenuation of the initial signal of the precipitation occurs also via a combination of in situ processes that take place after deposition. The porous medium of the firn column allows for an exchange of water molecules in the gas phase along the isotopic gradients of the profile. For the case of polar sites, this process has been studied extensively (Johnsen,

1977; Whillans and Grootes, 1985) and can be well described and quantified provided that a good estimate of the diffusivity coefficient and a strain rate history of the ice core site are available (Johnsen et al., 2000). The process ceases when the porous medium is closed-off and the diffusivity of air reaches zero at a density of $\approx$804 kg m^{-3}. Deeper in the ice, diffusion within the ice crystals takes place via a process that is considerably slower when compared with the firn diffusion. At a temperature of $-30\,^{\circ}$C the diffusivity coefficients of these two processes differ by 4 orders of magnitude (Johnsen et al., 2000).

Assuming an isotopic signal δ_{pr} for the precipitation, the total effect of the diffusive processes, in-situ and experimental, can be seen as the convolution of $\delta_{pr}(z)$ with a smoothing filter $\mathcal{G}_{tot}$.

$$\delta_m(z) = \int_{-\infty}^{\infty} \delta_{pr}(\tau)\mathcal{G}_{tot}(z-\tau)d\tau = [\delta_{pr} * \mathcal{G}_{tot}](z) \quad (3)$$

where $\delta_m(z)$ is the measured signal and $(*)$ denotes the convolution operation. Since instrumental and in-situ firn-ice diffusion are statistically independent, the variance of the total smoothing filter is the sum of the variances of the in-situ and experimental smoothing filters (hereafter $\mathcal{G}_{firn}$, σ_{firn}, $\mathcal{G}_{cfa}$, σ_{cfa}).

$$\sigma_{tot}^2 = \sigma_{firn}^2 + \sigma_{cfa}^2 \quad (4)$$

It can be seen that any attempt to study firn and ice diffusion by means of ice core data obtained with an on-line method similar to the one we present here, requires a good assesment of the diffusive properties of the experimental system. The latter is possible if one is able to estimate the variance of the smoothing filter $\mathcal{G}_{cfa}$ expressed by the variance σ_{cfa}^2 (hereafter diffusion length). One way to approach this problem is to measure the response of the system to a step function. Ideally, in the case of zero diffusion, a switch between two
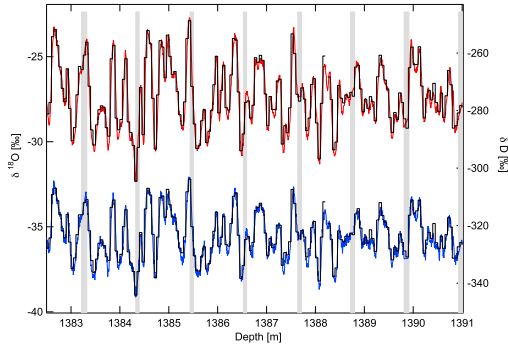
Fig. 6. Comparison CRDS-CFA with 5 cm discrete samples for δD (top) and $\delta^{18}O$ (bottom). Bars indicate the position and width of sections with missing/removed data.

isotopic levels would be described by a scaled and shifted version of the the Heaviside unit step function as:

$$\delta_H(z) = \begin{cases} C_2 & z < 0 \\ C_1 H(z) + C_2 & z \geq 0 \end{cases} \quad (5)$$

where the isotopic shift takes place at $z = 0$, $H(z)$ is the Heaviside unit step function and C_1 and C_2 refer to the amplitude and base line level of the isotopic step. Convolution of the signal of Eq. (5) with $\mathcal{G}_{cfa}$ and subsequent calculation of the derivative yields,

$$\frac{d\delta_m}{dz} = \frac{d\delta_H}{dz} * \mathcal{G}_{cfa} = C_1 \frac{dH}{dt} * \mathcal{G}_{cfa} = C_1 \delta_{Dirac} * \mathcal{G}_{cfa} \quad (6)$$

Thus the derivative of the measured signal, properly normalized, equals the impulse respone of the system. Applying the Fourier transform, denoted by the overhead hat symbol, in Eq. (6), and by using the convolution theorem, we deduce the transfer function $\hat{\mathcal{G}}_{cfa}$ of the system:

$$\widehat{\frac{d\delta_m}{dz}} = C_1 \hat{\delta}_{Dirac} \cdot \hat{\mathcal{G}}_{cfa} = C_1 \cdot \hat{\mathcal{G}}_{cfa} \quad (7)$$

In the case of the system presented here, an isotopic transition can be observed when the main CFA valve (V1 in Fig. 1) switches between mQ water and sample at the beginning and the end of each CFA run as shown in Fig. 4. By using these transitions we are able to construct isotopic steps and estimate the impulse response of the system. Such an isotopic step is illustrated in Fig. 7a. We fit the data of Fig. 7a with a scaled version of the cumulative distribution function of a normal distribution described as

$$\delta_{model}(z) = \frac{C_1'}{2} \left[1 + \text{erf}\left(\frac{z - z_0}{\sigma_{step}\sqrt{2}} \right) \right] + C_2' \quad (8)$$

The values of C_1', C_2', z_0 and σ_{step} are estimated by means of a least square optimization and used accordingly to normalize the length scale and the isotopic values of the step.

A nominal melt rate of $3.2\,\text{cm}\,\text{min}^{-1}$ is used for all the calculations presented here. We focus our analysis on the δD signal. The same approach can be followed for $\delta^{18}O$. In Fig. 7b we present the calculated impulse response of the system. The latter can be well approximated by a Gaussian type filter described as:

$$\mathcal{G}_{cfa}(z) = \frac{1}{\sigma_{cfa}\sqrt{2\pi}} e^{-\frac{z^2}{2\sigma_{cfa}^2}} \quad (9)$$

The diffusion length term σ_{cfa} is equal to $13.4 \pm 0.17\,\text{mm}$ (1σ) as calculated with the least squares optimization. The transfer function for this filter will be given by its Fourier transform, which is itself a Gaussian and is equal to (Abramowitz and Stegun, 1964):

$$\mathfrak{F}[\mathcal{G}_{cfa}(z)] = \hat{\mathcal{G}}_{cfa} = \frac{1}{2\pi} \int_{-\infty}^{\infty} \frac{1}{\sigma_{cfa}\sqrt{2\pi}} e^{-\frac{z^2}{2\sigma_{cfa}^2}} e^{-ikz} dk = e^{\frac{-k^2\sigma_{cfa}^2}{2}} \quad (10)$$

where $k = \frac{2\pi}{\lambda}$ and λ is the wavelength[4] of a harmonic of the isotopic signal. Harmonics with an initial amplitude A_0 and wavenumber k will be attenuated to a final amplitude equal to:

$$A = A_0 e^{\frac{-k^2\sigma_{cfa}^2}{2}} \quad (11)$$

An estimate of the transfer function based on the data and the cumulative distribution model is presented in Fig. 8 (blue and pink curve, respectively). As seen in this plot, cycles with wavelengths longer than 25 cm experience negligible attenuation, whereas cycles with a wavelength of 7 cm are attenuated by $\approx 50\%$.

The step response approach has been followed in the past for on-line chemistry data. In some studies such as Sigg et al. (1994) and Rasmussen et al. (2005), the resolution of the experimental system was assessed via the estimation of the transfer function. In other studies (Röthlisberger et al., 2000; Kaufmann et al., 2008), the characteristic time in which a step reaches a certain level (typically $1/e$) with respect to its final value, is used as a measure of the obtained resolution of the system. A common weakness of this approach as applied in the current, as well as previous studies, is that it is based on the analysis of a step that is introduced in the analytical system by switching a valve that is typically situated downstream of the melting and the debubbling system. Consequently, the impact of these last two elements on the smoothing of the obtained signals is neglected. In this study, this is the valve V1 in Fig. 1.

To overcome this problem we will present here an alternative way, based on the comparison of the spectral properties of the on-line CFA data and the off-line discrete data in 5 cm sampling resolution, presented in Sect. 3.2. In this approach

---

[4]Here the term wavelength refers to the isotopic signal in the ice and should not be confused with the wavelength of the light emitted by the laser diode of the spectrometer.
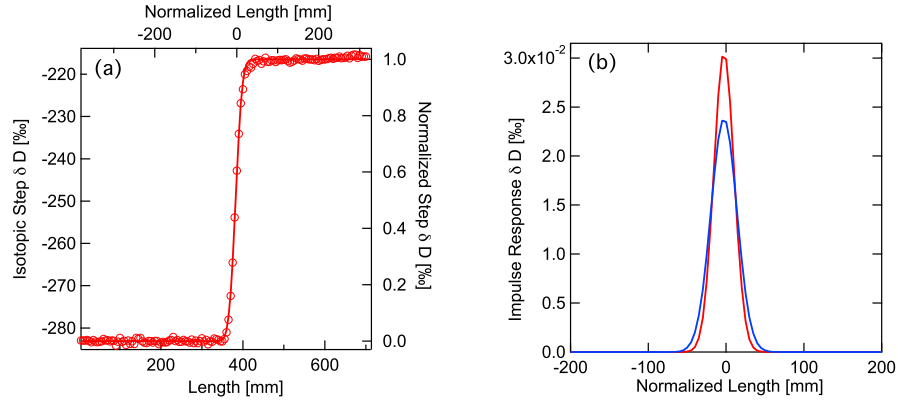
Fig. 7. (a) Isotopic δD step. The length scale is normalized so normalized length $= 0$ when the normalized δD value equals 0.5 ‰. **(b)** Impulse Response of the system for δD based on the step response (red) and the spectral analysis (blue) with $\sigma_{cfa} = 13.4$ and 16.4 mm, respectively.
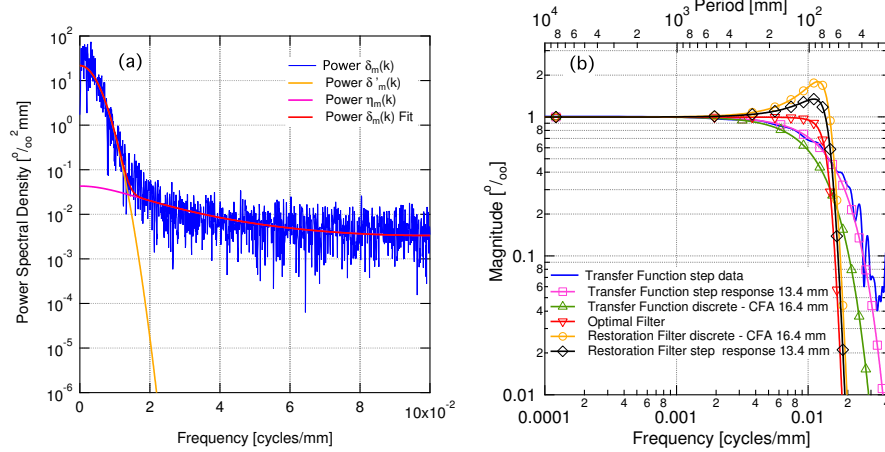
Fig. 8. (a) Power spectral density of δD. **(b)** Transfer function calculated based on the step response with $\sigma_{cfa} = 13.4$ mm (pink – squares) and the comparison between discrete and CFA analysis with $\sigma_{cfa} = 16.4$ mm (green – triangles). Restoration filters built considering the two different transfer functions are illustrated with orange circles ($\sigma_{cfa} = 16.4$ mm) and black diamonds ($\sigma_{cfa} = 13.4$ mm).

the diffusion length of the total smoothing filter for the off-line discrete analysis will be:

$$\sigma_{off}^2 = \sigma_{firn}^2 + \sigma_{5cm}^2 \qquad (12)$$

where σ_{5cm}^2 is the diffusion length of the smoothing imposed by the sample cutting scheme at a 5 cm resolution. If one averages the on-line CFA data at a 5 cm resolution by means of a running mean filter, the diffusion length of the total smoothing filter for the on-line CFA measurements averaged on a 5 cm resolution will be:

$$\sigma_{on}^2 = \sigma_{firn}^2 + \sigma_{5cm}^2 + \sigma_{cfa}^2 \qquad (13)$$

From Eqs. (12) and (13) we get:

$$\sigma_{cfa}^2 = \sigma_{on}^2 - \sigma_{off}^2 \qquad (14)$$

As a result, the term $\sigma_{on}^2 - \sigma_{off}^2$ is directly related to the diffusion length of the smoothing filter of the whole CFA-water isotope system including the melting and debubbling sections. Based on Eq. (11), the power spectral density of the signals will be:
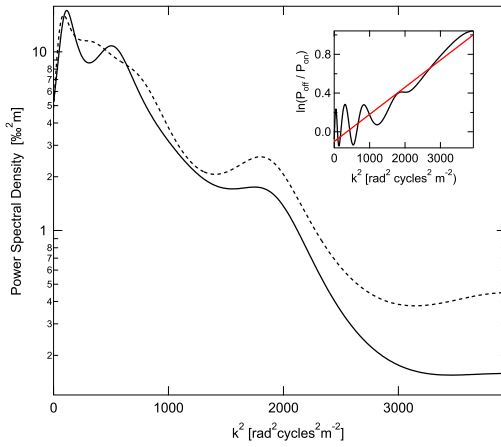
Fig. 9. Calculation of the diffusion length for the transfer function of the CFA system. The dashed and solid lines represent, respectively the power spectral density of the offline discrete data and the CFA data averaged on a 5 cm resolution.

$$P = P_0 e^{-k^2 \sigma^2} \tag{15}$$

where σ^2 refers in this case to σ_{on}^2 or σ_{off}^2. Combining the power spectral densities of the on-line and off-line time series we finally get:

$$\ln\left(\frac{P_{off}}{P_{on}}\right) = \ln\left(\frac{P_{0off}}{P_{0on}}\right) + \sigma_{cfa}^2 k^2 \tag{16}$$

Hence, the logarithm of the ratio P_{off}/P_{on} is linearly related to k^2 with a slope equal to σ_{cfa}^2. In Fig. 9 we perform this analysis for δD and by applying a linear fit we calculate the $\sigma_{cfa}[D]$ to be equal to 16.4 ± 2.4 mm. In a similar manner $\sigma_{cfa}[O18]$ is found to be equal to 16.8 ± 2.3 mm.

The higher value calculated with the spectral method points to the additional diffusion of the sample at the melter and debubbler system that could not be considered in the analysis based on the step response. The impulse response of the system based on the updated value of σ_{cfa}^2 is presented in Fig. 6.

3.5 Optimal filtering

In the ideal case of a noise-free measured signal $\delta_m'(z)$ and provided that the transfer function $\hat{\mathcal{G}}_{cfa}$ is known, one can reconstruct the initial isotopic signal $\delta_i(z)$ from Eq. (3) as:

$$\delta_i(z) = \frac{1}{2\pi} \int_{-\infty}^{\infty} \frac{\hat{\delta}_m'(k)}{\hat{\mathcal{G}}(k)} e^{ikz} dk \tag{17}$$

where the integral operation denotes the inverse Fourier transform and $k = \frac{2\pi}{\lambda}$ with λ being the wavelength of the

isotopic signals. In the presence of measurement noise $\eta(z)$, this approach will fail due to excess amplification of the high frequency noise channels in the spectrum of the signal.

Hereby we use the Wiener approach in deconvoluting the acquired isotopic signals for the diffusion that takes place during the measurement. Considering a measured isotopic signal

$$\delta_m(z) = \delta_m'(z) + \eta(z) \tag{18}$$

an optimal filter $\varphi(z)$ can be constructed that when used at the deconvolution step, it results in an estimate of the initial isotopic signal described as:

$$\tilde{\delta}_i(z) = \frac{1}{2\pi} \int_{-\infty}^{\infty} \frac{\hat{\delta}_m(k)}{\hat{\mathcal{G}}(k)} \hat{\varphi}(k) e^{ikz} dk \tag{19}$$

Assuming that $\delta_m'(z)$ and $\eta(z)$ are uncorrelated signals, the optimal filter is given by:

$$\hat{\varphi}(k) = \frac{|\hat{\delta}_m'(k)|^2}{|\hat{\delta}_m'(k)|^2 + |\hat{\eta}(k)|^2} \tag{20}$$

(Wiener, 1949); where $|\hat{\delta}_m'(k)|^2$ and $|\hat{\eta}(k)|^2$ are the power spectral densities of the signals $\delta_m'(z)$ and $\eta(z)$.

In the same fashion as in the previous section we assume that the spectrum of the noise free measured signal $|\hat{\delta}_m'(k)|^2$, is described by Eq. (15) where $\sigma^2 = \sigma_{tot}^2$. Regarding the noise, we assume red noise described by an AR1 process. The spectrum of the noise signal will then be described by (Kay and Marple, 1981):

$$|\hat{\eta}(k)|^2 = \frac{\sigma_\eta^2 \Delta z}{|1 + a_1 \exp(-ik\Delta z)|^2} \tag{21}$$

where σ_η^2 is the variance of the noise and a_1 is the coefficient of the AR1 process. We vary the parameters σ_{tot}^2, P_0, σ_η^2 and a_1 so that the sum $|\hat{\delta}_m(k)|^2 = |\hat{\delta}_m'(k)|^2 + |\hat{\eta}(k)|^2$ fits the spectrum of the measured signal. The set of parameters that results in the optimum fit is used to calculate the optimal filter.

The constructed filters together with the transfer functions that were calculated based on the two different techniques outlined in Sect. 3.4 are illustrated in Fig. 8. One can observe how the restoration filters work by amplifying cycles with wavelengths as low as 7 mm. Beyond that point, the shape of the optimal filter attenuates cycles with higher frequency, which lie in the area of noise. An example of deconvoluted δD data section is given in Fig. 10. It can be seen that the effect of the optimal filtering results in both the amplification of the signals that are damped due to the instrumental diffusion, as well as in the filtering of the measurement noise.

3.6 Information on deuterium excess

Combining $\delta^{18}O$ and δD gives the deuterium excess as $D_{xs} = \delta D - 8\delta^{18}O$ (Craig et al., 1963; Mook, 2000). The

www.atmos-meas-tech.net/4/2531/2011/ Atmos. Meas. Tech., 4, 2531–2542, 2011

page | 175
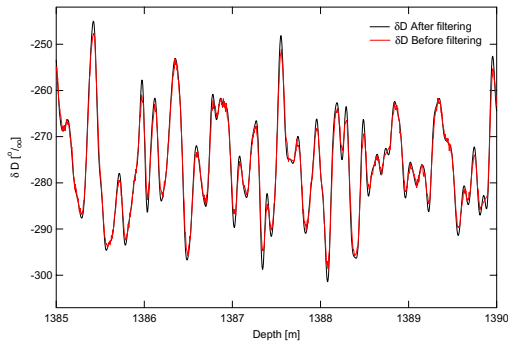
Fig. 10. δD signal before and after optimal filtering.

noise level of the D_{xs} signal can be calculated by the estimated noise levels of δ^{18}O and δD as:

$$\sigma_{D_{xs}} = \sqrt{\sigma_D^2 + 64 \cdot \sigma_{18}^2} = 0.48\ ‰ \tag{22}$$

As seen in Fig. 11, the D_{xs} signal presents a low signal to noise ratio. In this case, the technique of optimal filtering can effectively attenuate unwanted high frequency noise components, thus reveiling a "clean" D_{xs} signal.

The latter offers the possibility for the study of abrupt transitions as they have previously been investigated in δ^{18}O, δD and D_{xs} time series from discrete high resolution samples (Steffensen et al., 2008). The on-line fashion in which these measurements are performed has the potential to yield not only higher temporal resolution but also better statistics for those climatic transitions.

4   Summary and conclusions

We have succesfully demonstrated the possibility for on-line water isotopic analysis on a continuously melted ice core sample. We used an infrared laser spectrometer in a cavity ring down configuration in combination with a continuous flow melter system. A custom made continuous stream flash evaporator served as the sample preparation unit, interfacing the laser spectrometer to the melter system.

Local water standards have been used in order to calibrate the measurements to the VSMOW scale. Additionally, dependencies related to the sample size in the optical cavity have been accounted for. The melting procedure is recorded by an optical encoder that provides the necessary information for assigning a depth scale to the isotope measurements. We verified the validity of the applied calibrations and the calculated depth scale by comparing the CFA measurements with measurements performed on discrete samples in 5 cm resolution.

By means of spectral methods we provide an estimate of the noise level of the measurements. The combined uncertainty of the measurement is estimated at $\approx$0.06, 0.2, and
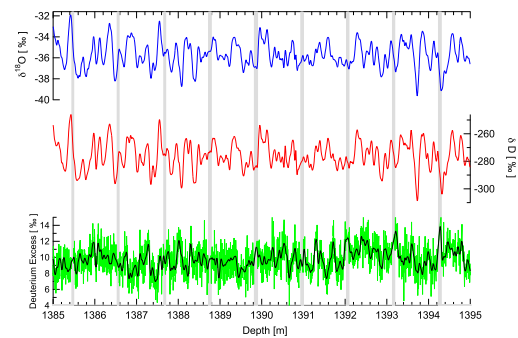
Fig. 11. δ^{18}O, δD and D_{xs} signals after the optimal filtering. For the D_{xs} we present the signal before (light green) and after (black) the filtering. Gray bars indicate the position and width of sections with missing/removed data.

0.5 ‰ for δ^{18}O, δD and D_{xs}, respectively. This performance is comparable to, or better than the performance typically achieved with conventional IRMS systems in a discrete mode.

Based on the isotopic step at the beginning of each CFA run, the impulse response, as well as the transfer function of the system can be estimated. We show how this method does not take into account the whole CFA system, thus underestimating the sample diffusion that takes place from the melter until the optical cavity of the spectrometer. We proposed a different method that considers the power spectrum of the CFA data in combination with the spectrum of a data set over the same depth interval measured in a discrete off-line fashion. The use of the optimal filtering deconvolution technique, provides a way to deconvolute the measured isotopic profiles for apparent sample dispersion effects.

The combination of infrared spectroscopy on gaseuous samples with continuous flow melter systems provides new possibilities for ice core science.The non destructive, continuous, and on-line technique offers the possibility for analysis of multiple species on the same sample in high resolution and precision and can potentially be performed in the eld.

References

Abramowitz, M. and Stegun, I. A.: Handbook of Mathematical Functions with Formulas, Graphs, and Mathematical Tables, Dover, New York, 1964.

Accoe, F., Berglund, M., Geypens, B., and Taylor, P.: Methods to reduce interference effects in thermal conversion elemental analyzer/continuous flow isotope ratio mass spectrometry $\delta^{18}O$ measurements of nitrogen-containing compounds, Rapid Commun. Mass Sp., 22, 2280–2286, 2008.

Andersen, N.: Calculation of filter coefficients for maximum entropy spectral analysis, Geophysics, 39, 69–72, 1974.

Begley, I. S. and Scrimgeour, C. M.: High-precision δ^2H and $\delta^{18}O$ measurement for water and volatile organic compounds by continuous-flow pyrolysis isotope ratio mass spectrometry, Anal. Chem., 69, 1530–1535, 1997.

Bigeleisen, J., Perlman, M. L., and Prosser, H. C.: Conversion of hydrogenic materials to hydrogen for isotopic analysis, Anal. Chem., 24, 1356–1357, 1952.

Brand, W. A., Geilmann, H., Crosson, E. R., and Rella, C. W.: Cavity ring-down spectroscopy versus high-temperature conversion isotope ratio mass spectrometry; a case study on δ^2H and $\delta^{18}O$ of pure water samples and alcohol/water mixtures, Rapid Commun. Mass Sp., 23, 1879–1884, doi:10.1002/rcm.4083, 2009.

Burg, J. P.: Maximum Entropy Spectral Analysis, Ph.D. thesis, Stanford University, 1975.

Craig, H., Gordon, L. I., and Horibe, Y.: Isotopic exchange effects in evaporation of water low-temperature experimental results, J. Geophys. Res., 68, 5079–5087, 1963.

Crosson, E. R.: A cavity ring-down analyzer for measuring atmospheric levels of methane, carbon dioxide, and water vapor, Appl. Phys. B-Lasers O., 92, 403–408, 2008.

Cuffey, K. M. and Vimeux, F.: Covariation of carbon dioxide and temperature from the Vostok ice core after deuterium-excess correction, Nature, 412, 523–527, 2001.

Dansgaard, W.: Stable isotopes in precipitation, Tellus, 16, 436–468, 1964.

Epstein, S. and Mayeda, T.: Variations of ^{18}O content of waters from natural sources, Geochim. Cosmochim. Ac., 4, 213–224, 1953.

Gehre, M., Hoefling, R., Kowski, P. and Strauch, G.: Sample preparation device for quantitative hydrogen isotope analysis using chromium metal, Anal. Chem., 68, 4414–4417, 1996.

Gkinis, V., Popp, T. J., Johnsen, S. J., and Blunier, T.: A continuous stream flash evaporator for the calibration of an IR cavity ring down spectrometer for isotopic analysis of water, Isot. Environ. Health S., 46, 1–13, 2010.

Gupta, P., Noone, D., Galewsky, J., Sweeney, C., and Vaughn, B. H.: Demonstration of high-precision continuous measurements of water vapor isotopologues in laboratory and remote field deployments using wavelength-scanned cavity ring-down spectroscopy (WS-CRDS) technology, Rapid Commun. Mass Sp., 23, 2534–2542, 2009.

Huber, C. and Leuenberger, M.: Fast high-precision on-line determination of hydrogen isotope ratios of water or ice by continuous-flow isotope ratio mass spectrometry, Rapid Commun. Mass Sp., 17, 1319–1325, 2003.

Johnsen, S.: Stable isotope homogenization of polar firn and ice, Isotopes and Impurities in Snow and Ice, 210–219, 1977.

Johnsen, S. J., Dansgaard, W., and White, J. W. C.: The origin of Arctic precipitation under present and glacial conditions, Tellus, 41B, 452–468, 1989.

Johnsen, S. J., Clausen, H., Dansgaard, W., Fuhrer, K., Gundestrup, N., Hammer, C., Iversen, P., Jouzel, J., Stauffer, B., and Steffensen, J.: Irregular glacial interstadials recorded in a new Greenland ice core, Nature, 359, 311–313, 1992.

Johnsen, S. J., Clausen, H. B., Cuffey, K. M., Hoffmann, G., Schwander, J., and Creyts, T.: Diffusion of stable isotopes in polar firn and ice, The isotope effect in firn diffusion, in: Physics of Ice Core Records, edited by: Hondoh, T., Hokkaido University Press, Sapporo, 121–140, 2000.

Johnsen, S. J., Dahl Jensen, D., Gundestrup, N., Steffensen, J. P., Clausen, H. B., Miller, H., Masson-Delmotte, V., Sveinbjörnsdóttir, A. E., and White, J. W. C.: Oxygen isotope and palaeotemperature records from six Greenland ice-core stations: Camp Century, Dye-3, GRIP, GISP2, Renland and North-GRIP, J. Quaternary Sci., 16, 299–307, 2001.

Jouzel, J. and Merlivat, L.: Deuterium and oxygen 18 in precipitation: modeling of the isotopic effects during snow formation, J. Geophys. Res.-Atmos., 89, 11749–11759, 1984.

Jouzel, J., Alley, R. B., Cuffey, K. M., Dansgaard, W., Grootes, P., Hoffmann, G., Johnsen, S. J., Koster, R. D., Peel, D., Shuman, C. A., Stievenard, M., Stuiver, M., and White, J. W. C.: Validity of the temperature reconstruction from water isotopes in ice cores, J. Geophys. Res.-Oceans, 102, 26471–26487, 1997.

Kaufmann, P. R., Federer, U., Hutterli, M. A., Bigler, M., Schüpbach, S., Ruth, U., Schmitt, J., and Stocker, T. F.: An improved continuous flow analysis system for high-resolution field measurements on ice cores, Environ. Sci. Technol., 42, 8044–8050, 2008.

Kavanaugh, J. L. and Cuffey, K. M.: Generalized view of source-region effects on δD and deuterium excess of ice-sheet precipitation, Ann. Glaciol., 35, 111–117, 2002.

Kay, S. M. and Marple, S. L.: Spectrum analysis – a modern perspective, P. IEEE, 69, 1380–1419, 1981.

Kerstel, E. R. T.: Handbook of Stable Isotope Analytical Techniques, Vol. 1, Elsevier B. V., Amsterdam, 2004.

Kerstel, E. R. T., van Trigt, R., Dam, N., Reuss, J., and Meijer, H. A. J.: Simultaneous determination of the $^2H/^1H$, $^{17}O/^{16}O$ and $^{18}O/^{16}O$ isotope abundance ratios in water by means of laser spectrometry, Anal. Chem., 71, 5297–5303, 1999.

Lis, G., Wassenaar, L. I., and Hendry, M. J.: High-precision laser spectroscopy D/H and O-18/O-16 measurements of microliter natural water samples, Anal. Chem., 80, 287–293, 2008.

Mook, W.: Environmental Isotopes in the Hydrological Cycle: Principles and Applications, Vol. I, International Atomic Energy Agency, 2000.

NGRIP members: High-resolution record of Northern Hemisphere climate extending into the last interglacial period, Nature, 431, 147–151, 2004.

Rasmussen, S. O., Andersen, K. K., Johnsen, S. J., Bigler, M., and McCormack, T.: Deconvolution-based resolution enhancement of chemical ice core records obtained by continuous flow analysis, J. Geophys. Res.-Atmos., 110, D17304, doi:10.1029/2004JD005717, 2005.

Rasmussen, S. O., Andersen, K. K., Svensson, A. M., Steffensen, J. P., Vinther, B. M., Clausen, H. B., Siggaard-Andersen, M. L., Johnsen, S. J., Larsen, L. B., Dahl-Jensen, D., Bigler, M., Röthlisberger, R., Fischer, H., Goto-Azuma, K.,

Hansson, M. E., and Ruth, U.: A new Greenland ice core chronology for the last glacial termination, J. Geophys. Res.-Atmos., 111, D06102, doi:10.1029/2005JD006079, 2006.

Röthlisberger, R., Bigler, M., Hutterli, M., Sommer, S., Stauffer, B., Junghans, H. G., and Wagenbach, D.: Technique for continuous high-resolution analysis of trace substances in firn and ice cores, Environ. Sci. Technol., 34, 338–342, 2000.

Schüpbach, S., Federer, U., Kaufmann, P. R., Hutterli, M. A., Bu-iron, D., Blunier, T., Fischer, H., and Stocker, T. F.: A new method for high-resolution methane measurements on polar ice cores using continuous flow analysis, Environ. Sci. Technol., 43, 5371–5376, 2009.

Sigg, A., Führer, K., Anklin, M., Staffelbach, T., and Zurmuhle, D.: A continuous analysis technique for trace species in ice cores, Environ. Sci. Technol., 28, 204–209, 1994.

Steffensen, J., Andersen, K., Bigler, M., Clausen, H., Dahl-Jensen, D., Fischer, H., Goto-Azuma, K., Hansson, M., Johnsen, S., Jouzel, J., Masson-Delmotte, V., Popp, T. J., Ras-mussen, S. O., Röthlisberger, R., Ruth, U., Stauffer, B., Siggaard-Andersen, M. L., Sveinbjörnsdóttir, A., Svensson, A., and White, J. W. C.: High-resolution Greenland ice core data show abrupt climate change happens in few years, Science, 321, 680–684 2008.

Vaughn, B. H., White, J. W. C., Delmotte, M., Trolier, M., Cat-tani, O., and Stievenard, M.: An automated system for hydrogen isotope analysis of water, Chem. Geol., 152, 309–319, 1998.

Whillans, I. and Grootes, P.: Isotopic diffusion in cold snow and firn, J. Geophys. Res., 90, 3910–3918, 1985.

Wiener, N.: Time Series, The MIT Press, Cambridge, Massachus-setts, 1949.